Spectroscopic studies of molten electrolyte mixtures, binary polar solvent mixtures and solvents under confinement

Thesis Submitted for the Degree of
Doctor of Philosophy (Science)
of
Jadavpur University

By

Biswajit Guchhait

Department of Chemical, Biological and Macromolecular Sciences
S. N. Bose National Centre for Basic Sciences
Block-JD, Sector-III, Salt Lake City
Kolkata – 700098, India
December 2012

Dedicated to

My Father Sri. Lakshman Chandra Guchhait

And

Mother Smt. Radha Rani Guchhait

Acknowledgement

I would like to express my sincere thank and deep sense of gratitude to my supervisor Professor Ranjit Biswas for his guidance and continued encouragement without which this work would not have been possible. The training I have received from him through the avenue of my research work will help me in the years to come. I also thank him for extreme care about my non-academic life.

I would also like to thank Dr. S. Mahiuddin, NEIST, Jorhat, Assam, Dr. Pradip Ghorai, IISER, Kolkata for their collaboration. I am also obliged to the Director, S. N. Bose National Centre for Basic Sciences, for providing the correct research atmosphere at the Centre. I would like to offer my heartfelt gratitude to Prof. Samir K. Pal, Prof. Jaydeb Chakraborti, Prof. Gautam Gangopadhyay and Prof. Priya Mahadevan for their deep concern about the progress of my research work. I thank Prof. Debabrata Mandal, Calcutta University, Kolkata for devoting his valuable time as an external expert. I am also thankful to all those faculty members and non-academic staffs of the centre who have supported me and made my stay here enjoyable.

I am thankful to my labmates who contributed in many ways: Snehasis, Tamisra, Anuradha, Sandipa, Suman, Kollol for providing me a homely and cheerful environment. I am also thankful to my ex-labmates, Dr. Tuhin Rradhan, Dr. Hemant Kashyap, Dr. Harun Al. Rasid Gazi for helping me in the initial days of my tenure. I am specially thankful to Dr. Pradhan for his help in many academic and non-academic related purposes.

I am also indebted to many of my teachers for drawing my attention in the subject of Chemistry.

I acknowledge Council of Scientific and Industrial Research, New Delhi for granting research fellowship.

I would like to thank Dr. Parijat Das for her encouragement and also express my love to cute Rwitoban and Arshaman.

I am grateful to all my friends Biswajit (B.D.), Kinshuk, Pramod, Prashant, Ambika, Debraj, Avinab, Hirak, Sudip, Avinandan, Nirmal, Surajit, Subrata, Ranajoy, Soumik, Anupam, Tanumoy, Avijit, Arka, Soumyajit, Arghya, who stood by my side whenever needed.

Special thanks to Pramod for helping me in many technical purposes. I also thank my friends Debasish, Sandip, Vishal for their assistance in some experimental measurements at IIT KGP.

I am really grateful to my uncle late Jhantu Guchhait for his love and care.

Finally, I express my homage and deep sense of gratitude to my parents (Sri. Lakshman Chandra Guchhait and Smt. Radha Rani Guchhait) and deep affection for my sisters (Namita and Mamata), brother-in-law (Sankar da and Lakshmi) and "Soma" for their patience and support.

Abstract

This Thesis deals with fluorescence spectroscopic investigations of rotational and solvation response of a dissolved dipolar dye in supercooled molten mixtures (deep eutectic solvents, DES), binary solvent mixtures and solvents under confinement. The DES considered are composed of amide and electrolytes and constitute a possible alternative to ionic liquids for industrial applications. Time-resolved fluorescence spectroscopy has been extensively used in tandem with steady state measurements to reveal not only the natural dynamics of these complex systems but also to unravel the interactions that dictates the timescales of the system response. A dye molecule which fluoresces and undergoes large change in dipole moment upon photo-excitation has been used. Our measurements with deep eutectics reveal viscosity decoupling of transport properties and subsequent fractional viscosity dependence at a temperature range ~100-150 K above the glass transition temperature of these individual melts. This is very similar to what has been found for deeply supercooled neat liquids. The investigations done in the binary mixtures have been aimed at generating a microscopic level understanding of the structure and dynamics of aqueous mixtures where phase-segregation at molecular level is expected to take place. The clustering of species and modification of hydrogen bonded network of water in such aqueous mixtures have been investigated by monitoring reactive and non-reactive dynamics. The origin of the slow dynamics reported by fluorescence measurements of reverse micelles have been explored by combining controlled time-resolved fluorescence measurements and simulation studies using realistic molecules.

Chapter 1 of the Thesis provides an introduction of the present work with a brief review of the relevant literature. Chapter 2 briefly describes main experimental technique and data analysis methods. In chapter 3-5 of the Thesis, fluorescence dynamics in various supercooled {alkylamide + electrolyte} molten mixtures is presented. Chapter 6 contains effects of surface charge on solute and solvent dynamics in confined environments. Chapter 7 describes a study of the effect of electrolyte/s on polymer (polyethylene glycol). The ion size effect is also investigated here. Structure and dynamics of aqueous solution of cycloethers is discussed in chapter 8. The Thesis ends with concluding remarks and several future research problems in chapter 9.

List of Publications

1. "*Fluorescence Spectroscopic Studies of (Acetamide + Sodium/ Potassium Thiocyantes) Molten Mixtures: Composition and Temperature Dependence*" by **Biswajit Guchhait,** Harun Al Rasid Gazi, Hemant Kashyap and Ranjit Biswas, Journal of Physical Chemistry B, **2010**, *114,* 5066.

2. "*Fluorescence Dynamics in Supercooled (Acetamide + Calcium Nitrate) Molten Mixtures*" by Harun Al Rasid Gazi, **Biswajit Guchhait,** Snehasis Daschakraborty and Ranjit Biswas, Chemical Physics Letters, **2011**, *501*, 358.

3. "*Influence of Chain Length of Alcohols on Stokes' Shift Dynamics in Catanionic Vesicles*" by Namrata Sarma, Jayanta M Borah, Sekh Mahiuddin, Harun Al Rasid Gazi, **Biswajit Guchhait** and Ranjit Biswas, Journal of Physical Chemistry B, **2011**, *115,* 9050.

4. "*Excited State Intramolecular Charge Transfer Reaction in Non-aqueous Reverse Micelles: Efects of Solvent Confinement and Electrolyte Concentration*" by Tuhin Pradhan, Harun Al Rasid Gazi, **Biswajit Guchhait** and Ranjit Biswas, Journal of Chemical Sciences, **2012**, *124,* 355.

5. "*Medium Decoupling of Dynamics at Temperatures ~100 K Above Glass-Transition Temperature: A Case Study with (Acetamide+ Lithium Bromide/ Nitrate) Melts*" by **Biswajit Guchhait**, Snehasis Daschakraborty and Ranjit Biswas, Journal of Chemical Physics, **2012**, *136*, 174503.

6. *"Solute and Solvent Dynamics in Confined Equal-Sized Aqueous Environments of Charged and Neutral Reverse Micelles: A Combined Dynamic Fluorescence and All-Atom Molecular Dynamics Simulation Study"* by **Biswajit Guchhait,** Ranjit Biswas and Pradip K. Ghorai, Journal of Physical Chemistry B, **2012** (minor revision).

7. *"Medium Heterogeneity in Presence of a Structure Breaker: Temperature Dependent Fluorescence Studies of Deep Eutectic (Alkylamide + Electrolyte) Melts"* by **Biswajit Guchhait**, Snehasis Daschakraborty and Ranjit Biswas. Journal of Physical Chemistry B, **2012** (submitted).

8. *"Exploring Solution Structures of Water/Cycloether Binary Mixtures by Reactive and non-reactive Dynamics"* by **Biswajit Guchhait** and Ranjit Biswas. Journal of Physical Chemistry B, **2012** (to be submitted soon).

9. *"Electrolyte Induced Heterogeneity and Break-down of Hydrodynamics in Polymer: Fluorescence Spectroscopic Evidence"* by **Biswajit Guchhait** and Ranjit Biswas. Journal of Chemical Physics, **2012** (to be submitted soon).

10. *“Binary mixtures under confinement”* by **Biswajit Guchhait**, P. K. Ghorai and Ranjit Biswas. *Chemical Physics Letter*, (in preparation).

11. *“Excited State Intramolecular Charge Transfer Reaction in Non-aqueous Solvent: Effect of pH”* by **Biswajit Guchhait** and Ranjit Biswas. *Chemical Physics* (in preparation).

Contents

Chapter 4: Medium Decoupling of Dynamics in (Acetamide + Lithium Bromide/ Nitrate) Melts at Temperatures ~100 K Above Glass-Transition Temperature.. 68

Chapter 1

Introduction

Solvent plays an important role in chemical reactions[1-20] and crucially determine biological functions.[21-38] Various processes, such as breaking and making of bonds, electron and proton transfer, protein folding, enzyme catalyzed reactions and stabilization of reactive species, to name but a few, have been affected by solvent with a modification of the potential energy surface, a frictional drag or stabilization of the product. Many of the above processes can take place in pure or multi-component mixtures on time scales that are accessible to modern laser spectroscopic techniques.[16,29,30,39-42] A complete understanding of chemical and biological processes require detailed knowledge of molecular pathways that are involved in reaction dynamics. Hence, a considerable attention, experimentalists' and theoreticians' alike, has been devoted to discover a set of unified principles describing the above dynamic processes in solvents.

Laser light possessing suitable energy and pulse duration can be used to selectively trigger the dynamic processes.[32,39-45] Photo induced processes involve a charge redistribution in absorbing species. The time dependent response of solvent molecules to an electronic redistribution of excited species dictates the rate of several photo induced processes.[46-54] This rearrangement of solvent molecules, which has been termed as solvation dynamics, gained considerable attention to understand dynamics and interaction in various media.[48,55-61] Solvent control arising out of complex interactions taking place in varied environments can be understood from solvation dynamics measurements and subsequent modelling. In fact, a convolution of dynamic measurements and suitable theory can lead to quantitative understanding of solvent control of a particular chemical reaction in a given medium.[1]

The above possibility fuels dynamic Stokes shift (DSS) measurements in systems that are nanoscopic and also systems possessing longer-ranged charge-charge interactions.[48,55,56,62-77] The following physical picture characterizes DSS measurements: a very dilute solution of a fluorescent probe molecule ($<10^{-5}$ mol/litre) is usually prepared in a given medium whose dynamics need to be measured. This level of dilution is necessary to avoid solute-solute interaction in the solution. In such a scenario, the solute is in its ground state (S_0) and in equilibrium with the surrounding solvent molecules. By shining with a laser pulse of appropriate energy, the solute goes to the first excited state (S_1) which may possess larger dipole moment than that of the S_0 state. It is generally assumed that the laser-excited solute couples only weakly to the medium and does not influence the natural dynamics of the medium. This is linear response and laser-excitation of the solute serves as a weak perturbation. The electronic transition is instantaneous compared to nuclear motion of the solvent molecules and thus such a situation is a non-equilibrium one. This drives the surrounding solvent molecules to rearrange so that the free energy of the solute-solvent composite system is minimized. This minimization process is reflected via the time-dependent red shift of the fluorescence spectrum emanating from the excited solute and a ruler for the timescales associated with the dynamical response of the medium. Again, this solvent relaxation process is related to reaction rate[50-53,78,79] because it provides an avenue for the medium for dynamical control of a reaction occurring in it. Additionally, the reaction rate can be modified by changing the static dielectric constant (ε_0) of the solvent via the modification of activation barrier. This is known as static solvent effects. Furthermore, investigation of solvent dynamics can reveal important information regarding intermolecular interactions, solvation modes and other related phenomena.[47,49,80-83] Dynamic fluorescence anisotropy measurements is another method that brings out solute-solvent interactions and compliments the DSS measurements.[49,80,69,70,74,84]

Research described in this Thesis involves solvation, rotation and charge transfer dynamics in molten (amide + electrolyte) mixtures, binary solvent mixtures, polymer-electrolyte and confined solvents created by reverse micelles. The molten mixtures (or deep eutectic mixtures) exhibit several different properties[85-97] from those of simple organic solvents. The important properties of these mixtures are high conductivity, nonvolatility, high thermal stability and large electrochemical window. Because of these unusual properties molten mixtures have potentials in electrochemical devices, supercapacitor technology[98] and as a media for synthesis of semiconducting films[99] and nanomaterials.[100] In recent time, it has been found that these deep eutectic mixtures can be used as an excellent electrolyte to improve the performance of battery.[101,102] Molten mixtures can easily be formed between short chain amides and electrolytes mixing in suitable proportions. Their physical properties can be tuned by changing the cation and anion of electrolyte, and alkyl substituent and functional group of amide. Therefore the ease of preparation, availability and various important applications make these mixtures possible alternatives to room temperature ionic liquids. Interestingly, while a lot of concern has been devoted to investigate the structure and dynamics of ionic liquids,[65,66,69,70,72-74,103,107] similar attention has been missing for these deep eutectic mixtures. Therefore, these systems need thorough investigation on this front provided one wants to project them as reaction media alternative to ionic liquids.

We took this opportunity by studying the dynamics in acetamide-electrolyte based molten mixtures in chapter 3. Here steady state and time resolved fluorescence spectroscopic techniques have been used to explore solute-medium interaction in deep eutectics of acetamide (CH_3CONH_2) with sodium and potassium thiocyanates (Na /KSCN) at T ~318 K and at several other higher temperatures. The dipolar solute probe employed for this study is coumarin 153 (C153). The mixtures composition has been kept at $0.75CH_3CONH_2 + 0.25[(1\text{-}f)NaSCN + fKSCN]$ in order to get a single liquid phase in either side of eutectic temperature (T_u). Fraction (f) of the above composition has been varied in order to investigate mixed alkali effects[108] and ion-solvent interaction. Stokes shift dynamics have been carried out in order to gain an understanding of mechanism and time scale of solvation in these media. Dynamic fluorescence anisotropy measurements have been employed in tandem with Stokes shift dynamics to characterize the solute-environment coupling. The conventional hydrodynamic model for diffusion has also been employed to further the understanding gained from the above measurements. Here we compare the average solvation and rotation time of C153 measured in molten mixtures to those in ionic liquids using the same solute reported earlier and show agreements and disagreement between the results in these two media.

In chapter 4 we have extended our understanding about the structure and dynamics of supercooled molten mixtures. Here the molten mixtures composed of acetamide with lithium nitrate and bromide having general formula, $[0.78CH_3CONH_2 + 0.22\{f\,LiBr + (1\text{-}$

f) $LiNO_3$}], where fractions of the anions, (bromide, Br^- and nitrate, NO_3^-) have been varied in order to investigate both the mixed anion effects[86,109,110] and the nature of solute-environment interaction. The viscosity of these mixtures has been measured and found to be significantly larger than those described in chapter 3. Temperature dependence of static and dynamic fluorescence behaviours of a dissolved solute (C153) has been explored to get further understanding about the solute-medium coupling in these supercooled melts. The amide concentration is kept fixed at 0.78 mole fraction because at this composition the mixture remains in the liquid phase[111] for the temperature range considered, $303 \le T/K \le 364$. Time-resolved fluorescence Stokes shift and anisotropy measurements using the solvation probe, C153 in these melts reveal a strong decoupling of medium dynamics from viscosity. Interestingly, this decoupling has been found to occur at temperatures ~50-100 K above the estimated glass transition temperatures of the above melt at various anion concentrations (f_{LiBr}). The decoupling is reflected via following fractional viscosity dependence (η) of the measured average solvation and rotation times ($\langle\tau_s\rangle$ and $\langle\tau_r\rangle$, respectively): $\langle\tau_x\rangle \propto (\eta/\mathrm{T})^p$ (x being solvation or rotation), with p covering the range, $0.20 < p < 0.70$. Although this is very similar to what is known for deeply supercooled liquids, it is very surprising because of the temperature range at which the above decoupling occurs for these molten mixtures. The kinship to the supercooled liquids is further exhibited via p which is always larger for $\langle\tau_r\rangle$ than for $\langle\tau_s\rangle$, indicating a sort of translation-rotation decoupling. Multiple probes have been used in steady state fluorescence measurements to explore also the extent of static heterogeneity.

In chapter 5 we have expanded the above investigation of heterogeneity effects in presence of an anion which is known to be a structure breaker. The eutectics considered here are made of alkylamide ($RCONH_2$) and lithium perchlorate ($LiClO_4$) with mixture composition {$0.81RCONH_2 + 0.19LiClO_4$}. The Stokes shift and anisotropy dynamics of a dipolar solute (C153) in these molten mixtures have been measured to explore the effects of alkyl chain length and temperature. The variation in alkyl chain length is performed via considering acetamide, propionamide and butyramide with alkyl chain as R=CH_3, CH_3CH_2, $CH_3CH_2CH_2$, respectively. The temperature range considered is 303 – 348 K. The glass transition temperatures (T_g) of these alkylamide molten mixtures have been measured by differential scanning calorimetry (DSC) and found to be ~200 K. Four different fluorophores (ANS, C153, PRODAN and DMASBT) having different fluorescence lifetimes have been used to investigate the excitation wavelength dependent shifts in steady state measurements. Heterogeneity due to hydrophobic interaction of alkyl chain is supposed to be important here and this aspect has also been addressed. Medium heterogeneity has been manifested via excitation wavelength dependence and break-down of hydrodynamics in these complex media. Despite the presence of a structure breaker ion (ClO_4^-), these systems show pronounced aggregation, although the extent of it is somewhat reduced compared to previous systems. Like in other molten mixtures, decoupling from viscosity of both $<\tau_s>$ and $<\tau_r>$ have been found, the extent of decoupling being weaker for $<\tau_r>$ than $<\tau_s>$. Thermophysical studies have also been performed to understand the physicochemical properties of these melts.

Water plays a vital role[17,18,21,29-33,56,59,62,63] as a solvent in biology and chemistry. Many important phenomena such as protein-protein interaction, enzymatic reaction, protein folding often require a limited number of water molecules in a confined environment.[29] Nanoscopic confinement by interface alters several properties of water molecules.[56,59,62-64,75,113] Reverse micelles are the elegant model systems for investigating the properties of water in geometrically confined environment.[56,59,62-64] Moreover, relaxation dynamics of water in confined environments have been investigated by measuring ultrafast time resolved infrared[59,113] and fluorescence spectroscopic techniques,[56,62-64] and computer simulations.[114-117] These works indicate that dynamics of water is much slower upon confinement compared to bulk water. Interestingly, different experiments provide results that are different from each other and thus a clear consensus is still to emerge. In addition, one does not know whether such confinement modifies the preferential solvation phenomenon by altering the solute-solvent and solvent-solvent interactions. In chapter 6, a combined dynamic fluorescence and all-atom molecular dynamics simulation study of solvation energy and rotational relaxations of a neutral dipolar solute, C153, in equal-sized aqueous pools confined within Aerosol OT (charged) and IGEPAL CO-520 (neutral) reverse micelles (RMs) at 298 K is described. The pool size dependent relaxation rates have been obtained by performing both experiments and simulations, and compared. RMs in simulations has been represented by a reduced model where SPC/E water molecules[118] interact with a trapped C153 that possesses realistic charge distributions for both of its ground and excited states. The experimental features have been qualitatively reproduced in the present all-atom simulations where the solute is found to reside always near the micellar interface, irrespective of the nature of the interface or size of the aqueous pool. The present study provides a resolution to a debate regarding the origin of the sub-nanosecond solvation component in dynamic fluorescence measurements[56,62-64] with aqueous RMs but not detected in ultrafast IR measurements.[113]

Aqueous electrolyte solution is a good system for electrochemical studies. Volatility of water makes the system less important in application at wide temperature range. Polymers, by virtue of much less volatility, can be used instead of water and the system is called ‘polymer-electrolyte’.[119-123] Polymer-electrolytes are considered very useful in electrochemical applications and extensively employed in battery technology.[119-123] Ion conductivity aspect and its improvement have been explored previously by many researchers.[124-129] One of the unique features of polymer-electrolyte composite is that ion transport involves segmental motion of host polymer and thus is closely related to the structural relaxation of polymer.[125,126] Thus information of structural relaxation is required to attain a microscopic picture of ion dynamics. Several experimental studies such as NMR,[130] dielectric relaxation[131] and QENS[132] have been performed to explore the relaxation dynamics of these systems. However, a clear microscopic mechanism is still missing and thus creates a space for us to contribute. As a result, we have employed dynamic Stokes shift and fluorescence anisotropy measurements to probe complex molecular interactions and the subsequent dynamics in polymer-electrolyte composites. In chapter 7, the heterogeneity aspects and validity of the conventional hydrodynamic relations in polyethylene glycol (PEG) based polymer-electrolyte systems have been investigated. Different electrolyte fractions and temperatures have been considered for this purpose. PEG has been chosen because it is a hydrophilic block copolymer and is used in many technological and medical purposes.[133] Depending on solubility of electrolyte/s in PEG,[134] we have used the polymer-electrolyte having general formula $[0.85\text{PEG} + 0.15\{f\text{LiNO}_3 + (1-f)\text{KNO}_3\}]$.

Aqueous solution of small amphiphilic molecules, for example, alcohols, ethers, amines and others exhibit various unusual properties due to specific interaction.[135-141] Several experimental studies have been performed earlier to understand the solution structure and an aggregation of species in such binary mixtures reported. However, in spite of various studies, heterogeneity aspects of binary mixtures have not been well understood. Chapter 8 presents one of our attempts in this direction where binary mixtures of water and cycloethers (1,4 dioxane and tetrahydrofuran) have been subjected to steady state and time resolved fluorescence spectroscopic interrogations. The clustering and strengthening as well as disruption of hydrogen bonded network structure in water-1,4 dioxane (DX) and water-tetrahydrofuran (THF) binary mixtures have been investigated by monitoring excited state intramolecular charge transfer (ICT) reaction of a reactive solute (4-(1-Azetidinyl)benzonitrile, P4C) and rotational dynamics of a non-reactive solute (C153) at 298 K. A domination of nuclear quadrupole moment of cycloethers over medium polarity at cycloethers rich region has been observed. The thesis then ends with a chapter (Chapter 9) on future problems that may be investigated to further enhance the understanding gained from the present study embodied here.

References:

1. Hynes, J. T. *Annu. Rev. Phys. Chem.* **1985**, *36*, 573.
2. Fleming, G. R.; Wolynes, P.G. *Phys. Today* **1990**, *43*, 36.
3. Mukamel, S.; Yan, Y.J. *Acc. Chem. Res.* **1989**, *22*, 301 and references therein.
4. Closs, G.L.; Miller, J.R. *Science* **1988**, *240*, 440.
5. Simon, J.D. *Acc. Chem. Res.* **1988**, *21*, 128.
6. Rossky, P.J.; Simon, J.D. *Nature* **1994**, *370*, 263.
7. Carrea, G.; Ottolina, G.; Riva, S. *Trends in Biotechnology* **1995**, *13*, 63.
8. Szenczi, Á.; Kardos, J.; Medgyesi, G. A.; Závodszky, P. *Biologicals* **2006**, *34*, 5.
9. Mclendon, G. *Acc. Chem. Res*. **1988**, *21*, 160.
10. Marcus, R. A.; Sutin, N.; *Biochem. Biophys. Acta* **1985**, *811*, 275.
11. Sumi, H.; Marcus, R.A. *J. Chem. Phys*. **1986**, *84*, 4894.
12. Kramers, H.A. *Physica* **1940**, *7*, 284.
13. Hänggi, P.; Talkner, P.; Borkovec, M. *Reviews of Modern Physics* **1990**, *62*, 251.
14. Fleming, G.R. *Chemical Applications of Ultrafast Spectroscopy*, Oxford University Press, **1986**.
15. *Femtosecond Reaction Dynamics*; edited by Wiersma, D.A. North Holland, Amsterdam, **1994**.
16. *Femtochemistry: Ultrafast Dynamics of the Chemical Bond*; edited by Zewail, A.H. World Scientific, Singapore, **1994**.
17. Bagchi, B. *Annu. Rev. Phys. Chem.* **1989**, *40*, 115.
18. Bagchi, B.; Chandra, A. *Adv. Chem. Phys*. **1991**, *80*, 1.
19. Orr-Ewing, A. J.; Glowacki, D. R.; Greaves, S. J.; Rose, R. A. *J. Phys. Chem. Lett.* **2011**, *2*, 1139.
20. Lomont, J. P.; Nguyen, S. C.; Schlegel, J. P.; Zoerb, M. C.; Hill, A. D.; Harris, C. B. *J. Am. Chem. Soc.* **2012**, *134*, 3120.
21. Wiggins, P. M. *Microbiol Rev.* **1990**, *54(4)*, 432.
22. Barron, L. D.; Hecht, L.; Wilson, G. *Biochemistry* **1997**, *36*, 13143.
23. Almond, A.; Brass, A.; Sheehan, J. K. *J. Phys. Chem. B* **2000**, *104*, 5634.
24. Mao, Y.; Ratner, M. A.; Jarrold, M. F. *J. Am. Chem. Soc* **2000**, *122*, 2950.
25. Vogler, E. A. *Adv. Colloid Interface Sci.* **1998**, *74*, 69.
26. Vogler, E. A. *J. Biomat. Sci. Polym. Edn.*, **1999**, *10*, 1015.

27. Vogler, E. A.; Graper, J. C.; Sugg, H. W.; Lander, L. M.; Brittain, W. J. *J. Biomed. Mat. Res.*, **1995**, *29*, 1017.
28. Vogler, E. A.; Graper, J. C.; Harper, G. R.; Lander, L. M.; Brittain, W. J. *J. Biomed. Mat. Res*. **1995**, *29*, 1005.
29. Pal, S. K.; Zewail, A. H. *Chem. Rev.* **2004**, *104*, 2099.
30. Zhong, D.; Pal, S. K.; Zewail, A. H. *Chem. Phys. Lett.* **2011**, *503,* 1.
31. urse, K. E.; Corcelli, S. A. *J. Am. Chem. Soc.* **2008**, *130*, 13103.
32. DeFlores, L. P.; Tokmakoff, A. *J. Am. Chem. Soc.* **2006**, *128,* 16520.
33. England, J. L.; Haran, G. *Annu. Rev. Phys. Chem.* **2011**, *62*, 257.
34. San Biagio, P. L.; Martorana, V.; Bulone, D.; Palma-Vittorelli, M. B.; Palma, M. U. *Biophys. J.* **1999**, *77*, 2470.
35. Fenimore, P. W.; Frauenfelder, H.; McMahon, B. H.; Parak, F. G. *Proc. Natl Acad. Sci. U.S.A.* **2002**, *99*, 16047.
36. Cheung, M. S.; García, A. E.; Onuchic, J. N. *Proc. Natl Acad. Sci. U.S.A.* **2002**, *99*, 685.
37. Tanimura, Y.; Leite, V. B. P.; Onuchic, J. N. *J. Chem. Phys.* **2002**, *117*, 2172.
38. Hay, S.; Brenner, S.; Khara, B.; Quinn, A. M.; Rigby, S. E. J.; Scrutton, N. S. *J. Am. Chem. Soc.* **2010**, *132*, 9738.
39. Khundkar, L. R.; Zewail, A. H. *Annu. Rev. Phys. Chem.* **1990**, *41*, 15.
40. Pedersen, S.; Banares, L.; Zewail, A. H. *J. Chem. Phys.* **1992**, *97*, 8801.
41. Potter, E. D.; Liu, Q.; Zewail, A. H. *Chem. Phys. Lett.* **1992**, *200*, 605.
42. *Ultrafast Processes in Chemistry and Photobiology*, Eds, El-Sayed, M. A.; Tanaka, I.; Molin, Y. University Press, Cambridge, **1995**.
43. Chung, J. K.; Thielges, M. C.; Lynch, S. R.; Fayer, M. D. *J. Phys. Chem. B* **2012**, *116*, 11024.
44. Fenn, E. E.; Wong, D. B.; Giammanco, C. H.; Fayer, M. D. *J. Phys. Chem. B* **2011**, *115*, 11658.
45. Thielges, M. C.; Chung, J. K.; Fayer, M. D. *J. Am. Chem. Soc.* **2011**, *133,* 3995.
46. Dahl, K.; Biswas, R.; Ito, N.; Maroncelli, M. *J. Phys. Chem. B* **2005**, *109,* 1563.
47. Lakowicz, J. R. *Principle of Fluorescence Spectroscopy*, 2nd ed.; Kluwer Academic Pub: New York, **1999**.
48. Horng, M. L.; Gardecki, J. A.; Papazyan, A.; Maroncelli, M. *J. Phys. Chem.* **1995**, *99*, 17311.

49. Horng, M. L.; Gardecki, J. A.; Maroncelli, M. *J. Phys. Chem. A* **1997**, *101*, 1030.
50. Maroncelli, M.; Macinnis, J.; Fleming, G. R. *Science* **1989**, *243*, 1674.
51. Moog, R. S.; Maroncelli, M. *J. Phys. Chem.* **1991**, *95*, 10359.
52. Horng, M. L.; Dahl, K.; Jones Ii, G.; Maroncelli, M. *Chem. Phys. Lett.* **1999**, *315*, 363.
53. Liu, M.; Ito, N.; Maroncelli, M.; Waldeck, D. H.; Oliver, A. M.; Paddon-Row, M. N. *J. Am. Chem. Soc.* **2005**, *127*, 17867.
54. Li, X.; Liang, M.; Chakraborty, A.; Kondo, M.; Maroncelli, M. *J. Phys. Chem. B* **2011**, *115*, 6592.
55. Jimenez, R.; Fleming, G. R.; Kumar, P. V.; Maroncelli, M. *Nature* **1994**, *369*, 471.
56. Bhattacharyya, K. *Acc. Chem. Res.* **2003**, *36*, 95 and references therein.
57. Thompson, W. H. *Annu. Rev. Phys. Chem.* **2011**, *62*, 599.
58. Leitner, D. M.; Gruebele, M.; Havenith, M. *HFSP Journal* **2008**, *2*, 314.
59. Fayer, M. D. *Acc. Chem. Res.* **2011**, *45*, 3.
60. de Boeij, W. P.; Pshenichnikov, M. S.; Wiersma, D. A. *Annu. Rev. Phys. Chem.* **1998**, *49*, 99.
61. Shirota, H.; Funston, A. M.; Wishart, J. F.; Edward W. Castner, J. *J. Chem. Phys.* **2005**, *122*, 184512.
62. Sarkar, N.; Datta, A.; Das, S.; Bhattacharyya, K. *J. Phys. Chem.* **1996**, *100*, 15483.
63. Sarkar, N.; Das, K.; Datta, A.; Das, S.; Bhattacharyya, K. *J. Phys. Chem.* **1996**, *100*, 10523.
64. Riter, R. E.; Undiks, E. P.; Levinger, N. E. *J. Am. Chem. Soc.* **1998**, *120*, 6062.
65. Karmakar, R.; Samanta, A. *J. Phys. Chem. A* **2002**, *106*, 4447.
66. Karmakar, R.; Samanta, A. *J. Phys. Chem. A* **2003**, *107*, 7340.
67. Shirota, H.; Segawa, H. *J. Phys. Chem. A* **2003**, *107*, 3719.
68. Mandal, P.K.; Sarkar, M.; Samanta, A. *J. Phys. Chem. A* **2004**. *108*, 9048
69. Chakrabarty, D.; Chakraborty, A.; Seth, D.; Sarkar, N. *J. Phys. Chem. A* **2005**, *109*, 1764.
70. Chakrabarty, D.; Seth, D.; Chakraborty, A.; Sarkar, N. *J. Phys. Chem. B* **2005**, *109*, 5753.
71. Grant, C. D.; DeRitter, M. R.; Steege, K. E.; Fadeeva, T. A.; Castner, E. W. *Langmuir* **2005**, *21*, 1745.

72. Halder, M.; Headley, L. S.; Mukherjee, P.; Song, X.; Petrich, J. W *J. Phys. Chem. A* **2006**, *110*, 8623.
73. Jin, H.; Baker, G. A.; Arzhantsev, S.; Dong, J.; Maroncelli, M. *J. Phys. Chem. B* **2007**, *111*, 7291.
74. Pramanik, R.; Rao, V. G.; Sarkar, S.; Ghatak, C.; Setua, P.; Sarkar, N. *J. Phys. Chem. B* **2009**, *113,* 8626.
75. Burai, T. N.; Datta, A. *J. Phys. Chem. B* **2009**, *113*, 15901.
76. Ghosh, R.; Mondal, J. A.; Palit, D. K. *J. Phys. Chem. B* **2010**, *114*, 12129.
77. Ghosh, R.; Mondal, J. A.; Ghosh, H. N.; Palit, D. K. *J. Phys. Chem. A* **2010**, *114*, 5263.
78. Van der Zwan, G. , Hynes, J. T. *Chem. Phys.* **1991**, *152*, 169.
79. Hynes, J. T., Simon, J. D. (editor): *Charge -Transfer Reactions and Solvation Dynamics in Ultrafast Dynamics of Chemical Systems,* Kluwer, Dodrecht, (1994); p.345.
80. Dutt, G. B. *Chem Phys Chem* **2005**, *6,* 413.
81. Aziz, E. F.; Rittmann-Frank, M. H.; Lange, K. M.; Bonhommeau, S.; Chergui, M. *Nat. Chem.* **2010**, *2*, 853.
82. Johnston Keith, P.; Kim, S.; Combes, J. In *Supercritical Fluid Science and Technology*; Am. *Chem. Soc*. **1989**, *406*, 52.
83. Lee, H.; Lee, G.; Jeon, J.; Cho, M. *J. Phys. Chem. A* **2011**, *116*, 347.
84. Dutt, G. B.; Ghanty, T. K. *J. Phys. Chem. A* **2004**, *108,* 6090.
85. Dev, S.; Das, D.; Ismail, K. *J. Chem. Eng. Data* **2004**, *49*, 339.
86. Kalita, G.; Sarma, K. G.; Mahiuddin, S. *J. Chem. Eng. Data* **1999**, *44*, 222.
87. Gusteri, M.; Bartocci, V.; Castellani, F.; Pucciarelli, F. *J. Electroanal. Chem.* **1979**, *102*, 199.
88. Castellani, F.; Berchiesi, G.; Pucciarelli, F.; Bartocci, V. *J. Chem. Eng. Data* **1981**, *26*, 150;
89. Berchiesi, G.; Angelis, M. D.; Rafaiani, G.; Vitali, G. *J. Mol. Liq.* **1992**, *51*, 11.
90. Castellani, F.; Berchiesi, G.; Pucciarelli, F.; Bartocci, V. *J. Chem. Eng. Data* **1982**, *27*, 45.
91. Berchiesi, G.; Lobbia, G. G.; Bartocci, V.; Vitali, G. *Thermochim. Acta,* **1983**, *70*, 317.
92. Lobbia, G. G.; Berchiesi, G.; Poeti, G. *Thermochim. Acta,* **1984**, *74,* 247.

93. Berchiesi, G.; Lobbia, G. G.; Berchiesi, M. A.; Vitali, G. *J. Therm. Anal.* **1984**, *29*, 729.

94. Lobbia, G. G.; Berchiesi, G. *Thermochim. Acta*, **1984**, *74*, 251.

95. Berchiesi, G.; Rafaiani, G.; Vitali, G.; Farhat, F. *J. Therm. Anal.* **1995**, *44*, 1313.

96. Berchiesi, G.; Vitali, G.; Passamonti, P.; Plowiec, R. *J. Chem. Soc. Faraday Trans. 2* **1983**, *79*, 1257.

97. Berchiesi, G. *J. Mol. Liq.* **1999**, *83*, 271.

98. Chen, R.; Wu, F.; Xu, B.; Li, L.; Qiu, X.; Chen, S. *J. Electrochem. Soc.*, **2007**, *154*, A703.

99. Dhanalakshmi, K.; Saraswathi, R.; Srinivasan, C. *Synth. Met.*, **1996**, *82*, 237.

100. Venkata Narayanan, N.S.; Sampath, S. *J. Clust. Sci.*, **2009**, *20*, 375.

101. Venkata Narayanan, N.S.; Ashokraj, B.V.; Sampath S. *J. Electrochem. Soc.*, **2009**, *156*, A863.

102. Venkata Narayanan, N.S.; Ashokraj, B.V.; Sampath, S. *Electrochem. Commun.*, **2009**, *11*, 2027–2031.

103. Del Pópolo, M. G.; Voth, G. A. *J. Phys. Chem. B* **2004**, *108*, 1744.

104. Bhargava, B. L.; Balasubramanian, S. *Chem. Phys. Lett.* **2006**, *417*, 486.

105. Karimi-Varzaneh, H. A.; Muller-Plathe, F.; Balasubramanian, S.; Carbone, P. *Phys. Chem. Chem. Phys.* **2010**, *12*, 4714.

106. Bhargava, B. L.; Balasubramanian, S. *J. Phys. Chem. B* **2007**, *111*, 4477.

107. Roy, D.; Maroncelli, M. *J. Phys. Chem. B* **2012**, *116*, 5951.

108. Kalita, G.; Rohman, N.; Mahiuddin, S. *J. Chem. Eng. Data*, **1998,** *43*, 148.

109. Chandra, A.; Chandra, S. *J. Phys. D: Apply. Phys.* **1994,** *27*, 2171.

110. Moynihan, C. T. *J. Electrochem. Soc.* **1979,** *126*, 2144.

111. McManis, G. E.; Fletcher, A. N.; Bliss, D. E.; Miles, M. H. *J. Electroanal. Chem.* **1985,** *190*, 171.

112. Papoian, G. A.; Ulander, J.; Wolynes, P. G. *J. Am. Chem. Soc.* **2003**, *125*, 9170.

113. Moilanen, D. E.; Levinger, N. E.; Spry, D. B.; Fayer, M. D. *J. Am. Chem. Soc.* **2007**, *129*, 14311.

114. Senapati, S.; Chandra, A. *J. Phys. Chem. B* **2001**, *105*, 5106.

115. Harpham, M. R.; Ladanyi, B. M.; Levinger, N. E. *J. Phys. Chem. B* **2005**, *109*, 16891.

116. Faeder, J.; Ladanyi, B. M. *J. Phys. Chem. B* **2005**, *109*, 6732.

117. Chowdhary, J.; Ladanyi, B. M. *J. Phys. Chem. A* **2011**, *115*, 6306.
118. Chowdhuri, S.; Chandra, A. *J. Phys. Chem. B* **2006**, *110*, 9674.
119. *Application of Electroactive* Polymers, Ed. Scrosati, B. Chapman &Hall, London, **1993**.
120. Tarascon, J. M.; Armand, M. *Nature* **2001**, *414*, 359.
121. Barnesy, A.; Despotakisy, A.; Wongz, T. C. P.; Andersonz, A. P.; Chambersz, B.; Wrighty, P. V. *Smart Mater. Struct.* **1998**, *7*, 752.
122. Croce, F.; Appetecchi, G. B.; Persi, L.; Scrosati, B. *Nature* **1998**, *394*, 456.
123. Naoi, K.; Morita, M. *J. Electroanal. Soc. Interface* **2008** (Spring), *17*, 44.
124. Watanabe, M.; Ogata, N. *British Polymer Journal* **1988**, *20*, 181.
125. Gadjourova, Z., Andreev, Y. G.; Tunstall, D. P.; Bruce, P. G. *Nature* **2001**, *412*, 520.
126. Gorecki, W.; Donoso, P.; Berthier, C.; Mali, M.; Roos, J.; Brinkmann, D.; Armand, M. B. *Solid State Ionics* **1988**, *28-30*, 1018.
127. Christie, A. M.; Lilley, S. J.; Staunton, E.; Andreev, Y. G.; Bruce, P. G. *Nature* **2005**, *433*, 50.
128. Zhou, D.; Mei, X.; Ouyang, J. *J. Phys. Chem. C* **2011**, *115,* 16688.
129. Smith, D. M.; Dong, B.; Marron, R. W.; Birnkrant, M. J.; Elabd, Y. A.; Natarajan, L. V.; Tondiglia, V. P.; Bunning, T. J.; Li, C. Y. *Nano Lett.* **2012**, *12*, 310.
130. Greenbaum, S. G. *Solid State Ionics* **1985**, *15*, 259.
131. Agrawal, S.; Singh, M.; Tripathi, M.; Dwivedi, M.; Pandey, K. *J. Mat. Sci.* **2009**, *44*, 6060.
132. Mao, G.; Perea, R. F.; Howells, W. S.; Price, D. L.; Saboungi, M.L. *Nature* **2000**, *405*, 163.
133. Saito, H.; Hoffman, A. S.; Ogawa, H. I. *J. Bioact. Compatible Polym.* **2007**, *22*, 589.
134. Kalita, G.; Sarma, K. G.; Mahiuddin, S. *J. Chem. Eng. Data* **2000**, *45*, 912.
135. Iwasaki, K.; Fujiyama, T. *J. Phys. Chem.* **1977**, *81*, 1908.
136. Bowron, D. T.; Finney, J. L.; Soper, A. K. *J. Phys. Chem. B* **1998**, *102*, 3551.
137. Arrigo, G.; Giordano, R.; Teixeria, J. *Eur. Phys. J. E* **2003**, 10, 135.
138. Schmitz, J.; Belkoura, L.; Woermann, D. *J. Chem. Phys.* **1994**, *101*, 476.
139. Pradhan, T.; Ghoshal, P.; Biswas, R. *J. Phys. Chem. A* **2008**, *112,* 915.

140. T. Pradhan, P. Ghoshal, and R. Biswas, J. Chem. Sci. 2008, 120, 275.

141. Schrödle, S.; Hefter, G.; Buchner, R. *J. Phys. Chem. B* **2007**, *111*, 5946.

Chapter 2

Main Experimental Techniques and Data Analysis Methods

The main experimental measurements used to investigate several problems discussed in this Thesis are via steady state and time resolved fluorescence spectroscopic techniques. Time Correlated Single Photon Counting (TCSPC) technique has been used for the time resolved measurements – both Stokes shift and anisotropy. This chapter briefly describes TCSPC technique and data analysis methods for solvation, rotation and charge transfer dynamics, which have been used to address the heterogeneity and solution dynamical aspects of various media.

2.1 TCSPC Technique

As already pointed out, time resolved fluorescence measurements have been carried out using time-correlated single photon counting technique (TCSPC), where each single photon emitted by fluorophore is detected after the excitation with a short pulse laser light.[1,2] The principle of TCSPC relies on the concept that the probability distribution for emission of a single photon from a fluorophore molecule following its excitation is identical to the time-dependent fluorescence intensity change of all photons emitted by the fluorophore after excitation. The schematic block diagram of a typical TCSPC system has been shown in Fig. 2.1. In this Thesis, TCSPC set up from Edinburgh (U.K.) has been used for fluorescence decay measurements. The experiment starts with an excitation pulse, which excites the sample kept in a sample chamber and creates a start signal. The signal is then passed through constant fraction discriminator (CFD), which accurately measures the arrival time of a laser pulse. Subsequently, the signal is passed to time-to-amplitude converter (TAC), which triggers the voltage ramp, i.e. voltage increases linearly with time. The voltage ramp is stopped when the first photon emitted by the sample fluorophore is detected. An output pulse from the TAC is proportional to the time delay (Δt) between the excitation and emission signals. This output pulse is then passed into the multichannel analyzer (MCA) where numerical value is generated by analog-to-digital converter (ADC). A histogram of the decay which is the photon count versus time channel, is built in MCA by repeating this process numerous times with a pulsed laser source.[3]

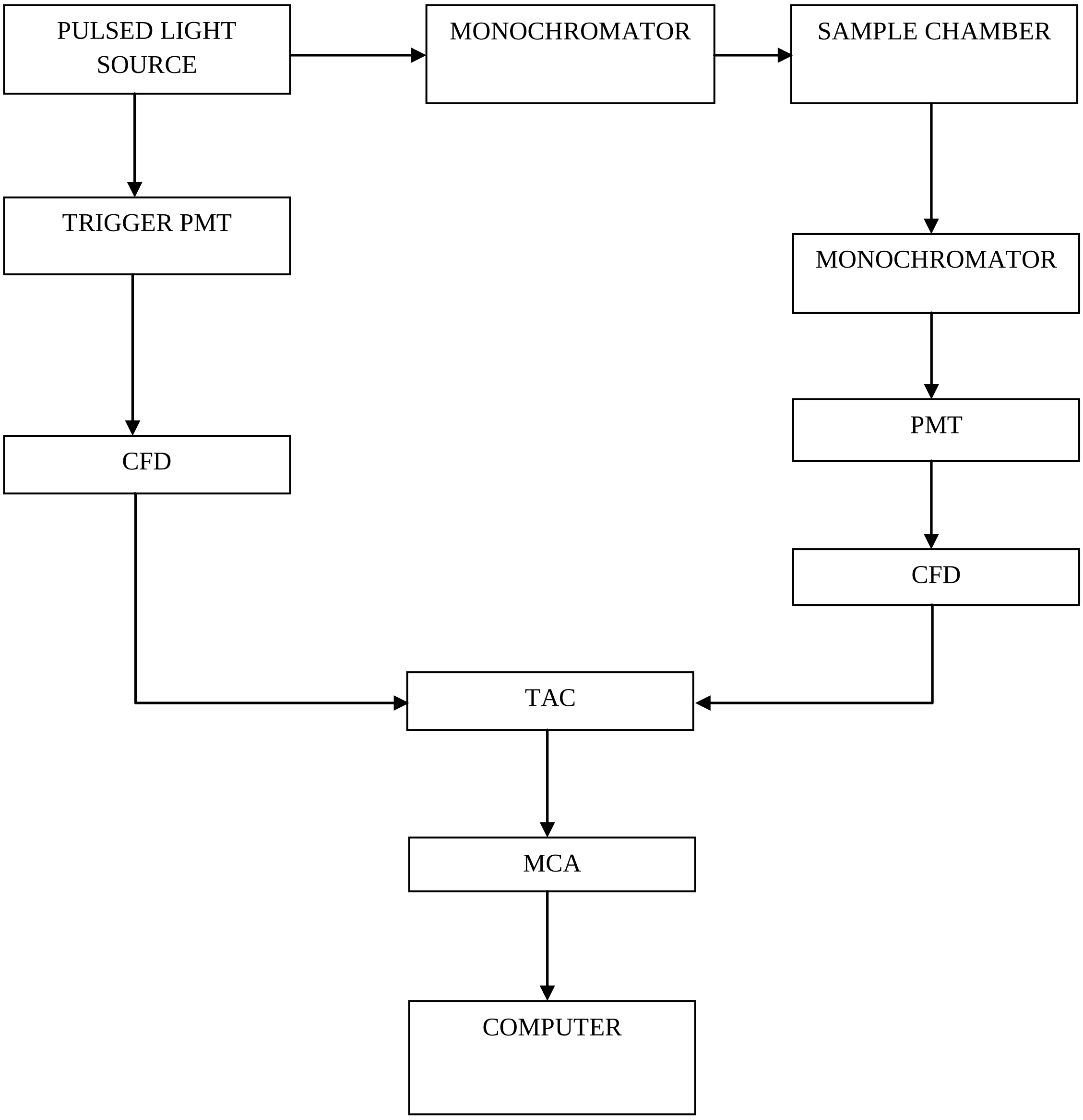

Fig. 2.1 The schematic diagram for a time correlated single photon counting system.

2.2 Data Analysis

2.2.1 Solvation Dynamics

In this Thesis, steady state absorption and fluorescence spectra were collected by using respectively a UV-visible spectrophotometer (UV-2450, Shimadzu) and Fluorimeter (Fluoromax-3, Jobin-Yvon, Horiba). Solvent blanks were subtracted prior to analysis. For solvation dynamics study, a series of 18-20 magic angle (54.7^0) decays were collected at equally spaced wavelengths across the steady-state emission spectrum of solute (fluorophore) dissolved in medium.[4] In our measurements, 409 nm dye laser was used as light source and the full width at half maximum (FWHM) of instrument response function (IRF) was ~ 70 ps. Only decay in blue end and a rise followed by decay in the red end of the emission spectra have generally been found in fluorescence transients where we intended to measure dynamical solvent response. The fluorescence decay ($N(t)$) collected from the instrument is a convolution of IRF ($R(t)$) and sample response ($I(t)$). To extract $I(t)$ from the measured $N(t)$ and $R(t)$ data, the iterative reconvolution method[5] using a nonlinear least square analysis was used. A sum of exponentials, $I(t)=\sum_{i=1}^{N}\alpha_i \exp(-t/\tau_i)$, (where α_i and τ_i are the pre-exponential factors and characteristic life times respectively) was used to fit the collected TCSPC decays.

Time-resolved emission spectra (TRES) were constructed following the literature method.[3-5] As illustrated above, the fluorescence decays collected at various wavelengths (λ_j) were fitted with the multi-exponential function,

$$I(\lambda_j,t)=\sum_{i=1}^{N}\alpha_i(\lambda_j)\exp(-t/\tau_i(\lambda_j)), \tag{2.1}$$

where $\alpha_i(\lambda_j)$ denote the pre-exponential factor, with $\sum_i \alpha_i(\lambda_j)=1$. A new set of normalized intensity decays were computed so that the time integrated intensity at each wavelength was equal to the steady state intensity at that wavelength ($F(\lambda_j)$). The normalization factor is

$$H(\lambda_j)=\frac{F(\lambda_j)}{\int_0^{\infty} I(\lambda_j,t)dt}=\frac{F(\lambda_j)}{\sum_i \alpha_i(\lambda_j)\tau_i(\lambda_j)} \tag{2.2}$$

The appropriate normalized intensity decay function was then obtained by,

$$I^{'}(\lambda_j,t)=H(\lambda_j)I(\lambda_j,t)=\sum_{i=1}^{N}\alpha_i^{'}(\lambda_j)\exp(-t/\tau_i(\lambda_j)), \tag{2.3}$$

where $\alpha_i^{'}(\lambda_j)=H(\lambda_j)\alpha_i(\lambda_j)$. The values of $I^{'}(\lambda_j,t)$ were used to calculate the intensity at any wavelength and time, and thus the time resolved emission spectra (TRES). The TRES were then converted to frequency representation for further analysis.[4] Each time resolved emission spectrum was fitted with a log-normal line shape function for continuous representation of the spectrum. The time dependent emission peak frequencies were extracted from the fitted spectra, and used to construct the normalized solvation response function ($S(t)$),

$$S(t)=\{\nu(t)-\nu(\infty)\}/\{\nu(0)-\nu(\infty)\}, \tag{2.4}$$

where $\nu(0)$, $\nu(t)$ and $\nu(\infty)$ denote some measure (usually peak) of frequency for the reconstructed emission spectrum respectively at $t=0$ (that is, immediately after excitation), at any given instant (t), and at a time sufficiently long ($t=\infty$) to allow for complete solvent relaxation. By construction, $S(t)$ is a normalized function which decays from unity to zero as the environment rearranges with time in response to the instantaneous alteration of the equilibrium charge distribution of the solute via laser excitation. Note for a given system $\nu(\infty)$ is expected to be equal to the frequency ($\nu_{fl.}$) of the steady state emission spectrum of the solute probe. However, in some cases solvent reorganization during the excited state lifetime of the probe may not be complete, leading to $\nu(\infty)<\nu_{fl.}$. Subsequently, average solvation time ($<\tau_s>$) was obtained via analytical integration of the multi-exponential fits to the measured $S(t)$ decay as follows:

$$\langle\tau_s\rangle=\int_0^\infty dtS(t)=\int_0^\infty dt[\textstyle\sum_i a_i\exp(-t/\tau_i)]=\sum_i a_i\tau_i\,, \tag{2.5}$$

where $\sum_i a_i=1$, and a_i and τ_i respectively denote the amplitude and time constant associated with the *i*-th component of the total decay.

2.2.2 Rotational Dynamics

TCSPC is also used to measure reorientational dynamics of a fluorophore dissolved in a medium.[3,5,6] This measurement is based on the principle of photoselective excitation of those fluorophore molecules whose absorption transition dipoles are parallel to the electric vector of polarized excitation light. The fluorescence intensity decays at parallel and perpendicular emission polarizations depend on reorientation of the excitated fluorophore. The loss of fluorescence anisotropy with time can be used to measure rotational diffusion of a fluorophore provided fluorescence lifetime is larger than the rotation diffusion timescale for that fluorophore. Time dependent fluorescence anisotropy ($r(t)$) is defined[3] as

$$r(t)=\{I_{\parallel}(t)-I_{\perp}(t)\}/\{I_{\parallel}(t)+2I_{\perp}(t)\} \tag{2.6}$$

Emission decays for time-resolved anisotropy studies are collected at the peak wavelength of steady state emission bands in order to minimize the effects (if any) on anisotropy of fast decay or rise due to solvent reorganization.[6] The vertically ($I_{\parallel}$), horizontally ($I_{\perp}$) and magic angle polarized fluorescence decays (with respect to the sample being excited with the vertically polarized light) are recorded. The polarization characteristics of optical setup have important consequences to the measured anisotropy. It is necessary to correct for the inaccuracy coming from the set-up geometry. This correction factor is usually termed as G-factor and is defined as the ratio between the transmission efficiency for vertically polarized light and that of horizontally polarized light ($G=I_{\parallel}/I_{\perp}$). Hence, the corrected time dependent fluorescence anisotropy, $r(t)$ can be represented as

$$r(t)=\{I_{\parallel}(t)-GI_{\perp}(t)\}/\{I_{\parallel}(t)+2GI_{\perp}(t)\} \tag{2.7}$$

In our analyses, the magic angle decay was first deconvoluted from the IRF and fitted to multi-exponential function of time. Subsequently, the parallel (I_{II}) and the perpendicular ($I_{\perp}$) decays were simultaneously fitted by using an iterative reconvolution method.[3,5] In this analysis method,[6] the longest life time obtained from the fitting of magic angle decay was kept fixed during the fit. $r(t)$ decays, so obtained, were then fitted to multi-exponential function as follows:

$$r(t)=r(0)\sum_{i}\alpha_{i}\exp(-t/\tau_{i}), \tag{2.8}$$

where τ_i (i = 1, 2) represents the time constants for the decay components (α_i) and $\sum_i \alpha_i = 1$. In this Thesis, the value for the initial anisotropy, $r(0)$, was fixed at 0.376 while fitting the $r(t)$ for C153 in all the solutions studied here.[6] The average rotational correlation time $\langle\tau_r\rangle$ was then determined as follows:

$$\langle\tau_r\rangle=\int_0^{\infty}dt\left[r(t)/r(0)\right]=\sum_i \alpha_i\tau_i \tag{2.9}$$

2.2.3 Intramolecular Charge Transfer Reaction

Photo-induced intramolecular charge transfer is an important fundamental process and has been carried in pure[7] and mixtures of solvents,[8,9] ionic liquids[10] and in confined environments.[11,12] In this Thesis (chapter 8) we carried out excited state intramolecular charge transfer reaction of 4-(1-azetidinyl)benzonitrile (P4C) in water- cycloether binary mixtures. Upon photo-excitation, this molecule (P4C) exhibits an anomalous fluorescence band which is red-shifted in addition to normal fluorescence in polar solvents. The appearance of the red-shifted fluorescence has been a matter of considerable debate and discussion.[7,13-28] Various existing models[7,13-28] clearly indicate that the anomalous fluorescence occurs from an electronic state which has charge transfer (CT) character. The state that exhibits normal fluorescence is assumed to possess charge distribution similar to that of the ground state and is termed as locally excited (LE) state. Upon photo-excitation, a substantial amount of charge is transferred from donor (amino group) to the acceptor (benzonitrile ring) moiety shown in SCHEME 1.

Recent study[7] of photo-induced intramolecular charge transfer reaction of substituted benzonitrile derivatives in several solvents of varying polarity have reported that the rate of reaction in those derivatives is substantially modified by the dynamical modes of the solvents in which the reaction is studied.

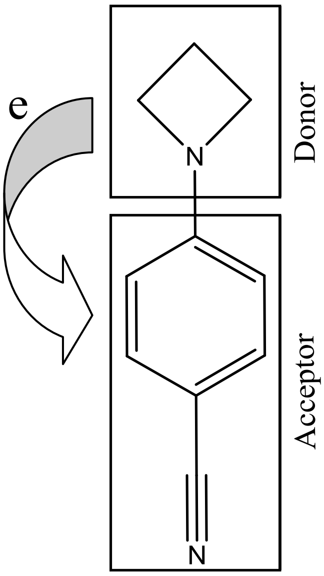

SCHEME 1

The photo-excitation of intramolecular charge transfer (ICT) molecule (P4C) and the subsequent charge transferred (CT) state formation is shown in SCHEME 2, where k_f and k_r are the forward and backward rate constants respectively. k_{LE} and k_{CT}

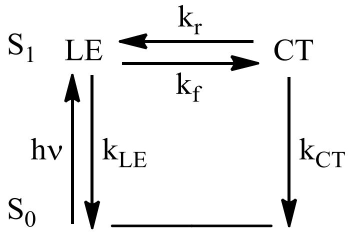

SCHEME 2

denote the net rate constants (radiative and non-radiative) for LE and CT states, respectively. The interconversion between LE and CT states, which is the intramolecular charge transfer reaction, is much faster in polar solvents near room temperature than the time constants associated with the population decays (inverse of k_{LE} and k_{CT}) to the ground state (S_0). Note that these rate constants are time independent quantities. As seen earlier and also later in this Thesis that inter-conversion between LE and CT states is the charge transfer reaction. Naturally therefore, modification of one of these factors affects the rate at which the reaction progresses. This molecule possesses higher dipole moments in CT states and hence formation of CT population is favored in polar solvents.[7] We synthesized the intramolecular charge transfer molecule (P4C) in our laboratory following the literature method.[17] Representative fluorescence spectra of P4C molecule in polar (acetonitrile) and non-polar (perfluorohexane) solvents are shown in Fig. 2.1. The presence of two distinct peaks in the fluorescence spectrum of P4C in acetonitrile and the absence of it in perfluorohexane clearly indicate that non-polar solvent does not support the formation of the CT state in this molecule. Considering the kinetic framework (SCHEME 2) of intramolecular charge transfer of P4C molecule, the time evolution of LE and CT intensities can be obtained[7,29,30] as follows :

$$I_{LE}(t) \propto k_{LE}^{rad} \frac{[LE(t)]}{[LE(0)]} = k_{LE}^{rad} \frac{1}{\lambda_1 - \lambda_2} \left\{ (Y - \lambda_2) e^{-\lambda_2 t} + (\lambda_1 - Y) e^{-\lambda t_1} \right\} \tag{2.10}$$

and $$I_{CT}(t) \propto k_{CT}^{rad} \frac{[CT(t)]}{[LE(0)]} = k_{CT}^{rad} \frac{k_f}{\lambda_1 - \lambda_2} \left\{ e^{-\lambda_2 t} - e^{-\lambda_1 t} \right\} , \qquad (2.11)$$

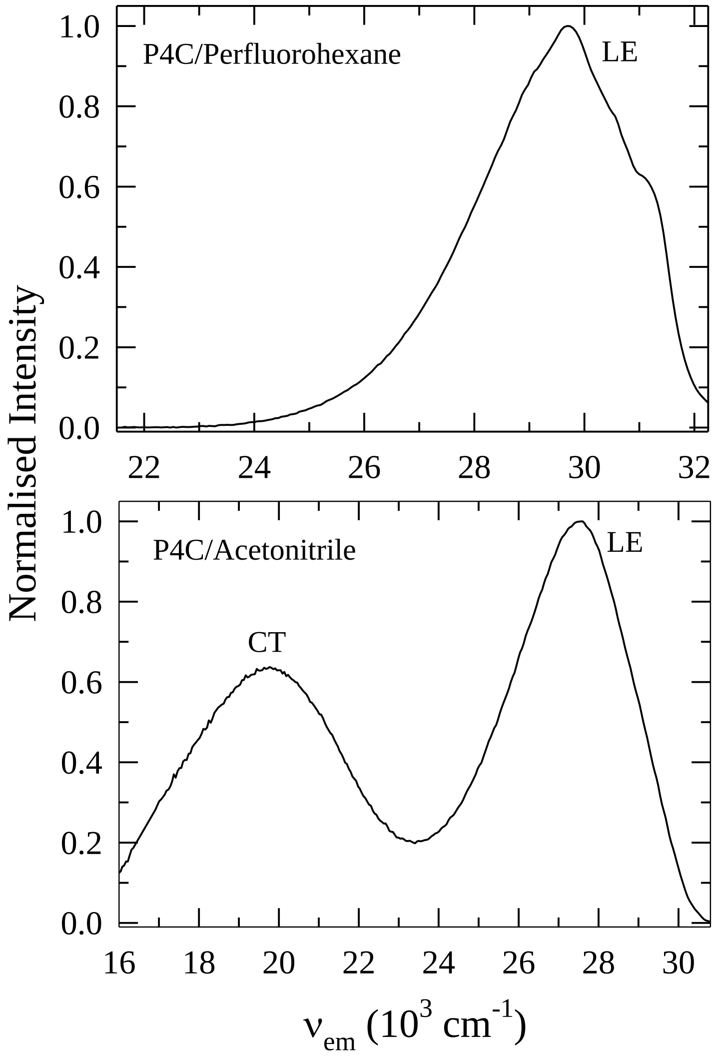

Fig. 2.1: Representative emission spectra of P4C in non-polar (perfluorohexane) and polar (acetonitrile) solvents.

where k_{LE}^{rad} and k_{CT}^{rad} represent respectively the rate constants associated with the LE and CT population decays to the ground state. Eqs. 2.10 and 2.11 suggest that in polar environments the time evolution of the LE intensity should be comprised by a fast and a slow decay components with very distinct time constants whereas that of CT intensity should show a fast rise followed by a slow decay. In earlier study[7] and also in the present Thesis, the time constants associated with the rise of CT state match well with those fast decays of LE state. So, the fast decay time of LE or the rise time of CT are associated with the reaction rate of LE → CT interconversion.[7] The slow time constants of the LE and CT intensity decays describe the time scales associated with the population decay from the S_1 to the S_0 state. This should be the scenario irrespective of the monitoring wavelength across either the LE or CT bands. However, in non-polar solvents where the charge transfer reaction is not supported, one expects a single exponential decay across the fluorescence emission spectrum of the ICT molecule.

The two-state reversible interconversion reaction shown in SCHEME 2 has been observed earlier and can successfully describe the time dependence of the LE and CT emission intensities of ICT molecule (P4C) in neat polar solvents. This reaction involving P4C in binary mixtures considered here gives rise to, as observed earlier in neat dipolar solvents, bi-exponential decay of the time dependent LE and CT intensities. These observations lend further support to the general validity of the reaction scheme discussed above. The fluorescence spectra of P4C in binary mixtures (water-cycloether) showed dual peaks. Subsequently, the fluorescence spectrum of P4C in perfluorohexane (reference spectrum) was used to deconvolute each fluorescence spectrum into two fragments.[7] The areas under the LE and CT band were obtained after the deconvolution. Fluorescence peak frequencies of LE and CT were calculated by adding the shifts of peak frequencies (with respect to reference spectra) in binary mixtures with reference frequency in perfluorohexane. Time-resolved fluorescence intensity decay measurements were carried out using a time correlated single photon counting (TCSPC) as discussed above. A light emitting diode (LED) that provides 299 nm light was used as excitation source for charge transfer solute (P4C). The full width at half-maximum (FWHM) of the instrument response function (IRF) was ~ 475 ps. The LE and CT fluorescence decays were recorded at magic angle (54.7^0) with a band-pass of 8 nm. Decays were then deconvoluted from the IRF and fitted to biexponential function using an iterative reconvolution algorithm.[3,5] Such fitting allowed one to detect decay component with a time constant as fast as ~100 ps with reasonable accuracy.[7]

References:

1. O'Cronnor, D. V.; Phillips, D. *Time Correlated Single Photon Counting*, Academic Press, London, **1984**.
2. Chang, M. C.; Courtney, S. H.; Cross, A. J.; Gulotty, R. J.; Petrich, J. W.; Fleming, G. R. *Analytical Instrumentation* **1985**, *14*, 433.
3. Lakowicz, J. R. *Principle of Fluorescence Spectroscopy*, 2nd ed.; Kluwer Academic Pub: New York, **1999**.
4. Horng, M. L.; Gardecki, J. A.; Papazyan, A.; Maroncelli, M. *J. Phys. Chem.* **1995**, *99*, 17311.
5. Birch, D. J. S.; Imhof, R. E. Time-Domain Fluorescence Spectroscopy Using Time Correlated Single Photon Counting, Topics in Fluorescence Spectroscopy; Lakowicz, J. R., Ed.; Plenum: New York, **1991**; *Vol 1*.
6. Horng, M. L.; Gardecki, J. A.; Maroncelli, M. *J. Phys. Chem. A* **1997**, *101*, 1030.
7. Dahl, K.; Biswas, R.; Ito, N.; Maroncelli, M. *J. Phys. Chem. B* **2005**, *109*, 1563.
8. Pradhan, T.; Ghoshal, P.; Biswas, R. *J. Phys. Chem. A* **2008**, *112*, 915.
9. Gazi, H. A. R.; Biswas, R. *J. Phys. Chem. A* **2011**, *115*, 2447.
10. Sahu, K.; Kern, S. J.; Berg, M. A. *J. Phys. Chem. A* **2011**, *115*, 7984.
11. Biswas, R.; Rohman, N.; Pradhan, T.; Buchner, R. *J. Phys. Chem. B* **2008**, *112*, 9379.
12. Pradhan, T.; Gazi, H.; Guchhait, B.; Biswas, R. *J. Chem. Sci.* **2012**, *124*, 355.
13. Zachariasse, K. A.; Druzhinin, S. I.; Bosch, W.; Machinek, R. *J. Am. Chem. Soc.* **2004**, *126*, 1705.
14. Techert, S.; Zachariasse, K. A., *J. Am. Chem. Soc.* **2004**, *126*, 5593.
15. Zachariasse, K. A. *Chem. Phys. Lett.* **2000,** *320*, 8.
16. Zgierski, M. Z.; Lim, E. C. *Chem. Phys. Lett.* **2004,** *393*, 143.
17. Rettig, W. *J. Luminesc*. **1980**, *26*, 21.
18. Rettig, W. *J. Phys. Chem*. **1982**, *86*, 1970.
19. Rettig, W.; Gleiter, R.; *J. Phys. Chem*. **1985**, *89*, 4674.
20. Rettig, W.; Wermuth, G. *J. Photochem.* **1985**, *28*, 351.
21. Al-Hassan, K. A.; Rettig, W. *Chem. Phys. Lett.* **1986**, *126*, 273.
22. LaFemina, J. P.; Duke, C. B.; Rettig, W. *Chem. Phys*. **1990**, *87*, 2151.
23. Braun, D.; Rettig, W. *Chem. Phys*. **1994**, *180*, 231.

24. Braun, D.; Rettig, W. *Chem. Phys. Lett.* **1997**, *268*, 110.
25. Rettig, W. *Ber. Bunsen-Ges. Phys. Chem.* **1991**, *95*, 259.
26. Yatsuhashi, T.; Trushin, S. A.; Fuss, W.; Rettig, W.; Schmid, W. E.; Zilberg, S. *Chem. Phys.* **2004**, *296*, 1.
27. Zachariasse, K. A.; Grobys, M.; von der Haar, T.; Hebecker, A.; Il'ichev, Y. V.; Jiang, Y.-B.; Morawski, O.; Kuhnle, W.; *J. Photochem. Photobiol. A* **1996**, *102,* 59.
28. Rettig, W.; Zeitz, B. *Chem. Phys. Lett.* **2000**, *317*, 187.
29. Pradhan, T.; Biswas, R. *J. Phys. Chem. A* **2007**, *111*, 11514.
30. Pradhan, T.; Biswas, R. *J. Phys. Chem. A* **2007**, *111*, 11524.

Chapter 3

Interaction and Dynamics in {Acetamide + Sodium/ Potassium Thiocyanates} Molten Mixtures: Composition and Temperature Dependence

3.1 Introduction

Acetamide, upon melting at around 353 K (boiling point ~495 K), forms a fairly mobile liquid (viscosity, η ~2.2 cP) and has long been known for its exquisite solvent properties.[1-5] Presence of several functional groups such as methyl, carbonyl, tautomeric hydroxyl and amide groups in a same molecule renders strong solvating power to this compound for a very large number of organic and inorganic substances except cellulose.[1] High dielectric constant of molten acetamide ($\varepsilon_0 \approx 60$) coupled with its large dipole moment (3.7 D) makes it an even better solvent than water for many ionic compounds.[4] Since addition of inorganic salts lowers down the melting temperature of acetamide considerably, molten binary and ternary mixtures of acetamide with metal halides have been used as reaction media and also in thermal salt cells to produce electricity.[6-7] The possibility of using acetamide as suitable medium for electrodeposition of metals from salt solutions has also been investigated.[2] Several other aspects such as ion conductance[5] and micellization of surfactants in molten acetamide have been studied by several authors in order to understand the role of the ion-solvent interactions in controlling the ion transport and self-aggregation in this medium.[8-13]

Because of industrial applications of molten acetamide as non-aqueous solvents for electrolytes and possible use in supercapacitor technology, the liquid-solid equilibrium temperature of (acetamide + electrolyte) mixtures have been explored extensively.[14-25] These studies reveal that mixtures of acetamide with certain electrolytes produce liquids that supercool (no spontaneous crystallization) until the glass transition temperature (T_g) is reached. Furthermore, the phenomenon of supercooling depends on the nature of the ion present in the mixture and Na^+ is found to produce the strongest supercooling effect. It is therefore evident that stronger ion-acetamide interaction (relative to the ion-ion and acetamide-acetamide interactions) inhibits the phase separation and leads to the supercooling of the molten mixture. Viscoelastic,[22-23] dielectric[24-25] and nuclear magnetic[22] relaxation studies of fused (acetamide + NaSCN) mixtures at temperatures above T_g have all indicated microscopic heterogeneity in the liquid structure. The observed multiple relaxation processes are subsequently explained in terms of an equilibrium between ordered (salt induced polymerized acetamide) and disordered solvent domains.[15(a,b)] In addition, dielectric relaxation measurements of fused acetamide in presence of NaSCN at 0.225 mole fraction (T_g ~230 K) report mega-value (10^6) of the static dielectric constant (ε_0) at T $\approx$274 K. Such a high value of static dielectric constant of this mixture has been explained in terms highly cooperative alignment of dipoles forming extended ordered domains.[25]

The formation of ordered domains and types of interactions present in these molten mixtures provide these systems kinship to the room temperature ionic liquids (RTILs) where solution heterogeneity and longer-ranged interactions govern much of the solvent properties.[26-32] In addition to these when one also considers the reported mega-value of the static dielectric constant[24], one cannot but wonder what would be the over-all medium effects on fluorescence Stokes' shift and its dynamics of a dipolar probe dissolved in these molten mixtures.[33] Moreover, a significant slow component[34-38] in the Stokes' shift dynamics is expected as the relevant dielectric relaxation (DR) measurements (T ~310 K)[24] report relaxation times in the milliseconds and nanoseconds for the low (0.1 – 100 Hz) and high (100 – 10^8 Hz) frequency dispersions, respectively. However, a large fraction of the total dispersion at higher frequency range ($\Delta\varepsilon = \varepsilon_\infty - n^2$, n being the refractive index of the medium) has remained inaccessible as these measurements could reach the infinite frequency dielectric constant (ε_∞) only upto ~18. Since the fast component of the orientational dynamics of a polar medium is naturally contained in this high frequency dispersion component,[39-42] no information regarding the fast dynamics of these molten mixtures can be obtained from these incomplete DR data. Surprisingly, even simple fluorescence spectroscopic measurements for these systems have not been done yet and, as a result, nothing is known about solute-solvent interaction in these multi-component molten mixtures.

The above scenario has motivated us to carry out dynamic fluorescence Stokes' shift and anisotropy measurements of a dissolved dipolar probe (coumarin 153, abbreviated as C153) in molten mixtures of acetamide (CH_3CONH_2) with potassium thiocyanate (KSCN) and sodium thiocyanate (NaSCN) at six different fractions (*f*) of KSCN, with mixture composition, $0.75CH_3CONH_2 + 0.25[(1-f)NaSCN + fKSCN]$ at T(K) ~318. Note that study of liquid-solid equilibrium temperature for mixtures of CH_3CONH_2 with either NaSCN or KSCN has indicated[15] *eutectic* temperatures (T_u) around 300K at thiocyanate mole-fraction ~0.2. A much closer look at these results[15] will reveal that mole-fraction of CH_3CONH_2 considered in the present study (0.75) actually allows one to investigate the solute-medium interaction in either side of the T_u where the mixture remains in a single (liquid) phase. The choice of temperature then decides the proximity of the mixture to the solid-liquid phase separation line and the consequent effects. The fraction (*f*) of KSCN in these mixtures is varied in the present study in order to convert the system from binary mixtures (*f* =0 & 1) to ternary ones so that the mixed alkali effects (MAE)[43-49] on fluorescence dynamics can be investigated. It is interesting to note that the MAE, which corresponds to deviation of various physical properties from the mole-fraction weighted additivity at a given temperature when one alkali metal ion is continuously replaced by another in a glass or melt, are not generally reflected in the equilibrium properties but show up in transport properties, such as, electrical conductivity and viscosity.

Since both the solvation and rotational dynamics of a dipolar solute probe would be substantially affected by the ion motions (independent or correlated) and medium viscosity, it would be worthwhile to investigate the MAE on average solvation and rotation times in these molten mixtures. The choice of this system is further motivated by the fact that density and viscosity of this mixture as a function of KSCN fraction have already been studied for a reasonably large temperature range.[44] These studies have revealed significant MAE for the composition dependent viscosity where a Vogel-Fulcher-Tammann (VFT) type of description has been found to be suitable for the temperature dependence of viscosity in these mixtures.[44] For the sake of completeness, we present in Fig. A1 (Appendix of the Thesis) a plot of solution viscosity as a function of KSCN concentration, measured at ~318 K.[44] Note also that the molten mixtures at six different fractions of KSCN considered here at 318 K are always in the liquid phase and far away from the respective glass transition temperatures. In addition, temperature dependencies (318 K – 375 K) of the average rotation times at two KSCN fractions (f = 0.2 and 0.8) have been studied to investigate further into the solute-environment interaction in these complex mixtures. Such a study for a solvation dynamics in these mixtures has also been attempted but meaningful results could not be obtained due to Stokes' shift dynamics becoming too fast at higher temperatures to be detected by the limited time resolution employed in the present experiments.

The rest of this chapter is structured as follows. Experimental details regarding sample preparation, data collection and their analysis methods have been described in the next section (3.2) . Section 3.3 contains results of our measurements and subsequent discussion. Comparison with theoretical predictions (wherever possible) has also been made in this section. The chapter then ends with concluding remarks provided in section 3.4.

3.2 Experimental Sections

3.2.1 Sample Preparation

Laser grade C153 was purchased from Exciton and used without further purification. Acetamide ($\geq$99%, SRL, India), sodium thiocyanate ($\geq$99%, SRL, India) and potassium thiocyanate ($\geq$98%, Merck Specialities, India) were vacuum-dried (~300 K) overnight before use. Samples were prepared by quickly transferring the required amounts of each of these compounds in proper volumetric flasks at a given composition at room temperature. No inert gas atmosphere was used during weighing and transferring the individual components of these mixtures. Each of the samples (in volumetric flasks) then heated carefully using a water-bath to about 325 K (Julabo, model F32) in order to melt the samples. An aliquot (~3 ml) of this stock melt was then transferred into a pre-heated quartz cuvette (path length 1 cm) which was previously loaded with C153 grains and sealed. C153 loading was done via taking ~5 μl of a stock solution of C153 in heptane and drying through heating the outer surface of the cuvette by mildly hot air and gently passing dry N_2 gas into the cuvette. The concentration of C153 in the stock C153/heptane solution was such that the final concentration of the probe (C153) in molten mixtures was always maintained at $\leq 10^{-5}$ M. The properly sealed (using Teflon tape) sample-cuvette (cuvette containing the molten mixture and C153) was then shaken gently for ~5 minutes and dipped into the water bath for ~10 minutes (maintained at 318 ± 0.5 K). This process was repeated for a few number of times before transferring the sample-cuvette into the sample chamber of a spectroscopic instrument. A wait-time of ~15 minutes was observed after loading the sample-cuvette into the temperature-maintained sample chamber of each of the spectrometers before data collection. A few samples (randomly chosen) were bubbled with dry N_2 gas before data collection but did not show any difference with those collected with the un-bubbled samples.

3.2.2 Steady State and Time Resolved Spectroscopic Measurements

Steady state and time resolved spectral data measurement techniques and the corresponding analysis procedures are essentially the same as described in chapter 2 and in refs.[50-56] Steady state absorption and fluorescence spectra were collected by using respectively a UV-visible spectrophotometer (UV-2450, Shimadzu) and fluorimeter (Fluoromax-3, Jobin-Yvon, Horiba). Solvent blanks were subtracted prior to analysis. Time resolved emission decays were measured using a time-correlated single photon counting instrument. 409 nm dye laser was used as excitation source. The full-width at half maximum (FWHM) of the instrument response function (IRF) with this excitation source was ~ 70 ps. Decay collection at each of these wavelengths was continued till the peak-count was reached ~5000 (dark count ~10). For solvation dynamics measurement 18-20 decays at wavelengths spanning emission spectrum were collected at magic angle. The collected decays were deconvoluted from the IRF and fitted to multi-exponential function using an iterative reconvolution algorithm.[33,50] Time resolved emission spectra (TRES) were then reconstructed from the decay fit parameters in conjunction with normalized intensities of the steady state emission spectrum as described in refs.[57-59] For the purpose of rotational dynamics measurement a set of three decays, namely, parallel, perpendicular and magic angle polarizations were collected. Time resolved fluorescence anisotropies, $r(t)$, were then calculated from the collected decays by using the method[60-62] described in chapter 2.

3.3 Results and Discussion

3.3.1 Steady State Spectroscopic Studies

Representative steady state absorption and fluorescence emission spectra of C153 dissolved in a molten mixture of composition, $0.75CH_3CONH_2 + 0.25[(1-f)NaSCN + fKSCN]$, at ~318 K with $f_{KSCN} = 0.6$ are shown in Fig. 3.1. Absorption and emission spectra of C153 in pure formamide (FA) at ~298 K are also shown in the same figure (blue) for comparison. Note in Fig. 3.1 the similarity in spectral position and shape between the absorption and emission spectra in ternary mixture and those in FA. More quantitatively, the *average* absorption and emission spectral peak frequencies[63] for C153 in this mixture are found to be respectively (in the unit of 10^3 cm^{-1}) 23.62 and 17.73, whereas those in FA are 23.91 and 17.96. The spectral widths (full width at half maximum, fwhm) are also very close in these two media (in the unit of 10^3 cm^{-1}) : for absorption, 4.43 in this mixture versus 4.77 in FA and, for emission, 3.48 (molten mixture) versus 3.44 (FA). As a result, the steady state Stokes' shifts (relative to that in

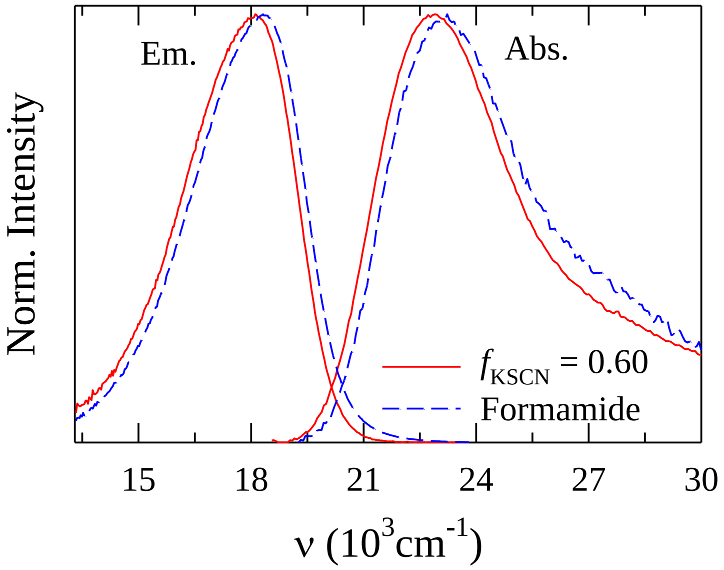

Fig. 3.1: Steady state absorption and fluorescence emission spectra (color coded) of C153 (solute) dissolved in molten mixture at f_{KSCN} = 0.60 (318 K) and in formamide at room temperature. Similar comparison with molten acetamide is not done because the ion-solute interaction contribution to the spectral shift in these mixtures is expected to be covered by the relatively larger average dielectric constant of formamide at room temperature ($\varepsilon_0 = 111$) .

heptane[63]) in these two media are very similar,~1450 cm^{-1} in molten mixture and ~1500 cm^{-1} in FA. The closeness of the spectral data therefore clearly indicates that the net interaction between the solute and the surrounding environment in this molten mixture is very similar to that in FA. This is somewhat surprising because a much greater difference with FA is expected on the basis of extremely large (~10^6) static dielectric constant reported earlier[24] for molten mixture of acetamide with sodium-thiocyanate at T ~310 K. Furthermore, similar spectral widths (both absorption and emission) in molten mixture and FA is also intriguing considering the fact that various studies with such molten mixtures have already suggested presence of strong heterogeneity in the solution phase.[22-25]

In fact, similarity of spectral data between molten mixture and FA has also been observed for other compositions as well. This is shown in Fig.3.2 where peak frequencies of absorption and emission spectra obtained at six different fractions of KSCN are shown along with the spectral widths (fwhm) and relative steady state Stokes' shifts. Note in the upper panel that while the absorption peak frequency shows a non-monotonic (though not very strong) KSCN concentration dependence, the emission frequencies remain almost independent to the variation of KSCN concentration. The apparent insensitivity of the emission peak frequency to the KSCN concentration in the ternary mixture does not indicate that the solvation environments around the solute in its ground and excited states are different. The slow movement of ions and other ion-solvent composite species present in these viscous mixtures (see Fig. A1 (Appendix) for viscosity range) may lead the fluorescence emission to take place from not a fully solvent-relaxed excited state. This might be particularly true for the more viscous NaSCN-rich region where Na^+ is believed to induce pronounced solvent polymerization.[15(b)] This means that in this (NaSCN-rich) region the emission frequencies are probably 'blue-shifted' compared to what should have been, had emission taken place from a completely solvent- relaxed state. Such a 'blue-shift' of spectral frequency has also been observed earlier for electrolyte solutions of multivalent ions in pure polar solvents.[52,59] Fluorescence emission frequency obtained after extrapolating the time resolved emission spectra to infinite time

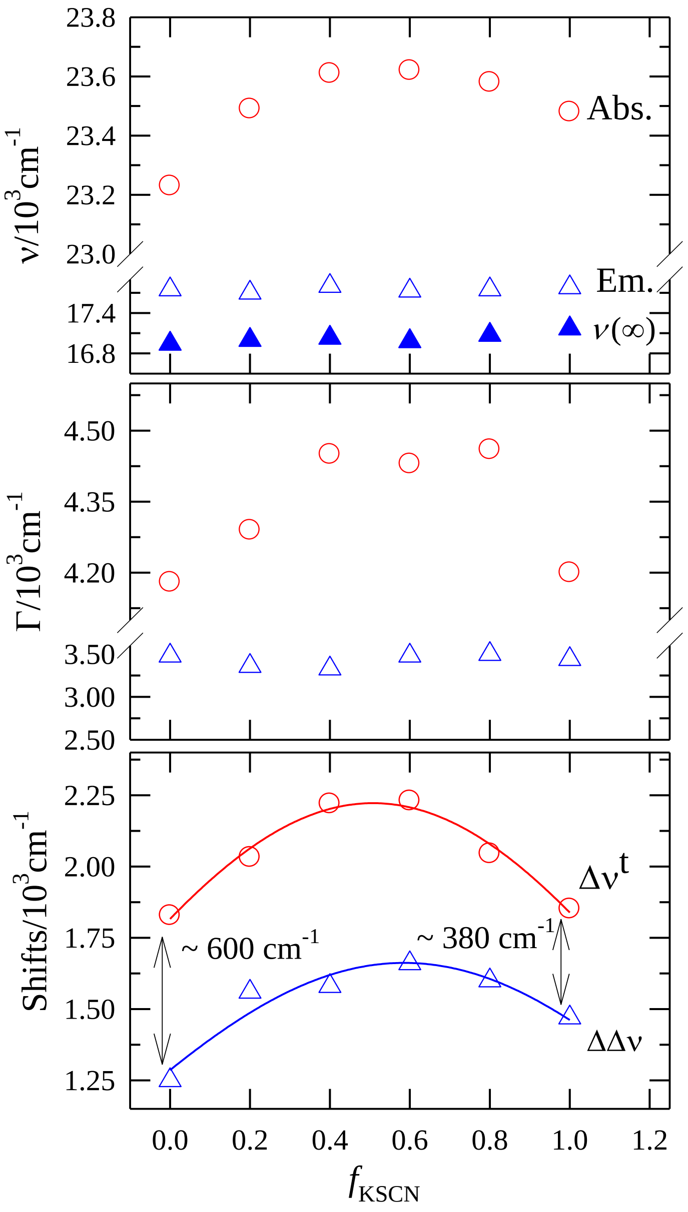

Fig. 3.2: Spectral data in six different fractions of KSCN: Concentration dependencies of absorption and emission peak frequencies (ν) are shown in the *upper panel* and those for full width at half maxima (Γ) and Stokes' shifts (steady state and dynamic) are presented respectively in the *middle* and *bottom* panels. ν_∞ shown in the upper panel represents emission peak frequencies obtained at $t=\infty$ from time resolved experiments. $\Delta\nu^t = \nu(t=0)-\nu(t=\infty)$ and $\Delta\Delta\nu = [\nu_{abs.} - \nu_{em.}]^{mixture} - [\nu_{abs.} - \nu_{em.}]^{heptane} = \Delta\nu^{mixture} - \Delta\nu^{heptane}$. $\nu(t=0)$ have been estimated by using the Fee-Maroncelli method (Ref. 58) and $\Delta\nu^{heptane}$ is measured as 4230 cm^{-1}.

($\nu_{em.}(t=\infty)$, shown by filled triangles) at each fraction of KSCN seems to indicate that the steady state emission in these mixtures has taken place from an incompletely solvent-relaxed excited state of the dissolved solute.

Spectral widths of absorption and emission spectra of C153, shown in the middle panel of Fig. 3.2, also vary with KSCN concentration much the same way as the respective spectral peak frequencies. It is interesting to note here that in the NaSCN-rich region the absorption spectrum blue-shifts and broadens while it red-shifts and narrows in the KSCN-rich region. Even-though both the spectral shift and width variation are small and limited to ≤ 300 cm^{-1}, the effect of replacement of Na$^+$ ion by the K$^+$ ion on solute absorption spectrum is evident. In addition, the correlation between the spectral shift and width seen here is very different from those observed earlier[33] in common polar solvents where broadening of the spectrum (absorption) associates with red-shift and narrowing with blue-shift. However, red-shift with narrowing in absorption spectrum has been observed earlier with C153 and other solute at very low alcohol concentrations in binary mixtures of water with tertiary butanol (TBA) and ethanol.[53, 64] In these works, a novel interplay between solution polarity and association among alkyl groups of alcohol molecules has been suggested to be responsible for the red-shift with concomitant narrowing of the absorption spectrum. A plausible explanation for the correlation between the spectral shift and width observed in these molten mixtures can be constructed as follows. As Na$^+$ is increasingly replaced by K$^+$ in the ternary mixture, the packing becomes less effective due to the resultant size constraint (size of K$^+$ is larger than that of Na$^+$)[42]. The less effective packing around the solute then leads to blue-shift of the absorption spectrum. Also, additional presence of K$^+$ enhances the heterogeneity, leading to an increase in the spectral width. Further addition of KSCN decreases the relative concentration of Na$^+$ in the mixture which, in turn, enhances the solute-solvent direct interaction by reducing the degree of solvent polymerization[15] and structural heterogeneity. Consequently, red-shift (relative to that at $f_{KSCN} \approx 0.5$) with concomitant narrowing is observed in the solute's absorption spectrum. Therefore, several factors, such as, packing of ions around the dissolved solute, heterogeneity in solution structure due to presence of different kind of ions and polymerization of acetamide due to the presence of alkali metal ions[15] could be responsible for the observed dependence of spectral properties on salt concentrations in these molten mixtures.

The non-monotonicity in absorption peak frequency dependence also gives rise to the non-monotonic alkali metal ion (K$^+$ or Na$^+$) concentration dependence of the steady state Stokes' shift (relative to heptane) in these mixtures. This is shown in the bottom panel of

Fig. 3.2 where the Stokes' shifts obtained after replacing the steady state emission frequency ($\nu_{em.}$) by the emission frequency extrapolated at $t = \infty$ from time-resolved experiments ($\nu_{em.}(t = \infty)$) are also presented. Note that the relative shift calculated by using $\nu_{em.}(t = \infty)$ is essentially the dynamic Stokes' shift measured in solvation dynamics experiments.[65] Interestingly, both the steady state and dynamic Stokes shifts go through maxima when plotted as a function of alkali metal ion concentration. Several transport properties, such as electrical conductivity and viscosity, of these mixtures also exhibit similar non-monotonic ion concentration dependence and has been explained in terms of what is known as mixed alkali effects.[10,44] Another important aspect of these data is that the estimated dynamic Stokes' shifts are larger by ~300 – 600 cm^{-1} than the steady state values which have also been observed earlier for strongly polar solvents with the same solute at ambient condition.[33] Therefore, whether a difference between steady state and dynamic shifts of ~300 cm^{-1} in the KSCN-rich region and ~600 cm^{-1} in the NaSCN-rich region is a consequence of slow (relative to the excited state life-time of the probe) environmental rearrangement or actually emerges from the subtle modifications in the underlying vibronic structure of the spectral line-shape in these mixtures at different compositions cannot be ascertained at this moment without further study.

3.3.2 Time-resolved Fluorescence Spectroscopic Studies

Typical fluorescence emission intensity decays collected at blue (485 nm) and red (665 nm) end of the steady state emission spectrum of C153 dissolved in the ternary mixture at $f_{KSCN} = 0.6$ and 318 K are shown in Fig. 3.3. Multi-exponential fits through these decays, fit parameters and instrument response function are also shown in the same panel (upper panel). As suggested by the fit parameters and non-regular pattern in the residuals (shown in the bottom panel), tri-exponential functions are adequate to describe the time-resolved emission decays at these wavelengths. Note that for decays collected at and around the peak wavelengths of the corresponding emission spectrum, bi-exponential functions of time have been found to be sufficient. The decay characteristics at these wavelengths (rise followed by decay at the red end

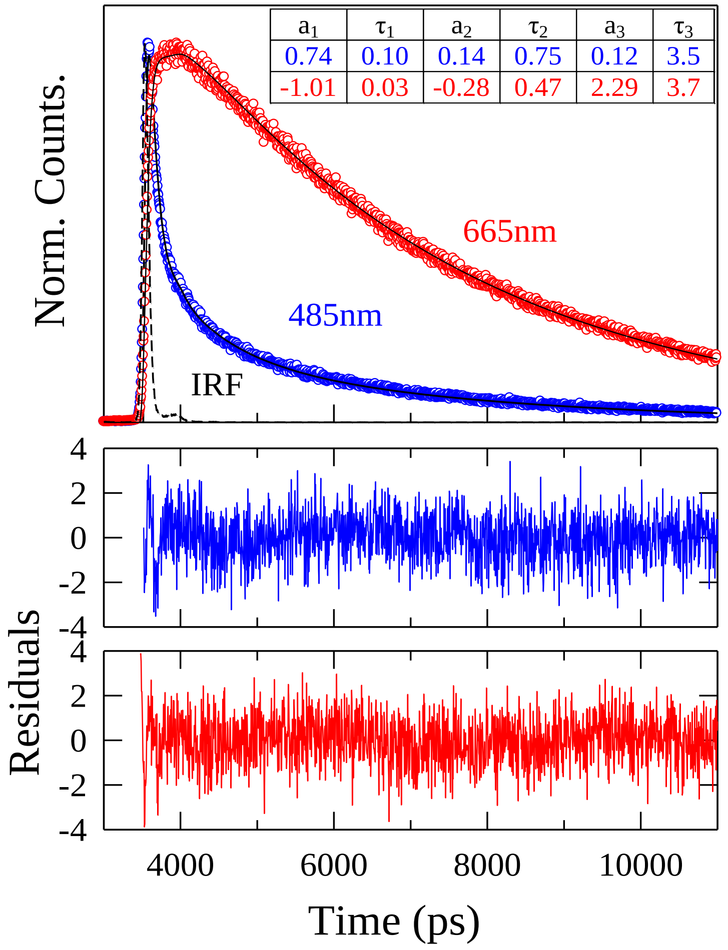

a_1	τ_1	a_2	τ_2	a_3	τ_3
0.74	0.10	0.14	0.75	0.12	3.5
-1.01	0.03	-0.28	0.47	2.29	3.7

Fig. 3.3: Representative fluorescence intensity decay of C153 at blue and red wavelengths at f_{KSCN} = 0.60 for a molten mixture (T~318 K). Experimental data are shown by circles and fit through them by solid lines. Instrument response function is also shown in the same figure (dashed lines). The respective residuals (color coded) are presented in the bottom panels. The fit parameters are shown in the inset of the upper panel. The time constants (τ_i) are in the unit of nano-second.

and decay only at the blue end) clearly indicate rearrangement of the environment in response to the instantaneously altered dipole moment of the solute dissolved in these molten mixtures. A point for concern is, however, that whether, in addition to the spectral relaxation, dynamic quenching of the fluorescence also contributes to the total decay in these mixtures. This we have checked by following the alkali metal ion concentration dependence of the longest time constant found in the fits of the collected emission intensity decays (see Fig. A2, Appendix). If the longest time constants (τ_2 for bi-exponential and τ_3 for tri-exponential fits) are identified with excited state life time (τ_{life}) of the fluorescent probe, then data shown in Fig. A2 do not reflect any drastic modification (no more than ~6%) of the probe's "life time" across the entire range of KSCN concentration in these molten mixtures. In addition, no significant intensity change has been detected in the controlled steady state spectroscopic experiments with these mixtures. Therefore, the decay components observed at this and other KSCN fractions may be considered as associated with the time dependent solvation of the laser-excited probe in these molten mixtures.

Representative time resolved emission spectra (TRES) of C153 in ternary molten mixture at f_{KSCN}= 0.6 and ~318 K are shown in the upper panel of Fig. 3.4. The lines going through the points are obtained from fitting the reconstructed data points to a log-normal line shape function.[54] The difference (peak to peak) between the reconstructed time-zero spectrum and that at $t = \infty$ is found to be ~1300 cm^{-1}, which is nearly 40% less than the estimated "true" dynamic Stokes' shift ($\Delta \nu_{est}^{t} \approx 2200$ cm^{-1}) for C153 in this mixture. The steady state emission spectrum of C153 in this mixture at this temperature is also shown in the same panel. Note that the steady state emission spectrum is 'blue-shifted' ~400 cm^{-1} relative to the time resolved emission spectrum at $t = \infty$. It is already discussed that this has been typical for these molten mixtures which is originating probably either from the sluggish movement of solvent and/or ion-solvent composite species, or, from the subtle changes in the vibronic structure of the spectrum. More importantly, the over-all spectral shape of the time resolved spectrum obtained at different time slices does not change with time. Also, the width, shown in the bottom panel, changes very little (except for spectrum at "t = 0") with time. The use of broader time resolution in the present experiments and consequently poor fitting of the data points for the time resolved spectrum at "t = 0" are probably the reasons for the relatively smaller width of the time-zero spectrum. If this small inconsistency for the time-zero spectrum is ignored then the widths of the time resolved emission spectra lie roughly in the range 3400 $\pm$ 200 cm^{-1} which is very similar to those of steady state emission spectra of C153 in this molten mixture

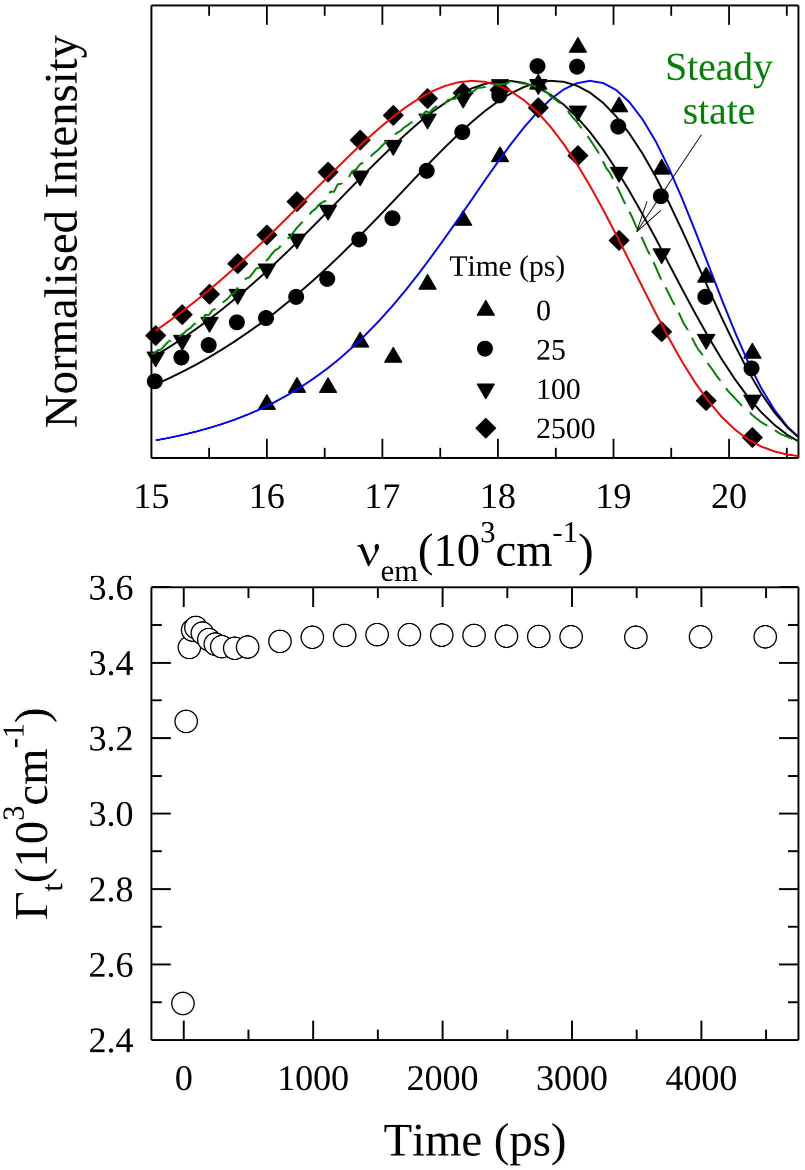

Fig. 3.4: Synthesized time resolved emission spectra (TRES) of C153 in ternary molten mixture at f_{KSCN} = 0.60 at various time intervals. The data representations are as follows: 0 (triangle), 25 (diamond), 100 (inverted triangle) and 2500 (circle) ps after solute excitation at ~ 318 K (upper panel). Spectral widths of the TRES are shown in the bottom panel.

and in ambient pure formamide. Therefore, the total end-to-end variation in spectral width (~400 cm^{-1}) is much smaller than the detected or estimated shift in this mixture and closely resembles to the findings in ionic liquids[57] and common dipolar solvents.[33] As near insensitivity to time of spectral shape and width is a hallmark for the measurement of non-reactive solvent dynamics in bulk liquids by using a solvatochromic probe, the spectral evolution presented in this figure (Fig. 3.4) can be considered as reflecting the medium-induced dynamic Stokes' shift in these complex molten systems.

Dynamic Stokes' shifts measured ($\Delta \nu_{obs}^{t}$) for other KSCN concentrations at ~318 K are summarized in Table 3.1 where the estimated shifts ($\Delta \nu_{est}^{t}$) are also tabulated in order to show the amount missed in the present studies of solvation dynamics in these mixtures. Data in the last column of Table 3.1 suggest that the relevant experiments have failed to detect nearly half of the total shifts in these molten mixtures. This indicates the existence of solvent dynamic components in these molten mixtures which are, *at least*, 3-4 times faster than the time resolution (~70 ps) employed in these measurements. We shall discuss more about it when we present results on solvation dynamics in these systems as missing of faster components poses a serious difficulty for ascribing physical origin to the observed time scales. We now focus on whether the shifts estimated for C153 at various KSCN concentrations in these mixtures can be described, even qualitatively, by a theory in terms of interactions of the dipolar solute with the dipolar component (acetamide) and the ions (Na^+, K^+ and SCN^-) present in the system.

Table 3.1: Dynamic Stokes' shift for C153 in molten mixtures of acetamide with Na^+ /K^+ thiocyanates at ~318 K: Comparison between theory and experiments

Theory				Experiment		
f_{KSCN}	ν^{t}_{sd} (cm^{-1})	ν^{t}_{si} (cm^{-1})	ν^{t}_{total} (cm^{-1})	ν^{t}_{est} (cm^{-1})	ν^{t}_{obs} (cm^{-1})	% Missed
0	1262	328	1590	1828	1082	41
0.2	1260	331	1591	2032	910	55
0.4	1259	335	1594	2120	981	54
0.6	1258	339	1597	2230	1337	40
0.8	1256	343	1599	2045	1046	49
1	1255	347	1602	1851	791	57

a) The estimated shifts are obtained by using the Fee-Maroncelli method described in Ref.58. The error bar associated with the measurements is approximately $\pm$ 250 cm^{-1}.

Since the molten mixtures of acetamide with sodium and/or potassium thiocyanates represent non-aqueous electrolyte solutions, the total dynamic Stokes shift in these media may be assumed to be comprised of the following: contributions from the dipole-dipole interaction between the dipolar solvent and the dipolar solute, and the dipole-ion interaction between the dipolar solute and the ions. Such an electrolyte solution model has recently been found to be very successful in predicting not only the measured Stokes' shift in several ionic liquids but also the observed dynamics in them.[66] As a detailed discussion on the calculation of dynamic Stokes' shift based on electrolyte solution model has already been provided in Ref. 66, we just show the calculated shifts here and compare with the experimental estimates. The calculated shifts are also summarized in Table 3.1 where the dipole-dipole interaction contribution ($\Delta \nu_{sd}^{t}$) at various values of f_{KSCN} are presented in the second column, dipole-ion ($\Delta \nu_{si}^{t}$) in the third and the total ($\Delta \nu_{Total}^{t}$) in the fourth. Note that in the absence of any systematic conductivity measurements for these systems, the salts are assumed to be completely dissociated. The polar solvent (acetamide) is assumed to be a collection of dipolar hard spheres each possessing a dipole moment (μ_d) of 3.7 D. This value of dipole moment produces average static dielectric constant (ε_0) as ~30 for the solvent composed of dipolar hard-spheres. The solute's size and dipole moments are taken as those of a C153 molecule. The KSCN fraction dependent static dielectric constant of the medium (ε_0) is calculated from the experimental density by using the mean spherical approximation (MSA) theory.[67] In addition, the ions are approximated as hard-sphere ions where the size disparity between cations has been neglected. Therefore, the theory reduces to that for a binary mixture of acetamide with a uni-univalent electrolyte in it where the effects of change in KSCN concentration enter in the calculation only via the use of experimental density. As a result, ion-specific effects (for example, difference in solvent polymerization[15] and packing ability) on dynamic Stokes shift would be completely missing in the predicted results. Also, the predicted shift would be nearly constant to the changes in KSCN concentration, as the density of molten mixture does not change significantly with the fraction of KSCN.[44]

A notable aspect of the comparison between the calculated total ($\Delta \nu_{Total}^{t}$) and experimentally estimated ($\Delta \nu_{est}^{t}$) shifts for C153 in these molten mixtures is that the predicted shifts are in general agreement with the estimated ones. Note also that the contribution due to the interaction of the dipolar solute with the surrounding ions ($\Delta \nu_{si}^{t}$) is only about 20% of the total shift. The ion-dipole interaction contribution ($\Delta \nu_{si}^{t}$) is thus smaller compared to the prediction for imidazolium ionic liquids[66] but close to what has been observed for electrolyte solutions in strongly polar solvents at room temperature.[50] Even-though the calculated total shifts are ~300-600 cm^{-1} less than the estimated values, the closeness in the agreement suggests that the present calculation scheme possesses certain degree of validity even for these complex ternary mixtures. More importantly, the level of agreement achieved here corresponds to an electrolyte solution in a model solvent of average dielectric constant ~30 which is *insignificant* compared to the reported huge value of ε_0 for the (CH_3CONH_2 + Na SCN) mixtures.[24] This clearly indicates the inaccuracy in the reported dielectric relaxation measurements,[24] and also explains why the steady state spectra in these mixtures closely resemble to those in formamide at room temperature (see Figs. 3.1 & 3.2).

Representative decay of the spectral or solvation response function, S(t), obtained from the time resolved emission spectra are shown in the upper panel of Fig. 3.5 for three different fractions of KSCN in the molten mixture at ~318 K. Note that the decay becomes faster upon increasing the fraction of KSCN (f_{KSCN}) in the mixture. This correlates well with the concomitant decrease in solution viscosity. Solvation response functions obtained by using two different measures of spectral frequency – the first moment (solid line) and the peak (broken lines) – are compared in the lower panel. These results suggest that, like in dipolar solvents[33], spectral movement with time is rather uniform which makes the decay largely insensitive to the choice of the frequency measure for constructing the S(t). The decays shown in this figure as well as those obtained at other KSCN fractions have been found to fit to tri-exponential functions of time, producing time constants in the ten, hundred and a few to several hundreds of picosecond regime. The fit parameters (amplitudes and time constants) describing S(t) and the corresponding average solvation time at each of the KSCN fractions studied are summarized in Table 3.2 along with the corresponding viscosity

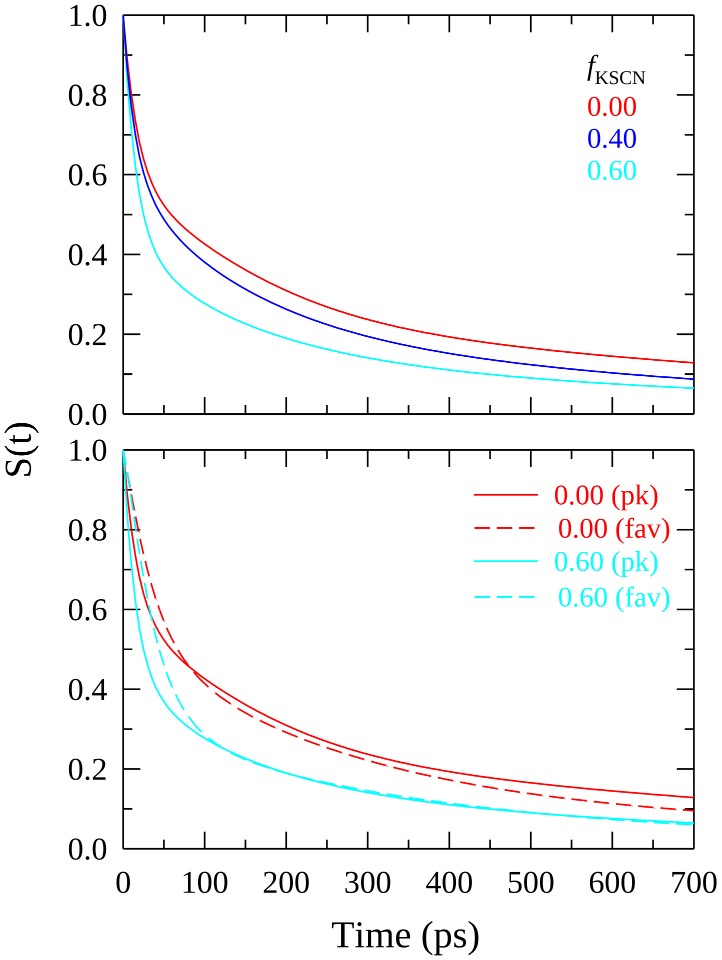

Fig. 3.5: Representative decays of solvent response function, S(t) at three different KSCN fractions (*upper panel*) and comparison of S(t) decays obtained from first moment (solid lines) and the peak (broken lines) frequencies (bottom panel) for two different KSCN fractions. The representations are color coded.

values. Although the fastest time constant (τ_1) is too short compared to the detection limit in the present experiments, the recurrent occurrence of it in each of the KSCN fractions indicate the presence of a very fast component in the over-all solvation response in these molten mixtures. Note that the other two time constants do not change much (varies within $\pm$5% of the reported values) even if the fastest time constant (τ_1) is fixed during fitting of the spectral response functions. The presence of low frequency (~100 cm^{-1}) intermolecular libration bands in amide systems[68] and

Table 3.2: Experimentally measured solvation response functions at different mixture compositions at ~318 K: Fit parameters[a]

f_{KSCN}	η (cP)	a_1	τ_1(ps)	a_2	τ_2(ps)	a_3	τ_3(ps)	$<\tau_s>$ (ns)
0.0	235.4	0.35	14	0.34	114	0.31	769	0.29
0.2	140.6	0.32	19	0.34	85	0.34	714	0.27
0.4	90.4	0.39	14	0.35	125	0.27	625	0.21
0.6	64.2	0.53	15	0.25	98	0.22	575	0.16
0.8	49.0	0.40	6	0.30	83	0.30	400	0.15
1.0	38.6	0.17	11	0.55	73	0.28	294	0.12

a) These numbers are better than ± 10% of the reported values (estimated based on limited data sets).

their relation to the ultrafast solvation energy relaxation in these[39-42,66] and other hydrogen-bonded solvents[69-70] have made an ultrafast solvation component (time constant ~1 ps or even faster) a distinct possibility for these molten acetamide and salt mixtures. We shall explore further on the origin of this time scale when we present model calculations on solvation dynamics in these mixtures. Interestingly, the other two time constants (τ_2 and τ_3) are roughly in the ranges of what have been observed earlier for biphasic solvation response of C153 in one component molten inorganic salts at elevated temperatures.[71] While those study have indicated a correlation between the ion-size and time constant without providing any quantitative information on the viscosity of the molten media, a clear correlation between the relatively larger time constants (τ_2 and τ_3) and solution viscosity can readily be seen in the present study. However, for these molten mixtures the following questions still remain to be answered. First, is it the ion-translation or dipolar solvent rotation or, a

Table 3.3(a): Tri-exponential fit parameters for the calculated solvation response functions at various mixture compositions in the *overdamped* limit (T ~318 K)[a]

f_{KSCN}	a_1	τ_1(ps)	a_2	τ_2(ps)	a_3	τ_3(ps)	$\langle\tau_s\rangle$ (ns)	$\langle\tau_s\rangle$expt (ns)
0.0	0.07	90	0.85	580	0.08	4544	0.86	0.29
0.2	0.08	58	0.84	355	0.08	3141	0.55	0.27
0.4	0.09	38	0.84	233	0.07	2198	0.35	0.21
0.6	0.09	28	0.83	167	0.07	1632	0.25	0.16
0.8	0.10	23	0.83	131	0.07	1217	0.20	0.15
1.0	0.09	17	0.83	102	0.8	1016	0.17	0.12

(a) Experimental average solvation times ($\langle\tau_s\rangle_{\exp}$) are mentioned again in this table to facilitate comparison with calculations.

Table 3.3(b): Bi-exponential fit parameters for the calculated solvation response functions in the *underdamped* limit at ~318 K.

f_{KSCN}	a_1	τ_1(ps)	a_2	τ_2(ps)	$\langle\tau_s\rangle$(ns)
0.0	0.46	0.084	0.54	841	0.45
0.2	0.47	0.085	0.53	512	0.27
0.4	0.47	0.086	0.53	336	0.18
0.6	0.47	0.087	0.53	243	0.13
0.8	0.47	0.088	0.53	182	0.097
1.0	0.47	0.089	0.53	149	0.079

combination of both responsible for the larger time constants (τ_2 and τ_3) in these multi-component mixtures? Second, what role the low frequency intermolecular collective librational modes of acetamide play in determining the time scale of solvation energy relaxation at early times in these systems? Below we elaborate on our theoretical study that discusses the possible origins of the time scales observed in the present experiments. It is already discussed that the Stokes' shift for a dipolar solute in these molten electrolyte solutions is determined mainly by the dipolar interaction between the solute and the dipolar host solvent molecules and ion-dipole interaction between the solute and the dissociated ions. However, the time scale of the Stokes' shift dynamics (or simply the solvation time scale) is governed by both the solute-medium interaction and the natural dynamics of the medium. Therefore, in addition to the solute-medium interactions, both the dipole-dipole interaction among the dipolar solvent molecules and ion-ion interaction among the dispersed ions contribute significantly to set the solvation time scales in these molten mixtures. Note that in the above model, it is assumed that the arrangement of the dipolar solvent particles (both spatial and orientational) is not perturbed in the solution and the dynamics of the pure solvent preserved. In addition, interaction between the ions and solvent molecules is not separately considered while calculating the Stokes' shift dynamics. This is an approximation as ion-solvent interaction can lead to modified solution properties that may or may not couple to the Stokes' shift dynamics in electrolyte solution. Ion-solvent interaction is also central to the *preferential solvation* of an ion[72-73] and the present model attempts neither to incorporate this effect on solvation of a dipolar solute nor study the preferential solvation of the latter in such multi-component mixtures. At the dynamic level, the effects of ion-solvent interaction are, however, partially incorporated through the use of experimental solution viscosity. Also note that the present theory expresses the measured Stokes' shift dynamics as a combination of separate contributions from 'ion dynamics' and 'dipolar solvent dynamics' where the 'separability' between these two dynamical responses is based purely on the wide difference in the time scales of dynamic fluctuations of the ion and dipolar densities.[50, 60(a)] Even such a separation at the dynamic level is somewhat arbitrary as ion motion would entail solvent motion (and vice-versa) but the fact that the solvent rotation being much faster than the ion translation provides some support to this approximation.[59,74]

In our first model study it is assumed that these molten mixtures respond to solute excitation via the *overdamped* dynamics where the environment rearranges through diffusion only.[75-76] Consequently, diffusive descriptions of both the solvent dynamic structure factor and ion dynamic structure factor are used to calculate the normalized total solvation response function ($S_E(t)$). The individual normalized response functions due to the solute-solvent dipole-dipole interaction ($S_{sd}(t)$) and solute-ion dipole-ion interaction

($S_{si}(t)$) have also been calculated in the *overdamped* limit of solvent response. Like the experimental S(t)s, the theoretically calculated normalized solvation response functions have also been found to fit to tri-exponential functions of time. Fit parameters for the calculated normalized response functions in the overdamped limit are summarized in Table 3.3(a) and the fit parameters for the individual response functions (S_{sd} and S_{si}) are provided in ref. 66(c). In order to facilitate comparison, the experimental average solvation times ($\langle\tau_s\rangle_{\exp}$) are again tabulated in the last column of Table 3.3(a). Representative tri-exponential fits to the calculated decays (S_{si} is considered as an example) revealing the quality of fits involved in these numerical descriptions of solvation response functions (see ref. 66(c) for figure of calculated decays). Since in the overdamped limit the time scale is set by the viscosity of the medium alone, the time constants associated with each individual response functions shown in this table (Table 3.3(a)) are not very different from each other. Interestingly, except the longest time constant which ranges between ~1 – 6 ns, the other two calculated time constants are very similar to the experimentally obtained longer time constants (τ_2 and τ_3) given in Table 3.2. This suggests that these experimental timescales (τ_2 and τ_3) are originating from the diffusive rearrangement of the environment surrounding the solute in these molten mixtures. The calculated longest time constant, which runs into several nanoseconds, has not been detected in the present experiments for these mixtures eventhough such a slow component for solvation dynamics in a few butylammonium ionic liquids near room temperature has been recently reported and explained in terms of longer-lived (relative to the excited state life-time of the solute) local structure around the probe.[77] In the present theory, these nanosecond time constants arise due to slow diffusive relaxations of both the orientational *solvent* dynamic structure factor at the nearest neighbor ($k\sigma \to 2\pi$) modes,[78] and translational *ion* dynamic structure factor involving the collective ($k\sigma \to 0$) modes.[66] It may therefore be stated that a slow component with a time constant ranging between a few to several nanoseconds is rather a *generic* property for solvent systems at or around the room temperature where ion-solute interaction makes a non-negligible contribution via slow ion translation to the total solvation energy relaxation. This is further supported by the fact that a time constant of a few nanoseconds has been observed for spectral evolutions even in electrolyte solutions of 'fast' solvents at ~296 K.[50] Lowering of solution temperature then further slows down the dynamics, lengthening the time constant dramatically. However, the respective contributions of $S_{sd}(t)$ and $S_{si}(t)$ to the total solvation energy relaxation $(S_E(t))$ determine the amplitudes of the components constituting the full decay and thus play a decisive role for the presence or absence of such an extremely slow component in the total solvation energy relaxation.

The next model study involves the calculation of the solute-solvent dipolar interaction contribution (S_{sd}) in the *underdamped* limit of dipolar solvent (acetamide for these mixtures) dynamics[39] In this limit where solvent frictional response includes the memory effects, proper calculations of the rotational and translational dissipative kernels are extremely important. Eventhough the calculation of the translational kernel is rather easy, the same for the rotational kernel is quite non-trivial. In the present study we use the calculation scheme elaborated in Ref. 39 for obtaining the rotational kernel from the experimental dielectric relaxation data and translation memory kernel from the diffusive description of the isotropic solvent dynamic structure factor. However, one still faces a problem to calculate the rotational kernel for these molten mixtures as complete dielectric relaxation data are not available for these media. In the absence of any reliable and experimentally measured dielectric relaxation data for these systems, it is assumed that liquid acetamide in these molten mixtures would *qualitatively* follow the dispersion steps as observed in the dielectric relaxation of liquid formamide at room temperature.[81] In such a model where the rotation of an acetamide molecule is approximated as that of a spherical particle, the relaxation time is obtained from the Debye-Stokes-Einstein (DSE) relation by using the stick boundary condition. Following the dielectric relaxation data of formamide at room temperature,[81] the dispersion from $\varepsilon_0 \approx$ 30 to $\varepsilon_1 \approx 5$ is attributed to the relaxation time calculated from the solution viscosity at each composition as described above. The remaining part, $\varepsilon_1 - n_D^2$, is then assumed to be carried out by the librational mode which are often found to be centered around 100 cm^{-1} in amide systems.[68] Note that although the present scheme allows one to investigate the effects of librational mode on the early time dynamics of solvation response in these mixtures, the calculated solvation time constants may not be quite accurate because of the use of model dielectric relaxation data. This drawback notwithstanding, these calculations should be able to suggest qualitatively the fastest time constant associated with the solvation response in these molten mixtures. This assumes even more importance when one considers that dynamic Stokes' shift measurements presented here indicates missing of almost half of the total shift due to a broad time resolution employed in experiments. The ion-dipole interaction part (S_{si}) has been calculated as before by assuming diffusive dynamics only, although calculations incorporating the inertial translational motions (of the ions) in the ion dynamic structure factor[79-80] did not produce any different results. This is because of the large translational friction (ς_{α}^{ion} in the expression given in Ref. 79) experienced by the ions while moving through these highly viscous media.

The calculated solvation response functions due to the solute-solvent dipolar interaction (S_{sd}) in the limit of *underdamped* solvent dynamics have been found to be bi-exponential function of time at all compositions of the molten mixture studied here (see ref. 66(c)). Fit parameters required to describe the calculated total solvation response function in this limit are summarized in Table 3.3(b) where one can find that a time constant of sub-hundred femtosecond component constitutes nearly 50% of the total calculated decay at all the mixture compositions. Note that the amplitude of this ultrafast component is surprisingly very similar to the missing portion of the total shift by our present measurements. In addition, the slowest time constants calculated in this limit is in qualitative agreement with both experimental data (τ_3 of Table 3.2) and those calculated in the overdamped limit (τ_2 of Table 3.3(a)). This is expected because the long-time dynamics is dominated by the diffusive motions of the solvating particles, and the present experiments have been able to detect mainly the slower part of the dynamics occurring relatively at the later stage of solvation in these systems. A very good agreement between the experimental and calculated average solvation times in these mixtures (last columns of Tables 3.2 and 3.3) is also a reflection of this fact as the average rate of solvation is dominated by the long-time constant.

Average solvation times ($\langle\tau_s\rangle$) measured for these molten mixtures have been found to follow a fractional viscosity dependence ($\langle\tau_s\rangle \propto \eta^p$) with $p = 0.46$. A power law dependence of average solvation time on solvent viscosity with $p \sim 1$ is expected if simple diffusion regulates the solvation of a large solute probe at long-time. In fact, a near proportionality between average solvation time and solvent viscosity (that is, $p \sim 1$) has been found when the relevant data in polar solvents and ionic liquids are considered together.[57] All these results are presented in Fig. 3.6 where the viscosity dependence of the calculated average solvation time from overdamped dynamics are also shown for comparison. The pronounced fractional viscosity dependence ($p \sim 0.5$) of $\langle \tau_s \rangle$ in these mixtures is therefore distinctly different from what have been observed earlier in polar solvents and ionic liquids, and indicates a much weaker coupling between the medium viscosity and translational motion of solvating particles. Fractional Stokes-Einstein (SE) behavior for particle diffusion ($D \propto \eta^{-p}$) is long-known for supercooled liquids near glass transition and sometimes argued as diagnostic for dynamic heterogeneity of a given medium.[82-87] A significant departure from the SE relation is also expected for small solutes diffusing through a medium of large particles.[88] In addition, fractional SE behavior has been experimentally observed for a variety of systems, ranging from diffusion of inert solute at room temperature in water and aqueous mixtures[89-90] and ion transport in ionic melts[91] to temperature dependence of diffusion of atomic and molecular solutes in alkane solvents.[92-94] Eventhough a number of alternative explanations have been proposed for the observed breakdown of SE relation in supercooled liquids and other viscous media, [95-98] a very recent work[99] suggests that fractional SE relation holds as well for normal solvents, ionic liquids and even for self-diffusion in Lennard-Jones fluid in the liquid and dense supercritical states. However, except for diffusion of a few inert atomic solutes and methane in several non-aqueous solvents where the fraction is found to lie in the range $0.6 > p > 0.4$, other studies[82-87, 89-91,99] have found p to vary approximately between 0.6 and 0.9. Therefore, the fractional power dependence on medium viscosity of average solvation time found in the present measurements is more similar to the diffusion-viscosity correlation observed for inert and small solutes in various solvents. This then raises the following question: is it the medium heterogeneity or the non-Fickian diffusion of relatively smaller alkali metal ions or even both responsible for the observed fractional power dependence? The diffusion of ions is relevant to the dynamic Stokes' shift since it is the ion-solvent exchange dynamics in the immediate neighborhood of the excited solute that contributes substantially to the spectral evolution in electrolyte solutions at longer times.[59] The medium heterogeneity can contribute to the solvation energy relaxation via the non-Gaussian dynamics of ions, such as, Levy flights.[100]

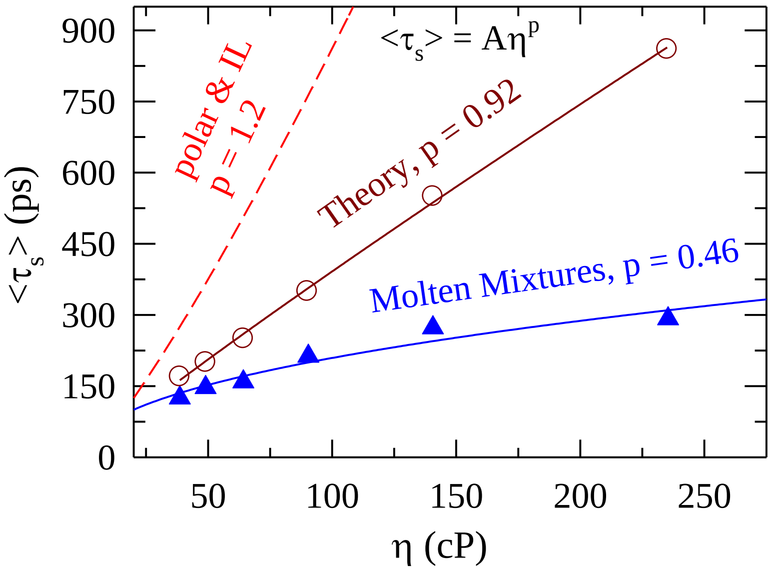

Fig. 3.6: Medium viscosity (η) dependence of average solvation time, $\langle \tau_s \rangle$, for C153 in molten mixtures of acetamide with sodium and potassium thiocyanates. Triangles represent experiments, circles denote calculations in the overdamped limit and the broken line shows dependence in polar solvents and ionic liquids together. Note the later results are taken from Ref. 57 where the same solute (C153) has been used for experimental measurements. The η dependence of $\langle \tau_s \rangle$ in these media can be described by the following generic relation: $\langle \tau_s \rangle = A\eta^p$. The values of A (in proper unit) for these media are as follows: 3.43 for polar solvents and ionic liquids together, 5.5 for the overdamped calculations, 25.36 for the molten mixtures. The respective values of the fraction (*p*) are indicated in the figure. The underdamped calculations (not shown here) produce 2.3 for *A* and 0.96 for *p*.

Recent simulation study of ionic liquids have indeed revealed presence of such dynamics where a certain percentage of ions are found to execute successive jumps that continued even much after the onset time of the diffusive motion.[101-102] Therefore, the hierarchical or multifractal dynamics of ‘fast’ and ‘slow’ ions found in simulations of ionic liquids may be one of the reasons for the observed decoupling of average solvation time from viscosity in these molten mixtures. The above argument, however, does not explain why the measured average solvation time in various ionic liquids exhibit a near proportionality to the medium viscosity. Further studies are thus required to completely understand the viscosity dependence of the solvation times in these complex mixtures.

3.3.3 Time Resolved Fluorescence Anisotropy $r(t)$ and its Temperature Dependence

Representative anisotropy decay of C153, constructed by using Eq. 2 from the collected parallel and perpendicular emission decays in one of these molten mixtures (at f_{KSCN}=0.2) at ~333 K is shown in Fig. 3.7. The bi-exponential fit through the data points (line) and the relevant fit parameters are also shown in the same figure. Following the anisotropy decay fits for C153 in several ionic liquids,[57,103] the value for the initial anisotropy (r_0) of C153 is fixed at 0.373 while fitting the anisotropy decays in these mixtures at all temperatures. The random nature of the residual (bottom panel) and the value of the *goodness of fit parameter* (χ^2) seem to suggest that a bi-exponential function of time reasonably describes the decay of $r(t)$ at this solution condition. In fact, considering the microscopic heterogeneity of these molten mixtures, fit to a stretched exponential function of the following form, $r(t) = r_0 \exp\left[-(t/\tau_{rot})^{\beta_{rot}}\right]$, was also attempted but produced worse fits than the bi-exponential descriptions. However, bi-exponential functions with a variation of ~10-15% in the amplitudes and time constants have been found to fit the decays equally well. Therefore, the error bar associated with these fit parameters is approximately $\pm$ 10-15% of the reported values. We would like to briefly discuss here the over-all results of anisotropy studies in ionic liquids since these liquids are somewhat linked (interaction-wise) to the molten mixtures under investigation. Both stretched and multi-exponential functions have been found to fit the measured anisotropy decays with different dipolar solutes in a variety of ionic liquids.[77, 103-107] The non-observation of stretched exponential kinetics of $r(t)$ for C153 in these molten mixtures may originate from the following factors: (i) the broad time resolution used in the present experiments[108] and (ii) larger average life time of the probe compared to the trapping time of the solute in the spatially heterogeneous quasistatic local solvent environments.[28, 31, 109-110] Since multi-exponential kinetics have also been observed in single component viscous liquids (“slow” solvents)[60] at ambient condition, it is conjectured that the non-Markovian nature of the rotational friction rather than the spatial heterogeneity in the environment which gives rise to the multi-exponential anisotropy decays in ionic liquids.[103,104] This can also be the reason for the observed biphasic nature of $r(t)$ in the present mixtures but the heterogeneity effects may also be responsible for the observed deviation from the exponential decay kinetics. Therefore, a more extensive study, probably with solute

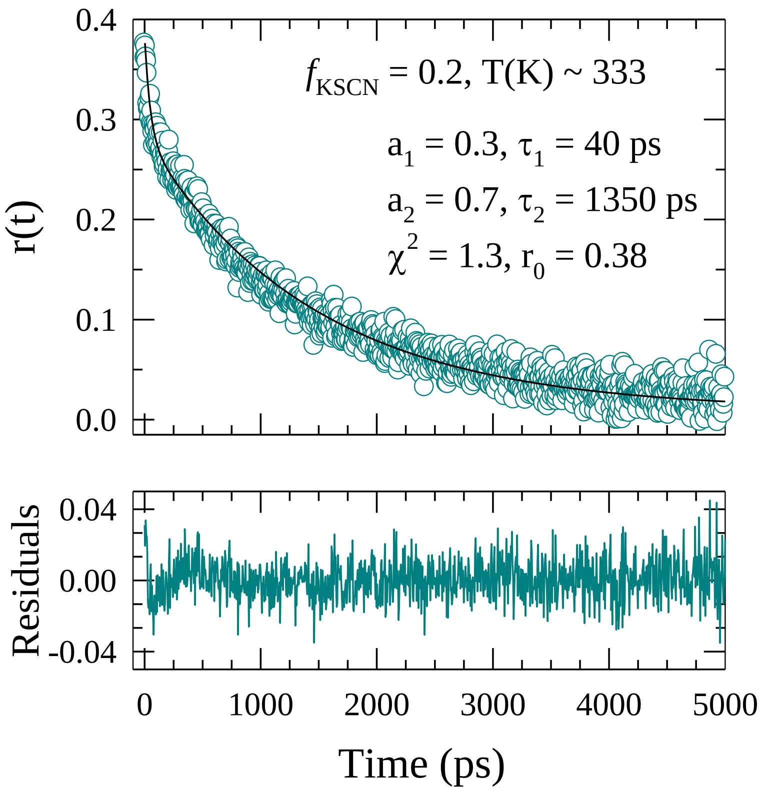

Fig.3.7: Representative fluorescence anisotropy decay, *r(t)*, of C153 at ~333 K in a molten mixture of acetamide with sodium and potassium thiocyanates with $f_{KSCN} = 0.20$. While circles represent experimental decay in the upper panel the solid line denotes the fit. The fit parameters are shown in the inset. Bottom panel shows the residuals.

probes of differing excited state average life times,[28] is required to fully explore the heterogeneity (spatial and temporal) and its effects on various relaxation processes in these molten mixtures.

The decay parameters shown in Fig. 3.7 suggests that the average rotation time ($\langle \tau_r \rangle$) of C153 in this mixture at 333 K is nearly a nanosecond ($\langle \tau_r \rangle$ = 957 ps). Now if one uses the *modified* Debye-Stokes-Einstein (DSE) relation, $\tau^{(2)} = \frac{V\eta}{k_B T} fC$, with solute volume V = 246 $\overset{0}{A}^{3}$, shape factor f = 1.71, then the slip boundary conditions (C = 0.24)[104] predict an average rotation time of ~2 ns for C153 in this mixture at this temperature ($\eta \approx 50\,\mathrm{cP}$)[44]. The same DSE relation with stick boundary conditions (C =1), on the other hand, estimates the $\langle \tau_r \rangle$ as ~8 ns. What is revealed by these calculations is that eventhough the DSE relation, with proper solute shape factor and boundary condition, correctly predicts the right order of magnitude for $\langle \tau_r \rangle$, the absolute magnitude is considerably different from what has been observed in these experiments. This is probably an indication of partial decoupling of solute rotation from the medium viscosity and is reminiscent of what has already been observed in supercooled liquids.[82] In order to explore further the relationship between the

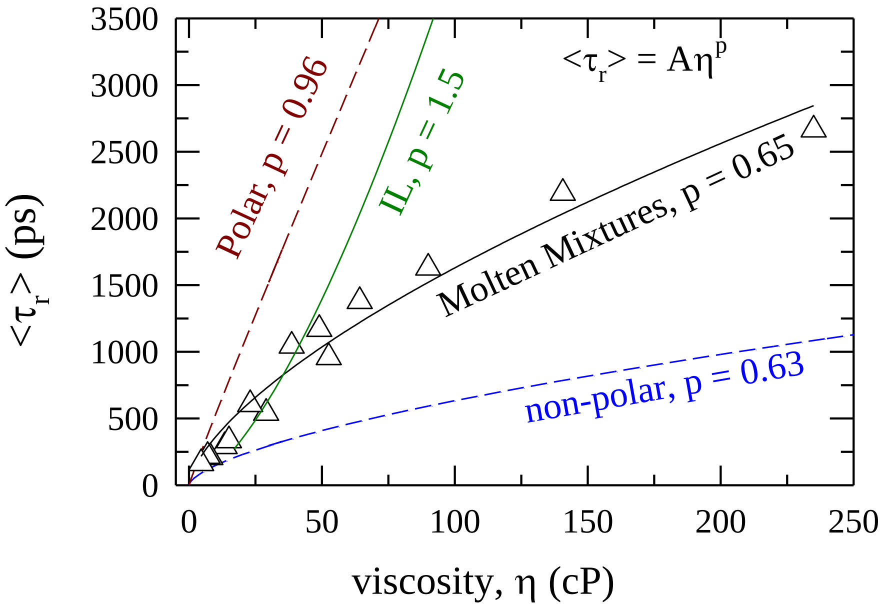

Fig. 3.8: Viscosity dependence of average rotational time for C153, $\langle \tau_r \rangle$, in molten mixtures of acetamide with sodium and potassium thiocyanates. While the triangles represent data from present experiments, the solid green line denotes dependence for ionic liquids, dashed red lines for polar solvents and dashed blue lines for non-polar solvents. Correlations for C153 in polar and nonpolar solvents have been taken from Ref. 60 and for ionic liquids, the correlation is generated by using data presented in Ref. 104. For rotation also, the viscosity dependence can be expressed as follows: $\langle \tau_r \rangle = A\eta^p$. The values of p for different media are indicated in the figure itself. A values are (in proper unit): 58.1 (polar solvents), 3.7 (ionic liquids), 80.6 (molten mixtures) and 34.8 (non-polar solvents).

viscosity and solute rotation, we have followed the temperature dependence of solute rotation at two different fractions of KSCN (f_{KSCN} = 0.2 and 0.8). For these two molten mixtures, anisotropy study have been carried out at five different temperatures at which viscosity values of the respective mixtures are already known.[44] Parameters obtained from bi-exponential fits to the anisotropy decays at these KSCN concentrations and temperatures are provided in Table 3.4 while the representative decays of $r(t)$ at three different temperatures at f_{KSCN} = 0.8 are presented in the Appendix (Fig. A3). The correlation between $\langle \tau_r \rangle$ and η obtained from these measurements as well as those observed with the same solute in common dipolar and

Table 3.4: Parameters obtained from bi-exponential fits to *r(t)* of C153 in molten mixture of acetamide with sodium and potassium thiocyanates at various mixture compositions and temperatures[a]

f_{KSCN}	T (K)	η (cP)	a_1	a_2	τ_1(ps)	τ_2(ps)	$<\tau_r>$(ps)
0.0	318	235.4	33.96	66.04	29	4021	2665
0.2	318	140.6	34.23	65.77	29	3192	2109
0.4	318	90.4	33.20	66.80	38	2419	1629
0.6	318	64.2	31.19	68.81	22	1994	1379
0.8	318	49.0	29.00	71.00	17	1640	1170
1.0	318	38.6	29.48	70.52	42	1462	1044
0.2	333	52.6	36.29	63.71	41	1480	958
	348	29.0	39.33	60.67	49	859	541
	363	(13.4)	37.13	62.87	27	447	291
	373	(8.00)	43.82	56.18	39	342	209
0.8	333	23.0	32.29	67.71	40	877	607
	348	15.0	40.09	59.91	47	527	335
	363	(6.98)	38.37	61.63	37	331	218
	373	(4.55)	47.85	52.15	42	277	164

a) Amplitudes are in percentage and values in parenthesis have been obtained from extrapolating the viscosity data provided in Ref.44.

non-polar solvents,[60] and ionic liquids[104] are shown in Fig. 3.8. A comparison among these results clearly indicate that eventhough the average rotation time in all these liquids exhibits a power-law dependence on viscosity (that is, $\langle\tau_r\rangle \propto \eta^p$), the dependence in molten mixtures is showing a *fractional* DSE behavior with $p = 0.65$. Surprisingly, the fractional power dependence of $\langle\tau_r\rangle$ on η is very similar to that found in non-polar solvents (p=0.63) and is somewhat *counter-intuitive* in the sense that solute rotation in these mixtures is expected to be much closer to that in ionic liquids rather than in homogeneous non-polar solvents where solute-solvent interaction is relatively much weaker.

It is interesting to note that a crossover from the conventional DSE behavior to fractional DSE type viscosity dependence for rotation time has been reported[111-121] in a number of systems at temperatures broadly located around $1.2\,T_g$. All these studies have shown considerable degree of decoupling ($0.25 \le p \le 0.75$) between the solute rotation and medium viscosity and this phenomenon is attributed to the heterogeneous dynamics of the media investigated. Interestingly, model calculations based on the presence of dynamic heterogeneities have predicted fractional DSE behavior for a solute guest with the fraction (p) ranging from 0.25 to 0.7 depending upon the number of solvent (guest) molecules required to rearrange during the process of solute rotation.[113] If we now recall that the T_g of a binary mixture of acetamide with 0.225 mole fraction of sodium thiocyanate is ~230 K[24-25], and melting temperature of acetamide is ~350 K, then these present ternary mixtures may be considered as supercooled liquids where the observed deviation from the conventional hydrodynamic behavior may be attributed to both the spatial and temporal heterogeneities of these molten mixtures. In addition, obstruction model for translational motion in glass-forming liquids have predicted a fractional viscosity dependence with p = 0.6[122] . This is surprisingly close to that found in the correlation between the average solvation time and viscosity in these molten mixtures. Further investigation involving these molten mixtures is therefore required to ascertain how much of the decoupling between $\langle\tau_s\rangle$ and η originates from the non-Gaussian dynamics of the solvent particles, and to what extent the observed fractional DSE behavior for $\langle\tau_r\rangle$ is dictated by the microscopic heterogeneity of these molten mixtures and the anisotropic diffusion around the individual molecular axes of the solute probe[54, 123-125].

Next we explore the usefulness of the conventional hydrodynamic relations for describing the solute rotation in these complex molten mixtures. The results are summarized in Fig. 3.9 where the average rotation times obtained from the temperature dependent study of these mixtures at KSCN fractions 0.2 and 0.8 are shown as a function of η/T. The DSE predictions at slip and stick boundary conditions for an ellipsoidal rotor have been obtained by using the necessary parameters discussed already in the text and also presented in the same figure for comparison (solid lines). These results clearly indicate for solute rotation a transition from *slip* behavior at high temperature and low viscosity regime to *sub-slip* dependence at high viscosity and low temperature. The observed non-conformity to the proportionality to η/T is rather interesting given the fact that rotation times in ionic liquids follow essentially the same correlation as established in common dipolar solvents.[57] The deviation from the DSE prediction is, however, nothing new as

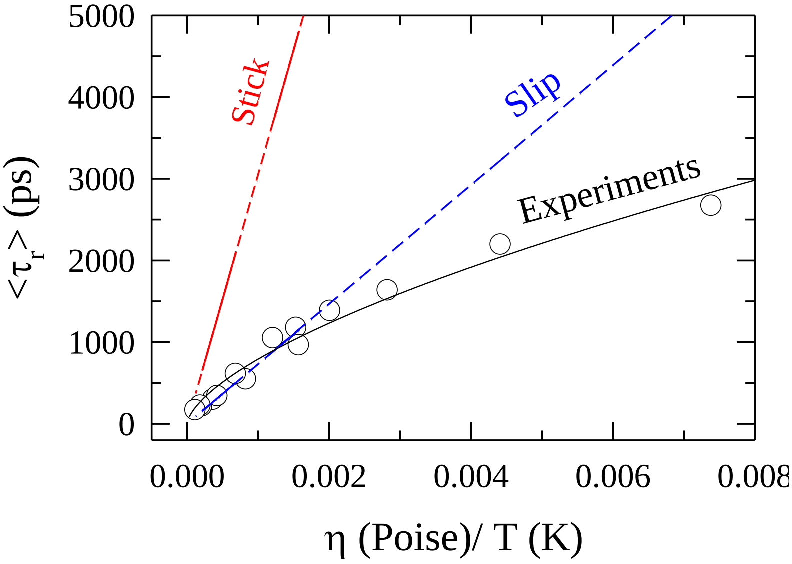

Fig. 3.9: Prediction of stick (red dotted line) and slip (blue dotted line) hydrodynamics for solute rotation in these molten mixtures and comparison with experimental data (circles). The line going through the circles is a fit to the relation: $\langle \tau_r \rangle = A\left(\frac{\eta}{T}\right)^{0.64}$ with A (proper unit)=64832 and R (correlation coefficient) = 0.98.

fluorescence anisotropy studies with C153 and other solutes in normal alkane solvents[60, 126-127] have already revealed such a fractional coupling between solute rotation and solvent viscosity. In alkane solvents, the solute-solvent coupling parameter (*C* in DSE) has been found to decrease with the increase in alkyl chain length due to inefficient solvent packing around the rotating solute.[60] In these molten mixtures, such a change in solute-solvent coupling may arise from distribution of solutes in different domains at low temperature and high viscous conditions. Given the results that rotation of relatively larger solutes

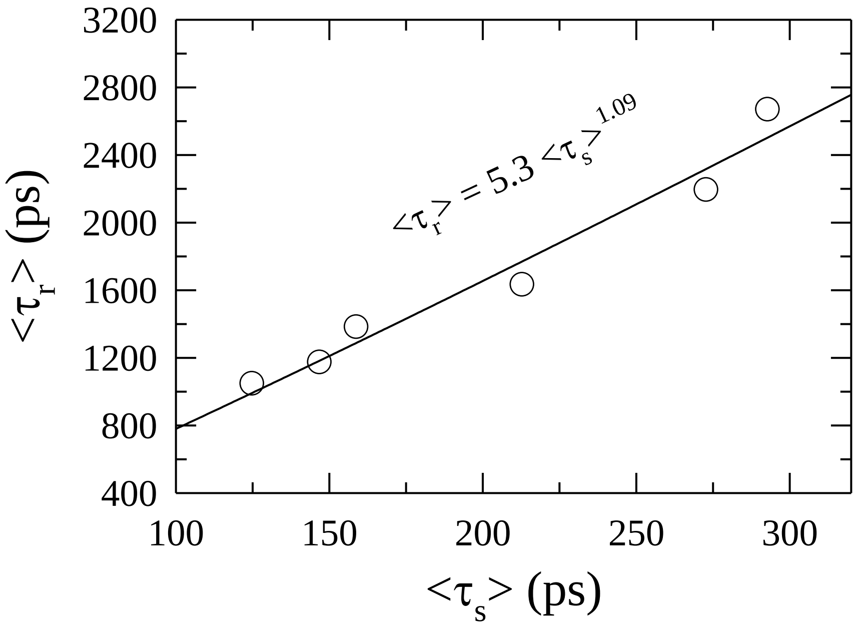

Fig. 3.10: Experimental average rotational correlation times ($\langle \tau_r \rangle$) versus solvation times ($\langle \tau_s \rangle$) for C153 in these molten mixtures at T ~318 K. $\langle \tau_s \rangle$ at higher temperatures could not be obtained because of the broader temporal resolution employed in the present experiments. The line going through the circles represents fit to the relation shown in the panel. A close examination of solvation and rotation data for most of the ionic liquids (except the phosphonium ones) summarized in Ref. 57also indicate such a proportionality: $\langle \tau_r \rangle = 9.33 \langle \tau_s \rangle^{1.03}$.

averages out environmental fluctuation more effectively than translation,[128-129] and observation of negligible λ_{exc} dependence of solute emission spectrum in these molten mixtures, it is not clear at the present moment how much of the fractional viscosity dependence arises from the medium heterogeneity and to what extent the interaction between the solute and polymerized (cation-induced) acetamide[22-25] (and thus less packing as in the case of alkanes) contributes to the break-down of the conventional DSE law in these media.

Since both average solvation and rotation times are dictated substantially by the fluidity of the medium and since both of these quantities exhibit fractional viscosity dependence in these molten mixtures, it may be interesting to explore whether these times, like in ionic liquids,[130] maintain a linear relationship between them in these media. Results shown in Fig. 3.10 clearly reveals such a relationship where the dependence can be expressed as follows: $\langle\tau_r\rangle = 5.26\langle\tau_s\rangle^{1.09}$,with a correlation coefficient (R) of 0.99. Note that these data correspond to the ternary mixture with different f_{KSCN}, but at a fixed temperature (318 K). Eventhough the above parameterization is based upon rather a limited set of data, a more extensive study (consideration of other KSCN fractions and different temperatures) is not expected to change the above relation significantly.[131] In addition, the present results are in conformity with the measurements of probe solvation and rotation in organic glass-forming liquids near T_g with several probes where average rotation times have been found to be always larger than the solvation times.[132] Interestingly, the fact that $\langle\tau_r\rangle$ is approximately five times larger than $\langle\tau_s\rangle$ in these molten mixtures is approximately in the midway between what have been observed for rotation and solvation of C153 in alkylphosphonium ionic liquids (a factor of ~2-3) and imidazolium ionic liquids (a factor of ~8-10).[103] This similarity with ionic liquids together with the fact that the greater degree of decoupling from solvent viscosity for $\langle\tau_s\rangle$ ($p = 0.46$) than for $\langle\tau_r\rangle$ ($p = 0.63$) construct a kinship to supercooled liquids where studies near T_g have shown stronger coupling between structural relaxation and rotation than that between the former and translation.[98]

3.4 Conclusion

The fluorescence spectroscopic study of molten mixtures of acetamide with sodium and potassium thiocyanates has generated several interesting results. Most important of them is the observation of fractional power law dependence on solution viscosity of both average solvation and rotational times for a dipolar solute in these molten multi-component mixtures. Curiously, the degree of decoupling from solution viscosity for average solvation is similar to the small molecule translation in ambient liquids and, for rotation, to the break-down of DSE law in supercooled liquids near to T_g. In addition, the translational decoupling (via average solvation time) has been found to be stronger than that in case of solute rotation – a result that resembles qualitatively the findings in supercooled liquids. A transition from slip to sub-slip behavior for solute rotation in these molten mixtures have been found as the temperature-scaled viscosity is increased. The role of multi-fractal dynamics in light of the very recent computer simulation study of ionic liquids[101] and effects of solution heterogeneity have been discussed in connection with the observed breakdown of conventional hydrodynamic relations for translation and rotation in these molten systems.

The observed nonmonotonic alkali metal ion concentration dependence of both steady state and dynamic fluorescence Stokes' shifts have been explained in terms of solute-solvent and solvent-solvent interaction and medium heterogeneity due to presence of dissimilar cations and ion-induced solvent polymerization.[15] The non-monotonic dependence is qualitatively similar to the results obtained by various physicochemical measurements done earlier for these mixtures and often explained in terms of mixed alkali effects. Eventhough solution heterogeneity has been found to play a greater role in explaining the viscoelastic, dielectric relaxation and other experimental results of these and similar systems, the present study finds no or secondary role of microscopic inhomogeneity of solution structure on fluorescence shifts or spectral evolution. Of course, it is to be remembered that the present experiments have missed almost half of the total dynamics due to limited time resolution and the non-finding of the heterogeneity effects could be linked to this inability of fast detection.

Further studies should be done in future with these molten systems in order to understand the extent of heterogeneity and its effects on dynamical events occurring in them. Neutron scattering and X-ray diffraction experiments may be carried out to ascertain the heterogeneity and the length scale associated with it in these complex ternary mixtures. Dielectric relaxation study with wider frequency coverage should be employed to study more carefully the low frequency as well as high frequency relaxation processes. The high-frequency dielectric relaxation results could then be complimented by Kerr spectroscopic studies and understand further the intermolecular vibrational dynamics in these non-aqueous electrolyte solutions at elevated temperature.[133-134] This is particularly important as the dielectric relaxation data constitute a crucially important input for the kind of theory used here in order to predict the solvation time scales in these molten mixtures. Since calculations presented here seem to suggest existence of ultrafast time scale in the range of sub-picosecond, dynamic Stokes' shift measurements with better time resolution would be helpful in uncovering the entire dynamics of these systems as well as the predictive power of the theory employed here. The heterogeneity effects can further be studied by using other solvatochromic probes possessing shorter average excited-state life-times than the one used here. Computer simulations with proper treatment of the longer-ranged ion-dipole and dipole-dipole interactions can significantly help understand results from many of the proposed experiments. Since dynamical studies of these molten mixtures with sophisticated time and space resolutions have not been done yet, these systems can offer interesting possibilities and results that can stimulate scientists for quite some time.

References and Notes:

1. Stafford, O. F. *J. Am. Chem. Soc.* **1933**, *55*, 3987.
2. Yntema, L. F.; Audrieth, L. F. *J. Am. Chem. Soc.* **1930**, *52*, 2693.
3. Dawson, L. R.; Sears, P. G.; Graves, R. H. *J. Am. Chem. Soc.* **1955**, *77*, 1986.
4. Wallace, R. A. *Inorg. Chem.* **1972**, *11*, 414.
5. Wallace, R. *J. Phys. Chem.* **1971**, *75*, 2687.
6. Jander, G.; Winkler, G. *J. Inorg. Nucl. Chem.* **1959**, *9*, 24.
7. Wallace, R.; Bruins, P. *J. Electrochem. Soc.* **1967**, *114*, 212.
8. Dev, S.; Das, D.; Ismail, K. *J. Chem. Eng. Data* **2004**, *49*, 339.
9. Dev, S.; Ismail, K. *J. Chem. Eng. Data* **2001**, *46*, 574.
10. Kalita, G.; Sarma, K. G.; Mahiuddin, S. *J. Chem. Eng. Data* **1999**, *44*, 222.
11. Dev, S.; Gunaseelan, K.; Ismail, K. *Langmuir* **2000**, *16*, 6110.
12. Akhter, M. S. *Colloids Surf. A* **1995**, *99*, 255.
13. Akhter, M. S.; Alawi, S. M.; Bose, A. N. *Colloids Surf. A* **1995**, *94*, 173.
14. Gusteri, M.; Bartocci, V.; Castellani, F.; Pucciarelli, F. *J. Electroanal. Chem.* **1979**, *102*, 199.
15. (a) Castellani, F.; Berchiesi, G.; Pucciarelli, F.; Bartocci, V. *J. Chem. Eng. Data* **1981**, *26*, 150; (b) Berchiesi, G.; Angelis, M. D.; Rafaiani, G.; Vitali, G. *J. Mol. Liq.* **1992**, *51*, 11.
16. Castellani, F.; Berchiesi, G.; Pucciarelli, F.; Bartocci, V. *J. Chem. Eng. Data* **1982**, *27*, 45.
17. Berchiesi, G.; Lobbia, G. G.; Bartocci, V.; Vitali, G. *Thermochim. Acta*, **1983**, *70*, 317.
18. Lobbia, G. G.; Berchiesi, G.; Poeti, G. *Thermochim. Acta*, **1984**, *74*, 247.
19. Berchiesi, G.; Lobbia, G. G.; Berchiesi, M. A.; Vitali, G. *J. Therm. Anal.* **1984**, *29*, 729.
20. Lobbia, G. G.; Berchiesi, G. *Thermochim. Acta*, **1984**, *74*, 251.
21. Lobbia, G. G.; Berchiesi, G. *Thermochim. Acta*, **1984**, *72*, 391.
22. Berchiesi, G.; Rafaiani, G.; Vitali, G.; Farhat, F. *J. Therm. Anal.* **1995**, *44*, 1313.
23. Berchiesi, G.; Vitali, G.; Passamonti, P.; Plowiec, R. *J. Chem. Soc. Faraday Trans. 2* **1983**, *79*, 1257.

24. Amico, A.; Berchiesi, G.; Cametti, C.; Biasio, A. D. *J. Chem. Soc. Faraday Trans. 2* **1987**, *83*, 619.
25. Berchiesi, G. *J. Mol. Liq*. **1999**, *83*, 271.
26. Wang, Y.; Voth, G. A. *J. Am. Chem. Soc*. **2005**, *127*, 12192.
27. Triolo, A.; Russina, O.; Bleif, H.; Cola, E. D.*; J. Phys. Chem. B* **2007**, *111*, 4641.
28. Mandal, P. K.; Sarkar, M.; Samanta,A. *J. Phys. Chem. A* **2004** , *108*, 9048.
29. Jin, H.; Li, X.; Maroncelli, M. *J. Phys. Chem. B* **, 2007** , *111* 13473.
30. Adhikari, A.; Sahu, A. K.; Dey, S.; Ghose, S.; Mandal, U.; Bhattacharyya, K. *J. Phys. Chem. B* **2007** , *111*, 12809.
31. Hu, Z.; Margulis, C. J. *Proc. Natl. Acad. Sci. U. S. A.* **2006**, *103*, 831.
32. Triolo, A.; Russina, O.; Fazio, B.; Appetecchi, G. B.; Carewska, M.; Passerini, S. *J. Chem. Phys.* **2009**, *130*, 164521.
33. Horng, M. L.; Gardecki, J. A.; Papazyan, A.; Maroncelli, M. *J. Phys. Chem.* **1995**, *99*, 17311.
34. Bhattacharyya, K.; Bagchi, B. *J. Phys. Chem. A* **2000**, *104*, 10603.
35. Bhattacharyya, K. *Chem. Comm.* **2008**, 2848.
36. Bhattacharyya, K. *Acc. Chem. Res.* **2003**, *36*, 95.
37. Ghosh, S.; Mandal, U.; Adhikari, A.; Dey, S.; Bhattacharyya, K. *Int. Rev. Phys. Chem.* **2007**, *26*, 421.
38. Biswas, R.; Rohman, N.; Pradhan, T.; Buchner, R. *J. Phys. Chem. B* **2000**, *112*, 9379.
39. Bagchi, B.; Biswas, R. *Adv. Chem. Phys.* **1999**, 109, 207.
40. Biswas, R.; Bagchi, B. *J. Phys. Chem.* **1996**, *100*, 1238.
41. Biswas, R.; Bagchi, B. *J. Phys. Chem.* **1999**, *103*, 2495.
42. Kashyap, H.; Pradhan, T.; Biswas, R. *J. Chem. Phys.* **2006**, *125*, 174506.
43. Sangma, P.; Mahiuddin, S.; Ismail, K. *J. Phys. Chem.* **1984**, *88*, 2378.
44. Kalita, G.; Rohman, N.; Mahiuddin, S. *J. Chem. Eng. Data* **1998**, *43*, 148.
45. Isard, J. O. *J. Non-Cryst. Solids* **1969**, *1*, 235.
46. Day, D. E. *J. Non-Cryst. Solids* **1976**, *21*, 343.
47. Dietzel, A. H. *Phys. Chem. Glasses* **1983**, *24*, 172.
48. Moynihan, C. T. *J. Electrochem. Soc.* **1979**, *126*, 2144.
49. Moynihan, C. T. In *Ionic Interactions;* Petrucci, S., Ed.; Academic Press: New York, 1971; Vol. 1.

50. Chapman, C. F.; Maroncelli, M. *J. Phys. Chem.* **1991**, *95*, 9095.
51. Dahl, K.; Biswas, R.; Ito, N.; Maroncelli, M. *J. Phys. Chem. B* **2005**, *109*, 1563.
52. Pradhan, T.; Biswas, R. *J. Phys. Chem. A* **2007**, *111*, 11524.
53. Pradhan, T.; Ghoshal, P.; Biswas, R. *J. Phys. Chem. A* **2008**, *112*, 915.
54. Maroncelli, M.; Fleming, G. R. *J. Chem. Phys.* **1987**, *86*, 6221.
55. Maroncelli, M. *J. Mol. Liq.* **1993**, *57*, 1.
56. The *average* peak frequency is obtained by taking the arithmatic mean of the first moment of the spectrum and the peak value obtained by fitting the upper 40% of the spectrum to an inverted parabola (see for details: (a) Lewis, J. E.; Biswas, R.; Robinson, A. G.; Maroncelli, M. *J. Phys. Chem. B* **2001**, *105*, 3306; (b) Song, W.; Biswas, R.; Maroncelli, M. *J. Phys. Chem. A* **2000**, *104*, 6924)
57. Jin, H.; Baker, G. A.; Arzhantsev, S.; Dong, J.; Maroncelli, M. *J. Phys. Chem. B* **2007**, *111*, 7291.
58. Fee, R. S.; Maroncelli, M. *Chem. Phys.* **1994**, *183*, 235.
59. Chapman, C. F.; Fee, R. S.; Maroncelli, M. *J. Phys. Chem.* **1995**, *99*, 4811.
60. Horng, M. L.; Gardecki, J. A.; Maroncelli, M. *J. Phys. Chem. A* **1997**, *101*, 1030.
61. Lakowicz, J. R. *Principles of Fluorescence Spectroscopy* (2nd edition).; Kluwer Academic: NY, 1999.
62. Cross, A. J.; Fleming, G. R. *Biophys. J.* **1984**, *46*, 45.
63. Biswas, R.; Lewis, J. E.; Maroncelli, M. *Chem. Phys. Lett*. **1999**, *310*, 485.
64. Pradhan, T.; Ghoshal, P.; Biswas, R. *J. Chem. Sci.* **2008**, *120*, 275.
65. Since fluorescence emission in these highly viscous mixtures may not occur from the fully solvent-relaxed state, we have calculated the "actual" shift (steady state) by using the formula, $\Delta\Delta\nu = \left[\nu_{abs.} - \nu_{em.}(t=\infty)\right]^{mixture} - \left[\nu_{abs.} - \nu_{em.}\right]^{heptane}$, where the steady state emission frequency ($\nu_{em.}$) at each of the mixture compositions is replaced by the emission frequency obtained from the time resolved measurements, $\nu_{em.}(t=\infty)$. Note that $\Delta\Delta\nu$ calculated by using the above formula is essentially the dynamic Stokes' shift (Fee-Maroncelli method, Ref. 58), as $\nu_{em.}^{mixture}(t=0) \approx \nu_{abs.}^{mixture} - [\nu_{abs.} - \nu_{em.}]^{nonpolar}$. If one uses heptane as nonpolar reference then the Stokes' shift calculated from the above formula approximately equals to the dynamic Stokes' shift ($\Delta\nu^{t}$) measured in time resolved experiments.

66. (a) Kashyap, H. K.; Biswas, R. *J. Phys. Chem. B* **2010**, *114*, 254; (b) Kashyap, H, K.; Biswas, R. *J. Phys. Chem. B* **2008**, *112*, 12431; (c) Guchhait, B.; Al Rasid Gazi, H.; Kashyap, H. K.; Biswas, R. *J. Phys. Chem. B* **2010**, *114*, 5066.
67. Gray, C. G.; Gubbins, K. E. *Theory of Molecular Fluids, Vol. I;* Clarendon: Oxford, 1984.
68. (a) Shirota, H.; Castner, Jr. E. W. *J. Am. Chem. Soc*. **2001**, *123*, 12877; (b) Chang, Y. J.; Castner, Jr. E. W. *J. Phys. Chem.* **1994**, *98,* 9712.
69. Roy, S.; Bagchi, B. *J. Chem. Phys.* **1993**, *99*, 9938.
70. (a) Nandi, N.; Roy, S.; Bagchi, B. *J. Chem. Phys.* **1995**, *102*, 1390; (b) Nandi, N.; Bagchi, B. *J. Phys. Chem.* **1996**, *100*, 13914.
71. (a) Bart, E.; Meltsin, A.; Huppert, D. *J. Phys. Chem.* **1994**, *98*, 3295.; (b) Bart, E.; Meltsin, A.; Huppert, D. *J. Phys. Chem.* **1994**, *98*, 10819.
72. (a) Kashyap, H. K.; Biswas, R. *J. Chem. Phys.* **2007**, *127*, 184502; (b) Kashyap, H. K.; Biswas, R. *J. Chem. Sci.* **2007**, *119*, 391.
73. (a) Marcus, Y.; Hefter, G. *Chem. Rev.* **2006**, *106*, 4585; (b) Marcus, Y.; Hefter, G. *Chem. Rev.* **2004**, *104*, 3405; (c) Hefter, G.; Marcus, Y.; Waghorne, W. E. *Chem. Rev.* **2002**, *102*, 2773; (d) Kalidas, C.; Hefter, G.; Marcus, Y. *Chem. Rev.* **2000**, *100*, 819.
74. (a) Chandra, A.; Patey, G. N. *J. Chem. Phys.* **1994**, *100*, 1552; (b) Chandra, A. *Chem. Phys. Lett.* **1995**, *244*, 314; (c) Chandra, A.; Jana, D.; Bhattacharjee, S. *J. Chem. Phys.* **1996**, *104*, 8662; (d) Mahajan, K.; Chandra, A. *J. Chem. Phys.* **1997**, *106*, 2360.
75. Bagchi, B. *Annu. Rev. Phys. Chem.* **1989**, *40*, 115.
76. Bagchi, B.; Chandra, A. *Adv. Chem. Phys.* **1991**, *80*, 1.
77. Funston, A. M.; Fadeeva, T. A.; Wishart, J. F.; Castner, Jr. E. W. *J. Phys. Chem. B*, **2007**, *111*, 4963.
78. Biswas, R.; Nandi, N.; Bagchi, B. *J. Phys. Chem. B.* **1997**, *101*, 2968.
79. The following expression for ion dynamic structure factor has been used to include the effects of inertial motion of ions on solvation energy relaxation: $S_{\alpha\beta}^{ion}(k;t) = S_{\alpha\beta}^{ion}(k)\exp\{-\frac{k^2 k_B T}{m_\alpha \varsigma_\alpha^{ion}}[t + \frac{1}{\varsigma_\alpha^{ion}}(e^{-t\varsigma_\alpha^{ion}} - 1)]\}$, ς_α^{ion} being the translational friction on the α^{th} type ion with mass m_α. ς_α^{ion} has been approximated by the Stokes' law and stick boundary condition for these ions.

80. Chandrasekhar, S. *Rev. Mod. Phys.* **1943**, *14*, 180.
81. Barthel, J.; Buchner, R.; Wurm, B. *J. Mol. Liq*. **2002**, *98-99*, 51.
82. Ediger, M. D. *Annu. Rev. Phys. Chem.* **2000**, *51*, 99.
83. Sillescu, H. *J. Non-Cryst. Solids* **1999**, *243*, 81.
84. Ediger, M. D.; Angell, C. A.; Nagel, S. R. *J. Phys. Chem.* **1996**, *100*, 13200.
85. Chang, I.; Fujara, F.; Geil, B.; Heuberger, G.; Mangel, T.; Sillescu, H. *J. Non-Cryst. Solids* **1994**, *172-174*, 248.
86. Moynihan, C. T. *J. Phys. Chem.* **1966**, *70*, 3399.
87. Angell, C. A. *J. Chem. Phys.* **1967**, *46*, 4673.
88. Egelstaff, P. A. *An Introduction to the Liquid State* (Clarendon, Oxford) 1992.
89. Pollack, G. L. *Phys. Rev. A.* **1981**, *23*, 2660.
90. Pollack, G. L.; Enyeart, J. J. *Phys. Rev. A.* **1985**, *31*, 980.
91. Voronel, A.; Veliyulin, E.; Machavariani, V. Sh.; Kisliuk, A.; Quitmann, D. *Phys. Rev. Letts.* **1998**, *80*, 2630.
92. Evans, D. F.; Tominaga, T.; Davis, H. T. *J. Chem. Phys.* **1981**, *74*, 1298.
93. Chen, S. H.; Davis, H. T.; Evans, D. F. *J. Chem. Phys.* **1981**, *75*, 1422.
94. Chen, S. H.; Davis, H. T.; Evans, D. F. *J. Chem. Phys.* **1982**, *77*, 2540.
95. Hiss, T. G.; Cussler, E. L. *AIChE Journal*, **1973**, *19*, 698.
96. Diezemann, G.; Sillescu, H.; Hinze, G.; Bohmer, R. *Phys. Rev. E.* **1998**, *57*, 4398.
97. Jung, Y. J.; Garrahan, J. P.; Chandler, D. *Phys. Rev. E.* **2004**, *69*, 061205-1.
98. Ngai, K. L. *J. Phys. Chem. B* **1999**, *103*, 10684.
99. Harris, K. R. *J. Chem. Phys*. **2009**, *131*, 054503.
100. Shlesinger, M. F.; Zaslavsky, G. M.; Klafter, J. *Nature* **1993**, *363*, 31.
101. Habasaki, J.; Ngai, K. L. *J. Chem. Phys.* **2008**, *129*, 194501.
102. Hu, Z.; Huang, X.; Annapureddy, H. V. R.; Margulis, C. J. *J. Phys. Chem. B* **2008**, *112*, 7837.
103. Ito, N.; Arzhantsev, S.; Heitz, M.; Maroncelli, M. *J. Phys. Chem. B.* **2004**, *108*, 5771.
104. Jin, H.; Baker, G. A.; Arzhantsev, S.; Dong, J.; Maroncelli, M. *J. Phys. Chem. B*, **2007**, *111*, 7291.
105. Paul, A.; Samanta, A. *J. Phys. Chem. B*, **2007**, *111*, 4724.
106. Paul, A.; Samanta A. *J. Phys. Chem. B*, **2008**, *112*, 947.

107. (a) Seth, D.; Chakraborty, A.; Setua, P.; Sarkar, N. *J. Phys. Chem. B*, **2007**, *111*, 4781. (b) Chakrabarty, D.; Seth, D.; Chakraborty, A.; Sarkar, N. *J. Phys. Chem. B*, **2005**, *109*, 5753.

108. Arzhantsev, S.; Jin, H.; Baker, G. A.; Maroncelli, M. *J. Phys. Chem. B*, **2007**, *111*, 4978.

109. Samanta, A. *J. Phys. Chem. B*, **2006**, *110*, 13704.

110. Mandal, P. K.; Samanta, A. *J. Phys. Chem. B*, **2005**, *109*, 15172.

111. Andreozzi, L.; Faetti, M.; Giordano, M.; Leporini, D. *J. Phys.: Condens. Matter* **1999**, *11*, A131.

112. Andreozzi, L.; Bagnoli, M.; Faetti, M.; Giordano, M. *J. Non-Cryst. Solids* **2002**, *303*, 262.

113. Andreozzi, L.; Di Schino, A.; Giordino, M.; Leporini, D. *Europhys. Lett.* **1997**, *38*, 669.

114. Andreozzi, L.; Di Schino, A.; Giordino, M.; Leporini, D. *J. Phys.: Condens. Matter*, **1996**, *8*, 9605.

115. Andreozzi, L.; Faetti, M.; Giordino, M.; Leporini, D. *J. Phys. Chem.* **1999**, *103*, 4097.

116. Andreozzi, L.; Giordino, M.; Leporini, D. *J. Non-Cryst. Solids* **1998**, *235-237*, 219.

117. Faetti, M.; Giordino, M.; Pardi, L.; Leporini, D. *Macromolecules* **1999**, *32*, 1876.

118. Hooker, J. C.; Torkelson, J. M. *Macromolecules* **1995**, *28*, 7683.

119. Dhinojwala, A.; Wong, G. K.; Torkeson, J. M. *J. Chem. Phys.* **1994**, *100*, 6046.

120. Ye, J. Y.; Hattori, T.; Nakatsuka, H. *Phys. Rev. B* **1997**, *56*, 5286.

121. Michele, D. C.; Leporini, D.; *Phys. Rev. E* **2001**, *63*, 036702.

122. Douglas, J. F.; Leporini, D. *J. Non-Cryst. Solids* **1998**, *235-237*, 137.

123. Barkley, M. D.; Kowalczyk, A. A.; Brand, L. *J. Chem. Phys.* **1981**, *75*, 3581.

124. Hu, Y.; Fleming, G. R. *J. Chem. Phys.* **1991**, *94*, 3857.

125. Jas, G. S.; Larson, E. J.; Johnson, C. K.; Kuczera, K. *J. Phys. Chem. A* **2000**, *104*, 9841.

126. Inamder, S. R.; Mannekutla, J. R.; Mulimani, B. G.; Savadatti, M. I. *Chem. Phys. Lett.* **2006**, *429*, 141.

127. Tan, X.; Gustafson, T. L. *J. Phys. Chem. A.* **2000**, *104*, 4469.

128. Huang, W.; Richert, R. *Phil. Mag.* **2007**, *87*, 371.

129. Cicerone, M. T.; Blackburn, F. R.; Ediger, M. D. *J. Chem. Phys.* **1995**, *102*, 471.

130. Ingram, J. A.; Moog, R. S.; Ito, N.; Biswas, R.; Maroncelli, M. *J. Phys. Chem. B.* **2003**, *107*, 5926.

131. Because of our limited temporal resolution, dynamic Stokes' shift measurements could not be done at higher temperatures. However, it is logical to expect that $\langle \tau_s \rangle$ will track the solvent viscosity at higher temperatures in roughly the same manner as it has done at T ~318 K. The extent of heterogeneity will, of course, be much less at elevated temperatures and the enhanced fluidity will increase the long-time solvation rate. If it is considered that the solute-solvent nearest neighbor interactions, which is believed to be important for polar solvation dynamics at long-time,[39] also control substantially the solute rotation, then a similar proportionality relation between $\langle \tau_r \rangle$ and $\langle \tau_s \rangle$ can be expected at higher temperatures as well.

132. Yang, M.; Richert, R. *Chem. Phys.* **2002**, *284*, 103.

133. Fujisawa, T.; Nishikawa, K.; Shirota, H. *J. Chem. Phys.* **2009**, *131*, 244519.

134. Turton, D. A.; Hunger, J.; Stoppa, A.; Hefter, G.; Thoman, A.; Walther, M.; Buchner, R.; Wynne, K. *J. Am. Chem. Soc.* **2009**, *131*, 11140.

135. Attard, P. *Phys. Rev. E,* **1993**, *48*, 3604.

136. Chandra, A.; Bagchi, B. *J. Chem. Phys.* **1999**, *110*, 10024.

137. Lebowitz, J. L. *Phys. Rev.* **1964**, *133*, A895.

Chapter 4

Medium Decoupling of Dynamics in (Acetamide + Lithium Bromide/ Nitrate) Melts at Temperatures ~100 K above Glass-Transition Temperature

4.1 Introduction

It is long-known that short chain aliphatic amides, when mixed with inorganic salts, produces liquids at or near room temperature with a remarkable tendency to supercool.[1-13] Acetamide has been one of the most frequently used amides because of its unique solvating power[14-19] which arises due to the presence of several functional groups, high molecular dipole moment (3.7 D) and fairly large static dielectric constant ($\varepsilon_0 \approx 60$)[17] in molten state (melting point ~353 K, boiling point ~495 K). These interesting solvent properties coupled with a wide thermal window have made molten mixtures of (acetamide + electrolyte) to be used not only as reaction media in chemical industry but also as materials for electrochemical applications at elevated temperatures.[20,21] These molten mixtures (or simply, melts) are characterized by estimated glass transition temperatures (T_g) $\sim 190 < T_g / K < 250$ range,[22-25], and are termed as supercooled mixtures as they remain in the liquid phase at temperatures much below the respective melting temperatures of the constituents. This 'supercooling' phenomenon and the associated importance for chemical industry have motivated much of the research on the basic scientific aspects, because developing these melts into useful dielectric materials[13,26] requires deeper understanding of medium structural and transport properties.

Presence of microheterogeneity in solution structure was suggested earlier by viscoelastic,[11,27] ultrasonic,[3,26] nuclear magnetic resonance (NMR)[10] and dielectric relaxation (DR)[3,12] experiments with (amide + salt) melts. A model solution structure consisting of salt domains, amorphous amide and amide interacting with ions was proposed[13] in order to uniformly explain the relaxation characteristics revealed by the above experiments. Most striking of these experimental studies had been the suggestion of colossal (~10^6) static dielectric constant (ε_0) for these melts by the DR measurements[3,12,13,26] performed in the frequency range, $0.1 \le \nu/Hz \le 10^6$, which also reported Cole-Cole[28] relaxation processes with a strong stretching exponent (or shape parameter), particularly at the high frequency region, for (CH_3CONH_2 + NaSCN) melt. In addition, depending upon temperature ($265 \le T/K \le 311$), extremely slow relaxation times - one varying between ~10 ms and ~0.5 s at the low frequency regime and the other between ~25 ns and ~250 ns at the high frequency regime - characterized the acetamide-thiocyanate melt data.[12] In contrast, similar measurements with (CH_3CONH_2 + CF_3COONa) and (CH_3CONH_2 + $Ca(NO_3)_2$) melts[3] reported that even-though the DR data were equally describable by either Cole-Cole or Davidson-Cole[29] processes, spectral characteristics did not deviate much from the conventional Debye description.[30] Interestingly, the diameter of the charged domain, thought to be responsible for the mega-value of ε_0 and formed via ion aggregation, was estimated to be ~10 nm and in equilibrium with two types of amide environements.[3] Further viscoelastic and ultrasonic relaxation measurements[27] revealed the proposed aggregation phenomenon was less pronounced for melts containing ions other than Na^+. This variation notwithstanding, microheterogeneity had been a recurrent theme in the early literature while analyzing the experimental results for these melts.

Recent steady state and time-resolved fluorescence spectroscopic studies with some of these melts have suggested that the average ε_0 of these molten mixtures is much smaller than the reported mega-value and, in fact, very similar to that of ambient liquid formamide (FA).[31,32] Average solvation and rotation times, obtained from dynamic Stokes shift and fluorescence anisotropy measurements[31] have indicated strong solution heterogeneity as these quantities ($\langle \tau_s \rangle$ and $\langle \tau_r \rangle$) exhibited a fractional solution viscosity dependence, $\langle \tau_x \rangle \alpha \, (\eta/\mathrm{T})^p$, with p much less than unity but larger for $\langle \tau_r \rangle$ than for $\langle \tau_s \rangle$. The fractional viscosity dependence of these quantities and the consequent departure from the conventional Stokes-Einstein (SE)[33] and Stokes-Einstein-Debye (SED)[34] predictions for these melts are reminiscent of environmental as well as translation-rotation decoupling observed in deeply supercooled liquids.[35-41] Furthermore, the microheterogeneity and the longer-ranged interactions (mainly those proportional to r^{-1}, r^{-2} and r^{-3}, r being the distance between two interacting species)[42] present in these systems jointly render a resemblance with many room temperature ionic liquids (IL) where microscopic inhomogeneity[43-57] and similar electrostatics govern the liquid properties. The closeness between these melts and dipolar ionic liquids is further evidenced when application of a semi-molecular theory that successfully described the Stokes shift dynamics in ILs and (ionic liquid + polar solvent) binary mixtures [58-62] could also semi-quantitatively predict the solvation time scales and dynamic Stokes shift in (CH_3CONH_2 + Na/KSCN) and (CH_3CONH_2 + $Ca(NO_3)_2$) melts.[31,32] It should be recognized here that the agreement between theory and experiments appears due mainly to the domination of the collective solvent polarization fluctuation in polar solvation energy relaxation where details of solvent structure around a dissolved dipolar solute assumes a secondary importance.[63-65] The striking difference, however, is while fluorescence studies with (CH_3CONH_2 + Na/KSCN) mixtures have revealed strong deviation from the SE and SED predictions, ILs show near hydrodynamic description[66] eventhough both of these different systems are characterized by heterogeneity and similar interactions.

In the present chapter we have expanded our fluorescence investigation into the molten mixtures of acetamide with lithium nitrate and bromide of the following general formula, [$0.78CH_3CONH_2$ + 0.22{f LiBr + (1-f) $LiNO_3$}], where fractions of the anions (bromide, Br^- and nitrate, NO_3^-) have been varied in order to investigate both the mixed anion effects (MAE)[67-72] and the nature of solute-environment interaction. Composition dependence (via varying f_{LiBr} from 0 to 1) of static and dynamic fluorescence characteristics of a dissolved fluorescent probe and temperature effects on them have been investigated to gain further insight into the solute-medium coupling in these supercooled melts. The amide concentration is kept fixed at 0.78 mole fraction because at this composition the mixture remains in the liquid phase[2,5,22] for the temperature range considered, $303 \le T/K \le 364$. In addition, density, and viscosity data in the same temperature range for these melts have been measured earlier by different authors [23] which also report, apart from the Vogel-Fulcher-Tammann[73] description of temperature dependent transport properties, presence of a moderate MAE for the electrical conductivity. Interestingly, both steady state and dynamic Stokes shifts measured using

C153 exhibit non-ideal anion concentration dependence, indicating fluorescence detection of MAE for [$0.78CH_3CONH_2$ + 0.22{*f* LiBr + (1-*f*) $LiNO_3$}] melts. Extent of heterogeneity, as suggested by the excitation wavelength ($\lambda_{exc.}$) dependence of the fluorescence emission spectrum and the magnitude of p associated with the fractional viscosity dependence, has been found to be more pronounced in these melts than in [$0.75CH_3CONH_2$ + 0.25{*f* KSCN + (1-*f*) NaSCN}] mixtures.[31] This is a result different from earlier suggestion[3,27] that (acetamide + electrolyte) melts containing cation other than Na^+ is relatively less inhomogeneous. As observed in our previous experiments,[31,32] UV-VIS absorption and fluorescence emission characteristics of C153 indicate an average polarity similar to that of liquid formamide at ambient condition, which is much smaller than what was indicated[3,12,13,26] for this kind of melts. Both $\langle\tau_s\rangle$ and $\langle\tau_r\rangle$ in the present measurements increase with Br^- concentration. This follows the mixture composition dependence of η, which, in our measurements, increases with Br^- concentration. Activation energy (E_{act}) estimated from $\langle\tau_r\rangle$ for a given composition has been found to be ~1.5 times larger than that obtained from $\langle\tau_s\rangle$ and the ratio between $E_a(\langle\tau_r\rangle)$ and $E_a(\langle\tau_s\rangle)$ closely follows that between respective p values. In addition, our application of a semi-molecular theory has revealed that the biphasic solvation response observed in these melts originates from the orientational solvent density fluctuations at the collective and nearest neighbor modes, and the isotropic density fluctuations involving the nearest neighbors. The organization of the rest of the chapter is as follows. Experimental details are given in the next section. Section 4.3 contains experimental results from our steady state and time resolved studies. Supporting information is given wherever necessary in Appendix. The article then ends with concluding remarks in section 4.4.

4.2 Experimental Sections

4.2.1 Sample Preparation

C153 (laser grade, Exciton) was used without further purification. Another probe, trans-2-[4-dimethylamino)styryl]benzothiazole (DMASBT), whose excited state lifetime is known to be a function of medium viscosity,[74] was used (as received[75]) only to investigate the

$\lambda_{exc.}$ dependence of its steady state fluorescence emission at a given composition of these melts. Acetamide ($\geq$99%, SRL, India), lithium nitrate ($\geq$99.5%, SRL, India) and lithium bromide (>99%, Merck Specialities, India) were vacuum-dried (~300 K) for 24 hours before use. Note here that lithium bromide is the most hygroscopic among these three chemicals and becomes liquid if salt grains are exposed to open air for about ~5-10 minutes. Presence of moisture in LiBr may originate from improper drying and exposure to open air during sample preparation at our experimental condition. Therefore, LiBr used in our samples should be correctly designated as $LiBr.xH_2O$, x denoting the unknown but small amount of water associated with LiBr present in the melt. This is important because presence of water can substantially affect melt viscosity and other dynamical quantities of interest here. Formamide (>99%, Sigma-Aldrich) was used as received. Since a detailed discussion regarding method of sample preparation for experiments with similar molten mixtures is already given in chapter 3, we do not repeat but only mention that the concentration of C153 in the sample was always regulated at $\leq 10^{-5}$ M. Proper equilibration of the quartz cuvette (1 cm path length) containing sample with the preheated sample chamber (through hot water circulation, Julabo) was ensured before spectral measurements. A few samples were bubbled with dry N_2 gas before data collection but did not produce any difference in data with those collected with the un-bubbled samples. Since phase separation occurs ~5 K below 303 K for a few of these melts and thus spectroscopic measurements were not carried out at $T(K) < 303$. Composition and temperature dependent viscosities of these melts were measured by using an AMVn automated micro-viscometer from Anton Paar (falling ball method).

4.2.2 Data Collection and Analyses for Stokes' Shift Dynamics and Rotational Relaxation

Steady state and time resolved spectral data measurement techniques and the corresponding analysis procedures are essentially the same as described in chapter 2 and in refs.[76-81] Steady state absorption and fluorescence spectra were collected by using respectively a UV-visible spectrophotometer (UV-2450, Shimadzu) and fluorimeter (Fluoromax-3, Jobin-Yvon, Horiba). Solvent blanks were subtracted prior to analysis. Time resolved emission decays were measured using a time-correlated single photon counting instrument. 409 nm dye laser was used as excitation source. The full-width at half maximum (FWHM) of the instrument response function (IRF) with this excitation source was ~ 70 ps. Decay collection at each of these wavelengths was continued till the peak-count was reached ~5000 (dark count ~10). For solvation dynamics measurement 18-20 decays at wavelengths spanning emission spectrum were collected at magic angle. The collected decays were deconvoluted from the IRF and fitted to multi-exponential function using an iterative reconvolution algorithm.[76-79] Time resolved emission spectra (TRES) were then reconstructed from the decay fit parameters in conjunction with normalized intensities of the steady state emission spectrum as described in refs.[79,82,84] For the purpose of rotational dynamics measurement a set of three decays, namely, parallel, perpendicular and magic angle polarizations were collected. Time resolved fluorescence anisotropies,[80,81] $r(t)$, were then calculated from the collected decays by using the method described in chapter 2.

4.3 Results and Discussion

4.3.1 Steady State Spectral Measurements: Heterogeneity Signatures

Fig. 4.1 depicts the absorption and emission spectra of C153 in [$0.78CH_3CONH_2 + 0.22\{f$ LiBr + (1-f) $LiNO_3\}$] melt at $f_{LiBr} = 0.6$ and 303 K, and also those in liquid formamide (broken lines) at the same temperature. The striking resemblance between the spectra in the melt and those in FA (ε_0=111)[83] indicates very similar solute-solvent interaction in these two different types of media. Interestingly, the closeness in spectral peak positions alone cannot suggest that ε_0 of this (acetamide + salt) melt is much less than the mega-value reported earlier for similar melts[3,12,13] because in the limit of large ε_0 the transition frequency (absorption or emission) becomes insensitive to the value of average static dielectric constant. Dynamic Stokes shift measurements and subsequent analyses using a suitable molecular theory, however, may provide a resolution to the debate. Since this issue would be discussed later at length, let us now present results from the steady state spectroscopic measurements revealing more on the equilibrium structural aspects of these molten mixtures.

Fig. 4.2 demonstrates the LiBr concentration (f_{LiBr}) dependence of the steady state absorption and fluorescence emission frequencies (upper panel), the steady state and

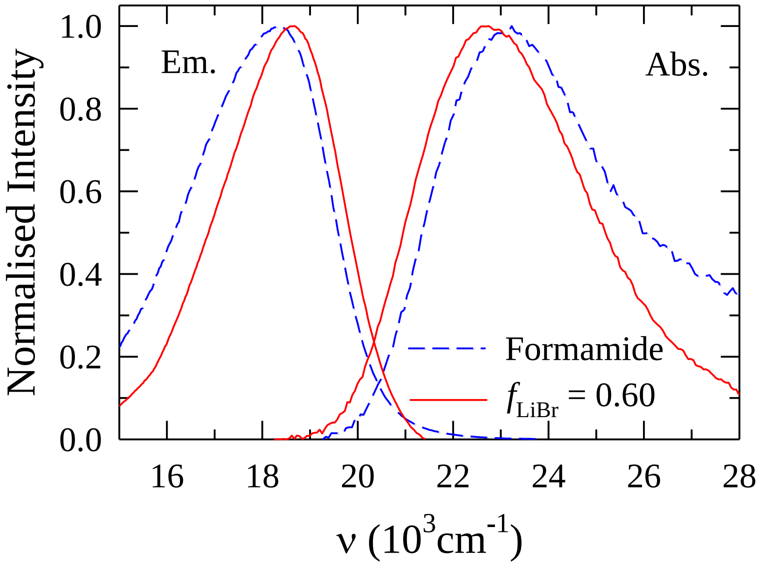

Fig. 4.1: Representative steady state absorption and emission spectra (color coded) of the dissolved solute (C153) at 303 K in $[0.78CH_3CONH_2 + 0.22\{f\ \text{LiBr} + (1\text{-}f)\ \text{LiNO}_3\}]$ molten mixtures at $f_{LiBr} = 0.60$ and those in formamide.

dynamic Stokes shifts (middle panel) and the difference between them (lower panel) at 303 K and 318 K. Corresponding data for 313 K are shown in Fig. A4 (Appendix) Note that the Stokes shift dynamics at ≥318 K is too fast to be measured by our present experiments and thus we show steady state data for these temperatures only. It is interesting to note that while the average absorption frequencies (ν_{abs})[85,86] at both the temperatures exhibit a non-monotonic f_{LiBr} dependence, emission frequencies (ν_{em}) remain largely insensitive to that. The initial blueshift (by ~200-300 cm^{-1}) of ν_{abs} with f_{LiBr} may arise from the following reasons: (i) reduced availability of acetamide molecules for interacting with the solute (C153) due to solvation of both NO_3^- and Br^- ions, (ii) the variation in packing due to difference in sizes of these solvated anions.[87] The presence of both NO_3^- and Br^- in the melt at this regime increases solution heterogeneity and this is reflected in the f_{LiBr} dependent absorption spectral width shown in Fig. A5 (Appendix). Further replacement of NO_3^- by Br^- probably enhances the extent of anion-C153 interaction that induces redshift and thus sets up the observed non-monotonic composition dependence. The heterogeneity in turn becomes less pronounced and

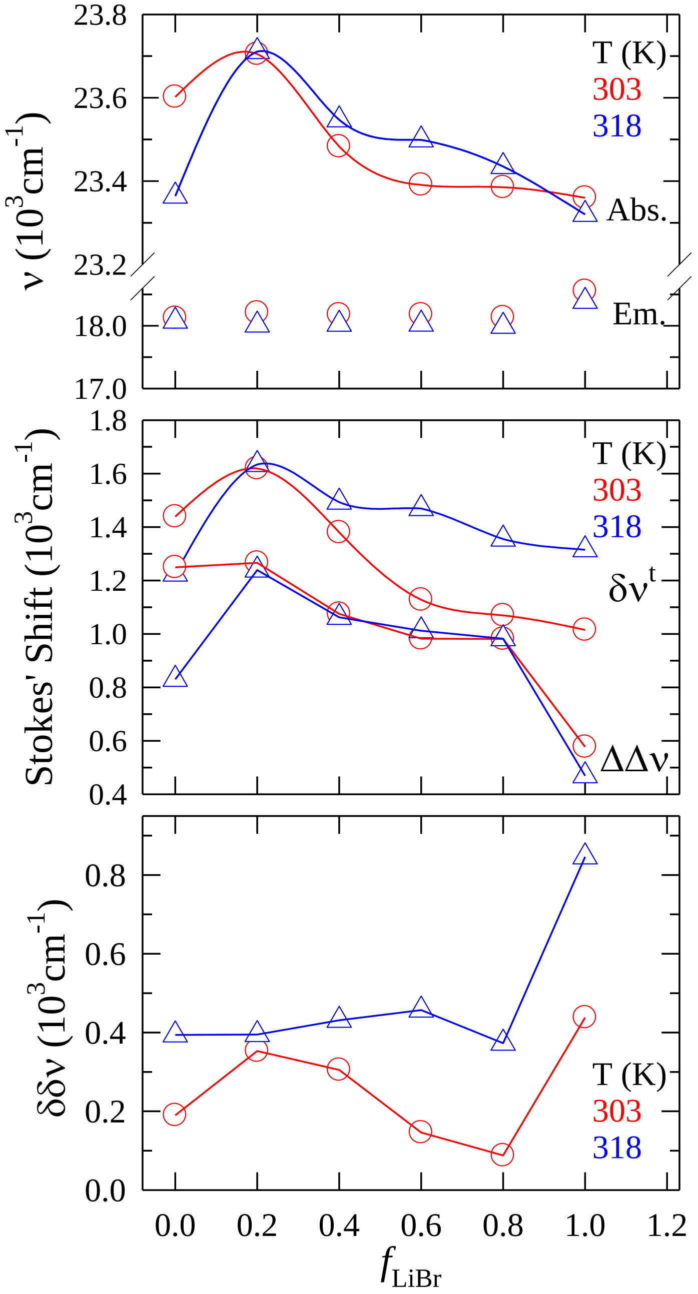

Fig. 4.2: Composition (f_{LiBr}) dependence of spectral parameters at different temperatures (color coded). While the f_{LiBr} dependent absorption and emission frequencies are shown in the upper panel, steady state relative Stokes' shift (ΔΔν) and estimated dynamic Stokes' shift ($\Delta\nu^{t}$) are presented in the middle panel. Lower panel shows the composition dependence of difference between the relative and dynamic shifts, defined as: $\delta\delta\nu = \Delta\nu^{t} - \Delta\Delta\nu$. The relative Stokes shift has been obtained by using the relation $\Delta\Delta\nu = [\nu_{abs.} - \nu_{em.}]^{mixture} - [\nu_{abs.} - \nu_{em.}]^{heptane} = \Delta\nu^{mixture} - \Delta\nu^{heptane}$ with $\Delta\nu^{heptane}$ = 4230 cm^{-1} , and $\Delta\nu^{t} = [\nu(t=0) - \nu_{em.}(t=\infty)]^{mixture}$. $\nu(t=0)$ has been obtained by using the Fee-Maroncelli method (Ref. 90). Measured frequencies are better than $\pm 150\,\mathrm{cm}^{-1}$.

consequently the spectral width decreases (see Fig. A5, Appendix). Since both NO_3^- and Br^- are uni-negative ions, the extent of electrical (ion-dipole) interaction between C153 and these anions is near-equivalent, producing very similar ν_{abs} for binary melts with f_{LiBr} =0 and f_{LiBr} =1. Another subtle aspect may be noted in Fig. 4.2 is that ν_{abs} at f_{LiBr} =0 is larger at 303 K than that at 318 K whereas the temperature-induced variation at f_{LiBr} =1 is negligible. This difference may be attributed to the relatively less solute-ion interaction at f_{LiBr} =0 because of higher lattice and gas-phase bond dissociation energies for $LiNO_3$ than that for LiBr.[88] The insensitivity of ν_{em} to mixture composition, also observed earlier for [$0.75CH_3CONH_2$ + 0.25{*f* KSCN + (1-*f*) NaSCN}] molten mixtures,[31] arises probably due to shorter heterogeneity lifetime than that of fluorescent probe in the excited state.[51,54(a),89] Note ν_{em} in binary melt with f_{LiBr} =1 at these temperatures are 'bluer' than expected and this could be due to relatively slower environmental relaxation[77,78] because of larger effective (solvated) size and heavier mass of Br^- compared to those of NO_3^-.

The composition dependent steady state Stokes' shift ($\Delta\Delta\nu$) and total dynamic Stokes' shift ($\delta\nu^t$) estimated[90] from time-resolved data, shown in the middle panel of Fig. 4.2, clearly indicate that steady state fluorescence emission in these melts occurs from an incompletely solvent-relaxed excited solute. The difference, $\delta\delta\nu = \delta\nu^t - \Delta\Delta\nu$, is positive and ranges between ~100 and 800 cm^{-1} and is similar - both in nonmonotonicity and magnitude - to our earlier results for [$0.75CH_3CONH_2$ + 0.25{*f* KSCN + (1-*f*) NaSCN}] melts.[31] What is striking though is that the composition dependent $\delta\delta\nu$, shown in the lower panel, is larger at higher temperature ($\delta\delta\nu$ values at 313 K are summarized in Table A1, Appendix). This suggests increased presence of ions at higher temperature forcing the steady state fluorescence to occur from excited solutes locked in solvent configurations which are far from completely relaxed.

The heterogeneity aspect of these melts is further investigated by following the excitation wavelength ($\lambda_{exc.}$) dependence of the steady state fluorescence emission from two dissolved probes, C153 and DMASBT. In common solvents, the average excited state lifetime ($<\tau_{life}>=\sum_i a_i\tau_i \big/ \sum_i a_i$) of DMASBT, a function of both η and ε_0, ranges between 20 – 100 ps[91] and thus significantly shorter than that (3 - 5 ns)[76] for C153. In addition, collected time-resolved decays (magic angle) of fluorescence emission from DMASBT dissolved in [$0.78CH_3CONH_2$ + 0.22{*f* LiBr + (1-*f*) $LiNO_3$}] molten mixture at 303 K with $f_{LiBr}=0.2$ and 0.8 have been found to fit to bi-exponential function of time, producing ~470 ps and ~600 ps respectively as $<\tau_{life}>$ at these compositions (see Fig. A6, Appendix). Fluorescence signature of DMASBT in these melts would therefore be more responsive to those 'shorter-lived' domains which could not be distinguished by the relatively longer-lived excited C153. $\lambda_{exc.}$ dependent emission frequencies ($\nu_{em.}$) for these two fluorophores in [$0.78CH_3CONH_2$ + 0.22{*f* LiBr + (1-*f*) $LiNO_3$}] molten mixture at 303 K with $f_{LiBr}=0.2$ are shown in the upper panel of Fig. 4.3. Note $\nu_{em.}$ for DMASBT shifts by ~1200 cm^{-1} for changing $\lambda_{exc.}$ from the bluest to the most red of the considered wavelengths, and is nearly double of what C153 exhibits in the equivalent $\lambda_{exc.}$ range. The $\lambda_{exc.}$ dependence of fluorescence spectral width ($\Gamma_{em.}$), shown in the middle panel, also follows the expected trend of narrowing down with increased solvation for both these probes, the extent of total narrowing for DMASBT being approximately thrice as large as that for C153. These results, eventhough cannot suggest any domain size or the length scale over which medium particles are correlated, do provide an idea about the lifetime of microscopic structures that render spatial heterogeneity in these melts. One of the implications of this finding is that in frequency domain experiments, such as dielectric relaxation spectroscopy, effects of such short-lived structures will probably not be reflected at the megahertz (MHz) region.

Composition dependence of the heterogeneity in [$0.78CH_3CONH_2$ + 0.22{*f* LiBr + (1-*f*) $LiNO_3$}] molten mixture at a given temperature is next investigated by monitoring the changes in spectral (emission) position and width for these solutes. Results are summarized in the lower panel of Fig. 4.3 where the differences between emission frequencies ($\Delta\nu$) and widths ($\Delta\Gamma$) obtained by exciting the solutes at the smallest (bluest, $\lambda_{exc.,b}$) and largest (most red, $\lambda_{exc.,r}$) wavelengths at a given composition and temperature are shown as a function of LiBr concentration, f_{LiBr}. These quantities are defined as follows: $\Delta x(f_{LiBr},T)=x(f_{LiBr},T,\lambda_{exc.,b})-x(f_{LiBr},T,\lambda_{exc.,r})$ with $x=\nu_{em.}$ or $\Gamma_{em.}$. Spectral

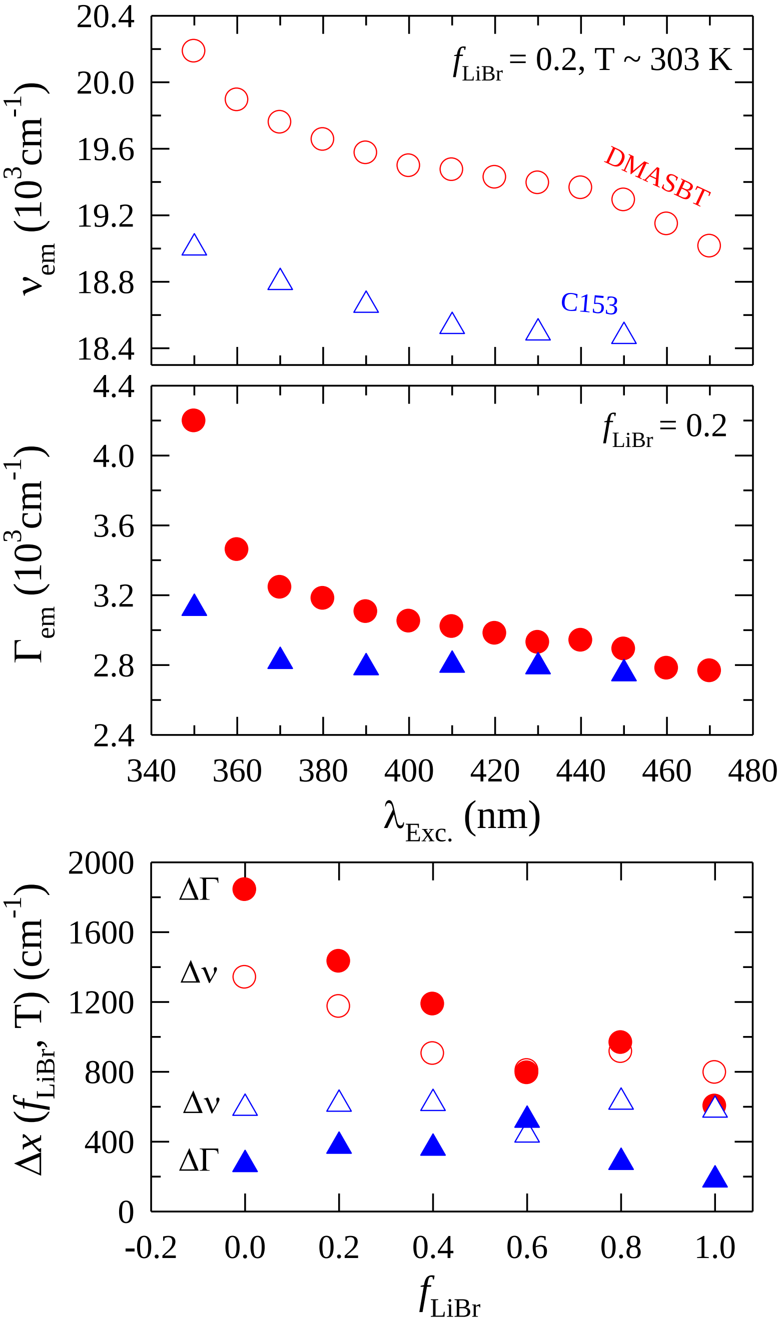

Fig. 4.3: Excitation wavelength dependence (λ_{exc}) of emission peak frequency (ν_{em}) for DMASBT and C153 (upper panel) and full-widths-at-half maxima (FWHM, Γ_{em}) of emission spectra of these two solutes in [0.78CH$_3$CONH$_2$ + 0.22{*f* LiBr + (1-*f*) LiNO$_3$)] molten mixtures at f_{LiBr} = 0.2 and 303 K (middle panel). Composition dependent total differences (Δx) in Γ_{em} and ν_{em} are shown in the lower panel. This is defined as $\Delta x(f_{LiBr},T) = x(f_{LiBr},T,\lambda_{exc.,b}) - x(f_{LiBr},T,\lambda_{exc.,r})$, x being Γ_{em} or ν_{em}. $\lambda_{exc.,b}$ and $\lambda_{exc.,r}$ are the shortest (bluest) and longest (most red) wavelengths used for solute excitation. The uncertainty in frequencies remains the same as in Fig. 2. Widths are better than $\pm 250\,\mathrm{cm}^{-1}$.

features ($\Delta\nu$ and $\Delta\Gamma$) displayed here have been obtained at $T = 303$ K, and represent the trend observed at few other higher temperatures. It is evident from this panel that the $LiNO_3$-rich solution is more heterogeneous and the extent of heterogeneity decreases upon progressive replacement of NO_3^- by Br^-. In addition, DMASBT reveals more pronounced heterogeneity at all compositions than that by C153. The increased heterogeneity in presence of $LiNO_3$ could arise from the presence of both ionic and non-ionic species because of less dissociation of $LiNO_3$ compared to LiBr. Higher lattice and gas-phase dissociation energies[88] for $LiNO_3$ than those for LiBr, and increase in electrical conductivity[23] of the melt upon replacing $LiNO_3$ by LiBr seem to support the above view.

4.3.2 Time-Resolved Measurements: Stokes Shift Dynamics and Relevant Density Fluctuation Modes

As already indicated, characteristics of fluorescence emission intensity decays collected at magic angle for C153 in these mixtures depend upon the detection wavelength, showing signatures of environmental rearrangement with time in response to an instantaneously altered charge distribution of a dissolved solute. A representative example is provided in Fig. 4.4 where emission decays collected at a shorter wavelength ("blue" with respect to the peak wavelength of the corresponding steady state emission spectrum) and at a longer wavelength ("red") along with their multi-exponential fits, residuals and fit parameters are shown for a melt with $f_{LiBr} = 0.6$ at 303 K. The presence of decays only at the blue wavelength and both rise and decay at the red wavelength clearly suggest time-dependent solvation of the excited solute in these melts. Note that eventhough most of the time-resolved emission intensity profiles require tri-exponential functions of time for adequate description, intensity profiles collected around the peak wavelength can be sufficiently represented by a sum of two exponentials. In addition, effects of fluorescence quenching on the detected spectral dynamics have been found to be secondary as the composition dependent longest time constant ($\tau_{Longest}$) associated with the decays at 303, 313 and 318 K, shown in Fig. A7 (Appendix), varies by a maximum of ~20%. Therefore, the decay characteristics at various emission wavelengths may be regarded as representing the dynamics of solvation of the excited solute (C153) in these molten mixtures.

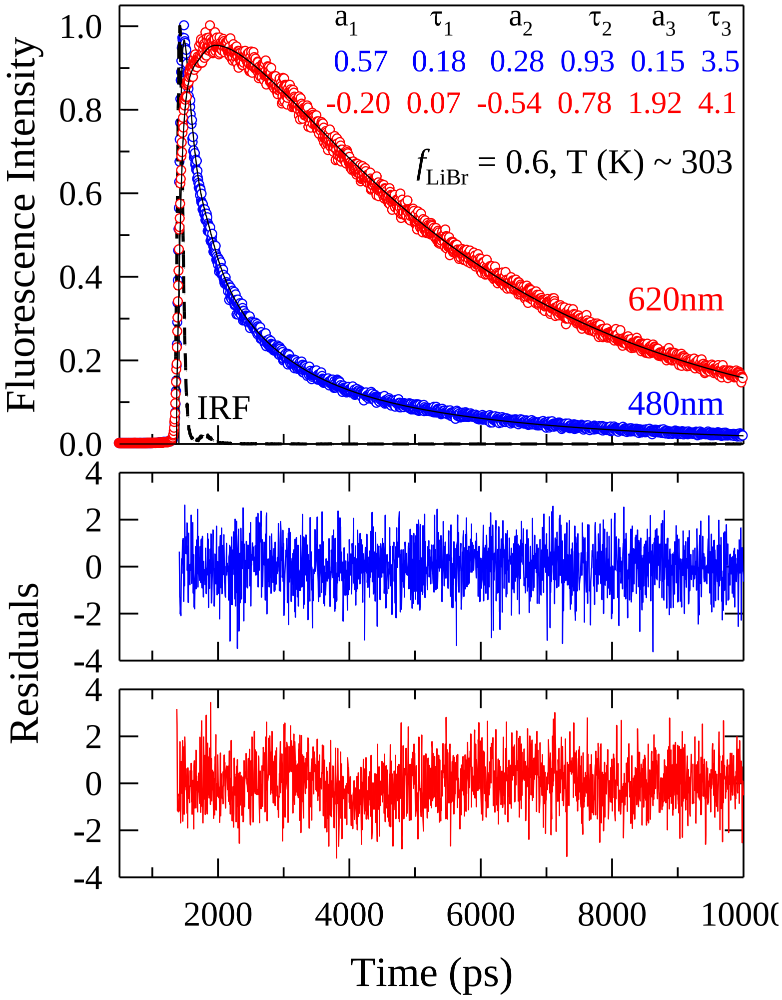

Fig. 4.4: Representative fluorescence intensity decays at blue (480nm) and red (620nm) wavelengths for C153 in molten mixtures at f_{LiBr} = 0.60 and ~303 K. Circles denotes the experimental data and solid lines fits through them. Instrument response function (IRF) is also shown in the same figure (dashed lines). The respective residuals (color coded) are presented in the bottom panels. The fit parameters are shown in the inset of the upper panel. Time constants (τ_i) are in the unit of nanosecond. The Goodness-of-fit parameters (χ^2) in these two wavelengths are 1.05 and 1.02, respectively.

Time-resolved emission spectra (TRES), obtained via fit through data points using a log-normal line-shape function,[92] are shown in the upper panel of Fig. 4.5 for C153 in [$0.78CH_3CONH_2 + 0.22\{f\,LiBr + (1\text{-}f)\,LiNO_3\}$] molten mixture along with the

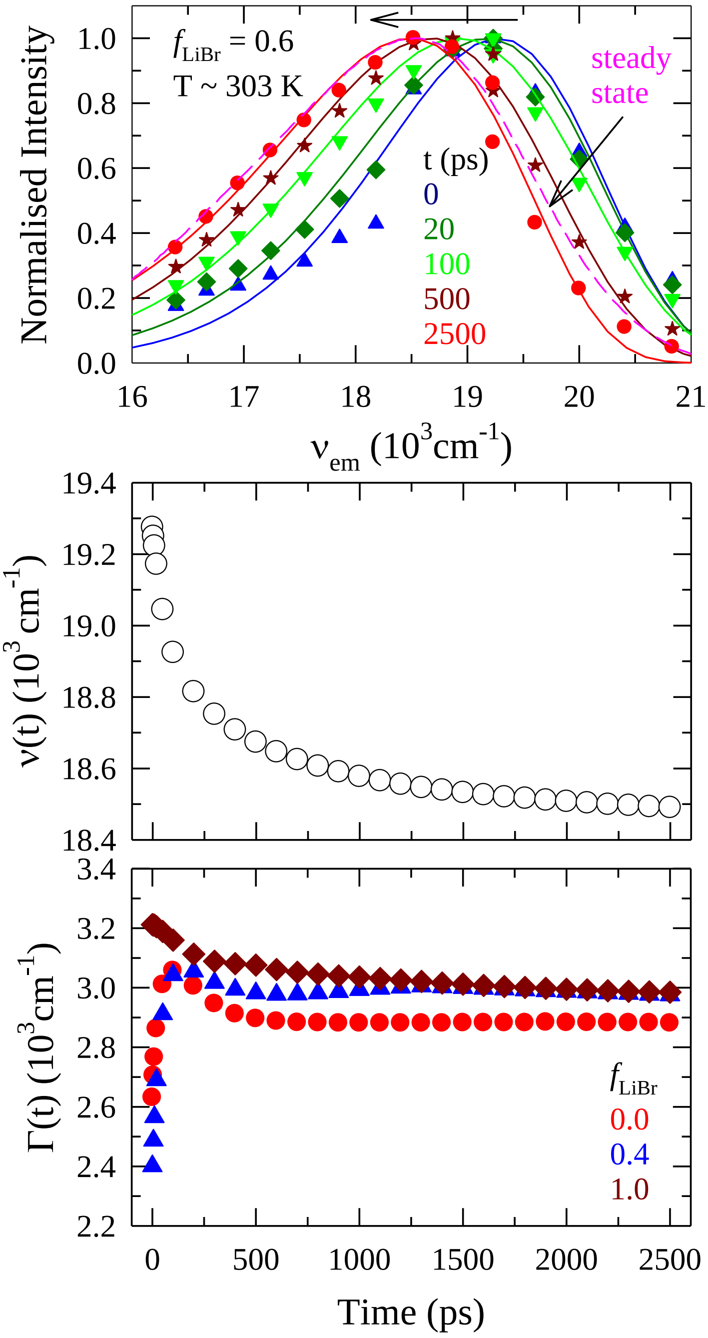

Fig. 4.5: Synthesized time resolved emission spectra (TRES) of C153 at different time slices from the experimentally obtained decays in [$0.78CH_3CONH_2$ + 0.22{*f* LiBr + (1-*f*) $LiNO_3$}] molten mixtures at f_{LiBr} = 0.6 and 303 K. TRES shown (upper panel) are at the following time intervals after solute excitation: 0 ps (triangles), 20 ps (diamonds), 100 ps (inverted triangles), 500 ps (asterisk) and 2500 ps (circles). While time evolution of the average peak frequencies ($\nu(t)$) at f_{LiBr} = 0.6 is shown in the middle panel, that of the width ($\Gamma(t)$) at three different compositions are shown in the lower panel. For lower panel, circles represent $\Gamma(t)$ for C153 in molten mixture at f_{LiBr} = 0, triangles at f_{LiBr} = 0.4 and diamonds at f_{LiBr} = 1.0.

corresponding steady state emission spectrum. The results are for $f_{LiBr} = 0.6$ at 303 K and representative of what have been observed at other compositions as well. Note the steady state emission spectrum and the time-resolved spectrum at $t = \infty$ do not overlap (difference between them being ~300 cm^{-1}) and may indicate incomplete environmental reorganization during the steady state fluorescence emission. The amount of dynamic Stokes shift, $\delta\nu^t = \nu(t=0) - \nu(t=\infty)$, observed at this composition and temperature is ~ 900 cm^{-1}, which is ~20% less than the estimated[90] shift in case of full detection. The broader time-resolution employed in the present experiments has not only led to the incomplete detection of the total dynamics but also inaccurately captured the evolution of the spectral width at early times. This is shown in the lower panel of Fig. 4.5 where evolution of the spectral width, $\Gamma(t)$, exhibits opposite trends at early times for melts at $f_{LiBr} = 0$ and $f_{LiBr} = 1$. However, $\Gamma(t)$ reaches a plateau as solvation progresses with time, an aspect also observed earlier for polar solvation energy relaxation in neat solvents[76] and molten mixtures.[31,32] This and the fact that even the maximum variation of $\Gamma(t)$ being substantially smaller than the observed dynamic shift further support that the observed time-evolution of the fluorescence spectrum occurs mainly due to the medium reorganization around the perturbed solute in these melts.

Table 4.1 summarizes the composition dependent observed ($\Delta\nu^t_{obs.}$) and estimated ($\Delta\nu^t_{est.}$) dynamic Stokes shifts for C153 in these molten mixtures at three different temperatures. These data suggest that approximately 20-50% of the full dynamics, depending upon composition and temperature, has not been detected in the present experiments. Interestingly, even after missing such a significant portion, the observed shift is quite large and lies in the range, ~650 – 1300 cm^{-1}. The estimated shift, on the other hand, ranges between ~1000 cm^{-1} and 1700 cm^{-1}, and is somewhat smaller than $\Delta\nu^t_{est.}$ for C153 in [0.75CH_3CONH_2 + 0.25{f KSCN + (1-f) NaSCN}] melts.[31] Reduced ion-solute interaction due to larger effective size[90] of solvated Li^+ ion compared to those for solvated Na^+ and K^+ ions could be one of the reasons behind the difference between the estimated shifts in (CH_3CONH_2 + LiBr/NO_3) and (CH_3CONH_2 + Na/KSCN) molten mixtures. It should be noted that presence of a picosecond component or even a faster one in these mixtures is quite natural because amides and partially substituted amides possess intermolecular libration modes[93-94] centered around 50-100 cm^{-1}, and these collective

Table 4.1: Dynamic Stokes' Shift of C153 in [0.78CH_3CONH_2 + 0.22{*f* LiBr + (1-*f*) $LiNO_3$)] molten mixtures at 303, 313 and 318 K: Comparison between experiments and theoretical calculations. Uncertainty associated with the measured shift is $\pm 200\,cm^{-1}$.

Experiment				Theory		
f_{LiBr}	$\Delta\nu^t_{obs.}$ (cm^{-1})	$\Delta\nu^t_{est.}$ (cm^{-1})	% missed	$\Delta\nu^t_{total}$ (cm^{-1})	$\Delta\nu^t_{sd}$ (cm^{-1})	$\Delta\nu^t_{si}$ (cm^{-1})
303 K						
0.0	993	1439	31	1727	1147	580
0.2	1305	1619	19	1717	1139	578
0.4	963	1380	30	1705	1129	576
0.6	909	1128	19	1684	1112	572
0.8	847	1069	21	1674	1104	570
1.0	650	1015	36	1658	1091	567
313 K						
0.0	956	1409	32	1678	1103	575
0.2	1175	1606	27	1667	1094	573
0.4	871	1655	47	1655	1084	571
0.6	1067	1413	24	1641	1073	568
0.8	975	1295	25	1631	1065	566
1.0	844	1265	33	1619	1055	564
318 K						
0.0	886	1224	28	1656	1083	573
0.2	1042	1634	36	1644	1073	571
0.4	896	1493	40	1633	1064	569
0.6	1057	1469	28	1618	1052	566
0.8	954	1355	30	1607	1044	563
1.0	891	1315	32	1596	1035	561

modes have been shown earlier[95-98] to generate ultrafast polar solvation response in associated molecular solvents. This will be discussed in some detail when we explore the origin of the timescales revealed by dynamic Stokes shift measurements. Let us now focus on understanding the composition dependent dynamic Stokes' shift estimated for these mixtures at different temperatures in terms of solute-ion and solute-solvent interactions.

We follow our earlier model[31,32] in considering the molten mixtures of acetamide with lithium bromide and nitrate as non-aqueous electrolyte solutions where ions, from complete dissociation of the added salts, are dispersed in dipolar solvent, acetamide. In an extremely dilute solution of a solute probe (concentration $\leq 10^{-5} M$) in such a multi-component mixture, an equilibrium is established mainly via solute-solvent dipolar interaction and solute-ion dipole-ion interaction in addition to ion-ion, ion-solvent and solvent-solvent interactions. Probe-probe interaction is believed negligible because of its presence at extreme dilution, and interactions between particles (solvent-solvent, ion-ion and ion-solvent) are considered unchanged in presence of solute molecules at this dilution. In such a model, the solute-medium total interaction energy can be approximated to be composed of solute-solvent dipole-dipole interaction and solute-ion dipole-ion interaction. Note in real mixtures salts are not always completely dissociated and various complex entities, such as ion-pairs, triple ions and neutral triple ions,[99-102] exist, and contribute to some extent to the solution energetics and dynamics. However, solute-solvent (dipole-dipole) and solute-ion (dipole-ion) interactions are expected to be the dominant contributors to the dynamic Stokes shift in these (acetamide + salt) melts and hence contributions from more complex species are considered to be of secondary importance. In addition, acetamide molecule is assumed to be spherical with point dipole at the centre, and characterized by a diameter, $\sigma = 4.52$ Å (obtained from van der Waals volume[103]) and a dipole moment,[17] $\mu = 3.7D$. Ions (both cation and anion) are treated as hard spheres with central point charges with diameters (σ_i) 1.8 Å[104] for Li^+, 3.92 Å[105] for NO_3^- and 3.64 Å[104] for Br^-. Note here that NO_3^- is not spherical and the actual shape of this ion and other species may have some effects on probe solvation and rotation dynamics. Since the main focus of the present treatment is to understand, at best qualitatively, the observed dynamics in these complex systems in terms of simple microscopic picture, we have avoided considerations of shape asymmetry and medium inhomogeneity while obtaining the static correlation functions. This is done to preserve the analytical simplicity of the theoretical treatment. As before,[31] the composition dependent ε_0 at a particular temperature has been calculated by using the experimental density and dipole moment (3.7 D) in a relation given by the mean spherical approximation (MSA) theory.[106] The calculated composition dependent ε_0, depicted in Fig. A8 (Appendix), is ~30 for these molten mixtures. Parameters used to characterize the solute are the diameter for C153 (7.8 Å) and its excited state dipole moment (14 D).[76] See ref. 84 for necessary equations for the calculations of dynamic Stokes shift, details of which can be found elsewhere.[31,59-62] We only state here that orientational solvent-solvent direct correlation function and static structure factor, required for the calculations,[31] have been obtained from the MSA theory, and the solute-ion static correlations from our earlier works.[59-62] The average spatial arrangement of ions (static ion structure factor) in such mixtures has been obtained by following the method as described previously.[107-109]

Calculated composition dependent dynamic Stokes shifts ($\Delta\nu^t_{total}$) at 303 K, 313 K and 318 K are summarized in Table 4.1 along with the solute-solvent dipole-dipole and solute-ion dipole-ion interaction contributions, $\Delta\nu^t_{sd}$ and $\Delta\nu^t_{si}$, respectively. Note the calculated total shift ($\Delta\nu^t_{total}$) spans rather a narrow range (~1600 – 1700 cm^{-1}) and similar to the range of estimated shift from experiments ($\Delta\nu^t_{est}$) at these temperatures, 1300 – 1800 cm^{-1}. This is an important result because a model calculation with ε_0 as moderate as ~30 could produce such a close agreement with experimental estimates for these molten mixtures whose dielectric constants are supposed to be colossal. The agreement also indicates the validity of the present model that dynamic shift in these molten mixtures could be expressed in terms of solute-medium dipole-dipole and dipole-ion interactions without much adherence to the solution structural complexity. The dipole-dipole interaction contributes ~65% to the total shift in all these melts and thus dominates over the solute-ion (dipole-ion) contribution. A close inspection of these data also indicates a linear decrease of the calculated shift with composition, the maximum decrease being ~4% for the total calculated shift, ~5% and ~2% respectively for the dipole-dipole and dipole-ion contributions. Eventhough mass density of the melt increases upon addition of

LiBr in the melt,[23] a decrease in number densities of both the dipolar and ionic species (see Fig. A9, Appendix) reduces the interaction contributions. Note, however, that experimental estimated shifts show a non-linear composition dependence and the extent of variation is much larger (~30 - 45%) than the decrease in calculated shifts. The non-linearity is absent in the calculations probably because of the neglect of specific solute-ion interaction, solution heterogeneity and interactions between the solute and other complex ionic species present in these melts.

The dependences of the measured solvation response function, $S(t)$, on mixture composition and temperature are depicted in Fig. 4.6 where $S(t)$ decays at three different compositions at 318 K are shown in the upper panel, and those at different temperatures at a fixed composition ($f_{LiBr} = 0$) in the lower panel. Both the composition and temperature dependent decays follow the changes in solution viscosity (η) as the latter, summarized in Table A2 (Appendix), increases upon increasing LiBr concentration in the melt at a fixed temperature and a decreases upon raising the solution temperature at a fixed composition. Note here that η measured by us increases with LiBr concentration at a fixed temperature which is opposite to the trend reported in Ref. 23. As already mentioned, presence of substantial amount of moisture in LiBr might have led to the erroneous trend reported in Ref. 23. Note in the lower panel that even the slowest of the decays (the one at 303 K) continues only up to 2.5 ns. Such a shorter time-spread for $S(t)$ decays in these melts is unexpected. The reason is the following. According to continuum model, solvation time correlation function for a dipolar solute in a polar continuum is single exponential characterized by a time constant,[110] $\tau_L = \frac{(2\varepsilon_\infty + \varepsilon_c)}{(2\varepsilon_0 + \varepsilon_c)}\tau_D \approx \frac{(\varepsilon_\infty + 1)}{(\varepsilon_0 + 1)}\tau_D$. As reported by DR experiments in Ref. 12, use of the following parameters, ε_0 ~ 40 x 10^6, ε_∞ ~20 and τ_D ~ 10 ms, leads to τ_L ~50 ns at ~300 K) predicts a solvation time constant (τ_L) of ~50 ns for a dipolar probe in these melts at 303 K, should they possess, as reported for (CH_3CONH_2 + NaCNS) melts[12], an extremely large ε_0 (~10^6) and a Debye relaxation time (τ_D) of ~10 ms. The fact that the solvent reorganization is nearly complete within a couple of nanosecond only suggests that either both the ε_0 and τ_D are much smaller than their

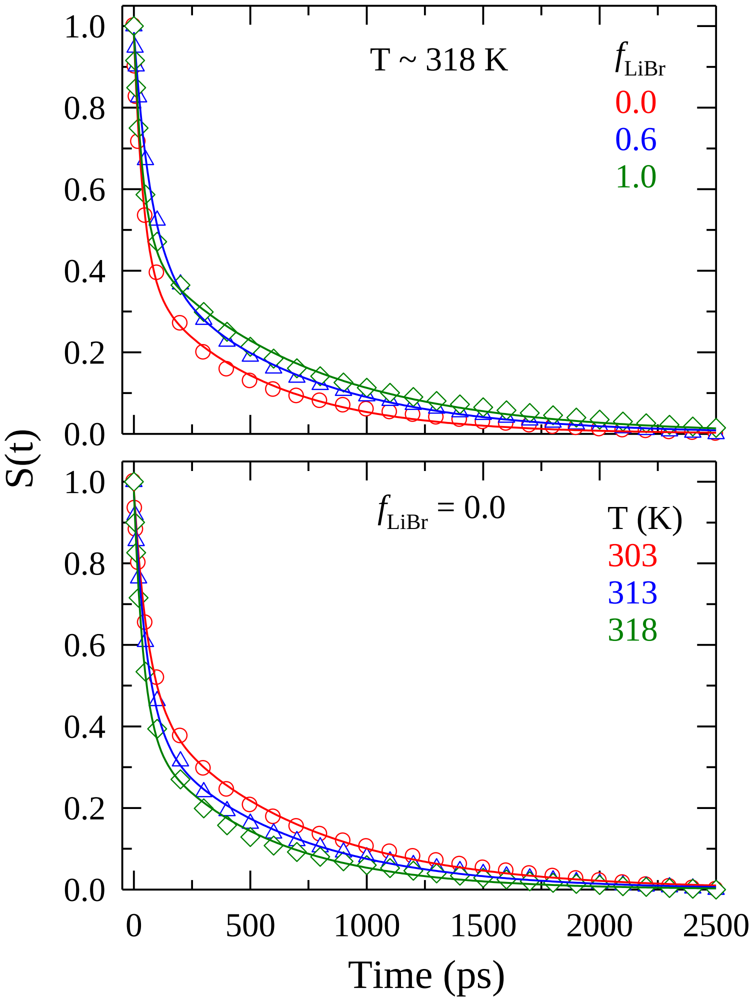

Fig. 4.6: Decays of solvation response function, $S(t)$, measured using C153 at 318 K in [$0.78CH_3CONH_2$ + 0.22{*f* LiBr + (1-*f*) $LiNO_3$)] molten mixtures at f_{LiBr} = 0.0 (red), 0.6 (blue) and 1.0 (green) are shown in the upper panel. Temperature effects are shown in the lower panel by presenting $S(t)$ decays at three different temperatures, 303 K (red), 313 K (blue) and 318 K (green), for C153 in the molten mixture with composition f_{LiBr} = 0.0.

projected values, or, their coupling to solvation processes renders undetectably small contribution in the 20 ns time-window employed in the present measurements. Eventhough the second possibility could be a reason for the non-observation of the predicted extremely slow dynamics, it is difficult to understand why the present experiments would not be able to capture a timescale, if exists, 2-3 times slower than the observed one. Such a slower timescale is expected to originate from the coupling of the millisecond motion of ion-solvent clusters or ion-induced solvent aggregates[3,12,13] to the time-dependent density fluctuations at different wavevectors.[32] In contrast, solvation response functions presented in this figure and other measured ones have been found to fit to bi-exponential functions of time, substantial portion ($0.24 \le a_1 \le 0.60$) of which decays with a time constant $32 \le \tau_1 / ps \le 112$, followed by a slower component (a_2) with a time constant $475 \le \tau_2 / ps \le 770$. Parameters obtained from bi-exponential fits to the measured decays have been summarized in Table A3 (Appendix). Note that these time scales resemble those associated with biphasic solvation observed earlier for one component molten inorganic salts at elevated temperatures.[111]

Next we investigate the possible mechanisms for the observed biphasic solvation in these complex mixtures because motions of both ions and host polar solvent molecules couple to solvation energy relaxation in these non-aqueous electrolyte solutions. As in Ref. 31, both the overdamped and the underdamped dynamics of solvation have been considered. While solvation in the overdamped limit is known to be carried out by the diffusive modes (both rotational and translational) and thus governed entirely by the solution viscosity, underdamped limit accounts also for the contributions from the inertial motions of the particles.[63,110(a)] Method of calculation, discussed in the ref. 84, illustrates how dielectric relaxation parameters[110(b)] have been approximated in the absence of any experimental data for these mixtures and how these parameters incorporated into the subsequent calculations. We only mention here that the calculated total solvation response functions are composed of 90% contributions from pure polar solvent dynamics and only 10% from ion dynamics, although a small variation in the relative contributions does not affect the qualitative feature of the predicted results. This means the calculated total solvation response function is constructed as, $S_{ss}(t) = 0.9S_{sd}(t) + 0.1S_{si}(t)$, the calculations of $S_{sd}(t)$ and $S_{si}(t)$ were given in ref. 84. Such an approach has not only provided a successful description of experimental Stokes shift dynamics in neat ionic liquids[59,60] and (ionic liquid + polar solvent) binary mixtures[62(b)] but also explained semi-quantitatively the measured dynamics in a few such molten mixtures.[31,32] Note the above construction of $S_{ss}(t)$ closely follows the observation made earlier in experimental studies of Stokes shift dynamics of polar probe in electrolyte solutions at ambient condition,[112] where ion-dynamics has been found to contribute ~20% to the total dynamics and that too at the later stage of the solvation energy relaxation.

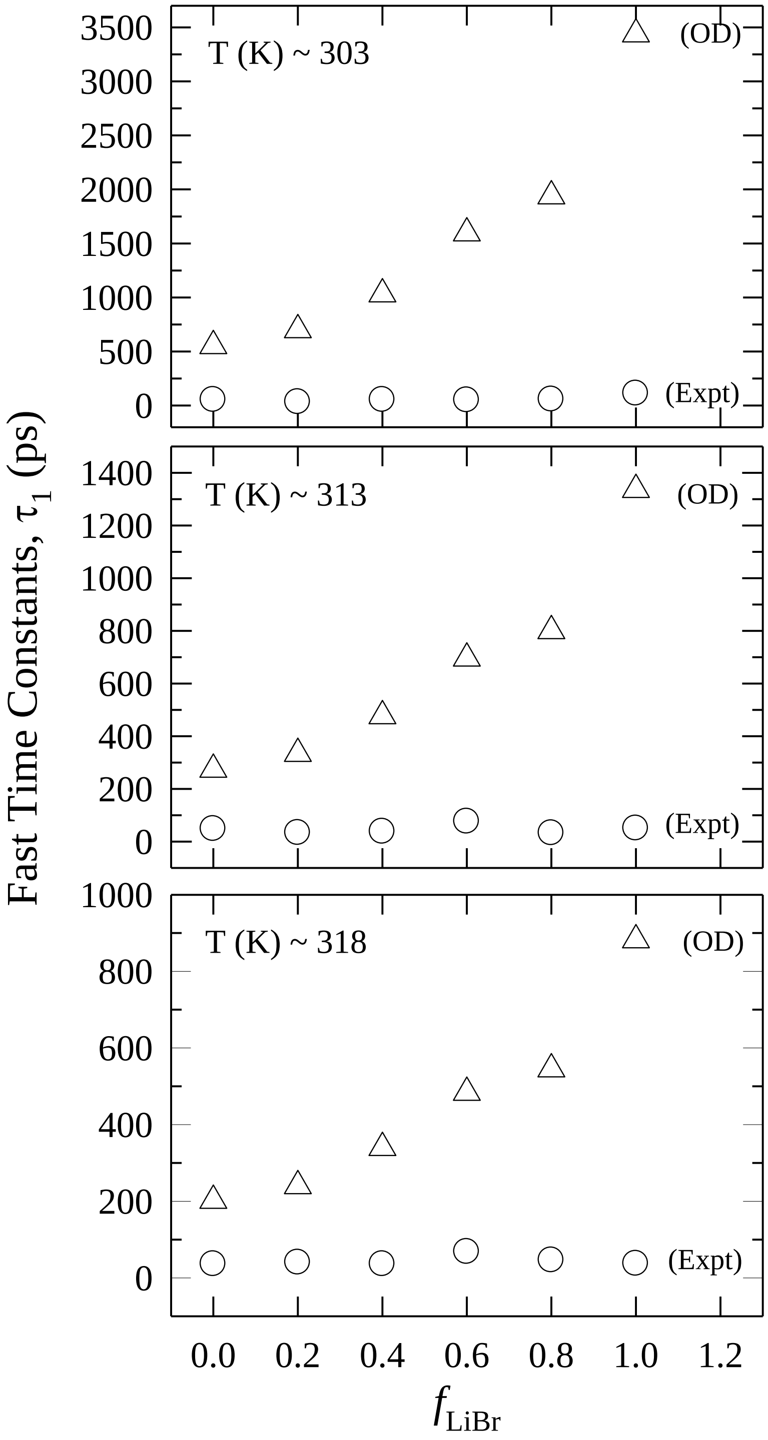

Fig. 4.7: A comparison between the composition dependent measured fast solvation time constants (circles) and those calculated from our semi-molecular theory in the overdamped limit (triangles) at 303 K (upper panel), 313 K (middle panel) and at 318 K (lower panel). These time constants (τ_1) have been obtained from fitting of the measured and calculated solvation response functions as described in the text. The uncertainty associated with the experimental times is ± 5% of the reported values.

As observed in experiments for these melts, $S_{ss}(t)$, calculated in both the overdamped and the underdamped limits, have been found to be bi-exponential function of time at all compositions and temperatures studied. The fast solvation time constants (τ_1), obtained from the overdamped calculations at three different temperatures, are compared in Fig. 4.7 with those from experiments. The amplitudes associated with τ_1 are also ~50% (see Table A4, Appendix) and thus close to experimental data. τ_1 from underdamped calculations have not been shown because they are too short ($0.9 < \tau_1 / ps < 3$) to be presented in the same figure although their amplitudes are quite substantial (38 – 40%). Interestingly, the comparison reveals while the calculated fast time constant (τ_1) increases with LiBr concentration in the melt (which follows LiBr concentration dependence of viscosity), the experimental counter-part remains nearly insensitive. This indicates that either the experimental fast time constant is not entirely controlled by the medium viscosity or a certain degree of decoupling between motions of solvating particles and medium viscosity exists. Participation of underdamped solvent modes (such as amide intermolecular librations[93,94]) is known[63] to reduce the importance of viscosity for the initial fast component of the total polar solvation energy relaxation in liquid solvents. For these multi-component mixtures, this is demonstrated in Fig. 4.8 where composition dependent calculated slow solvation time constants (τ_2) at three different temperatures have been compared with those from experiments. Better agreement between the underdamped calculations and the experiments for τ_2 only reinforces the notion that much faster timescales than those set by particle diffusion exist in these melts, and significant portion of the polar solvation energy relaxes via the participation of the solvent librational modes. Interestingly, the agreement between the time constants from underdamped calculations and experiments are not as good at 303 K as those at the other two higher temperatures. Like in supercooled liquids, if the heterogeneity is more pronounced at higher medium viscosity, then the molten mixtures at 303 K are expected to be more heterogeneous than at 313 K and 318 K. Consequently, solvation times would be more decoupled from solution viscosity at 303 K, showing poorer agreement between experiments and such simple calculations where heterogeneity has not been considered at all. It should, however, be recognized that overdamped predictions at the highest temperature, eventhough not as quantitative as those from underdamped calculations, are

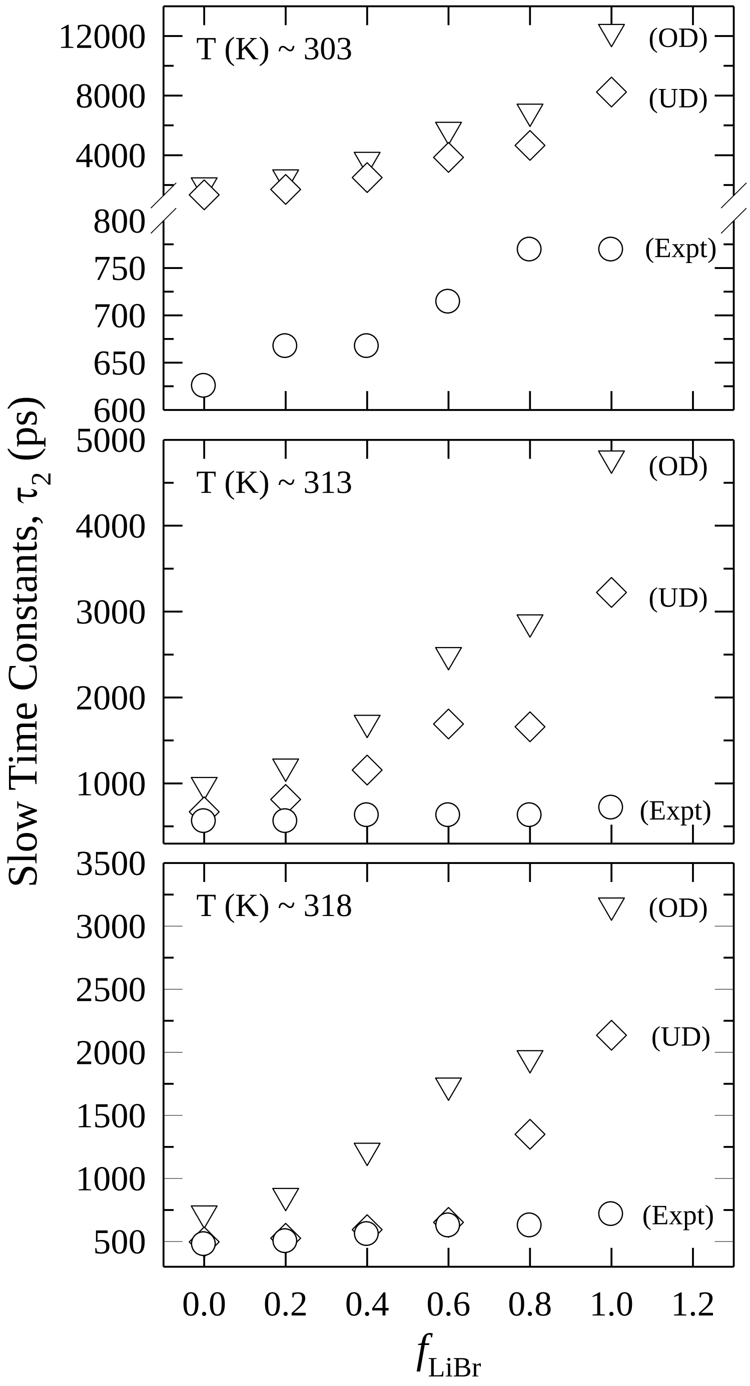

Fig. 4.8: Similar comparison as in Fig. 4.7 but for the slower solvation time constants (τ_2) obtained from measurements (circles) and from calculations in the overdamped limit (inverted triangles) and underdamped limit (diamonds) at three different temperatures for C153 in these melts at different compositions. Uncertainty in measured τ_2 remains the same as for measured τ_1.

qualitatively in the same range ($400 < \tau_2(OD)/ps < 3200$) as observed in experiments ($400 < \tau_2(Expt.)/ps < 1000$). Such an observation encourages one to investigate, within the framework of a simplistic model, the density fluctuation length-scales which are probably associated with the solvation time constants (τ_1 and τ_2) measured in the present experiments.

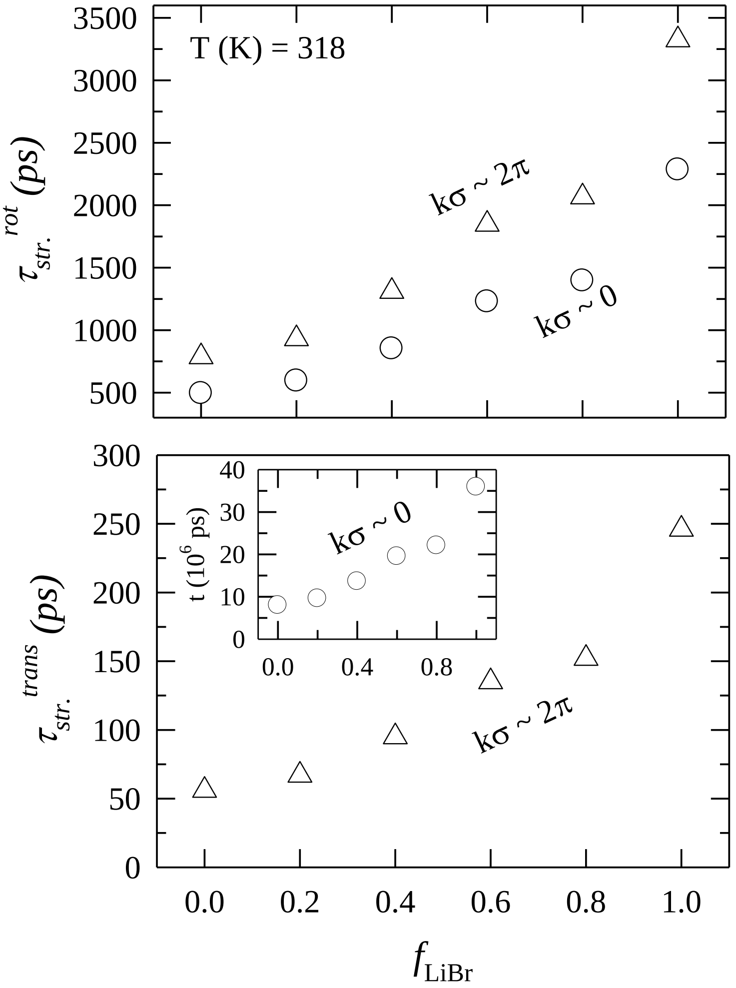

Fig. 4.9: Origin of the fast and slow solvation timescales as predicted by the semi-molecular theory for these molten mixtures at different compositions. Timescales arising from density fluctuations at relevant wavenumber modes are specified in each of the panels.

Fig. 4.9 shows the mixture composition dependent structural relaxation times corresponding to medium density fluctuations at the collective ($k\sigma \sim 0$) and nearest-neighbor ($k\sigma \sim 2\pi$) wavevectors, calculated in the overdamped limit at 318 K where the heterogeneity is supposed to be the minimum. While the upper panel depicts the composition dependence of the orientational structural relaxation time (τ_{str}^{rot}), the time constants associated with the relaxation of the ion dynamic structure factor (τ_{str}^{trans}) are presented in the lower panel (see ref. 84 for detailed calculation of τ_{str}^{rot} and τ_{str}^{trans}). Data in Fig. 4.9 suggest that the fast timescale measured in the present experiments ($32 \le \tau_1 / ps \le 112$) originates from the diffusive ion density fluctuations at $k\sigma \sim 2\pi$ modes, whereas the slow ones ($400 < \tau_2 / ps < 1000$) are associated with the orientational density fluctuations of the polar solvent involving both the collective ($k\sigma \sim 0$) and the nearest neighbor ($k\sigma \sim 2\pi$) modes. These results in conjunction with the underdamped prediction of ~50% solvation energy relaxation with time constants in ~1-3 ps range, and missing of a substantial portion (~20-50%) of the dynamics by the present experiments clearly indicate the domination of the orientational solvent density fluctuations involving the collective modes. In addition, the predicted near insensitivity of fast time constant ($0.9 < \tau_1 / ps < 3$) on f_{LiBr} in the underdamped limit is in accordance with the general results from simulation studies[113-115] of solvation dynamics in electrolyte solutions. Note that similar fast timescale has also been predicted earlier for (acetamide + sodium/potassium thiocyanate)[31] and (acetamide + calcium nitrate)[32] molten mixtures. *Inset* (lower panel) shows the timescale associated with the collective ($k\sigma \sim 0$) ion density fluctuations, which is extremely slow and has not been observed in our experiments. This seems to suggest that either the collective ion density fluctuations are irrelevant for polar solvation energy relaxation in these melts or their contribution is too small to be detected by the present experimental set-up.

4.3.3 Stokes Shift Dynamics: Decoupling from Medium Viscosity

Next we illustrate the coupling between average solvation time ($<\tau_s>$) and medium viscosity (η) in Fig. 4.10 where, in a log-log plot, the composition dependent $<\tau_s>$ measured for these melts at 303 K, 313 K and 318 K are shown as a function of temperature-reduced viscosity, η/T. Since $<\tau_s>$ is dominated by the spatial diffusion timescale of medium particles (τ_2 in these cases) and since the Stokes-Einstein (SE) relation predicts, $D^{-1} \infty (\eta/T)$ (D being diffusion coefficient), such a plot is expected to

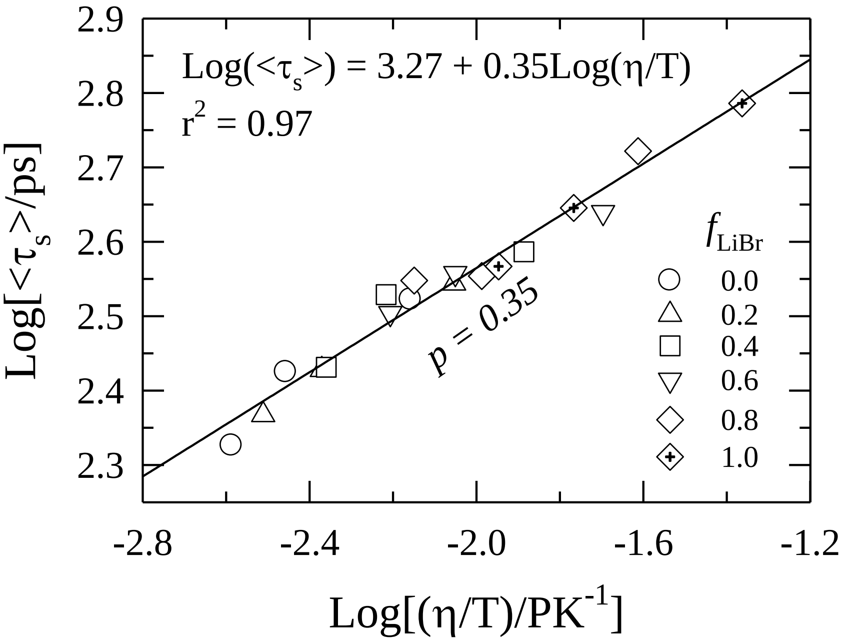

Fig. 4.10: Log-Log plot of average solvation time, $<\tau_s>$ of C153 versus η/T in molten mixtures of acetamide with lithium nitrate and lithium bromide. The solid line shows the best fit of the experimentally measured data to the relation Log[$<\tau_s>$] = B + *p*Log[η/T], the associated B and *p* value are given in the figure. Different symbols represent data at different mixture compositions.

reflect on the validity of the SE relation in these melts. Fig. 4.10, however, exhibits a power-law dependence on reduced viscosity, $< \tau_s > \infty (\eta/T)^p$, with an average value for the power ($p = 0.35$) much less than unity. Treatment of $< \tau_s >$ as separate sets (see Fig. A10, Appendix) produces slightly different values for p : 0.34 at 303 K, 0.32 at 313 K and 0.40 at 318 K. Our attempt to fit to the form, $< \tau_s > \infty \eta^p$, also produces equally good description with p values nearly the same as above. These analyses confirm presence of pronounced heterogeneity in these molten mixtures, the extent being the larger at lower temperature, providing an experimental support to the logic used earlier while explaining the relatively poorer agreement between predicted and measured slower solvation time constants at 303 K (see Fig. 4.8). Note the pronounced fractional viscosity dependence of $< \tau_s >$ is quite reminiscent of viscosity-decoupling of diffusion in deeply supercooled liquids, and may therefore indicate presence of both static (distribution of environments) and dynamic heterogeneities (distribution of relaxation times)[35-41] in these molten mixtures. Surprisingly, dynamic Stokes shift measurements in ionic liquids, systems which are somewhat similar to these multi-component mixtures both in interaction and heterogeneity aspects, do not show fractional SE behavior,[66] eventhough such a fractional viscosity dependence has been experimentally observed for ion transport in ionic melts.[116] In addition, significant departure from the conventional SE relation is also expected for diffusion of small solutes in a medium of large particles.[117] Therefore, non-hydrodynamic diffusion of lighter alkali metal ions- Li^+ for the present melts and Na^+/K^+ for other molten mixtures[31] might be one of the reasons for the observed fractional viscosity dependence of $<\tau_s>$.

4.3.4 Dynamic Fluorescence Anisotropy Measurements: Heterogeneity and Medium Decoupling

Representative fluorescence anisotropy decays of C153 at different temperatures and compositions are presented in Fig. 4.11 in order to show the effects on $r(t)$ of temperature (upper panel) and Br^- ion concentration (lower panel). Both the effects of temperature on $r(t)$ at a given composition and that of LiBr concentration at a fixed temperature can be explained by the temperature and composition dependence of viscosity of these melts (see Table A2, Appendix). As already mentioned, $r(t)$ decays, collected at various temperatures and mixture compositions, can be adequately described by a sum of two exponentials. A representative fit is provided in the Appendix (Fig. A11) along with the residual, which shows the general quality of the unconstrained bi-exponential fits to the experimental $r(t)$ decays. Fit parameters summarized in Table A5 (Appendix) demonstrate that these biphasic anisotropy decays are characterized by a substantial (~30-65%) fast amplitude with time constant in ~10-30 ps range, and a very slow component with time constant spreading between ~0.7 ns and ~12 ns. The fast time constants are therefore too short to be accurately detected by the present experiments and hence any particular dependence of them on Br^- concentration or temperature cannot be explored. Also note that missing of these fast components might have led to the observation of bi-exponential dynamics in place of stretched exponential ones expected for these heterogeneous molten mixtures.[118]

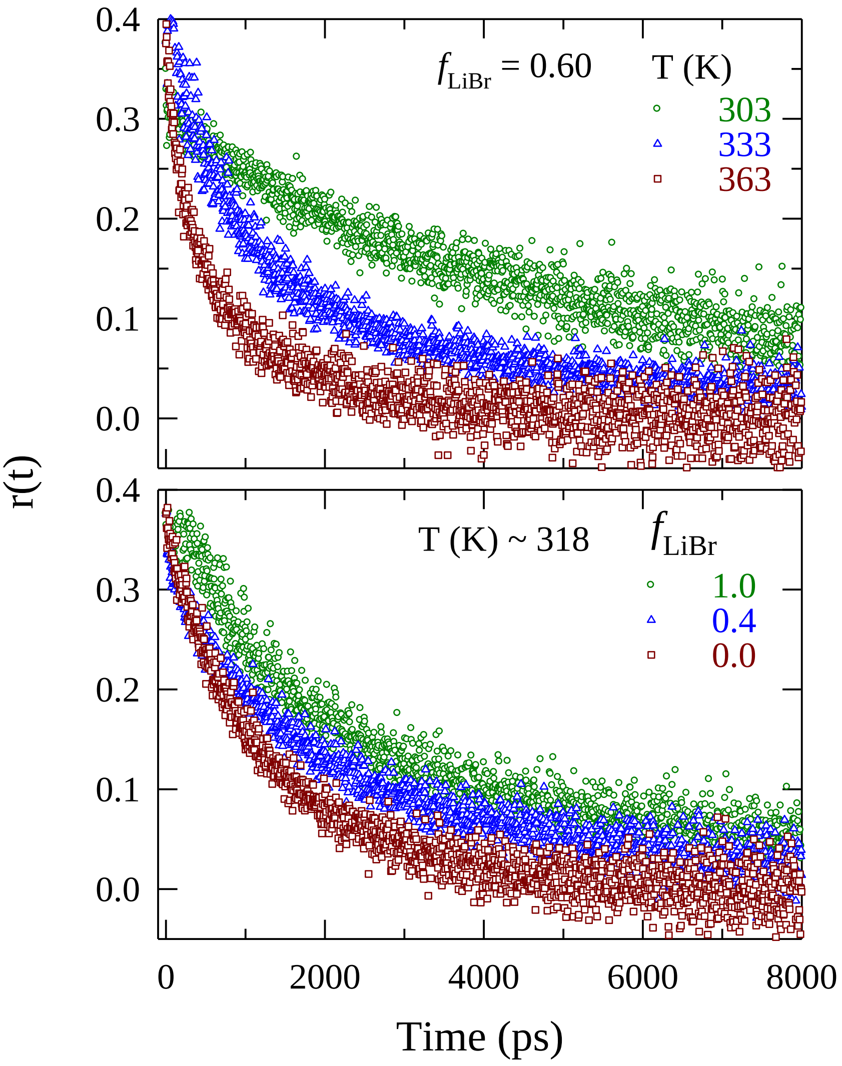

Fig. 4.11: Temperature and composition effects on fluorescence anisotropy ($r(t)$) decay of C153 in [$0.78CH_3CONH_2$ + 0.22{*f* LiBr + (1-*f*) $LiNO_3$)] molten mixtures. Data representations are clearly explained inside the panels.

The slow time constant, on the other hand, decreases with temperature at a given composition and increases with Br^- concentration at a given temperature. These are in accordance with the hydrodynamic prediction because we find viscosity at a fixed composition reduces upon increasing temperature and increases with Br^- concentration (at a given temperature). Effects of temperature and composition on C153 rotation in these melts are more clearly depicted in Fig. A12 (Appendix) where the average rotation and solvation times ($<\tau_r>$ and $<\tau_s>$, respectively), and experimental viscosities from our independent isocomposition and isothermal measurements are shown as a function of

f_{LiBr} for different temperatures. Note both $<\tau_s>$ and $<\tau_r>$ increase with viscosity and decrease with temperature, suggesting a dominant role for the medium viscosity in controlling the average rates for the time-dependent solvation and fluorescence anisotropy in these melts. However, this does not rule out the possibility of complexation between C153 and ions present in the melt, as found during the study of rotational relaxation of resorufin in electrolyte solutions,[119] contributing to the measured $<\tau_r>$. Note that the slow rotation time constants at high Br^- concentrations (particularly those at 303 K) are ~2-3 times larger than the excited state lifetime (~5 ns) of C153. Such a longer time constant for these melts is not improbable because in ionic liquids near room temperature rotational time constants for solutes larger by a factor of ~2 – 20 than their respective excited state lifetimes have been reported and explained in terms of heterogeneous solution structure.[66,120-122] However, this does not anyway confirm that the observed biphasic behavior of $r(t)$ originates exclusively from solutes trapped in different solvent environments but rather suggests that both the non-Markovian nature of the underlying friction and solution structural heterogeneity could be responsible for the biphasic character of the measured anisotropy decays.[80]

Next the appropriateness of the Stokes-Einstein-Debye (SED) relation in describing the solute rotational diffusion in these melts is explored in Fig. 4.12 where the measured $<\tau_r>$ at all compositions and temperatures have been shown as a function temperature-reduced viscosity, η/T. Note the data are shown in a log-log plot. The corresponding SED values have been calculated by using the formula, $<\tau_r>=\frac{V\eta}{k_B T}fC$, with solute volume $V=246$ Å^3, shape factor $f=1.71$, and solute-solvent coupling parameter $C=$ 0.24 (for slip boundary condition) and 1.0 (for stick boundary condition).[66] A comparison with the SED predictions indicates that, at higher temperatures (in low η/T limit), measured $<\tau_r>$ lies between the slip and stick predictions but becomes sub-slip in the large η/T limit at low temperature. The departure from the SED predictions is quantified as, $<\tau_r>\infty(\eta/T)^p$, with an average $p=0.55$. This can be explained by considering that shorter heterogeneity lifetime at higher temperatures allows better environmental

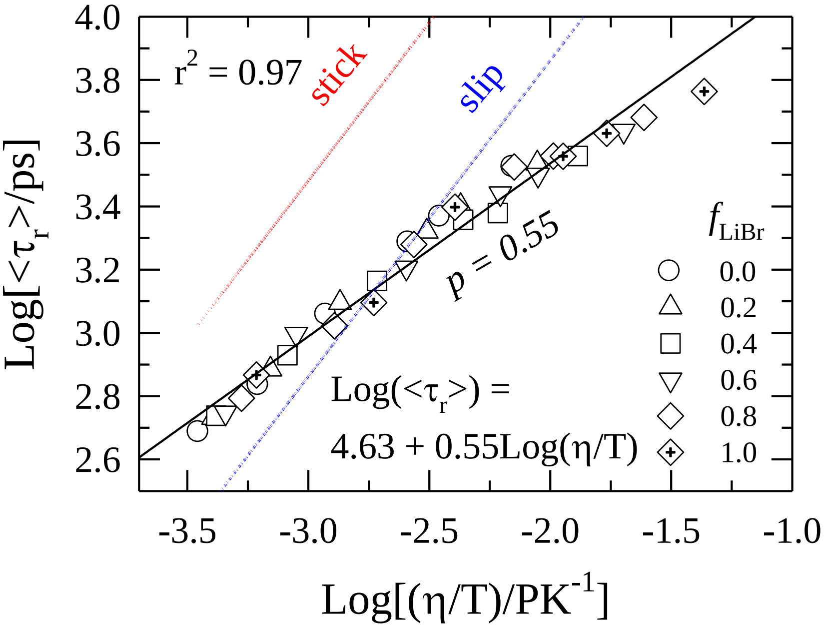

Fig. 4.12: Log-Log plot of average rotation time, $<\tau_r>$ of C153 versus η/T in molten mixtures of acetamide with lithium nitrate and lithium bromide. The solid line shows the best fit of the experimentally measured data to the relation $\mathrm{Log}[<\tau_r>] = B + p\mathrm{Log}[\eta/T]$, the associated B and p value are given in the figure. The dashed lines show the prediction of hydrodynamic stick and slip limits. Different symbols denote data at different mixture compositions.

averaging of the relaxation dynamics, leading to a more hydrodynamic behavior.[123] At lower temperatures where heterogeneities are longer-lived than $<\tau_r>$, molecular aspects get prominence and a departure from the SED description ensues. Results obtained from experimental studies of reactive and non-reactive dynamics in ionic liquids,[52, 124-125] and those from very recent measurements after isothermal introduction of ~2 nm structural inhomogeneity in an otherwise homogeneous liquid[126] suggest that both the static and dynamic heterogeneities could contribute to the observed decoupling between solute rotation and viscosity in these melts. In the absence of $LiNO_3$ ($f_{LiBr} = 1.0$) the extent of decoupling becomes even stronger as one finds $p = 0.50$ at this composition (See Fig. A13, Appendix). This is expected as larger viscosity in an inhomogeneous medium is known to produce larger decoupling.[35] The deviation at the high η/T regime is likely to originate from non-Brownian moves, such as large angle jumps[127] and retention of inertia-driven motion even much after the onset of the typical diffusion timescale.[128,129] These alternative dynamic modes significantly reduce the frictional resistance against the diffusing particle arising from the macroscopic viscosity and thus strongly promotes

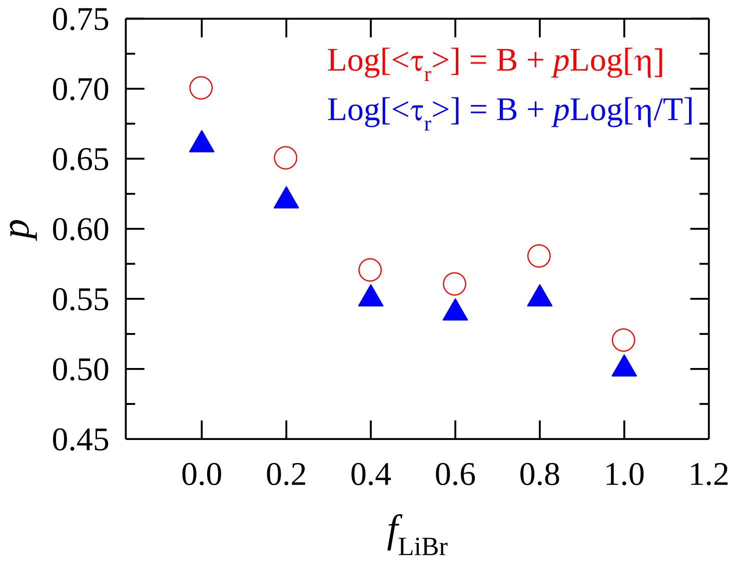

Fig. 4.13: Composition (f_{LiBr}) dependence of p, obtained from fitting the measured $<\tau_r>$ in these molten mixtures to the following expressions: Log[<τ_r>] = B + *p*Log[η/T] (triangles), and Log[<τ_r>] = B + *p*Log[η] (circles). Note that both fits produce comparable p values and quite smaller than unity.

departure from the conventional hydrodynamic description. Note that complexation through an interaction between the π-electron system and halide, particularly for compounds with electron-deficient aromatic ring, is a well-known phenomenon[130,131] and therefore formation of C153-Br^- complex in presence of LiBr in these melts may also modify the expected hydrodynamic behavior of the solute rotation.

Eventhough the viscosity dependence of $<\tau_r>$ in these melts at different compositions could be represented in Fig. 4.12 by $<\tau_r> \infty (\eta/T)^p$ with an *average* value of p, there exists a subtle composition dependence for p. This is depicted in Fig. 4.13 where p obtained from fits of the measured $<\tau_r>$ to both the medium viscosity ($<\tau_r> \infty \eta^p$) and the temperature-reduced viscosity ($<\tau_r> \infty (\eta/T)^p$) are shown as a function of the mixture composition, f_{LiBr}. Fig. 4.13 clearly shows that the composition dependent p values obtained from both fits are not very different from each other, indicating that the temperature dependence of $<\tau_r>$ is essentially that of the medium viscosity, η. Interestingly, these data indicate LiBr-rich region is more heterogeneous than the $LiNO_3$ enriched melt, an observation is contrary to the steady state measurements shown in Fig.

4.3. Although this heterogeneity character (as revealed by the present anisotropy measurements using C153) is expected on viscosity consideration, is opposite to the trend reported for the η-α relationship (α being the stretching exponent required to numerically fit the measured DR spectra) explored via DR experiments for several alkylimidazolium aluminate ionic liquids.[132] All these experimental results therefore indicate more extensive studies to explore the molecular origin for viscosity decoupling of dynamical variables in complex systems where electrostatic interactions play a significant or dominant role.

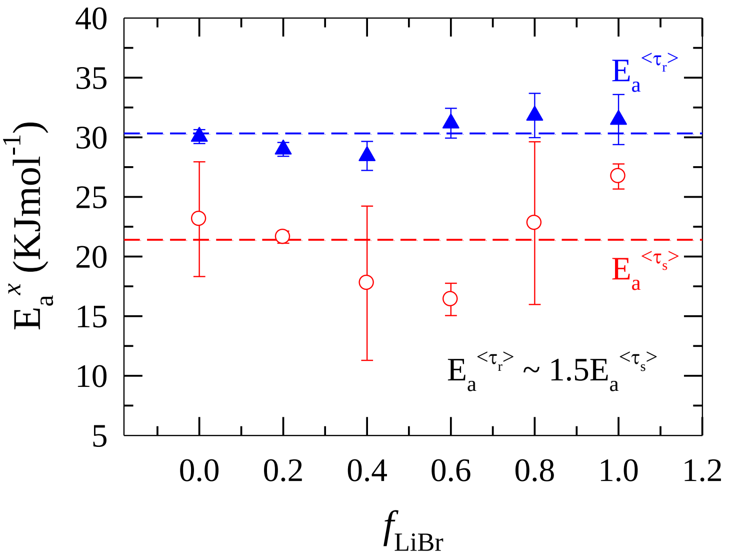

Fig. 4.14: Activation energies (E_a^x) obtained from the measured average solvation and rotation times ($<\tau_s>$ and $<\tau_r>$ respectively). Note the ratio between activation energies at any composition closely follows that between p values.

Since the temperature dependence of viscosity of these melts shows a weak deviation from the linearity in Arrhenius description (that is, $\ln\eta$ vs. $1/T$ plot), one can extract activation energies from the measured average times ($<\tau_r>$ and $<\tau_s>$) and correlate their ratio with that between fraction powers (p) associated with the probe solvation and rotation. If the small nonlinearity is neglected and the temperature dependence of viscosity is approximated to be Arrhenius-type, one obtains the following general expression for the temperature dependence of average rates (solvation and rotation),

$\ln(1/<\tau_x>) = C - E_a^x/RT$, where E_a^x denote the activation energy obtained from either average solvation times ($<\tau_s>$) or from average rotation times ($<\tau_r>$). This is related to the viscosity activation energy (E_a) as follows: Assume $\eta = \eta_0 \exp(E_a/RT)$ and recall that the measured average times have shown the following viscosity dependence: $<\tau_x> = A_x \eta^p$, x denoting solvation (s) or rotation (r). Insertion of the above Arrhenius description of temperature dependent η into the expression of $<\tau_x>$ leads to $\ln(1/<\tau_x>) = C - E_a^x/RT$, where $E_a^x = pE_a$. Therefore, $E_a^r/E_a^s = p^r/p^s$, where p^x is the fractional power obtained from the viscosity dependence of average rotation or solvation times): $E_a^x = p^x E_a$. Fig. A14 (Appendix) indicates $\ln(1/<\tau_x>)$ vs. $1/T$ plots are approximately linear for these melts, and therefore activation energies at various compositions of the melt can be obtained from the respective slopes. Activation energies (E_a^x) thus obtained are presented in Fig. 4.14 where E_a^x from both the measured average solvation and rotation times are shown as a function of LiBr concentration, f_{LiBr}. Note that activation energies obtained from $<\tau_r>$ are, on an average, 1.5 times larger than those obtained from $<\tau_s>$. This is expected because in these melts the extent of coupling to medium viscosity is approximately 1.5 times stronger for solute rotation than that for solute solvation (see Table A6, Appendix). Composition dependent p values summarized in this table also reveal that solute-solvent interaction in these melts does not alter much even for moving from one binary end to the other. This is the reason for near-insensitivity of both $E_a^{<\tau_r>}$ and $E_a^{<\tau_s>}$ on mixture composition shown in Fig. 4.14. Estimation of composition dependent activation energies using our earlier rotation data for C153 in [0.75CH_3CONH_2 + 0.25{*f* KSCN + (1-*f*) NaSCN)] melts[31] have produced ~40 $KJmol^{-1}$ and 35 $KJmol^{-1}$ as $E_a^{<\tau_r>}$ respectively for $f_{KSCN} = 0.2$ and $f_{KSCN} = 0.8$, which are very close to what have been observed in the present [0.78CH_3CONH_2 + 0.22{*f* LiBr + (1-*f*) $LiNO_3$)] molten mixtures. Interestingly, average activation energies obtained from $<\tau_r>$ in both these melts are quite close to that determined from viscoelastic measurements of (CH_3CONH_2 + CF_3COONa) binary melt at the highest salt concentration.[3] This similarity perhaps indicates near-equivalence in modifications of solution structure and dynamics by different alkali metal salts in molten acetamide.

4.4 Conclusion

In summary, the fluorescence spectroscopic results presented here indicate pronounced solution heterogeneity in molten mixtures of acetamide with lithium nitrate and bromide, the extent of which is perhaps even stronger than that in molten mixtures of acetamide with sodium and potassium thiocyanates. Particularly interesting in this mixture is the anisotropy sensing of stronger heterogeneity in Br^- dominated region which is anti-correlated with the steady state fluorescence results from excitation wavelength dependence study. Breakdown for both the SE and DSE relations along with strong decoupling between solute diffusion and medium viscosity have been observed. Quite reminiscent of the behavior of transport properties in deeply supercooled neat liquids, a strong decoupling between translation and rotation in these melts has also been demonstrated. These results have been explained in terms of both static and dynamic heterogeneities eventhough quantitative measurements of neither spatial nor temporal heterogeneities have been made in the present work. Measured Stokes shift dynamics and application of a semi-molecular theory suggest presence of a significant sub-picosecond solvation response in these highly viscous melts. This theory also indicates that the measured solvation timescales originate from the orientational polarization density relaxations involving both the collective and nearest neighbor solvent modes, and the isotropic structural relaxation involving only the nearest neighbor modes. Remarkably, consideration of fluorescence spectroscopic (both steady state and time-resolved) results together with the theoretical predictions does not support the idea of colossal dielectric constant and extremely slow relaxation timescale in these melts.

Since the heterogeneity character of these melts could not be quantified, the present study should motivate small angle neutron scattering (SANS) and X-ray scattering (SAXS) measurements so that the length-scales over which the particles are correlated are revealed. Excitation wavelength dependent measurements of solute rotation and solvation, on the other hand, will be useful in understanding the temporal heterogeneity in these complex systems. The applicability of the fractional single-file diffusion model[133,134] in explaining the observed breakdown of the SE and SED relations could be investigated. Our recent model simulation studies with a similar melt have indicated presence of strong dynamic heterogeneity and cooperative blockage in ion motions.[135] An atomistic simulation studies should therefore be carried out to quantify the roles of both static and dynamic heterogeneities in determining the viscosity decoupling observed in these melts. It would also be interesting as well as challenging to connect the particle jump, anisotropic local stress relaxation and the leading density modes to the observed decoupling.[136-138] While stating these it should be kept in mind that the break-down of SE and SED relations can occur for a variety of reasons. For example, several theories have indicated that the mechanism for breaking down of these hydrodynamic relations for high temperature melts could very well be different from that causing the break-down of SE relation near $1.2T_g$ in structural glass formers.[139-140] Indeed, the break-down is expected for molecular systems because these hydrodynamic relations were developed for macroscopic particles moving in a continuum field. Therefore, further studies involving experiments, atomistic simulations and analytical theories would be required to fully understand these complex molten systems.

References:

1. Gusteri, M.; Bartocci, V.; Castellani, F.; Pucciarelli, F. *J. Electroanal. Chem.* **1979**, *102*, 199.
2. Castellani, F.; Berchiesi, G.; Pucciarelli, F.; Bartocci, V. *J. Chem. Eng. Data* **1981**, *26*, 150.
3. Berchiesi, G.; Angelis, M. D.; Rafaiani, G.; Vitali, G. *J. Mol. Liq.* **1992**, *51*, 11.
4. Castellani, F.; Berchiesi, G.; Pucciarelli, F.; Bartocci, V. *J. Chem. Eng. Data* **1982**, *27*, 45.
5. Berchiesi, G.; Lobbia, G. G.; Bartocci, V.; Vitali, G. *Thermochim. Acta*, **1983**, *70*, 317.
6. Lobbia, G. G.; Berchiesi, G.; Poeti, G. *Thermochim. Acta*, **1984**, *74*, 247.
7. Berchiesi, G.; Lobbia, G. G.; Berchiesi, M. A.; Vitali, G. *J. Therm. Anal.* **1984**, *29*, 729.
8. Lobbia, G. G.; Berchiesi, G. *Thermochim. Acta*, **1984**, *74*, 251.
9. Lobbia, G. G.; Berchiesi, G. *Thermochim. Acta*, **1984**, *72*, 391.
10. Berchiesi, G.; Rafaiani, G.; Vitali, G.; Farhat, F. *J. Therm. Anal.* **1995**, *44*, 1313.
11. Berchiesi, G.; Vitali, G.; Passamonti, P.; Plowiec, R. *J. Chem. Soc. Faraday Trans. 2* **1983**, *79*, 1257.
12. Amico, A.; Berchiesi, G.; Cametti, C.; Biasio, A. D. *J. Chem. Soc. Faraday Trans. 2* **1987**, *83*, 619.
13. Berchiesi, G. *J. Mol. Liq.* **1999**, *83*, 271.
14. Stafford, O. F. *J. Am. Chem. Soc.* **1933**, *55*, 3987.
15. Yntema, L. F.; Audrieth, L. F. *J. Am. Chem. Soc.* **1930**, *52*, 2693.
16. Dawson, L. R.; Sears, P. G.; Graves, R. H. *J. Am. Chem. Soc.* **1955**, *77*, 1986.
17. Wallace, R. A. *Inorg. Chem.* **1972**, *11*, 414.
18. Wallace, R. *J. Phys. Chem.* **1971**, *75*, 2687.
19. Kerridge, D. H. *Chem. Soc. Rev.* **1988**, *17*, 181.
20. Jander, G.; Winkler, G. *J. Inorg. Nucl. Chem.* **1959**, *9*, 24.
21. Wallace, R.; Bruins, P. *J. Electrochem. Soc.* **1967**, *114*, 212.
22. McManis, G. E.; Fletcher, A. N.; Bliss, D. E.; Miles, M. H. *J. Electroanal. Chem.* **1985**, *190*, 171.

23. Kalita, G.; Sarma, K. G.; Mahiuddin, S. *J. Chem. Eng. Data*, **1999**, *44*, 222.
24. Kalita, G.; Rohman, N.; Mahiuddin, S. *J. Chem. Eng. Data* **1998**, *43*, 148.
25. Mahiuddin, S. *J. Chem. Eng. Data* **1996**, *41*, 231.
26. Berchiesi, G.; Farhat, F.; Angelis, M. D. *J. Mol. Liq.* **1992**, *54*, 103.
27. Berchiesi, G.; Vitali, G.; Plowiec, R.; Barocci, S. *J. Chem. Soc. Faraday Trans. 2* **1989**, *85*, 635.
28. Cole, K. S.; Cole, R. H. *J. Chem. Phys.* **1949**, *9*, 341.
29. Davidson, D. W.; Cole, R. H. *J. Chem. Phys.* **1951**, *19*, 1484.
30. Debye, P. *Polar Molecules* ,Chemical Catalogue Company, New York, 1929.
31. Guchhait, B.; Gazi, H. A. R.; Kashyap, H.; Biswas, R. *J. Phys. Chem. B* **2010**, *114*, 5066.
32. Gazi, H. A. R.; Guchhait, B.; Daschakraborty, S.; Biswas, R. *Chem. Phys. Lett.* **2011**, *501*, 358.
33. Atkins, P. W. *Physical Chemistry* (5th edition); Oxford University Press, Oxford, 1994.
34. Lakowicz, J. R. *Principles of Fluorescence Spectroscopy* (2nd edition).; Kluwer Academic: NY, 1999.
35. Ediger, M. D. *Annu. Rev. Phys. Chem.* **2000**, *51*, 99.
36. Sillescu, H. *J. Non-Cryst. Solids* **1999**, *243*, 81.
37. Ediger, M. D.; Angell, C. A.; Nagel, S. R. *J. Phys. Chem.* **1996**, *100*, 13200.
38. Chang, I.; Fujara, F.; Geil, B.; Heuberger, G.; Mangel, T.; Sillescu, H. *J. Non-Cryst. Solids* **1994**, *172-174*, 248.
39. Moynihan, C. T. *J. Phys. Chem.* **1966**, *70*, 3399.
40. Angell, C. A. *J. Chem. Phys.* **1967**, *46*, 4673.
41. Chakrabarti, D.; Bagchi, B. *Phys. Rev. Lett.* **2006**, *96*, 187801.
42. (a) Gray, C. G.; Gubbins, K. E. *Theory of Molecular Fluids, Vol. I;* Clarendon: Oxford, 1984; (b) Egelstaff, P. A. *An Introduction to the Liquid State* (Clarendon, Oxford) 1992.
43. Castner, Jr.; E. W.; Margulis, C. J.; Maroncelli, M.; Wishart, J. F. *Annu. Rev. Phys. Chem.* **2011**, *62*, 85.
44. (a) Wang, Y.; Voth, G. A. *J. Am. Chem. Soc.* **2005**, *127*, 12192; (b) Wang, Y.; Voth, G. A. *J. Phys. Chem. B* **2006**, *110*, 18601.
45. (a) Bhargava, B. L.; Klein, M. L.; Balasubramanian, S. *ChemPhysChem* **2008**, *9*,

67; (b) Bhargava, B. L.; Devane, R.; Klein, M.; Balasubramanian, S. *Soft Matter* **2007**, *3*, 1395; (c) Raju, S. G.; Balasubramanian, S. *J. Phys. Chem. B* **2010**, *114*, 6455.

46. Lopes, J. A. C.; Padua, A. A. H. *J. Phys. Chem. B* **2006**, *110*, 3330.
47. Urahata, S. M.; Ribeiro, M. C. C. *J. Chem. Phys.* **2004**, *120*, 1855.
48. (a) Andrade, J. D.; Boes, E. S.; Stassen, H.; *J. Phys. Chem. B* **2008**, *112*, 8966; (b) Andrade, J. D.; Boes, E. S.; Stassen, H.; *J. Phys. Chem. B* **2009**, *113,* 7541.
49. (a) Triolo, A.; Russina, O.; Bleif, H.; Cola, E. D.*; J. Phys. Chem. B* **2007**, *111*, 4641; (b) Triolo, A.; Russina, O.; Fazio, B.; Appetecchi, G. B.; Carewska, M.; Passerini, S. *J. Chem. Phys.* **2009**, *130*, 164521; (c) Triolo, A.; Russina, O.; Fazio, B.; Triolo, R.; Cola, E. D. *Chem. Phys. Lett.* **2008**, *467*, 362.
50. (a) Zheng, W.; Mohammed, A.; Hines, L. G.; Xiao, D.; Martinez, O. J.; Bartsch, R. A.; Simon, S. L.; Russina, O.; Triolo, A.; Quitevis, E. L. *J. Phys. Chem. B* **2011**, *115*, 6572; (b) Xiao, D.; Rajian, J. R.; Li, S.; Bartsch, R.; Quitevis, E. L. *J. Phys. Chem. B*, **2006**, *110*, 16174; (c) Xiao, D.; Rajian, J. R.; Cady, A.; Li, S.; Bartsch, R.; Quitevis, E. L. *J. Phys. Chem. B*, **2007**, *111*, 4669; (d) Xiao, D.; Hines, L. G. Jr.; Bartsch, R. A.; Quitevis, E. L. *J. Phys. Chem. B*, **2009**, *113,* 4544; (e) Xiao, D.; Rajian, J. R.; Hines, L. G. Jr.; Li, S.; Bartsch, R. A.; Quitevis, E. L., *J. Phys. Chem. B*, **2008**, *112*, 13316; (f) Xiao, D.; Hines, L. G. Jr.; Li, S.; Bartsch, R. A.; Quitevis, E. L.; Russina, O.; Triolo, A. *J. Phys. Chem. B*, **2009**, *113*, 6426; (g) Russina, O.; Triolo, A.; Gontrani, L.; Caminti, R.; Xiao, D.; Hines, L. G. Jr.; Bartsch, R. A.; Quitevis, E. L.; Plechkova, N.; Seddon, K. R. *J. Phys.: Condens. Matter* **2009**, *21*, 424121.
51. Mandal, P. K.; Sarkar, M.; Samanta,A. *J. Phys. Chem. A* **2004** , *108*, 9048.
52. Jin, H.; Li, X.; Maroncelli, M. *J. Phys. Chem. B* **, 2007** , *111* 13473.
53. (a) Adhikari, A.; Sahu, A. K.; Dey, S.; Ghose, S.; Mandal, U.; Bhattacharyya, K. *J. Phys. Chem. B* **2007** , *111,* 12809; (b) Sasmal, D. K.; Mandal, A. K.; Mondal, T.; Bhattacharyya, K. *J. Phys. Chem. B* **, 2011** , *115,* 7781.
54. (a) Hu, Z.; Margulis, C. J. *Proc. Natl. Acad. Sci. U. S. A.* **2006**, *103,* 831; (b) Annapureddy, H. V. R.; Kashyap, H. K.; De Biasse, P. M.; Margulis, C. J. *J. Phys. Chem. B* **, 2010**, *114*, 16838.
55. (a) Turton, D. A.; Hunger, J.; Stoppa, A.; Hefter, G.; Thoman, A.;Walther, M.; Buchner, R.; Wynne, K. *J. Am. Chem. Soc.* **2009**, *131*, 11140; (b) Hunger, J.;

Stoppa, A.; Schrodle, S.; Hefter, G.; Buchner, R. *Chem. Phys. Chem.* **2009**, *10*, 723; (c) Stoppa, A.; Hunger, A.; Buchner, R.; Hefter, G.; Thoman, A.; Helm, H. *J. Phys. Chem. B* **, 2008** , *112*, 4854.

56. (a) Aoun, B.; Goldbach, A.; Gonzalez, M. A.; Kohara, S.; Price, D. L.; Saboungi, M.-L. *J. Chem. Phys.* **2011**, *134*, 104509; (b) Aoun, B.; Goldbach, A.; Kohara, S.; Wax, J.-F. Gonzalez, M. A.; Saboungi, M.-L. *J. Phys. Chem. B* **, 2010**, *114*, 12623; (c) Aoun, B.; Gonzalez, M. A.; Olivier, J.; Russina, M.; Izaola, Z.; Price, D. L.; Saboungi, M.-L. *J. Phys. Chem. Lett.* **2010**, *1*, 2503.
57. Hardacre, C.; Holbrey, J. D.; Mullan, C. L.; Youngs, T. G. A.; Bowron, D. T. *J. Chem. Phys.* **2010**, *133*, 074510.
58. Kashyap, H. K.; Biswas R. *J. Phys. Chem. B* **2008**, *112*, 12431.
59. Kashyap, H. K.; Biswas R. *J. Phys. Chem. B* **2010**, *114*, 16811.
60. Kashyap, H. K.; Biswas R. *J. Phys. Chem. B* **2010**, *114*, 254.
61. Kashyap, H. K.; Biswas R. *Ind. J. Chem.* **2010**, *49A*, 685.
62. (a) Daschakraborty, S.; Biswas, R. *Chem. Phys. Lett.* **2011**, *510*, 202, (b) Daschakraborty, S.; Biswas, R. *J. Phys. Chem. B*, **2011**, *115*, 4011.
63. Bagchi, B.; Biswas, R. *Adv. Chem. Phys.* **1999**, *109*, 207.
64. Biswas, R.; Bagchi, B. *J. Phys. Chem. B* **1996**, *100*, 4261.
65. Biswas, R.; Nandi, N.; Bagchi, B. *J. Phys. Chem. B* **1997**, *101*, 2968.
66. Jin, H.; Baker, G. A.; Arzhantsev, S.; Dong, J.; Maroncelli, M. . *Phys. Chem. B* **2007**, *111*, 7291.
67. Chandra, A.; Chandra, S. *J. Phys. D: Apply. Phys.* **1994**, *27*, 2171.
68. Choi, B.-K.; Kim, Y.-K. *Mat. Res. Soc. Symp. Proc.* **1995**, *369*, 535.
69. Kalita, G.; Dass, N. N.; Mahiuddin, S. *Can. J. Chem.* **1998b**
70. Day, D. E. *J. Non-Cryst. Solids* **1976**, *21*, 343.
71. Moynihan, C. T. *J. Electrochem. Soc.* **1979**, *126*, 2144.
72. (a) Dietzel, A. H. *Phys. Chem. Glasses*, **1983**, *24*, 172; (b) Ingram, M. D. *Phys. Chem. Glasses*, **1987**, *28*, 215.
73. (a) Vogel, H. *Phys. Z.* **1921**, *22*, 645; (b) Fulcher, G. S. *J. Am. Ceram. Soc.* **1923**, *8*, 339 (); (c) Tammann, G.; Hesse, W. Z. *Anorg. Allgem. Chem.* **1926**, *156*, 245. (d) Angell, C. A. *Chem. Rev.* **2002**, *102*, 2627.
74. (a) Saha, S. K.; Purkayastha, P.; Das, A. B.; Dhara, S. *J. Photochem. Photobiol. A: Chem.* **2008**, *199*, 179; (b) Saha, S. K.; Purkayastha, P.; Das, A. B. *J. Photochem.*

*Photobiol. A: Chem***. 2008**, *195*, 368.

75. DMASBT was received as a gift from Prof. M. Maroncelli, Penn. State University, USA.
76. Horng. M. L.; Gardecki, J. A.; Papazyan, A.; Maroncelli, M. *J. Phys. Chem. B* **1995**, *99*, 17311.
77. Chapman, C. F.; Fee, R. S.; Maroncelli, M. *J. Phys. Chem.* **1995**, *99*, 4811.
78. Pradhan, T.; Biswas, R. *J. Phys. Chem. A* **2007**, *111*, 11514.
79. Sarma, N.; Borah, J. N.; Mahiuddin, S.; Gazi, H. A. R.; Guchhait, B.; Biswas, R. *J. Phys. Chem. B* **2011**, *115*, 9050.
80. Horng, M. L.; Gardecki, J. A.; Maroncelli, M. *J. Phys. Chem. A* **1997**, *101*, 1030.
81. (a) Biswas, R.; Das, A. R.; Pradhan, T.; Touraud, D.; Kunz, W.; Mahiuddin, S. *J. Phys. Chem. B* **2008**, *112*, 6620; (b) Pradhan, T.; Ghoshal, P.; Biswas, R. *J. Chem. Sci.* **2008**, *120*, 275.
82. Cross, A. J.; Fleming, G. R. *Biophys. J.* **1984**, *46*, 45.
83. Riddick, J. A.; Bunger, W. B.; Sakano, T. K. *Organic Solvents*, Wiley: New York, 1986.
84. Guchhait, B.; Daschakraborty, S.; Biswas, R. *J. Chem. Phys.* **2012**, *136*, 174503.
85. Biswas, R.; Lewis, J. E.; Maroncelli, M. *Chem. Phys. Lett.* **1999**, *310*, 485.
86. Gazi, H. A. R.; Biswas, R. *J. Phys. Chem. A*, **2011**, *115*, 2447.
87. Marcus, Y. *Ion Solvation*; John Wiley and Sons Ltd.: Chichester, U. K., 1985.
88. Kim, C. K.; Won, J.; Kim, H. S.; Kang, Y. S.; Li, H. G.; Kim, C. K. *J. Comput. Chem.* **2001**, *22*, 827.
89. Pradhan, T.; Ghoshal, P.; Biswas, R. *J. Phys. Chem. A* **2008**, *112*, 915.
90. Fee, R. S.; Maroncelli, M. *Chem. Phys.* **1994**, *183*, 235.
91. Maroncelli, M. *private communication*.
92. Maroncelli, M.; Fleming, G. R. *J. Chem. Phys.* **1987**, *86*, 6221.
93. Shirota, H.; Castner, Jr. E. W. *J. Am. Chem. Soc*. **2001**, *123*, 12877.
94. Chang, Y. J.; Castner, Jr. E. W. *J. Phys. Chem.* **1994**, *98*, 9712.
95. Biswas, R.; Bagchi, B. *J. Phys. Chem.* **1996**, *100*, 1238.
96. Biswas, R.; Bagchi, B. *J. Phys. Chem.* **1999**, *103*, 2495.
97. Kashyap, H.; Pradhan, T.; Biswas, R. *J. Chem. Phys.* **2006**, *125*, 174506.
98. Roy, S.; Bagchi, B. *J. Chem. Phys.* **1993**, *99*, 9938.
99. Huppert, D.; Ittah, V.; Kosower, M. *Chem. Phys. Lett.* **1992**, *195*, 37.

100. (a) Eberspacher, P.; Wismerth, E.; Buchner, R.; Barthel, J. *J. Mol. Liq.* **2006**, *129*, 3; (b) Barthel, J., Hetzenauer, H.; Buchner, R. *Ber. Bunsen-Ges. Phys. Chem.* **1992**, *96*, 1424.

101. (a) Rudolph, W. W.; Irmer, G.; Hefter, G. T. *Phys. Chem. Chem. Phys.* **2003**, *5*, 5253; (b) Buchner, R.; Chen, T.; Hefter, G. *J. Phys. Chem. B* **2004**, *108*, 2365; (c) Buchner, R.; Hefter, G. T.; May, P. M. *J. Phys. Chem. A* **1999**, *103*, 1.

102. (a) Delsignore, M.; Farber, H.; Petrucci, S. *J. Phys. Chem.* **1985**, *89*, 4968; (b) Delsignore, M.; Farber, H.; Petrucci, S. *J. Phys. Chem.* **1986**, *90*, 66; (c) Saloman, M.; Uchiyama, M.; Xu, M.; Petrucci, S. *J. Phys. Chem.* **1989**, *93*, 4374; (d) Petrucci, S.; Eyring, M. *J. Phys. Chem.* **1991**, *95*, 1731.

103. Edward, J. T. *J. Chem. Edu.* **1970**, *47*, 261.

104. Shanon, R. D. *Acta. Cryst.* **1976**, *A32*, 751.

105. Masterton, W. L.; Bolocofsky, D.; Lee, T. P. *J. Phys. Chem.* **1971**, *75*, 2809.

106. Gray, C. G.; Gubbins, K. E. *Theory of Molecular Fluids, Vol. I;* Clarendon: Oxford, 1984.

107. Attard, P. *Phys. Rev. E*, **1993**, *48*, 3604.

108. Chandra, A.; Bagchi, B. *J. Chem. Phys.* **1999**, *110*, 10024.; Bagchi, B. *Annu. Rev. Phys. Chem.* **1989**, *40*, 115.

109. Lebowitz, J. L. *Phys. Rev.* **1964**, *133*, A895.

110. (a) Bagchi, B.; Chandra, A. *Adv. Chem. Phys.* **1991**, *80*, 1.; (b) Barhel, J.; Buchner, R.; Wurm, B. *J.Mol. Liq. 2002*, *98-99*, 51.

111. (a) Bart, E.; Meltsin, A.; Huppert, D. *J. Phys. Chem.* **1994**, *98*, 3295.; (b) Bart, E.; Meltsin, A.; Huppert, D. *J. Phys. Chem.* **1994**, *98*, 10819.

112. Chapman, C. F.; Maroncelli, M. *J. Phys. Chem.* **1991**, *95*, 9095.

113. Neria, E.; Nitzan, A. *J. Chem. Phys.* **1994**, *100*, 3855.

114. Chandra, A.; Patey, G. N. *J. Chem. Phys.* **1994**, *100*, 1552.

115. (a) Chandra A. *Chem. Phys. Lett.* **1995**, *244*, 314; (b) Chandra A.; Jana, D.; Bhattacharjee, S. *J. Chem. Phys.* **1996**, *104*, 8662.

116. Voronel, A.; Veliyulin, E.; Machavariani, V. Sh.; Kisliuk, A.; Quitmann, D. *Phys. Rev. Letts.* **1998**, *80*, 2630.

117. Egelstaff, P. A. *An Introduction to the Liquid State* (Clarendon, Oxford) 1992.

118. Arzhantsev, S.; Jin, H.; Baker, G. A.; Maroncelli, M. *J. Phys. Chem. B* **2007**, *111*, 4978.

119. Balabai, N.; Waldeck, D. H. *J. Phys. Chem. B* **1997**, *101*, 2339.

120. Ingram, J. A.; Moog, R. S.; Ito, N.; Biswas, R.; Maroncelli, M. *J. Phys. Chem. B* **2003**, *107*, 5926.

121. Ito, N.; Arzhantsev, S.; Heitz, M.; Maroncelli, M. *J. Phys. Chem. B* **2004**, *108*, 5771.

122. Funston, A. M.; Fadeeva, T. A.; Wishart, J. F.; Castner, Jr. E. W. *J. Phys. Chem. B* **2007**, *111*, 4963.

123. (a) Huang, W.; Richert, R. *Phil. Mag.* **2007**, *87*, 371; (b) Anderson, J. E.; Ullman, R. *J. Chem. Phys.* **1967**, *47*, 2178.

124. (a) Santhosh, K.; Banerjee, S.; Rangaraj, N.; Samanta, A. *J. Phys. Chem. B* **2010**, *114*, 1967; (b) Santhosh, K.; Samanta, A. *J. Phys. Chem. B* **2010**, *114*, 9195.

125. Kimura, Y.; Fukuda, M.; Suda, K.; Terazima, M. *J. Phys. Chem. B* **2010**, *114*, 11847.

126. Ueno, K.; Angell, C. A. *J. Phys. Chem. B* **2011**, *115* (in press); doi: jp111398r.

127. Shlesinger, M. F.; Zaslavsky, G. M.; Klafter, J. *Nature* **1993**, *363*, 31.

128. Habasaki, J.; Ngai, K. L. *J. Chem. Phys.* **2008**, *129*, 194501.

129. Hu, Z.; Huang, X.; Annapureddy, H. V. R.; Margulis, C. J. *J. Phys. Chem. B* **2008**, *112*, 7837.

130. Berryman, O. B.; Johnson, D. W. *Chem. Commun* **2009**, 3143.

131. Tarakeshwar, P.; Lee, S. J.; Yong Lee, J.; Kim, S. K. *J. Chem. Phys.* **1998**, *108*, 7217.

132. Huang, M. –M.; Bulut, S.; Crossing, I.; Weingartner, H. *J. Chem. Phys.* **2010**, *133*, 10101.

133. (a) Metzler, R.; Klafter, J. *Phys. Rep.* **2000**, *339*, 1.; (b) Metzler, R.; Barkai, E.; Klafter, J. *Phys. Rev. Lett.* **1999**, 82, 3563.

134. (a) Bandyopadhyay, T. *Europhys. Lett.* **2008**, *81*, 16003.; (b) Bandyopadhyay, T. *J. Chem. Phys.* 2008, 128, 114712.

135. Pal, T.; Biswas, R. *Chem. Phys. Lett.* **2011**, *517*, 180.

136. Bhattacharyya, S.; Bagchi, B. *Phys. Rev. Lett.* **2002**, *89*, 025504.

137. Bhattacharyya, S. M.; Bagchi, B.; Wolynes, P. G. *Proc. Natl. Acad. Sci. USA*, **2008**, *105*, 16077.

138. Bhattacharyya, S. M.; Bagchi, B.; Wolynes, P. G. *J. Chem. Phys.* 2010, **132**, 104503.

139. Jung, Y. J.; Garrahan J. P.; Chandler, D. *Phys. Rev. E* **2004**, *69*, 061205.

140. Garrahan, J. P. Chandler, D. *Phys. Rev. Lett.* **2002**, *89*, 035704.

Chapter 5

Medium Heterogeneity in Presence of a Structure Breaker: Temperature Dependent Fluorescence Studies of Deep Eutectic (Alkylamide + Electrolyte) Melts

5.1 Introduction

The eternal quest for commercially viable and eco-friendly reaction media has led to the development of several fascinating solvents such as room temperature ionic liquids (RTILs),[1,2] room temperature supercritical fluids (RTSFs)[3,4] and gas expanded liquids (GXLs).[5,6] Deep eutectic solvents (DES), which are mixtures of components with high individual melting temperature ($\mathrm{M_p}$) but upon mixing at certain proportions constitute a liquid phase near or below room temperature, are another set of exotic reaction media which exhibit close resemblance to RTILs in solubility and wide liquidous range.[5-13] By carefully choosing components one can introduce in these melts similar longer-ranged interaction length-scales (those varying as r^{-1}, r^{-2} and r^{-3}) to those in dipolar RTILs (RTILs containing dipolar cation and/or anion)[14-19] and moisture stability. Such flexibility provides a boost to construct designer solvents for carrying out chemical reactions with specific and targeted yield. This coupled with the ease at which DES can be prepared at a cost much cheaper than the well-studied imidazolium ILs has rendered these multi-component melts as sustainable alternatives for chemical industry. DES made of alkylamide ($RCONH_2$, R=CH_3, CH_3CH_2, $CH_3CH_2CH_2$) and lithium perchlorate ($LiClO_4$) constitute the subject of the present study where we focus on the solution structure and dynamics because intelligent applications of these solvents as reaction media warrants proper understanding of these solution properties. The relevance to chemical reaction further emerges from the strong and well-established relationship between solvent control and reaction rate.[20,21] Note a tuning of the control via modification and/or alteration of mixture components provides an avenue for solvent engineering to suit the tailoring capability. Interestingly, these solution aspects of DES have not been explored much even-though these melts possess potential for large scale applications in a variety of sectors ranging from metal extraction[9] to catalytic reactions.[2]

The melting temperatures of acetamide (CH_3CONH_2), propionamide ($CH_3CH_2CONH_2$) and butyramide ($CH_3CH_2CH_2CONH_2$) are 353 K, 354 K and 388 K whereas that of $LiClO_4$ is 509 K.[22,23] However, mixing of these amides with $LiClO_4$ at 81:19 mole ratio produces a colourless liquid at a temperature below 298 K. Electrolyte-induced lowering of melting temperature for acetamide has been observed earlier as well and termed as 'super-cooled' melts.[24-26] Substantial lowering of M_p is also observed for mixtures of choline chloride with either carboxylic acids[9] or divalent metal halides[11] and some of these room temperature melts have been found to accelerate and/or augment certain chemical reactions. This is similar to observations in RTILs where 'ionic liquid effects'[1] due to both microscopic phase-segregation and longer-ranged electrostatic interactions on a chemical reaction have been experienced. Micro-heterogeneity in solution structure may also arise in these (alkylamide +electrolyte) DES as hydrophobic interaction among alkyl groups and electrostatic interaction between the polar amide group and ions can generate microscopic phase-segregation, leading to formation of microscopic polar and nonpolar domains. A competition between the lifetime of these domains and the timescale of a chemical reaction occurring in such a media will then dictate the spatial heterogeneity-induced modulation of a reaction rate. In addition, different rates of motions (centre-of-mass and angular) of the environmental particles (that is, temporal heterogeneity)[27-32] can modify a reaction through dynamic solvent effects.[20,33] As a result, understanding heterogeneity of these media is crucially important from basic scientific point of view. Our earlier studies of molten (acetamide + sodium/potassium thiocyanate)[34] and (acetamide + lithium nitrate/bromide)[35] have revealed strong fractional viscosity dependence of solute solvation and rotation rates, and decoupling between rotation and translation akin to that observed in neat supercooled liquids near glass transition.[27] This observation is in sharp contrast with the results for RTILs where the measured solvation and rotation rates nearly follow the hydrodynamics[36-38] although these RTILs are known to possess high degree of both spatial[39-45] and temporal[46-50] heterogeneities. This interesting scenario motivates us to investigate DES made of ($RCONH_2$ + $LiClO_4$) where the extent of spatial heterogeneity on one hand can be regulated via altering the alkyl chain length, and on the other it can be assessed whether this inhomogeneity is at all affected by perchlorate (ClO_4^-) ion whose structure-breaking ability[51-60] in aqueous media has been debated for a long time. The latter aspect emerges from the H-bonding ability of the amides used in the present DES. Note increase in alkyl chain length is known to produce enhanced spatial heterogeneity in RTILs[40] but a systematic study of such an effect in DES has neither been attempted before nor even discussed. Our results on the present DES, when juxtaposed against those on molten (acetamide + electrolyte) systems,[34-35,61-62] reveal the dependence of the medium heterogeneity on the identity of the ions. This is an important aspect which has not been investigated earlier and thus discussed for the first time here.

Apart from the above new features in the proposed study, it is to be mentioned here that the construction of DES containing $RCONH_2$ and $LiClO_4$ at 0.81:0.19 mole fractions have been inspired by the existing phase diagram for molten (alkylamide + sodium trifluoroacetate) system[63] although an accurate determination of M_p for each member of the present DES has not been carried out. However, glass transition temperatures (T_g) have been measured, and the temperature dependence of the mixture density (ρ), and viscosity coefficient (η) have been followed. The measured T_g for these DES is ~190 K (see Fig. A15, Appendix), which is also found to be insensitive to the alkyl chain length. In addition, this value is close to the T_g (<200 K) estimated from the viscosity and conductivity measurements of DES containing acetamide and calcium nitrate tetrahydrate.[64] More interestingly, this T_g and its sensitivity to alkyl chain length are very close to what have already been observed for a number of RTILs.[65] An over-all resemblance to RTIL can also be detected in temperature dependent ρ and η which are shown respectively in Fig. A16 and Fig. A17 (Appendix). More specifically, for variation of the temperature between 303 K and 343 K, ρ and η cover ranges for these DES spanned by imidazolium cation based RTILs[18,55] for the similar temperature range. The refractive indices (n_D) for these DES at ~300 K are somewhat larger compared to those for these RTILs[65] at this temperature. A point to note here is that the alkyl chain length dependence of n_D follows a trend reverse to that found for ρ and originates from larger size and electronic polarizability of the amide with longer alkyl chain. Relatively larger isothermal sound velocity (u) in molten (CH_3CONH_2 + $LiClO_4$) and compressibility (κ_s) of ($CH_3CH_2CH_2CONH_2$ + $LiClO_4$) shown in Fig. A17 are correlated with the chain-length dependence of density for these DES.

With such a characterization of these DES, the heterogeneity aspect of these systems has been studied by carrying out both steady state and time-resolved fluorescence measurements by using multiple probes of varying lifetime in the temperature range, $303 \leq T/(K) \leq 348$. The signature of medium heterogeneity has been identified with the excitation wavelength (λ_{exc}) dependence of the steady state fluorescence response of a dissolved dye and the deviation from conventional hydrodynamics of the average solvation or rotation rates of the same dye measured in time-resolved experiments. Present experiments have also revealed a decoupling between solute solvation and rotation rates in these media. These may be interpreted as arising from the solution phase alkyl chain aggregation and variations in relaxation rates of the environmental particles. Even-though this attribution is similar to that commonly used for observations in deeply supercooled neat liquids,[66,67] deviation from hydrodynamics and decoupling of sorts between rotation and translation in these DES are occurring at a temperature ~100-150 K above the measured T_g. Interestingly, λ_{exc} dependence of fluorescence emission (steady state) of a solute probe dissolved in ($RCONH_2$ + $LiClO_4$) DES is noticed which becomes more pronounced either upon increasing the alkyl chain length (R) or using a solute of relatively shorter lifetime. This suggests presence of spatial heterogeneity with a distribution of survival time for the micro-domains and this distribution is skewed towards shorter domain-lifetime. This is qualitatively similar to the earlier observation for several RTILs.[42] However, time-resolved fluorescence experiments bring out the quantitative differences as measured average solvation and rotation times ($\langle \tau_s \rangle$ and $\langle \tau_r \rangle$, respectively) of a solute in imidazolium and pyrrolidinium RTILs of comparable viscosities are at least twice as large[68] as those found in these DES at ~300 K. The effects of perchlorate ion ($\mathrm{ClO_4^-}$) on medium heterogeneity can be readily recognized as the extent of λ_{exc} dependence for solute emission in (CH_3CONH_2 + LiX) is considerably reduced when the anion (X) is $\mathrm{ClO_4^-}$ in place of nitrate ($\mathrm{NO_3^-}$) or bromide ($\mathrm{Br^-}$).[35] The effects of $\mathrm{ClO_4^-}$ is also manifested in relaxation measurements as the fractional viscosity dependence of $\langle \tau_s \rangle$ and $\langle \tau_r \rangle$ in (CH_3CONH_2 + $LiClO_4$) DES has been found to be relatively less severe compared to that in (CH_3CONH_2 + $\mathrm{Li\,Br^-/NO_3^-}$) deep eutectics[35] although in the present DES, like in other melts, stronger decoupling of $\langle \tau_s \rangle$ than $\langle \tau_r \rangle$ from medium viscosity has been witnessed. The organization of the rest of the chapter is as follows. Experimental details are given in the next section. Section 5.3 contains results and discussion. The chapter then ends with concluding remarks in Sec. 5.4.

5.2 Experimental Sections

5.2.1 Materials

C153 (laser grade, Exciton), 6-propionyl-2-(*N*,*N*-dimethylamino)naphthalene (PRODAN, Fluka), 8-anilino-1-naphthalenesulfonic acid (ANS, sigma-aldrich) were used as received. Trans-2-[4-dimethylamino)styryl]benzothiazole, DMASBT was used without further purification.[35] Acetamide (≥99 %, Sigma-aldrich), propionamide (>97 % sigma-aldrich), butyramide (98 % Merck, Germany) and lithium perchlorate (≥99 %, Fluka), were vacuum-dried (at ~300 K) for 48 hours before use.

5.2.2 Sample Preparation

The detail of sample preparation was described in previous works.[34,35] The concentration of a given fluorophore in each of the ($0.81RCONH_2$ + $0.19\ LiClO_4$) sample taken in an optically transparent quartz cuvette (1 cm path length) was maintained at $\leq 10^{-5}$ M. A temperature controller (Julabo, model-F32) was used for temperature equilibration before data collection.

A few samples were bubbled with dry N_2 gas before data collection but did not produce any difference in data with those collected with the un-bubbled samples.

5.2.3 Density and Viscosity Measurements

Density and ultrasonic velocity of the mixtures were measured by using automated density cum sound analyzer (Anton Paar, model DSA 5000). Subsequently, viscosity and refractive index were measured by using an automated, temperature-controlled micro viscometer (AMVn, Anton Paar) and refractometer (RUDOLPH, J357), respectively.

5.2.4 Measurements of Glass Transition Temperature

T_g of the molten mixtures were measured using differential scanning calorimetry (DSC, TA Instruments Q2000). The temperature and heat flow were calibrated using a certified indium sample. Measurements were performed in the range of 103 to 423 K under a flow of 50 mL/min dry N_2 and 25 mL/ min He. The samples were hermetically sealed in an aluminium pan (40 μL, Tzero, TA Instruments) to prevent evaporation during the measurement. A heating/cooling rate of 10 K/ min and 2 min isothermal periods at 103 K were used for all measurements.

5.2.5 Steady State Spectroscopic Measurements

Steady-state absorption and emission spectra were collected using a UV-visible spectrophotometer (UV-2450, Shimadzu) and a fluorimeter (Fluoromax-3, Jobin-Yvon, Horiba), respectively. Precautionary measures were taken to avoid moisture absorption by samples during measurements. Solvent blank spectra were subtracted prior to analysis. All samples were excited at their respective absorption maxima for steady state fluorescence measurements.

5.2.6 Time-Resolved Spectroscopic Measurements

The time resolved measurement were performed using Time Correlated Single Photon Counting (LifeSpec-ps, Edinburgh Instruments, U. K.) fitted with a diode laser producing excitation light of 409 nm.[34,35] The instrument response function (IRF) measured using water was found to be ~ 70 ps. We used 409 nm excitation for C153, ANS and DMASBT, and 375 nm for PRODAN. For solvation dynamics measurement 18-20 decays at wavelengths spanning emission spectrum were collected at magic angle. The collected decays were deconvoluted from the IRF and fitted to multi-exponential function using an iterative reconvolution algorithm.[69] Time resolved emission spectra (TRES) were reconstructed from the decay fit parameters of in conjunction with normalized intensities of the steady state emission spectrum as described in refs.[69] For the purpose of rotational dynamics measurement a set of three decays, namely, parallel, perpendicular and magic angle polarizations were collected. Time resolved fluorescence anisotropies, $r(t)$, were then calculated from the collected decays by using the method[70-72]described in chapter 2.

5.3 Results and Discussions

5.3.1 Solvation Characteristics: Steady State Spectral Measurements

Solute-medium interactions in these DES have been probed by absorption and fluorescence spectra of C153 and the resultant spectral characteristics at different temperatures are presented in Fig. 5.1. The alkyl chain length dependence of such interactions at 303 K is depicted in the first panel where a small blue-shift (in emission) upon replacing acetamide by butyramide can be detected. This is density effect (see Fig. A16) and thus connected to tighter packing of the solvation shell around the solute.[4,73] Note the absorption and emission frequencies in these DES are in the same range as observed in (CH_3CONH_2 + LiBr + $LiNO_3$) melts[35] but ~200-400 cm^{-1} blue-shifted compared to those in (CH_3CONH_2 + NaSCN + KSCN) systems.[34] Interestingly, fluorescence emission in the present DES exhibits red-shift upon increasing temperature eventhough the medium density decreases with it. Similar effects of temperature on dynamic Stokes shift have been predicted for several imidazolium ionic liquids[18] and explained in terms of enhanced solute-ion interaction due to lowering of static dielectric constant upon raising temperature.[74] Since these DES contain ions, it is possible that enhanced solute-ion interaction also lead here to lowering of the emission frequency with temperature. The kinship to RTIL is further extended as the absorption and emission frequencies of C153 measured here span the similar range observed with the same solute in several imidazolium ILs.[36] However, the solvation free energy difference ($\Delta_{sol}G$)

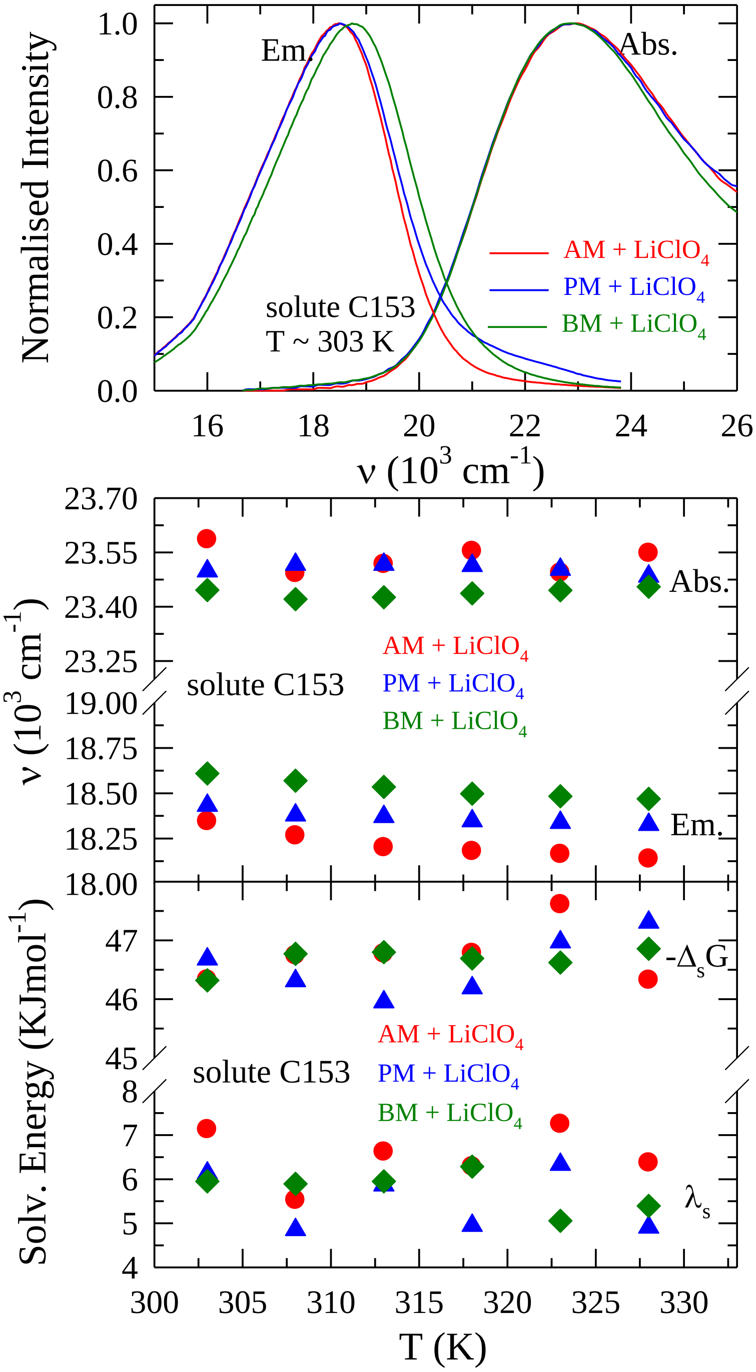

Fig. 5.1: Steady state spectra of C153 and their characteristics (data are color coded). Representative absorption and emission spectra in three {alkylamide + LiClO$_4$} mixtures at 303 K are shown in upper panel. Frequencies (ν_{abs} and ν_{em}) and solvation energies ($-\Delta_s G$ and λ_s) as a function of temperature for all the mixtures are shown in middle and lower panels respectively. The two types of solvation energies, free energy ($-\Delta_s G$) and reorganisation energy (λ_s) are defined in the text. AM, PM, and BM represent acetamide, propionamide and butyramide respectively.

and the solvent reorganization energy (λ_{sol}) do not match as these values are lower by ~5-10 kJmol^{-1} than those obtained for these ILs.[36] Temperature dependent of $\Delta_{sol}G$ and λ_{sol}, shown in the lower panel, have been calculated from the following formulae:[36] $\Delta_{sol}G = 1/2\{h(\nu_{abs} + \nu_{\infty})\} - \Delta G_0$ and $\lambda_{sol} = 1/2\{h(\nu_0 - \nu_{\infty})\}$ with a gas phase value (approximate) ΔG_0 =295.9 kJmol^{-1}, $\nu_0 = \nu(0)$ and $\nu_{\infty} = \nu(\infty)$ coming from the dynamic Stokes shift measurements. The non-availability of experimental static dielectric constant (ε_0) for these DES did not allow construction of a correlation of these quantities with dielectric field factors as was done for common dipolar solvents; but an attempt to correlate them with the effective molar volume (V_m, from sound velocity measurements) saw substantial departure from such a correlation obtained for RTILs.[36] The reason behind such a departure lies in the relatively lower effective V_m for these DES (see Table A7, Appendix) than the RTILs.

Another aspect of steady state fluorescence emission in these highly viscous ($10 < \eta/\text{cP} < 210$) medium that needs consideration is whether the emission occurs from the fully solvent relaxed state of the excited solute. This can be quantified by following the difference between the dynamic Stokes shift ($\Delta\nu^t = \nu_0 - \nu_{\infty}$) and steady state Stokes shift relative to a non-polar solvent ($\Delta\Delta\nu = (\nu_{abs} - \nu_{em})_{DES} - (\nu_{abs} - \nu_{em})_{NP} = \Delta\nu_{DES} - \Delta\nu_{NP}$). We find that this difference, $\delta\delta\nu = \Delta\nu^t - \Delta\Delta\nu$, is the maximum (~400 cm^{-1}) for the butyramide containing DES and the minimum (~200 cm^{-1}) for the acetamide containing one (see Fig. A18, Appendix) after using $\Delta\nu_{NP}(\text{heptane}) = 4230\ \text{cm}^{-1}$. Such a difference between the shifts ($\delta\delta\nu$ ~200-400 cm^{-1}) in these DES due to sluggish solvent relaxation is smaller by a factor of ~3-4 than those observed for RTILs with similar viscosity.[36] However, these results suggest that static heterogeneity may be present in these DES as slow solvent movements (relative to the lifetime of the excited probe) can give rise to temporary trapping of the solute inside a micro-domain.[48] Furthermore, hydrophobic interaction induced association among the alkyl groups[40,75-77] is expected to be the strongest for the butyramide containing deep eutectic, ($CH_3CH_2CH_2CONH_2$ + $LiClO_4$).

Consequently, the static heterogeneity aspect is next investigated by using solute probes of differing lifetimes so that a qualitative understanding of the stability of the heterogeneous domains, if formed in these DES, can be generated. We have used ANS, C153, PRODAN and DMASBT for this purpose and the excited state lifetimes ($\tau_{life} \equiv \tau_{\text{Long}}$ of the bi-exponential intensity decay) for these probes in these DES have been found to be ~6 ns, 4 ns, 3 ns and 0.5 ns, respectively (see Fig. A19 and Table A8). These τ_{life} values are well-correlated with the literature values[35,69,78,79] and thus dynamic quenching effects by ions in the present study can

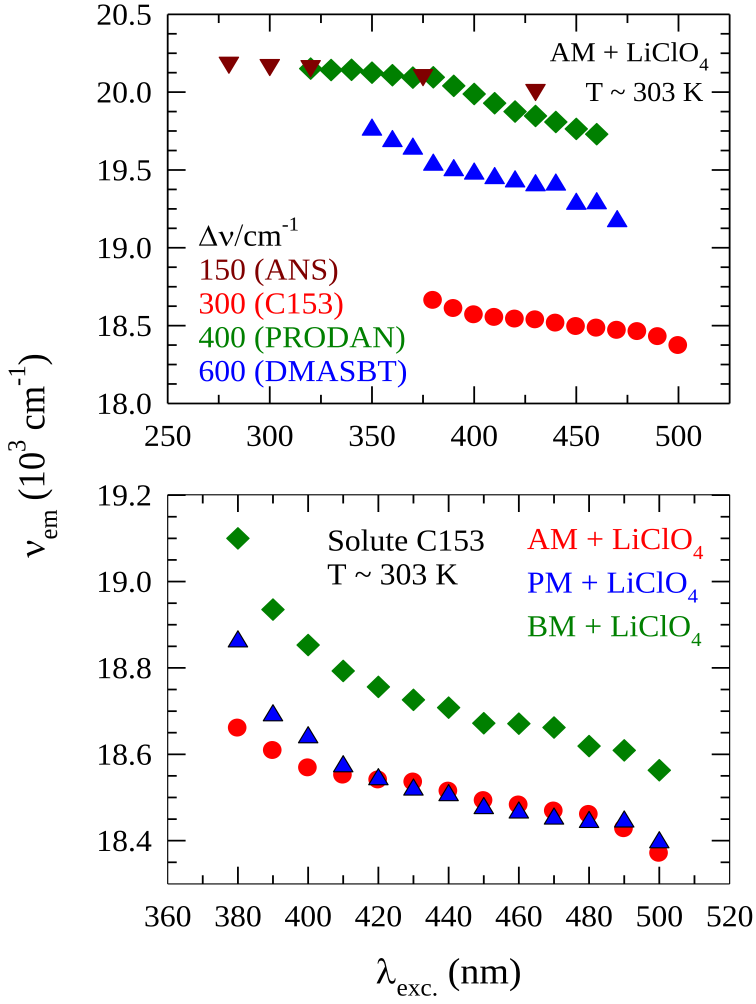

Fig. 5.2: Excitation wavelength dependence (λ_{exc}) of emission peak frequency (ν_{em}) for four dipolar solutes, ANS, C153, PRODAN and DMASBT in {AM + $LiClO_4$} mixture (upper panel) and for C153 in three {alkylamide + LiClO4} mixtures (lower panel) at 303 K. Data are color coded.

be regarded as either secondary or negligible. Fig. 5.2 displays the results of steady state photo-selection investigation with the above fluorescent solutes where the peak frequencies of the emission spectra generated after exciting at different wavelengths ($\lambda_{exc.}$) are presented as a function of $\lambda_{exc.}$. While the upper panel shows the solute dependence of the $\lambda_{exc.}$ induced emission peak shift in (CH_3CONH_2 + $LiClO_4$) melt at ~303 K, the lower panel displays the alkyl chain length dependence of it with C153 at the same temperature. Results from similar study using PRODAN and DMASBT are shown in Fig. A20 (Appendix). Note the total emission shift, $\Delta\nu^{em}$, induced by $\lambda_{exc.}$ for (CH_3CONH_2 + $LiClO_4$) melt at ~303 K is the largest (~600 cm^{-1}) for DMASBT and the smallest for ANS (~150 cm^{-1}) and follows a probe sequence reverse to the one if arranged in terms of decreasing τ_{life}. When the solute probe is kept fixed, $\Delta\nu^{em}$ becomes the largest (~600 cm^{-1}) for ($CH_3CH_2CH_2CONH_2$ + $LiClO_4$) melt and the smallest (~300 cm^{-1}) for (CH_3CONH_2 + $LiClO_4$), confirming alkyl chain aggregation being the strongest for butyramide containing melt.

The lifetime dependence of $\Delta\nu^{em}$ in the above DES at 303 K are summarized in Fig. 5.3 which clearly shows that the static heterogeneity increases with alkyl chain length (as discussed in the Introduction) and the extent of this spatial heterogeneity is the largest for a probe which posses the smallest τ_{life}. This is qualitatively similar to earlier observation (with different probes though) in RTILs[42] and indicates a distribution of the stability time of the fluctuating micro-domains in these DES which is skewed towards lower values (of stability time) with an accompanying tail of longer-lived domains. This observation is important because it provides a sense of the timescales associated with domain fluctuations (or inter-conversion) in these DES without directly measuring the relaxation rates. Another interesting observation is that $\Delta\nu^{em}$ is sensitive to the nature of the anion (X) present in the melt. For example, shifts in (CH_3CONH_2 + LiX)[35] DES at ~303 K measured with DMASBT and C153 are respectively ~600 cm^{-1} and ~300 cm^{-1} when X is ClO_4^-; ~1300 cm^{-1} and ~300 cm^{-1} for X = NO_3^-, and ~800 cm^{-1} and ~600 cm^{-1} for X = Br^-. Additionally, for a given solute $\Delta\nu^{em}$ does not follow any linear correlation with anion size as the anionic radii are 2.4 Å, 1.96 Å and 1.82 Å for ClO_4^-, NO_3^- and Br^-, respectively.[35,80] These $\Delta\nu^{em}$ data also do not follow the

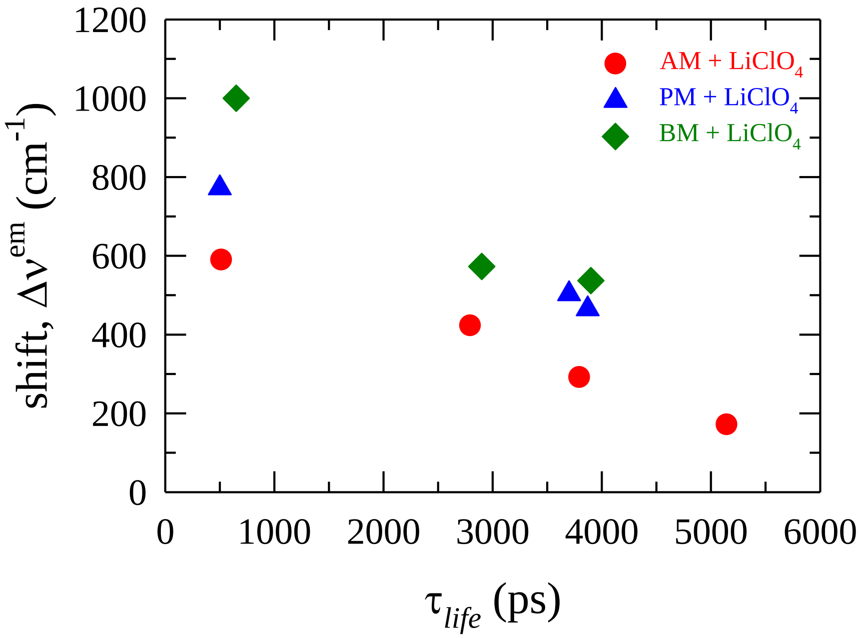

Fig. 5.3: Solute's life time dependent $\Delta\nu^{em}$ (shift) in {alkylamide + LiClO4} DES at 303 K.

Hofmeister sequence of solubility of potassium salts in non-aqueous media.[81] The observation that $\Delta\nu^{em}$ in presence of NO_3^- is twice as large as that when replaced by ClO_4^- may be linked to the geometrical shape of these anions (trigonal planar versus tetrahedral)[82] and the degree of perturbation in the liquid structure (as large positive solvation entropy suggests[81]) induced by them. This warrants further study.

5.3.2 Medium Dynamics and Solute-Solvent Coupling: Time-resolved Measurements

The above signature of anion identity on static heterogeneity then naturally lead us to investigate how solute-based dynamics respond to this variation and how solute-medium interaction gets modified. For this we have considered temperature dependence of rotational and solvation energy relaxations of C153 in these DES. The nature of interaction is then understood by exploring the diffusion-viscosity relationship and comparing with the conventional hydrodynamic description, $D \propto \eta^{-1}$. This allows further testing of kinship to

RTILs as solute rotation and solvation energy relaxation in RTILs exhibit stretched exponential character but the average rates ($\langle \tau_s \rangle^{-1}$ and $\langle \tau_r \rangle^{-1}$) nearly follow the hydrodynamics.[36,37,68] This is essentially exploration of the temporal heterogeneity of these DES and effects of ion identity on it but only partial because these dynamic measurements correspond to a single λ_{exc} and *not* carried out by exciting solute-solvent configurations of different energies by varying λ_{exc}. Fig. 5.4 depicts representative magic angle intensity decays (upper panel) collected at the red and blue ends of the emission spectrum of C153 dissolved in ($CH_3CH_2CH_2CONH_2$ + $LiClO_4$) melt at ~303 K, time-resolved emission spectra at different time slices (middle panel) and the variation in spectral width as solvation of the excited probe progresses with time (lower panel). Rise followed by decay at 620 nm and decays only at 470 nm reflected by the fits (shown inside the upper panel) indicate presence of dynamic Stokes shift in these DES. In addition, if the longest time constant (τ_3) of these fits are assigned as τ_{life} then these decays also suggest presence of ~100 ps and ~1 ns timescales in these melts which are qualitatively similar to earlier findings with DES made of acetamide and other electrolytes.[34,35,61]

Time-resolved emission spectra in the middle panel of Fig. 5.4 provide further support in favour of the slower dynamics as spectral movement exists in the nanosecond timescale where the time-resolved spectrum extrapolated at $t = \infty$ moves beyond the corresponding steady state emission by ~500 cm^{-1}. As already discussed, this is due to slow environmental relaxation where fluorescence emission occurs from the incompletely solvent-equilibrated excited solute. The spectral width, $\Gamma(t)$, of the constructed time-resolved emission spectrum shown in the lower panel, depicts a non-monotonic variation with time. Note the transient spectral broadening followed by over-all narrowing, as reflected by $\Gamma(t)$ here, has been detected earlier for a wide variety of systems that include conventional dipolar solvents,[69,83] supercooled liquids,[84] multi-component melts[34,35] and confined aqueous environments,[85] and explained in terms of inhomogeneous distribution of solvent configurations. Recent dynamic Stokes shift measurements of C153 in RTILs of comparable viscosity have, however, reported monotonic decrease of $\Gamma(t)$ and attributed the observation to the vibrational

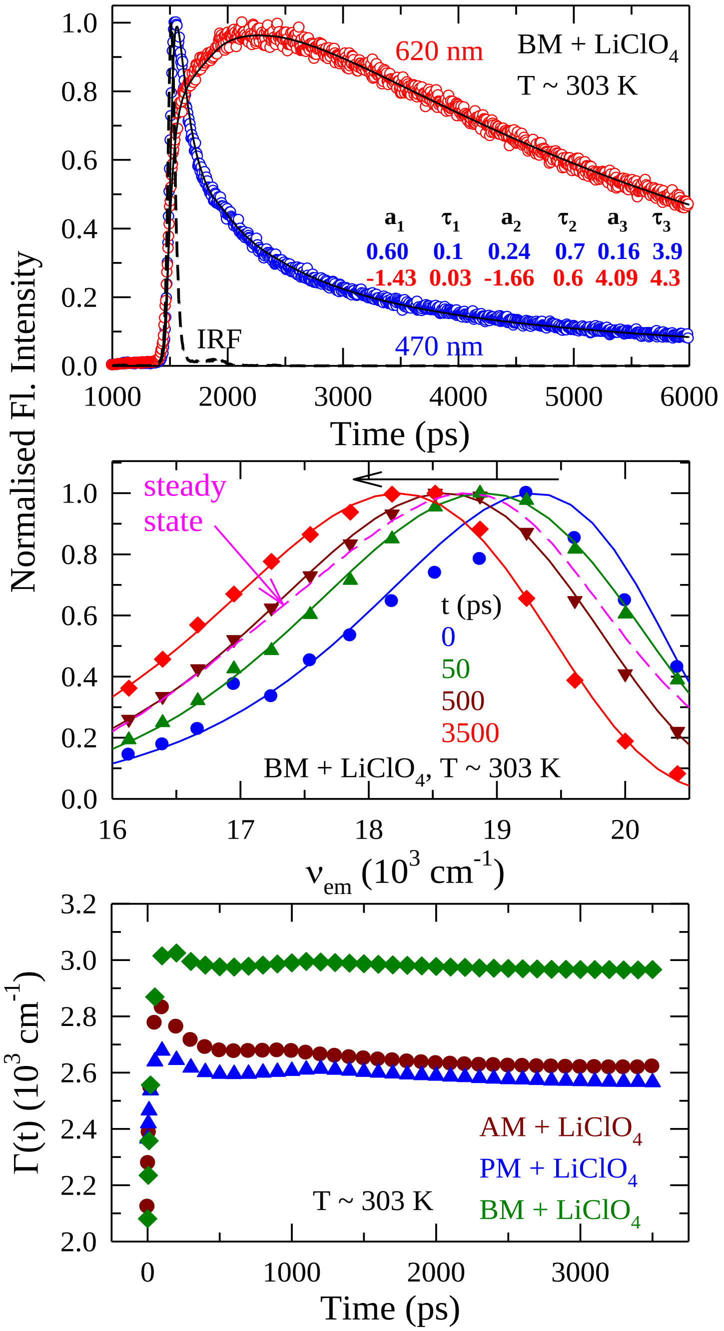

Fig. 5.4: Time resolved fluorescence behavior of C153 (data are color coded). Representative fluorescence intensity decays at blue (470 nm) and red (620 nm) wavelengths in upper panel and TRES at various time slices, 0 ps (circles), 50 ps (triangles), 500 ps (inverted triangles), and 3500 ps (diamonds) in middle panel for {BM + LiClO$_4$} molten mixture at 303 K. Lower panel represents the width ($\Gamma(t)$) of the TRES for three mixtures. Inset of upper panel shows the decay fitting parameters.

cooling[68] of the excited solute. Both these factors – inhomogeneous solvent distribution and local heating due to vibrational energy relaxation – may therefore be responsible for the observed behaviour of $\Gamma(t)$ for these DES.

The temperature dependent dynamic Stokes shifts ($\Delta\nu_{obs}^{t}$) observed for these DES are summarized in Table 5.1 along with the estimated values ($\Delta\nu_{est}^{t}$)[88] and the percentage detected. Note the $\Delta\nu_{obs}^{t}$ values for these DES are approximately within 900-1200 cm^{-1} and decrease with increase of the alkyl chain length. This probably reflects a decrease in average medium polarity with chain length as dielectric relaxation measurements of ionic liquids indicate reduction in static dielectric constant (ε_0) upon increase in chain length of the alkyl group attached to the dipolar cation.[89] The temperature dependence of the shift is very weak which suggests that the decrease with temperature of solute-amide dipole-dipole interaction contribution is probably counter-balanced, as predicted for ionic liquids,[18] by the dipole-ion contribution. Interestingly, $\Delta\nu_{est}^{t}$ values for these DES are smaller than those estimated for (acetamide + Na/K thiocyanates)[34] and (acetamide + Li nitrate/bromide)[35] deep eutectics. In addition, the $\Delta\nu_{obs}^{t}$ values for the present DES are quite close to the corresponding $\Delta\nu_{est}^{t}$, suggesting thereby a much less missing component eventhough the same temporal resolution (~75 ps) as before[34,35] has been employed in the present experiments. This indicates a definite role for the ClO_4^- anion in regulating the medium response to solute-excitation. In this context it is necessary to recall that amide systems are known to possess collective librational modes centered around ~50-100 cm^{-1} (due to intermolecular H-bonding)[90,91] and these modes, when incorporated in relevant calculations,[92-96] have been shown to produce sub-picosecond solvation response. It is possible that ClO_4^- anion forms complexes with amide in these DES in such a way that the amide hydrogens are no longer available for establishing the intermolecular H-bonding network and, as a result, these low frequency collective librational modes are effectively quenched. Despite this being a conjecture and thus warrants cross-examination via more sophisticated experiments (for example, dielectric relaxation with wide frequency coverage and fluorescence measurements employing much sharper temporal

Table 5.1: Dynamic Stokes shifts ($\Delta\nu_{est}(t)$ and $\Delta\nu_{obs}(t)$) and detected portion of the total dynamics of C153 in molten {alkylamide + $LiClO_4$} mixtures with varying alkyl chain length in amide at several temperatures. AM, PM, and BM represent acetamide, propionamide and butyramide respectively

T(K)	$\Delta\nu_{est}(t)$ (10^3 cm^{-1})	$\Delta\nu_{obs}(t)$ (10^3 cm^{-1})	% detected
AM + LiClO4			
303	1.243	1.191	96
308	1.263	0.923	82
313	1.181	1.106	94
318	1.254	1.050	84
323	1.273	1.211	95
328	1.168	1.065	91
PM + LiClO4			
303	1.129	1.025	91
308	1.103	0.811	74
313	1.043	0.980	94
318	1.077	0.827	76
323	1.186	1.058	89
328	1.204	0.820	68
BM + LiClO4			
303	0.963	0.994	103
308	0.988	0.985	100
313	1.003	0.994	99
318	1.007	1.050	104
323	1.012	0.845	83
328	1.071	0.901	84

resolution), the present results do suggest that the difference brought out by ClO_4^- anion in Stokes shift dynamics of (amide + electrolyte) DES is due to its ability to terminate, at least partially, the interlocking among the amide molecules through H-bonding and thus effectively 'breaking' the usual network structure of amides[90,91] in liquid phase.

When we use a semi-molecular theory which is based upon the assumption of complete dissociation of the dissolved electrolyte in these DES,[34,35] we find ~25-35% contribution arising from the dipole-ion interaction between the dipolar solute (C153) and the ions, and the rest from the solute-amide dipolar interaction. This is qualitatively similar to earlier findings with DES containing acetamide and other non-perchlorate anions. The calculated total shifts and the individual (dipole-dipole and ion-dipole) interaction contributions are summarized in Table A9 (Appendix). A comparison with the experimental estimated shifts suggests much better agreement for ($CH_3CH_2CH_2CONH_2$ + $LiClO_4$) DES where dipole-dipole contribution ($\Delta\nu_{sd}^{t}$) is reduced drastically. This is a density effect where bigger size of the solvent dipole (here butyramide) induces less effective interaction with the dipolar solute. Accordingly, the effective size of the dipolar entity interacting with the solute dipole in the case of (CH_3CONH_2 + $LiClO_4$) DES may be much larger than that of a single CH_3CONH_2 molecule which will bring the calculated shifts for this system much closer to the experiments. This proposition is akin to association of acetamide molecules in presence of alkali metal ions suggested earlier[7,8,24-26] and can be verified via all-atom simulations using realistic potentials for all the species constituting the DES.

Next we investigate the temperature and alkyl chain length dependence of solvation response function in Fig. 5.5 where the measured $S(t)$ for these DES at there different temperatures are shown as a function of time. As expected, the decay profiles follow, on an average, the medium viscosity and its temperature dependence. Bi-exponential fits to these decays and to those obtained at other temperatures produce a faster component (~50-75%) with timescale (τ_1) in the ~50-100 ps range, followed by a much slower component with time constant (τ_2) spread over ~0.5-1 ns (see Table A10, Appendix). The relatively slower time constant, τ_2, shows a dependence on viscosity and thus related to structural relaxation of the solvating medium.[97,98] Interestingly, the average solvation times found for these DES are ~2-4 times faster than those measured recently with the same solute in RTILs of comparable viscosity,[68] reflecting a qualitative difference between these two kinds of media.

Subsequently, the solute-medium coupling is investigated in Fig. 5.6 where the measured average solvation times ($\langle\tau_s\rangle$) are shown as a function of temperature-reduced viscosity

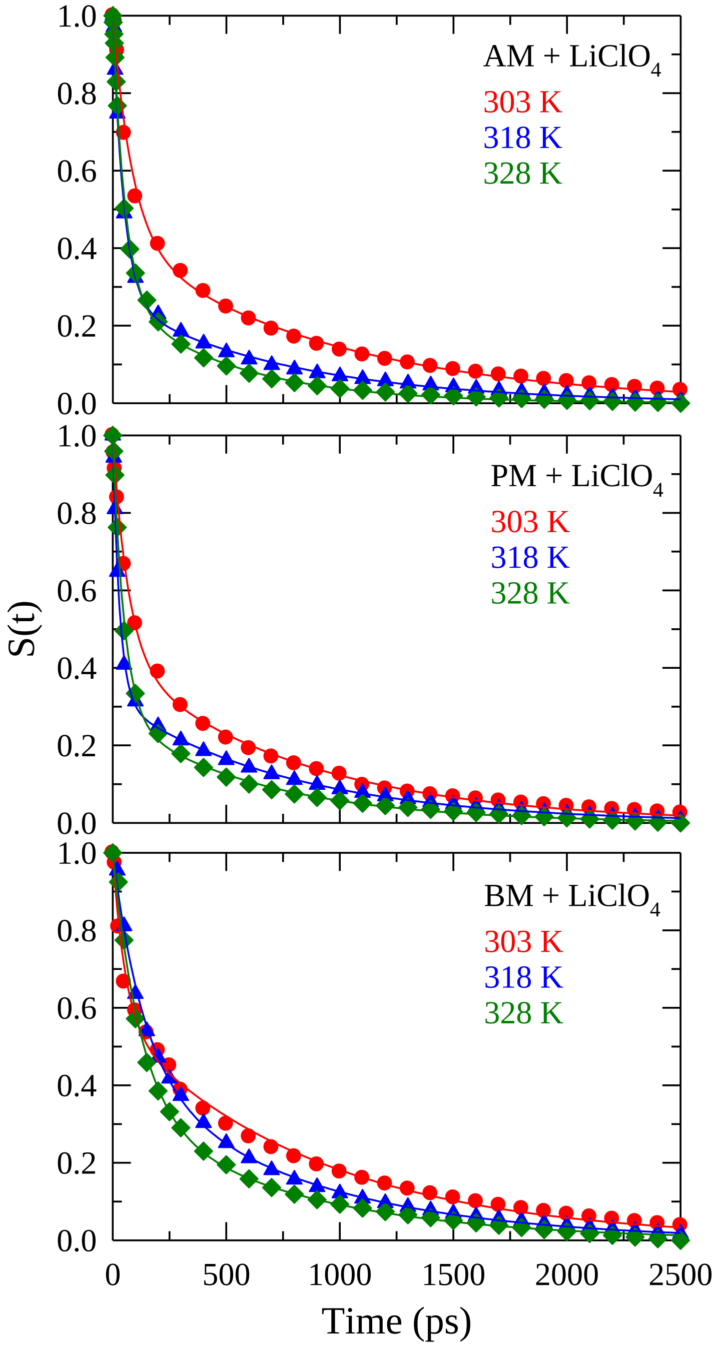

Fig. 5.5: Decays of solvent response function ($S(t)$) of C153 at 303, 318 and 328 K (color coded). The upper, middle and lower panels show the data in AM, PM and BM molten mixtures (deep eutectics) respectively. The solid lines show the biexponential fits to data.

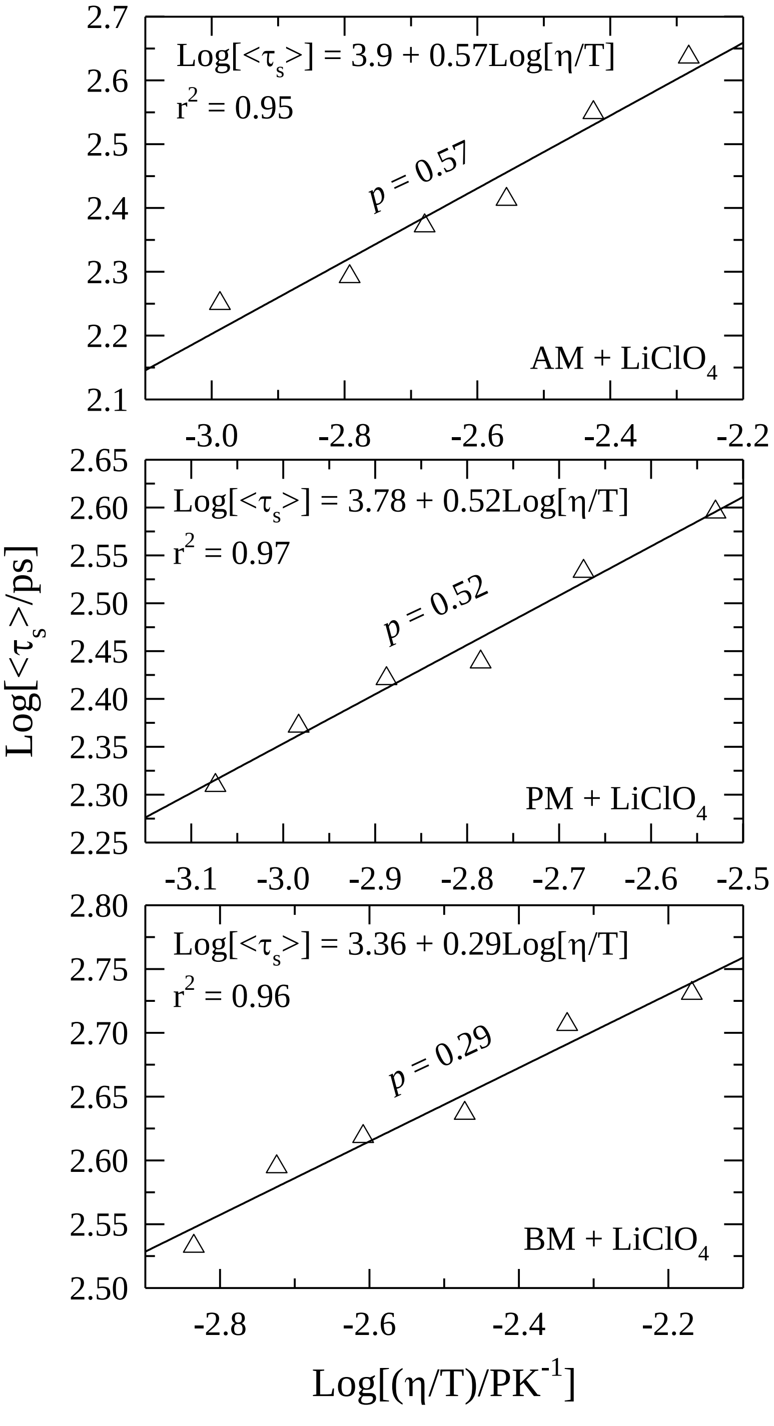

Fig. 5.6: Log-Log plot of average solvation time, $<\tau_s>$ of C153 versus η/T in {alkylamide + LiClO$_4$} DES. The solid lines show the best fits of the experimentally measured data to the relation $Log[<\tau_r>] = B + pLog[\eta / T]$, the associated B and *p* values are given in the figure. Different panels represent data at different alkyl chain lengths.

(η/T) in a log-log plot for these three DES. The fits going through the data points indicate fractional viscosity dependence, $\langle \tau_s \rangle = \mathrm{A}(\eta/\mathrm{T})^p$, with p not only significantly smaller than unity ($0.6 > p > 0.3$) but deviates most for DES that contains amide with the longest alkyl chain. Since $\langle \tau_s \rangle$ is dominated by the translational diffusion of the solvating particles, the decoupling reflected by the above fractional viscosity dependence resembles the diffusion-viscosity decoupling normally observed for deeply supercooled neat liquids.[27-32] The observation that p being smaller for larger amide (from time-resolved measurements) is consistent with the steady state fluorescence results shown earlier in Fig. 5.2 which suggested stronger spatial heterogeneity for amide with longer alkyl chain. This result can also be paralleled with observations in dielectric relaxation measurements of RTILs where stronger heterogeneity (reflected by larger value of α there)[89] is suggested for the RTIL with larger alkyl chain attached to the dipolar imidazolium cation. However, similar fractional viscosity dependence has not been found for $\langle \tau_s \rangle$ in RTILs[18,36] in spite of the presence of other signatures of medium heterogeneity in these Coulomb fluids. Interestingly, p from solvation studies obtained for (CH_3CONH_2 + LiBr/NO_3) DES is nearly twice as smaller (p =0.35)[35] as that ($p \approx 0.6$) determined for (CH_3CONH_2 + $LiClO_4$) DES. This suggests that molten CH_3CONH_2 in presence of ClO_4^- anion exhibits less heterogeneity than in presence of other anions (cation being fixed) and this may be ascribed to the extensive interaction (structure breaking) ability of the ClO_4^- anion with acetamide molecules effectively preventing association among amides in the corresponding DES. In fact, the extent of heterogeneity shown by (acetamide + electrolyte) DES varies with the identity of the electrolyte as one finds p =0.46 from solvation studies with (CH_3CONH_2 + Na/KCNS) DES.[34]

The solute-medium coupling and the consequent resemblance to the behaviour observed for deeply supercooled liquids have been further investigated via the temperature dependent dynamic fluorescence anisotropy of C153 in these media. Fig. 5.7 depicts one such representative example where the measured anisotropy is shown as a function of time along with the bi-exponential fit and the residual. Attempt to fit using a stretched exponential,

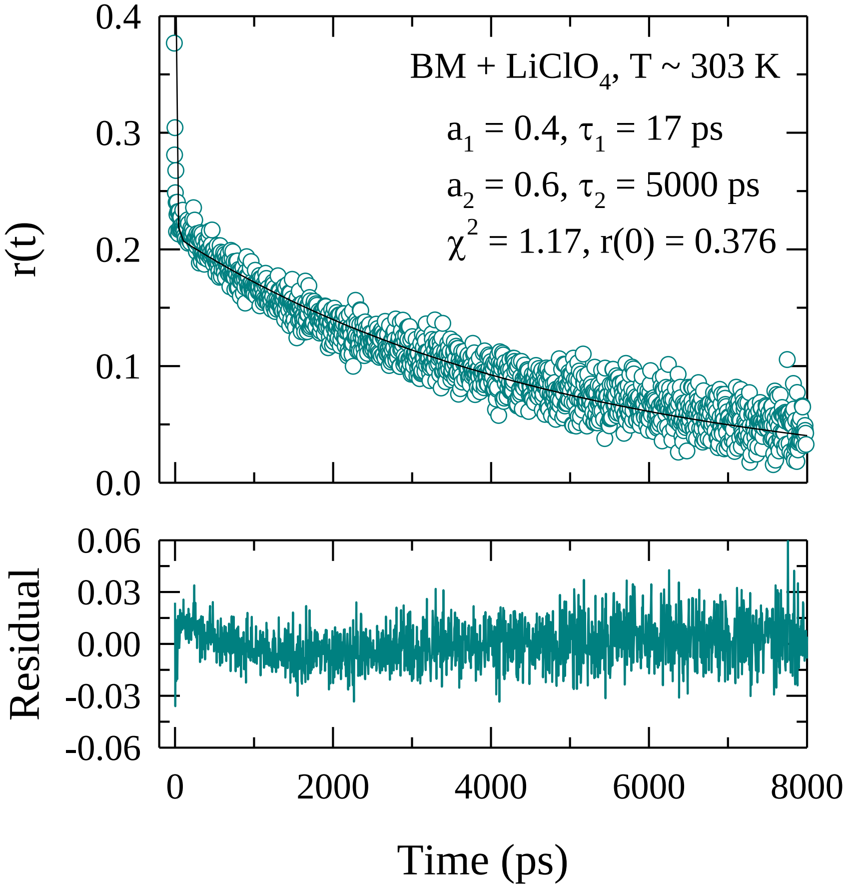

Fig. 5.7: Representative fluorescence anisotropy decay ($r(t)$) of C153 in {BM + LiClO4} DES (upper panel) and residuals of the biexponential fit (lower panel) at 303 K.

$r(t) = r_o \exp[-(t/\tau_r)^{\beta}]$, did not provide adequate description of the measured $r(t)$. The fit parameters shown in the inset indicate presence of to widely separated time constants – one in the few tens of picoseconds and the other in the nanosecond regime. Time constants and amplitudes obtained from the bi-exponential fits to the $r(t)$ measured for these DES at different temperatures are summarized in Table A11 (Appendix) which suggests bimodal anisotropy decay as being a signature for these DES, irrespective of electrolyte or amide identity.[34,35,61] This is different from the stretched exponential behaviour of $r(t)$ measured with C153 in RTILs over the same time-window (20 ns)[36] and somewhat unexpected given the λ_{exc} dependence of steady state emission shown in Fig. 5.2. Similar applicability of bi-exponential function of time has also been witnessed for the measured temperature dependent $S(t)$ decays in these DES and thus raises the following question: does the presence of different, photo-selectable solute-solvent configurations guarantee the emergence of stretched exponential relaxation of solute-centred dynamics? While the reverse can be understood in terms of dynamic heterogeneity and has indeed been observed in model systems,[62,99,100] the parent question warrants further study given that the experimental temperature window here (303-348 K) is much above the measured glass transition temperature (~195 K) of these DES.

Fig. 5.8 displays the viscosity dependence of average rotation times ($\langle \tau_r \rangle$) via plotting the logarithm of the measured $\langle \tau_r \rangle$ at various temperatures with C153 in these DES as a function of logarithm of temperature-reduced viscosity (η/T). Calculated rotation times for C153 in the stick and slip limits of the modified Stokes-Einstein-Debye (SED) expression using the proper solute volume (246 Å^3) and shape factor (f =1.71)[34-36] are also shown in the same figure. A comparison between the model calculations and the experimental data clearly indicate inadequacy of the hydrodynamics which is expected given the static heterogeneity and complex interactions present in these DES. The most important aspect of this figure is that $\langle \tau_r \rangle$ in these media, as previously observed for $\langle \tau_s \rangle$, exhibit a fractional viscosity dependence but with a fraction value ($0.75 \geq p \geq 0.52$) larger than that ($0.57 \geq p \geq 0.29$) observed in solvation studies. As in the case of solvation, p associated with solute rotation has also been found to be smaller for amide with longer alky chain length. Strikingly, p obtained for solute rotation in (CH_3CONH_2 + $LiClO_4$) DES is comparable to the composition averaged value (p =0.55) obtained earlier in (CH_3CONH_2 + LiBr/NO_3), indicating much less importance of the ‘structure breaking’ ability of ClO_4^- anion for solute rotation. This is in accordance with the observation that rotation is ‘better averaged’ than translation[101,102] which mitigates the solution structural effects on rotational relaxation. Another important observation here is that in these DES p values determined from solute solvation are uniformly smaller than those obtained from solute rotation, suggesting a sort of

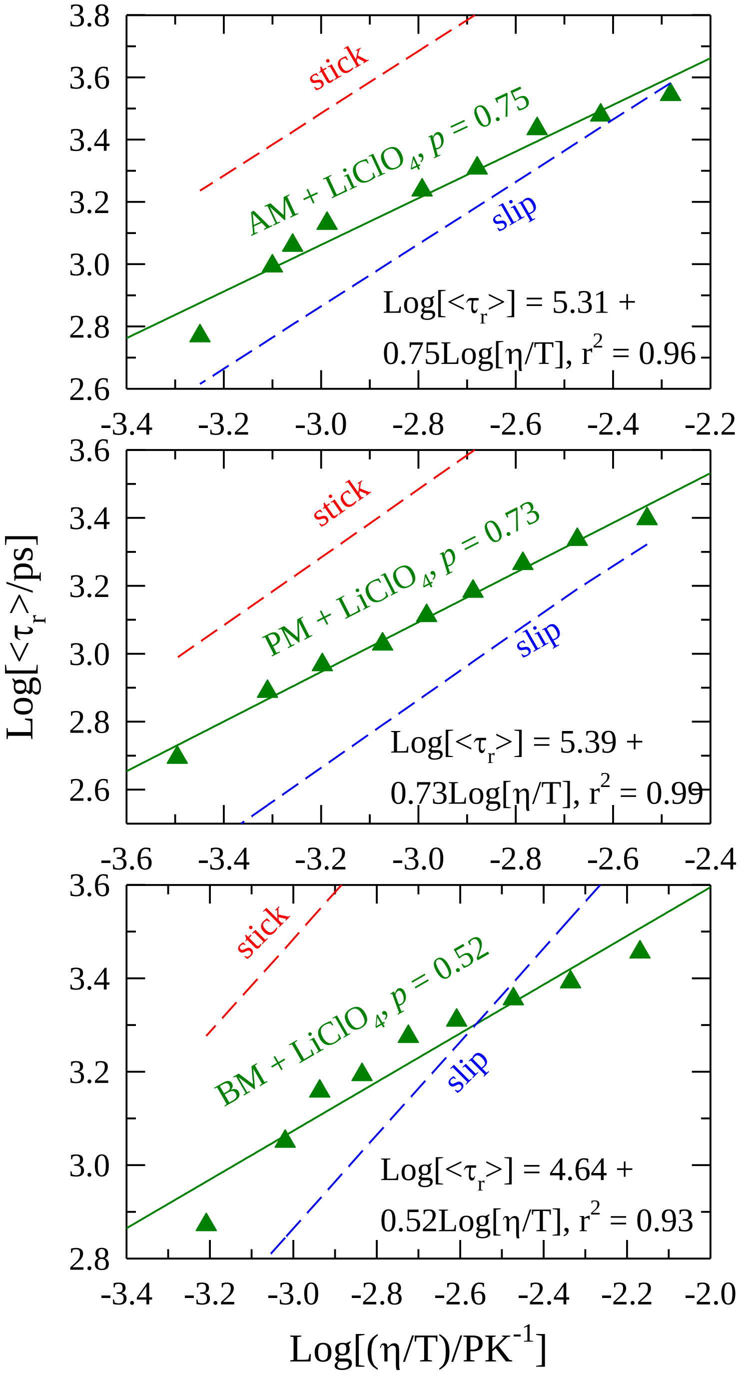

Fig. 5.8: Log-Log plot of average rotation time, $<\tau_r>$ of C153 versus η/T in {alkylamide + LiClO$_4$} deep eutectic mixtures. The solid lines show the best fits of the experimentally measured data to the relation $Log[<\tau_r>] = B + pLog[\eta/T]$, the associated B and *p* values are given in the figure. The dashed lines show the prediction of hydrodynamic stick and slip limits. Different panels denote data at different alkyl chain lengths.

translation-rotation (T-R) decoupling often observed in deeply supercooled liquids. This has been noticed earlier also with DES containing acetamide and other ions,[34,35] the significance being that this T-R decoupling in DES occurs at a temperature much above the T_g as opposed to supercooled liquids where such a decoupling takes place near (~20% above) the T_g . Note this kind of behaviour for the stretching exponent (β being larger for solute rotation than solute solvation) has also been detected in experiments with RTILs.[36]

5.4 Conclusion

The main result of this chapter is that ClO_4^- anion manifests its structure breaking ability via inducing less pronounced λ_{exc} dependence of steady state emission and fractional viscosity dependence of average solvation and rotation times of a dissolved probe in (CH_3CONH_2 + $LiClO_4$) DES in comparison to those observed in DES containing the same amide but non-perchlorate anions. In addition, the static heterogeneity recognizes the anion identity which may be linked to the structural complexity of the anions considered. The extent of heterogeneity increases with increase in alkyl chain length attached to the amide. However, the degree of the spatial heterogeneity reflected via λ_{exc} dependence depends critically on the excited state lifetime of a used probe. The finding that λ_{exc} dependence is stronger for a probe with comparatively shorter lifetime strongly suggests a distribution for the stability time of the fluctuating domains which is skewed toward shorter time (< 1 ns) with a tail reaching out to the more stable domains. Even with these static heterogeneity signatures, none of the DES considered forces stretched exponential relaxation of solute's rotation or solvation energy which is somewhat different from the observations in case of RTILs. This dissimilarity is further carried over into the solute-solvent coupling where, in contrast to RTILs, a strong fractional viscosity dependence for average solvation and rotation times has been observed for these DES. Further analyses of the observed viscosity dependence of solute-based dynamical quantities reveal a sort of translation-rotation decoupling reminiscent of what is normally encountered in deeply supercooled liquids. The most interesting point of this decoupling aspect (and probably ill-understood at this moment) is that this occurs for DES at a temperature ~100-150 K above the glass transition temperature. Further studies involving all-atom molecular dynamics simulations and relaxation measurements using more sophisticated techniques as well as scattering experiments with atomic resolutions are therefore required to generate a thorough understanding of the fluorescence results obtained for these and other deep eutectic solvents containing ions. Apart from the intellectual stimulations that the proposed study would generate, comprehensive knowledge derived from such a study will be immensely useful for better and intelligent applications of the material aspects of these DES in technology sector and chemical industry.

References:

1. Welton, T. *Chem. Rev*. **1999**, *99*, 2071-2083.
2. Wasserscheid, P.; Keim, W. *Angew. Chem. Int. Ed.* **2000**, *39*, 3772-3789.
3. Noyori, R. (Ed.) *Chem. Rev.* **1999**, *99*, 353-354.
4. Lewis, J. E.; Biswas, R.; Robinson, A. G.; Maroncelli, M. *J. Phys. Chem. B* **2001**, *105*, 3306-3318.
5. Hallett, J. P.; Kitchens, C. L.; Hernandez, R.; Liotta, C. L.; Eckert, C. A. *Acc. Chem. Res.* **2006**, *39*, 531-538.
6. Eckert, C. A.; Liotta, C. L.; Bush, D.; Brown, J. S.; Hallett, J. P. *J. Phys. Chem. B* **2004**, *108*, 18108-18118.
7. Amico, A.; Berchiesi, G.; Cametti, C.; Biasio, A. D. *J. Chem. Soc. Faraday Trans*. 2 **1987**, *83*, 619-626.
8. Berchiesi, G. *J. Mol. Liq.* **1999**, *83*, 271-282.
9. Abbott, A. P.; Boothby, D.; Capper, G.; Davies, D. L.; Rasheed, R. K. *J. Am. Chem. Soc.* **2004**, *126*, 9142-9147.
10. Abbott, A. P.; Capper, G.; Davies, D. L.; Rasheed, R. K.; Tambyrajah, V. *Chem. Commun.* **2003,** 70-71.
11. Abbott, A. P.; Capper, G.; Davies, D. L.; Munro, H. L.; Rasheed, R. K.; Tambyrajah, V. *Chem. Commun.* **2001,** 2010-2011.
12. Abbott, A. P.; Capper, G.; Davies, D. L.; Rasheed, R. K. *Inorg. Chem.* **2004**, *43*, 3447-3452.
13. Abbott, A. P.; Capper, G.; Davies, D. L.; Rasheed, R. K. *Chem. Eur. J.* **2004**, *10*, 3769-3774.
14. Jin, H.; O'Hare, B.; Arzhantsev, S.; Baker, G.; Wishart, J. F.; Binesi, A. J.; Maroncelli, M. *J. Phys. Chem. B* **2008**, *112*, 81-92.
15. Bhargava, B. L.; Balasubramanian, S. *J. Phys. Chem. B* **2007**, *111*, 4477-4487.
16. Kashyap, H. K.; Biswas, R. *J. Phys. Chem. B* **2008**, *112*, 12431-12438.
17. Kashyap, H. K.; Biswas, R. *J. Phys. Chem. B* **2010**, *114*, 254-268.
18. Kashyap, H. K.; Biswas, R. *J. Phys. Chem. B* **2010**, *114*, 16811-16823.

19. Daschakraborty, S.; Biswas, R. *J. Chem. Phys.* **2012,** *137*, 114501(1)-114501(11).
20. Zwan, van der G.; Hynes, J. T. *Chem. Phys.* **1991**, *152*, 169-183.
21. Pradhan, T.; Biswas, R. *J. Phys. Chem. A* **2007,** *111*, 11524-11530.
22. Mitchell, J. A.; Reid, E. E. *J. Am. Chem. Soc.* **1931**, *53*, 1879-1883.
23. Lide, D. R. (Ed.) *CRC Handbook of Chemistry and Physics*, 81st edition, CRC Press, Taylor & Francis, 2007, Boca Raton, FL.
24. Gusteri, M.; Bartocci, V.; Castellani, F.; Pucciarelli, F. *J. Electroanal. Chem.* **1979**, *102*, 199-203.
25. Castellani, F.; Berchiesi, G.; Pucciarelli, F.; Bartocci, V. *J. Chem. Eng. Data* **1981**, *26*, 150-152.
26. Berchiesi, G.; Angelis, M. D.; Rafaiani, G.; Vitali, G. *J. Mol. Liq.* **1992**, *51*, 11-38.
27. Ediger, M. D. *Annu. Rev. Phys. Chem.* **2000**, *51*, 99-128.
28. Ediger, M. D.; Angell, C. A.; Nagel, S. R. *J. Phys. Chem.* **1996**, *100*, 13200-13212.
29. Sillescu, H. *J. Non-Cryst Solids* **1999**, *243*, 81-108.
30. Chakrabarti, D.; Bagchi, B. *Phys. Rev. Lett.* **2006**, *96*, 187801(1)-187801(4).
31. Moynihan, C. T. *J. Phys. Chem.* **1966**, *70*, 3399-3403.
32. Angell, C. A. *J. Chem. Phys.* **1967,** *46*, 4673-4679.
33. Dahl, K.; Biswas, R.; Ito, N.; Maroncelli, M. *J. Phys. Chem. B* **2005**, *109*, 1563-1585.
34. Guchhait, B.; Gazi, H. A. R.; Kashyap, H. K.; Biswas, R. *J. Phys. Chem. B* **2010**, *114*, 5066-5081.
35. Guchhait, B.; Daschakraborty, S.; Biswas, R. *J. Chem. Phys.* **2012,** *136*, 174503(1)-174503(16).
36. Jin, H.; Baker, G. A.; Arzhantsev, S.; Dong, J.; Maroncelli, M. *J. Phys. Chem. B* **2007**, *111*, 7291-7302.
37. Ito, N.; Arzhantsev, S.; Heitz, M.; Maroncelli, M. *J. Phys. Chem. B* **2004**, *108*, 5771-5777.
38. Samanta A. *J. Phys. Chem. B* **2006**, *110*, 13704-13716.
39. Triolo, A.; Russina, O.; Bleif, H.; Cola, E. D. *J. Phys. Chem. B* **2007**, *111*, 4641-4644.
40. Triolo, A.; Russina, O.; Fazio, B.; Triolo, R; Cola, E. D. *Chem. Phys. Lett.* **2008**, *457*, 362-365.

41. Triolo, A.; Russina, O.; Fazio, B.; Appetecchi, G. B. Carewska, M.; Passerini, S. *J. Chem. Phys.* **2009,** *130*, 164521(1)-164521(6).
42. Mandal, P. K.; Sarkar, M.; Samanta, A. *J. Phys. Chem. A* **2004**, *108*, 9048-9053.
43. Sasmal, D. K.; Mandal, A. K.; Mondal, T.; Bhattacharyya, K. *J. Phys. Chem. B* **2011**, *115*, 7781-7787.
44. Jin, H.; Li, X.; Maroncelli, M. *J. Phys. Chem. B* **2007**, *111*, 13473-13478.
45. Adhikari, A.; Sahu, A. K.; Dey, S.; Ghosh, S.; Mandal, U.; Bhattacharyya, K. *J. Phys. Chem. B* **2007**, *111*, 12809-12816.
46. Wang, Y.; Voth, G. A. *J. Am. Chem. Soc.* **2005**, *127*, 12192-12193.
47. Sarangi, S. S.; Zhao, W.; Muller-Plathe, F.; Balasubramanian, S. *Chem. Phys. Chem.* **2010**, *11*, 2001-2010.
48. Hu, Z.; Margulis, C. J. *Proc. Natl. Acad. Sci.* USA **2006**, *103*, 831-836.
49. Habasaki, J.; Ngai, K. L. *J. Chem. Phys.* **2008**, *129*, 194501(1)-194501(14).
50. Pal, T.; Biswas, R. *Theo. Chem. Acct.* **2012** (in press).
51. Walrafen, G. E. *J. Chem. Phys.* **1970**, *52*, 4176-4198.
52. Bondarenko, G. V.; Gorbaty, Y. E. *Mol. Phys.* **2011**, *109*, 783-788.
53. Chandrasekhar, J.; Jorgensen, W. L. *J. Chem. Phys.* **1982**, *77*, 5080.
54. Obst, S.; Bradaczek, H. *J. Phys. Chem.* **1996**, *100*, 15677.
55. Tongraar, A.; Liedl, K. R.; Rode, B. M. *J. Phys. Chem. A* **1998**, *102*, 10340.
56. Chandrasekhar, J.; Spellmeier, D. C.; Jorgensen, W. L. *J. Am. Chem. Soc.* **1984**, *106*, 903.
57. Zhu, S.-B. Robinson, G. W. *J. Chem. Phys.* **1992**, *97*, 4336.
58. White, J. A.; Schwegler, E.; Galli, G.; Gygi, F. *J. Chem. Phys.* **2000**, *113*, 4668.
59. Lightstone, F. C.; Schwegler, E.; Hood, R. Q.; Gygi, F.; Galli, G. *Chem. Phys. Lett.* **2001**, *343*, 549.
60. Omta, A. W.; Kropman, M. F.; Woutersen, S.; Bakker, H. J. *Science,* **2003**, *301*, 347-349.
61. Gazi, H. A. R.; Guchhait, B.; Daschakraborty, S.; Biswas, R. *Chem. Phys. Lett.* **2011**, *501*, 358-363.
62. Pal, T.; Biswas, R. *Chem. Phys. Lett.* **2011**, *517*, 180-183.
63. Lobbia, G. G.; Berchiesi, G. *Thermochimica Acta* **1984**, *74*, 251-254.

64. Mahiuddin, S. *J. Chem. Eng. Data* **1996**, *41*, 231-234.
65. Jin, H.; O'Hare, B.; Dong, J.; Arzhantsev, S.; Baker, G. A.; Wishart, J. F.; Benesi, A. J.; Maroncelli, M. *J. Phys. Chem. B* **2008**, *112*, 81-92.
66. Jung, Y. J.; Garrahan, J. P.; Chandler, D. *Phys. Rev. E* **2004**, *69*, 061205(1)-061205(7).
67. Garrahan, J. P.; Chandler, D. *Phys. Rev. Lett.* **2002**, *89*, 035704(1)-035704(4).
68. Zhang, X.-X.; Liang, M.; Ernsting N. P.; Maroncelli, M. *J. Phys. Chem. B* **2012** (in press); doi: jp305430a.
69. Horng, M.-L.; Gardecki, J. A.; Papazyan, A.; Maroncelli, M. *J. Phys. Chem.* **1995**, *99*, 17311-17337.
70. Horng, M.-L.; Gardecki, J. A.; Papazyan, A.; Maroncelli, M. *J. Phys. Chem. A* **1997**, *101*, 1030-1047.
71. Biswas, R.; Das, A. R.; Pradhan, T.; Touraud, D.; Kunz, W.; Mahiuddin, S. *J. Phys. Chem. B* **2008**, *112*, 6620-6628.
72. Sarma, N.; Borah, J. M.; Mahiuddin, S.; Gazi, H. A. R.; Guchhait, B.; Biswas, R. *J. Phys. Chem. B* **2011**, *115*, 9040-9049.
73. Biswas, R; Lewis, J. E.; Maroncelli, M. *Chem. Phys. Lett.* **1999**, *310*, 485-494.
74. Hunger, J.; Stoppa, A.; Schrodle, S.; Hefter, G.; Buchner, R. *Chem. Phys. Chem.* **2009**, *10*, 723.
75. Pradhan, T.; Ghoshal, P.; Biswas, R. *J. Phys. Chem. A* **2008**, *112*, 915-924.
76. Gazi, H. A. R.; Biswas, R. *J. Phys. Chem. A* **2011**, *115*, 2447-2455.
77. Pradhan, T.; Ghoshal, P.; Biswas, R. *J. Chem. Sci.* **2008**, *120*, 275-287.
78. Sun, Z.; Jin, L.; Shi, W.; W. M.; Evans, D. G.; Duan, X. *Langmuir*, **2011**, *27*, 7113-7120.
79. Ito, N.; Arzhantsev, S.; Maroncelli, M. *Chem. Phys. Lett.* **2004**, *396*, 83-91.
80. Bianchi, A.; Bowman-James, K.; Garcia-Espana, E. (Ed.) In *Supramolecular Chemistry of Anions*, pp. 1-44, Wiley-VCH, NY **1997**.
81. Peruzzi, N.; Ninham, B. W.; Nostro, P. L.; Baglioni, P. *J. Phys. Chem. B* **2012** (in press); doi: jp309157x.
82. Gloe, K.; Stephan, H.; Grotjahn, M. *Chem. Eng. Technol.* **2003**, *26*, 1107-1117.
83. Maroncelli, M. *J. Mol. Liq.* **1993**, *57*, 1-37.

84. Richert, R.; Wagener, A. *J. Phys. Chem.* **1991**, *95*, 10115-10123.
85. Guchhait, B.; Biswas, R.; Ghorai, P. "Solute and Solvent Dynamics in Confined Equal-Sized Aqueous Environments of Charged and Neutral Reverse Micelles: A Combined Dynamic Fluorescence and All-Atom Molecular Dynamics Simulation Study" *J. Phys. Chem. B* **2012** (submitted).
86. Carter, E. A.; Hynes, J. T. *J. Chem. Phys.* **1991**, *94*, 5961-5979.
87. Maroncelli, M. *J. Chem. Phys.* **1991**, *94*, 2084-2103.
88. Fee, R. S.; Maroncelli, M. *Chem. Phys.* **1994**, *183*, 235.
89. Hunger, J.; Stoppa, A.; Schrodle S.; Hefter, G.; Buchner, R. *Chem. Phys. Chem.* **2009**, *10*, 723.
90. Chang, Y. J.; Castner, E. W. Jr. *J. Phys. Chem.* **1994**, *98*, 9712.
91. Shirota, H.; Castner, E. W. Jr. *J. Am. Chem. Soc.* **2001**, *123*, 12877.
92. Biswas, R.; Bagchi, B. *J. Phys. Chem.* **1996**, *100*, 1238.
93. Kashyap, H. K.; Pradhan, T.; Biswas, R. *J. Chem. Phys.* **2006**, *125*, 174506(1) –(10).
94. Bagchi, B.; Biswas, R. *Adv. Chem. Phys.* **1999**, *109*, 207-433.
95. Roy. S.; Bagchi, B. *J. Chem. Phys.* **1993**, *99*, 9938.
96. Nandi, N.; Roy. S.; Bagchi, B. *J. Chem. Phys.* **1995**, *102*, 1390.
97. Bart, E.; Meltsin, A.; Huppert, D. *J. Phys. Chem. B* **1994**, *98*, 3295.
98. Bart, E.; Meltsin, A.; Huppert, D. *J. Phys. Chem. B* **1994**, *98*, 10819.
99. Daschakraborty, S.; Biswas, R. *J. Chem. Sci.* **2012,** *124*, 763-771.
100. Harris, K. R. *J. Chem. Phys.* **2009**, *131*, 054503.
101. Huang, W.; Richert, R. *Philos. Mag.* **2007**, *87*, 371.
102. Cicerone, M. T.; Blackburn, F. R.; Ediger, M. D. *J. Chem. Phys.* **1995**, *102*, 471.

Chapter 6

Solute and Solvent Dynamics in Confined Equal-Sized Aqueous Environments of Charged and Neutral Reverse Micelles

6.1 Introduction

Understanding confined or interfacial water is fundamentally important because confined aqueous environments share commonalities with water molecules near biologically active surfaces[1-11] and those trapped in various mineral samples.[12-16] Apart from this relevance to biology and geology, confined aqueous environment is also chemically very appealing as microscopic encapsulation affects both the polarity and dynamics of bulk water.[7-10,17-20] Such encapsulation can be accessed via formation of aqueous reverse micelles (RMs) through the aggregation of surfactant molecules in a non-polar solvent in presence of water.[21] The size of aqueous RMs can be regulated by changing the concentrations of surfactant and water in the aqueous ternary mixture. Given the roles played by the medium polarity and dynamics for a solution phase chemical reaction,[22-24] a rather easy control on the size of such encapsulations offers a tunability of medium effects on a chemical reaction without changing the identity of medium particles. Possibility of these encapsulated environments for application as nano-reactors and the basic scientific aspects of how confined water differs from bulk have driven much of the research in this area. Extensive fluorescence,[25-46] infra-red[47-62] and computer simulation[63-73] studies have been carried out to bring out the key features of confined water in reverse micelles. Dissimilarities have been observed, as confined aqueous environments exhibit frustrated hydrogen bond (H-bond) network[64,74,75] and slowed down dynamics relative to those in bulk.

The most extensively studied RMs are those made of sodium bis(2-ethylhexyl) sulfosuccinate, a double-alkyl chain containing surfactant with a negatively charged head group and known as AOT, and water with either isooctane or heptane as dispersion medium. See Appendix for the chemical structure of AOT. The aqueous AOT RMs are known to remain spherical for a large range of water-to-surfactant concentration ratios,

$w_0 = [\text{water}]/[\text{surfactant}]$.[76,77] For $w_0 = 2 - 20$, the diameter of the AOT confined aqueous pool follows the relation,[76] $d_{\text{AOT}}(\text{nm}) = 0.29w_0 + 1.1$ and thus provides an easy route to alter the aqueous pool size. Computer simulation studies[68-72] have indicated presence of at least two types of water molecules, bound and free,[78,79] in the aqueous pool of AOT RMs. This core-shell structure of the encapsulated aqueous environment has subsequently been re-examined in ultrafast infrared (IR) spectroscopic measurements[49] and simulations.[64] In the limit of large RMs, while those water molecules forming the core have been found to behave more like bulk, the interfacial (shell) water molecules show significantly slowed down dynamics. Interaction of water molecules with the AOT head groups (creating the interface) renders a frustration in the H-bond arrangements in the immediate neighbourhood that propagates through the aqueous layers and also leads to both faster and slower than bulk dynamics.[75] Depending on pool size, the extent of slowing down (for the interfacial water molecules) in IR measurements has been found to be ~2-20.[49] Qualitatively similar results have also been observed in the ultrafast IR measurements with aqueous RMs made of non-ionic surfactant Igepal CO-520 (IGPAL, see Appendix)[50,55] that follows the size-concentration relationship,[80] $d_{\text{IGPAL}}(\text{nm}) = 0.38w_0 + 1.4$, suggesting a domination of the confinement effects over the chemical nature (charged or uncharged) of the surfactant head groups in slowing down the dynamics of the interfacial water molecules. Interestingly, this extent of slowing down is much smaller than that (two to three orders of magnitude) reported via dynamic Stokes shift measurements.[32-34,38-46] Note in the above IR experiments the hydroxyl stretch of the confined water molecules plays the role of an internal ‘probe’ whereas the dynamic Stokes shift measurements have been carried out by following the fluorescence of an externally added solute molecule at extremely low concentration.

The difference between the dynamic Stokes shift and ultrafast IR results in assessing the slowing down of the water dynamics confined in these types of RMs constitutes one of the main foci of the present work with a particular emphasis on the solute location inside these RMs. In addition, the following questions have also been investigated: (i) does a change in the chemical nature of the surfactant head group modifies the solute location inside the confined pool and, if so, how the fluorescence dynamics is affected?, (ii) does photo-excitation drive the dissolved solute to a more polar region inside the aqueous pool and what role the charged interface play to influence such internal solute migration?, (iii) Does the excited solute move during fluorescence measurements and what are the implications of such solute motions on the rate of solvation energy relaxation and width of the time-resolved spectrum? (iv) how does the mobility of water molecules in different layers change as a function of pool size?, (v) is there any distance (from the interface) beyond which the effects of charged interface are completely screened?, and (vi) does the polyethylene oxide (-CH_2-CH_2-O-) and –OH groups in IGPAL interact with the solute and influence the relaxation dynamics studied?

In order to address the above questions, we have followed rotational and solvation energy relaxations of a dipolar solute trapped in the aqueous environment at different pool sizes of AOT and IGPAL RMs via both time-resolved fluorescence experiments and computer simulations. In experiments, RMs with pool sizes of equal diameters have been prepared from the known formulae[76,80] for AOT and IGPAL surfactants and a dipolar solute, coumarin 153 (C153),[81] has been used as a fluorescent probe. These experiments have been performed to serve mainly the following two purposes. First, these measurements allows for the first time a uniform comparison of fluorescence dynamics in equal-sized aqueous environments between charged and neutral RMs for both small and large pool diameters. This helps understanding the relative effects of confinement and surfactant charge on a solute's solvation energy and rotational relaxations. Note that the difficulty in analyzing the ultrafast IR spectroscopic data for smaller sized IGPAL RMs does not create a constraint for the fluorescence measurements, and, as a result, a comparison of fluorescence dynamics between AOT and IGPAL RMs for both small and large aqueous pools can be made. However, a possible distortion from spherical shape for small IGPAL RMs[82] should be kept in mind while making this comparison. Second, as we are doing molecular dynamics simulations with realistic charge distribution for C153, a direct comparison between simulations and experiments can be performed to check the fidelity of the simulation results as well as to provide microscopic explanations to the experimental data. However, we would like to state that in our simulation studies neither we are looking at the H-bond dynamics and structure of the confined water molecules nor we offer any explanations for our experimental results in terms of them. Instead, our approach here is solute-centric and we focus on the possible impact of solute location (relative to the interface) on the observed fluorescence dynamics. It is to be mentioned here that although simulation studies of solvation dynamics of model charged solutes in aqueous AOT RMs have been performed earlier,[66,69] such a study using a neutral dipolar solute with realistic charge distributions has never been done before. Moreover, those earlier simulation studies have investigated only the short time (~ 5 ps) dynamics leaving out the slower part occurring at later times. In contrast, here we extend our simulations up to a few nanoseconds so that both the fast and slow dynamics are captured and compared (at least qualitatively) with experiments. Centre-of-mass and orientational motions of confined water molecules at different layers have also been traced in the present simulations and the relative influences of confinement and surface charge on dynamics discussed.

The main results of the present chapter are as follows. For both these types of RMs with C153 in aqueous pools of diameters ~2-7 nm, the observed and estimated shifts[83] increase with pool diameter and ranges respectively between ~1000-2000 cm^{-1}, and ~2300-3000 cm^{-1}. Measured solvation response functions are bi-exponential with one time constant varying between ~30-60 ps and the other between 300-700 ps, and average solvation rate increases with pool diameter. However, the average rate of solvation energy relaxation in the charged (AOT) RMs is faster at all sizes than that for the neutral (IGPAL) RMs. This is counter-intuitive on the grounds of chemical nature of these surfactants. Time-resolved fluorescence anisotropy decays for the encapsulated solute in these RMs are also bi-exponential, and fast and slow time constants lie in the ranges of ~15-30 ps and ~700-1300 ps, respectively. However, the average anisotropy decay rate decreases with pool diameter for the neutral RMs which is opposite to the trend observed for the charged RMs. This has led to an anti-correlation between the pool size dependent average solvation and rotation rates in the neutral RMs. As will be shown later while presenting simulation results, the close proximity of the solute to the interface may be attributed to this "unexpected" trend in the observed fluorescence results. Simulated solvation response functions, as found in experiments, are bi-exponential for both charged and neutral RMs at all pool sizes where a bulk-like ultrafast component with time constant ≤ 100 fs characterizes the decays. The simulated long time constants are in semi-quantitative agreement with the experimental slower ones, leading to a good comparison between simulated and experimental results. As found in experiments, simulated anisotropy decays are also bi-exponential for both types of RMs at three representative sizes and capture the experimental trend qualitatively. Simulations suggest that the solute always resides away from the centre of the pool and in the first two water layers near the interface, irrespective of the chemical nature of the surfactant molecules and size of the aqueous pool. Increase in water mobilities in larger pool sizes accounts for the observed enhancement of the relaxation rates at higher water loadings. Interestingly, simulated results suggest photo-excitation does not drive the solute to relocate near the centre of the aqueous pool in either of the RMs because of longer ranged interactions of the excited solute with the charged interface (for AOT RMs), and with the polyethylene oxide and hydroxyl groups of neutral interface (for IGPAL RMs). The organization of the rest of the chapter is as follows. Experimental and Simulation details are given in the next section. Section 6.3 contains results and discussion. The chapter then ends with concluding remarks in Sec. 6.4.

6. 2 Experimental and Simulation Details

Laser grade Coumarin-153 was used as received (Exciton). Surfactants (AOT and IGPAL), isooctane, n-hexane, and cyclohexane were purchased from Sigma-Aldrich and used without further purification. AOT was vacuum dried before use. Deionised (milipore) water was used for preparing the aqueous reverse micelles.

0.5 M AOT in isooctane and 0.3 M IGEPAL in 50/50 weight % of cyclohexane/n-hexane stock solution were prepared. Confined aqueous pool of required diameters were obtained by adding the requisite amount of deionised water into the (surfactant + nonpolar solvent) solutions. 5 μl from the stock solution of C153 (concentration ~10^{-5} M) in heptane was transferred in an optically transparent and dried quartz cuvette (inner volume ~3.5 ml with 1 cm optical path-length) and the carrier nonpolar solvent was removed by gently blowing hot air around it. Subsequently, RM solution was added into the cuvette, allowed to equilibrate for an hour with occasional gentle stirring. The cuvette containing sample was then inserted into the already temperature-equilibrated sample chamber of a spectrophotometer and waited for temperature equilibration before data recording. This procedure was followed for each independent measurement.

Steady state and time resolved spectral data measurement techniques and the corresponding analysis procedures are essentially the same as described in chapter 2 and in refs.[83-92] Steady state absorption and emission spectra were collected by a UV-visible spectrophotometer (UV-2450, Shimadzu) and a fluorimeter (Fluoromax-3, Jobin-Yvon, Horiba), respectively. Solvent blanks were subtracted before further processing of the steady state spectra. Time resolved emission decays were measured using a time-correlated single photon counting instrument. 409 nm dye laser was used as excitation source. The full-width at half maximum (FWHM) of the instrument response function (IRF) with this excitation source was ~ 70 ps. Decay collection at each of these wavelengths was continued till the peak-count was reached ~5000 (dark count ~10). For solvation dynamics measurement 18-20 decays at wavelengths spanning emission spectrum were collected at magic angle. The collected decays were deconvoluted from the IRF and fitted to multi-exponential function using an iterative reconvolution algorithm.[83,85,87] Time resolved emission spectra (TRES) were then reconstructed from the decay fit parameters in conjunction with normalized intensities of the steady state emission spectrum as described in refs.[86-91] For the purpose of rotational dynamics measurement a set of three decays, namely, parallel, perpendicular and magic angle polarizations were collected. Time resolved fluorescence anisotropies, $r(t)$, were then calculated from the collected decays by using the method[84,92] described in chapter 2.

We followed the reduced model for RM simulations developed earlier[68-70] for the present simulations where we approximated the interior of an aqueous RM as a rigid spherical cavity. The hydrogen atoms were treated implicitly by considering the united atom model for CH_3 and CH_2 groups for the surfactant molecules. However, for IGPAL we treated hydrogen atoms explicitly for the groups (polyethylene oxide and hydroxyl groups) which are inside the water pool. Interaction between different RMs was neglected and periodic boundary condition was not considered. The interaction potentials between different interaction sites of the system were handled in the standard manner as a sum of Lennard-Jones (LJ) and point charge interactions.[93] Subsequently, the cavity was filled with SPC/E water[94]. The Dreiding force field for the LJ interaction potentials of the surfactant was used.[95] The LJ interactions between the sites of different types were determined from the usual Lorentz-Berthelot combination rules.[96] Electrostatic interactions were treated via direct coulomb summation technique.[97] The existence of the nonpolar solvent (dispersion medium) outside the RM was neglected completely. Solute's charge distribution in the ground (S_0) and excited (S_1) states have been taken from the works reported earlier.[98] The dipole moments corresponding to these charge distributions are 6.24 D and 13.59 D respectively for the S_0 and S_1 states of the solute, which are quite close to the experimental data.[81] For simulations with a solute inside confined environments, the solute (in S_0 or S_1 states) was first placed at the centre of the aqueous pool and then allowed to locate itself via equilibration.

We computed the dynamical properties for three different sized RMs of both types (charged and neutral) with water pool diameters 1.8, 5.0 and 6.5 nm. We constructed the AOT reverse micelle by implementing the procedure followed elsewhere.[99] The total number of AOT surfactant molecules considered for these three different RMs were 48, 190 and 284, respectively and the corresponding number of water molecules were 140, 2060 and 4590. To construct the IGPAL RM, we used less number of surfactant molecules (34, 130 and 194) because in experiments IGPAL concentration was less than that of AOT. We also unfolded the alkyl chain as RMs grew bigger. For example, the alkyl chain length was 2.85 A inside the water pool for RM with aqueous pool diameter of 1.8 nm whereas for RMs with aqueous pools of 5.0 and 6.5 nm diameters the intruding alkyl chain lengths were 5.6 and 8.12 A, respectively.

Integration of the molecular dynamic trajectories was performed using the velocity-Verlet algorithm.[96] The time step was 2 fs throughout the simulations. The temperature was controlled by the Nose-Hoover thermostat[100,101] with a time constant 0.5 ps. All the simulations were performed at 300 K. The cut-off radius for the short range interaction was 15 A. The equilibration was done for a time period of 5 ns and production run was for another 20 ns. We used DL_POLY molecular simulation package[102] and employed NVT ensemble for all the simulations described here.

6.3 Results and Discussion

6.3.1 Steady state spectral characteristics: comparison between charged and neutral RMs

Fig. 6.1 compares the steady state absorption and emission spectra of C153 in aqueous AOT RMs (upper panel) to those in IGPAL (lower panel) RMs at four different pool diameters. Absorption and emission spectra of C153 in hexane (static dielectric constant $\varepsilon_0 \approx 2$)[103] and acetonitrile ($\varepsilon_0 \approx 36$) are also shown in the upper panel. These bulk solvent spectra serve as 'reference spectra' because the dispersion medium is a nonpolar solvent (or a mixture of nonpolar solvents) and the estimated ε_0 (via spectral shift)[17] of the AOT

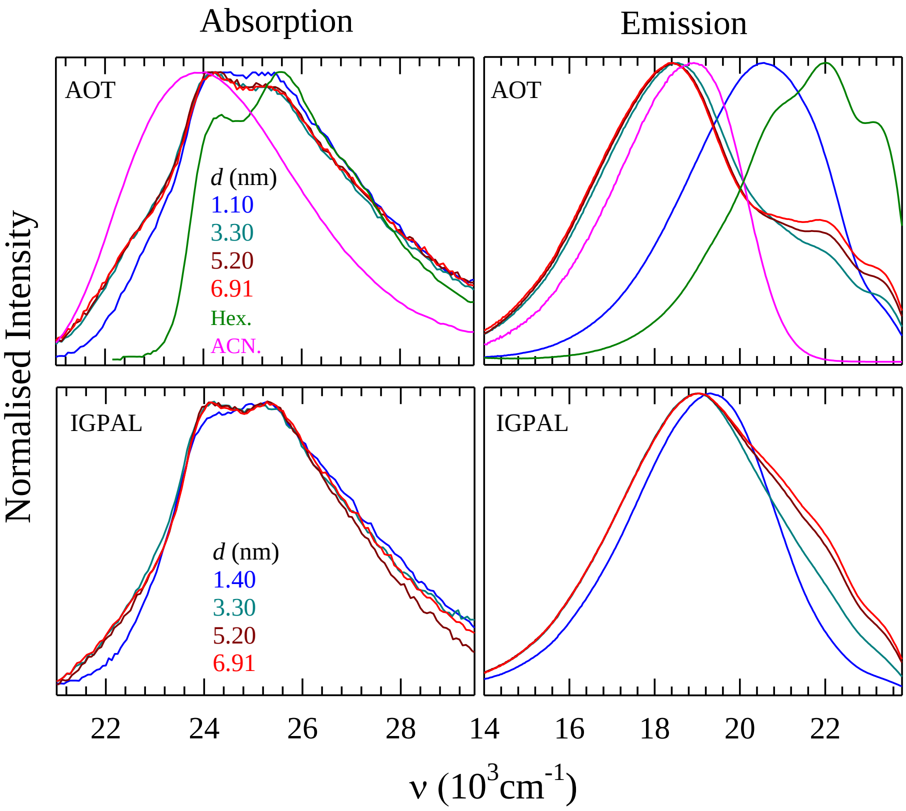

Fig. 6.1: Representative absorption (left panels) and emission (right panels) spectra of C153 in at different pool sizes of aqueous AOT and IGPAL RMs. The spectra of the same solute in hexane and acetonitrile are also shown in upper panels for comparison. Note the spectra are color-coded.

aqueous pool with diameter ~7 nm has been found to be similar to that of methanol or acetonitrile. It is evident from this figure that the emission spectrum shows stronger pool size dependence than the absorption spectrum, the emission shift being larger for the charged (AOT) RMs than that for the neutral (IGPAL) ones. While the absorption profiles in these charged and neutral RMs lie in between the ranges covered by the absorption spectra of C153 in bulk acetonitrile and hexane, the RM spectra are somewhat more broadened than the spectra in bulk solvents.

The above spectral characteristics are more quantitatively shown in Fig. 6.2 as a function of pool diameter where the insensitivity to pool size and the chemical nature of the surfactant head groups of the absorption peak frequencies are clearly depicted. The absorption spectral widths (full-width-at-half-maximum, FWHM) do not show much

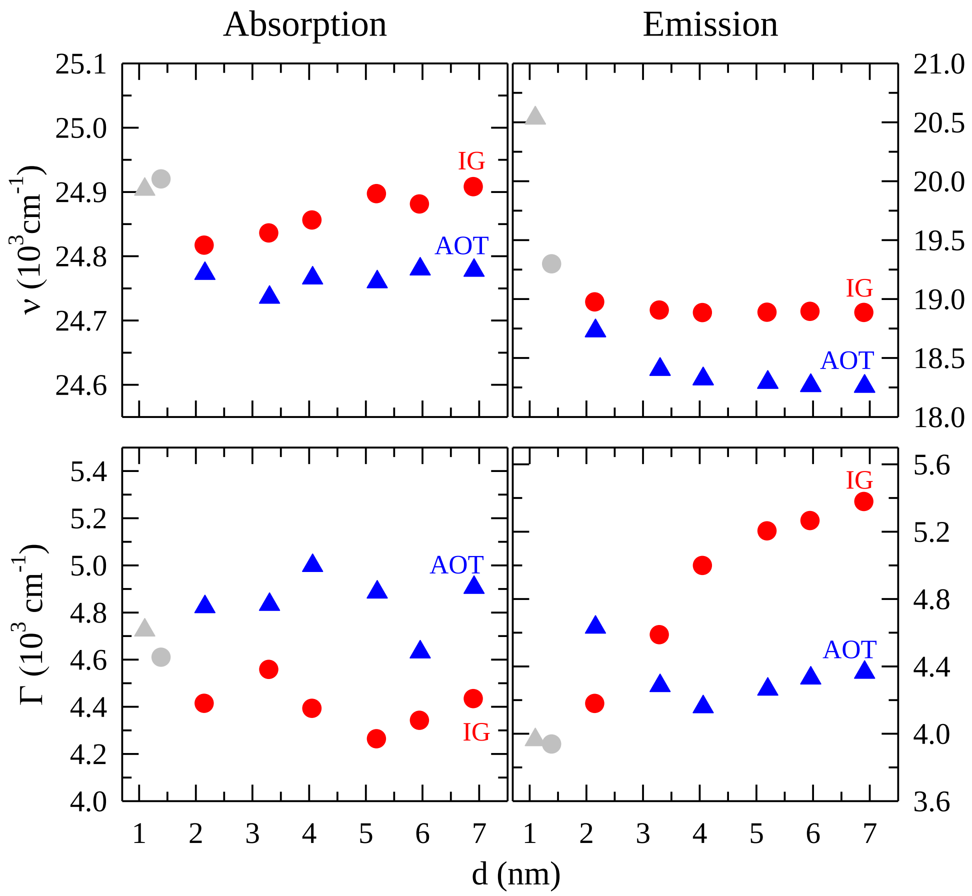

Fig. 6.2: Pool size dependence of absorption and emission spectral frequencies (upper panels) and bandwidths (lower panels) of C153 in charged (AOT) and neutral (IGPAL) reverse RMs. Pool size is represented by the diameter (d) of the confined aqueous environment. Gray symbols denote spectral characteristics for 'dry' (no addition of external water) RMs. Triangles denote data for AOT RMs and circles for IGPAL RMs.

variation but are larger than those in bulk acetonitrile (Γ_{abs}^{acn}= 4.25 x 10^3 cm^{-1}) and hexane (Γ_{abs}^{hex}= 3.92 x 10^3 cm^{-1}). The total emission spectral shift for AOT RMs in this pool size range (~1.25 -7 nm) is ~2200 cm^{-1} which is nearly 7 times larger than that for IGPAL RMs. This reflects a difference in excited solute-interface interaction between the charged and neutral interface. The corresponding spectral widths are not only larger than those in acetonitrile (Γ_{em}^{acn}= 3.49 x 10^3 cm^{-1}) and hexane (Γ_{em}^{hex}= 3.49 x 10^3 cm^{-1}) but also show a variation with pool size that seems to reflect the character of the surfactant head groups. For example, Γ_{em} increases by ~400 cm^{-1} for increasing the pool diameter from ~1.25 nm to 7 nm for the charged RMs but the increase is ~1500 cm^{-1} for neutral RMs in the same range. This indicates increased heterogeneity of the environment surrounding the solute inside the IGPAL RMs which may arise from the interaction of the solute with, in addition to water molecules, the intruding polyethylene oxide and hydroxyl groups. This is possible if the solute resides close to the interface. Note also that in both types of RMs with $d\,(\text{pool size}) \geq 4$ nm, the emission shift is limited to within ~200 cm^{-1} whereas the emission width exhibits much larger (~400-800 cm^{-1}) variation. This suggests that although the average polarity of the environment as reflected by spectral shift in large pools does not vary much (see Fig. A21, Appendix), the heterogeneity aspect is evident through Γ_{em} as the latter is also coupled to subtle variations of the interfacial structure due to the location of the excited solute.

Fig. 6.3 presents the simulation snapshots of solute location inside these RMs for the smallest and the largest aqueous pools where only one solute has been considered in the confined aqueous pool. The solute is in its ground state. Note both water hydrogens and surfactant tail groups are not shown explicitly in these pictures to avoid clutter. These snapshots indicate that the dipolar solute (C153) resides away from the centre of the pool, regardless of the pool size and the chemical nature of the surfactant head groups. The generality of this preference (solute location) is then explored through distance distribution, $P(r)$, for four different sizes of aqueous pools in these RMs. Here, the distance is from the centre of the pool and is measured by considering the closest approach of any solute atom to any atom of the surfactant head groups constituting the interface. Note solute's orientational degrees of freedom can alter the identity of this 'closest' atom

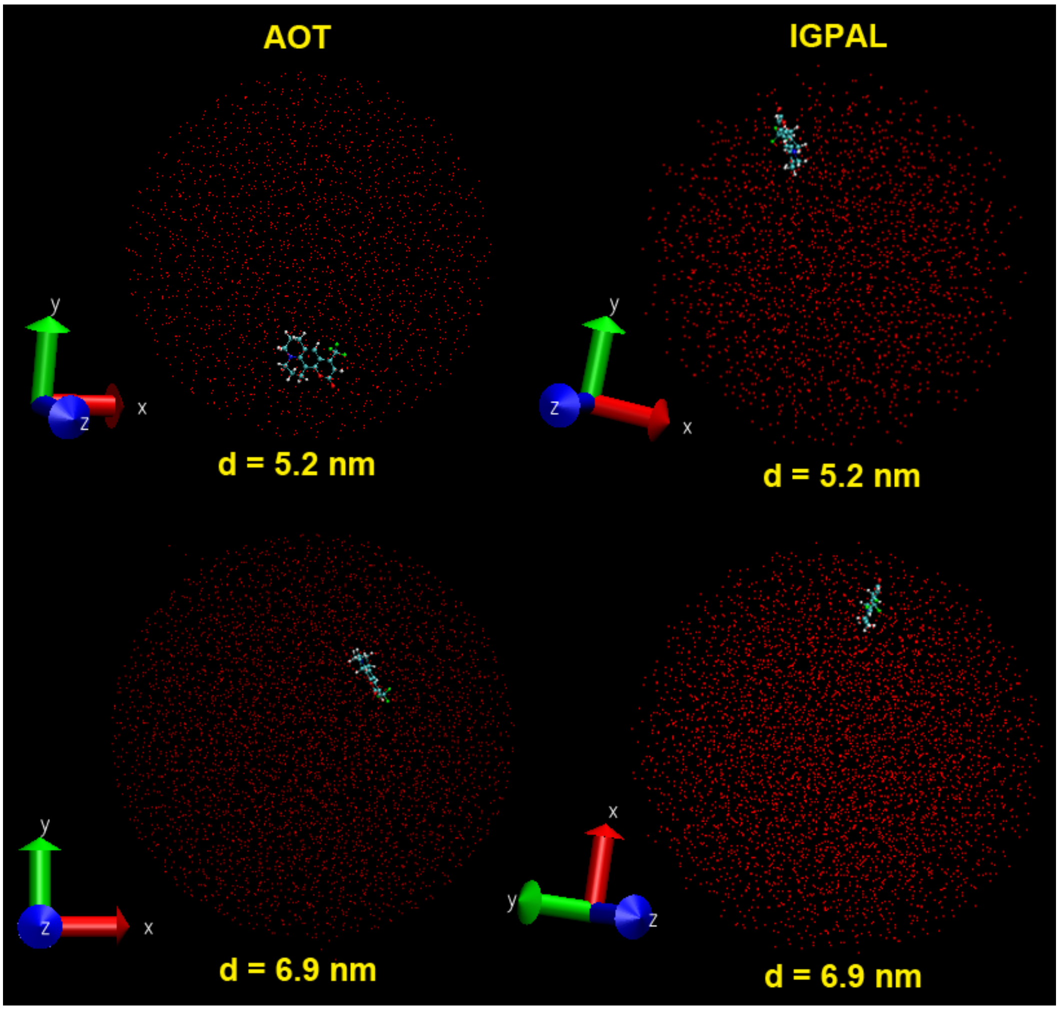

Fig. 6.3: Simulation snapshots of equilibrated solute location inside aqueous AOT (right panels) and IGPAL (left panels) RMs for two pool diameters, d (nm) = 5.2 and 6.9. For clarity, water molecules are represented by dots and surfactant boundaries are not explicitly shown.

(of the solute to the interface) while the centre-of-mass of the solute remaining unchanged over a period of time. This is orientational fluctuation of the solute location and will contribute to the width of $P(r)$, shown in Fig. A22 (Appendix). The fluctuation is larger for bigger pools because of decreased environmental rigidity in those cases. The average solute location is then determined from the formula, $\langle r_{loc}\rangle = \int_0^\infty drrP(r) \Big/ \int_0^\infty drP(r)$. The distance from the interface is then calculated as follows, $\Delta d = r_{pool} - \langle r_{loc}\rangle$, r_{pool} being the radius ($\equiv d_x/2$, x = AOT or IGPAL) of a given pool.

Fig. 6.4 depicts the simulated solute location in different RMs where Δd is shown as a function of r_{pool} for both types of RMs. Strikingly, this figure suggests that the dipolar ground state solute resides closer to the interface in neutral RMs than in charged RMs for all pool sizes. This is counter-intuitive since dipole-charge interaction is supposed to hold the solute closer to the AOT interface than that for the neutral case. In addition, the solute is moving away from the interface (Δd increases) upon increasing the pool size for both types of RMs. This observation has, at least, two implications. First, moving away from the interface with pool size indicates the solute is increasingly probing more mobile environment. This might be the reason for experimental observation that relaxation rates increase upon increasing the pool size. Second, the different locations of the ground state solute suggests that comparison of absorption spectral characteristics between these RMs may not be proper as the solute location differs and thus *not* probing exactly the same environment of equal-sized aqueous pools.

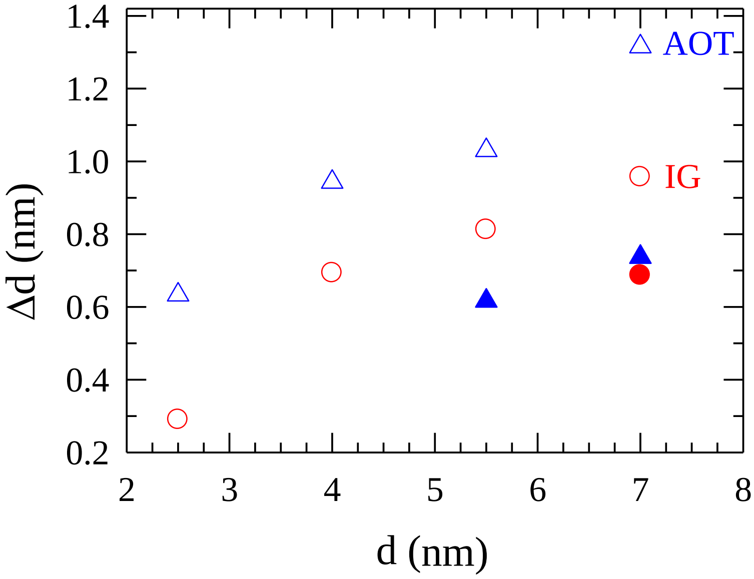

Fig. 6.4: Simulated solute locations inside the neutral (IGPAL) and charged (AOT) RMs. The solute is C153 and its locations inside AOT is represented by triangles and those inside IGPAL RMs by circles. While the ground state solute is denoted by the open symbols, the photo-excited solute associates with the filled ones. Δd is the distance of the solute from the interface. For further details, see text.

However, the question why C153 in its ground state is closer to the interface in IGPAL RMs than in AOT ones is not understood yet. The following factors may be responsible. C153, being sparingly soluble in bulk water, naturally stays away from an aqueous environment which closely resembles bulk water (in terms of H-bonding network). This hydrophobic character repels C153 from the centre of the aqueous pool to the outer layers close to the interface which play a better host for C153. This is because the extent of H-bonding among interfacial water molecules (in RMs or micelles) is greatly decreased, perturbing severely the bulk water structure in these layers.[71,73,75,104-115] The presence of the counter ions (Na^+) and the stronger charge-charge interaction between Na^+ and the AOT interface, on the other hand, does not allow C153 to move as close to the charged interface as in the cases for IGPAL RMs. The interaction between C153 and the oxygen of the polyethylene oxide group in IGPAL can also favour C153 to get much closer to the IGPAL interface. The close proximity to the IGPAL interface of C153 is probably responsible for the observed larger broadening of the C153 emission spectra in these neutral RMs than that in AOT RMs.

The next question is what happens to the location of the solute inside RMs after photo-excitation? This is an issue pertinent to fluorescence measurements of the confined water dynamics as larger dipole moment due to photo-excitation can drive the excited solute to the relatively more polar layers toward the centre of the aqueous pool. [32,35,67,116,117] The translational diffusion of the excited (S_1) solute during time-resolved measurements can generate a timescale slower than that produced by diffusion (both orientational and translational) of bulk-like water molecules inside the RM and may even become comparable to the timescale generated by the quasi-bound[78] interfacial water molecules. Simulated locations of excited C153 in these charged and neutral RMs at representative sizes are also shown in Fig. 6.4, which suggest the photo-excited solute moves away from the centre of the pool and toward the interface for both types of RMs. This is opposite to what is expected on the grounds of solvent polarity near the pool centre. Note the extent of movement in the charged RM for the largest pool is nearly double of that found for the corresponding smaller neutral RM. The associated distance distribution and a comparison with the ground state solute are presented in Fig. A23 (Appendix). Note the locations of the excited solute in charged RMs with pool diameters ~5 and 7 nm differ. Relatively ‘closer-to-the-interface’ location of the excited solute inside neutral RM (largest pool size shown as a representative example) means more heterogeneity encountered by the excited solute and thus accounts for the comparatively larger change in emission spectral width (Fig. 6.2) observed for these RMs. We would, however, like to mention here that these results have been obtained via the model description of the aqueous RMs (that includes the spherical RM cavity, SPC/E water molecules, non-inclusion of interactions between surfactant alkyl chain and nonpolar solvent etc.) in simulations in which certain properties may differ from those in real systems (for example, ε_0 of bulk SPC/E water is ~70[118]). This may lead to a difference in solute locations between the simulated and real systems and thus requires further study. Despite this possibility, it can be stated that the simulated solute locations provide a microscopic picture for explaining the observed behaviour of spectral characteristics of a neutral dipolar fluorescent solute in these RMs.

6.3.2 Solute solvation and rotational dynamics: Difference between charged and neutral RMs

Fig. 6.5 depicts representative decays of the time-resolved fluorescence intensity collected at the blue (440 nm) and red (630 nm) ends of the emission spectrum of C153 trapped in an aqueous pool of ~2 nm diameter in these two types of RMs (upper panel) and the constructed time-resolved emission spectra (TRES, lower panel). The fit parameters associated with the decay and rise components shown in the upper panel suggest presence of substantial solvent reorganization and similar timescales at this small pool size in these RMs. Steady state emission spectra of the solute at this pool size for these RMs are also shown for comparison in the lower panels with emission frequencies (ν_{em} and ν_{∞}) listed in Table A12 (Appendix). Similar decays for RMs with pool size of ~7 nm diameter presented in Fig. A24 (Appendix) also indicate that decay time constants, eventhough vary somewhat, do not reflect strong dependence on the chemical nature of the interface. This reflects the dominance of the confinement effects on medium dynamics over the chemical nature of the interface – an observation that has already been made in ultrafast IR measurements.[55] In fluorescence measurements the confinement effects get accentuated

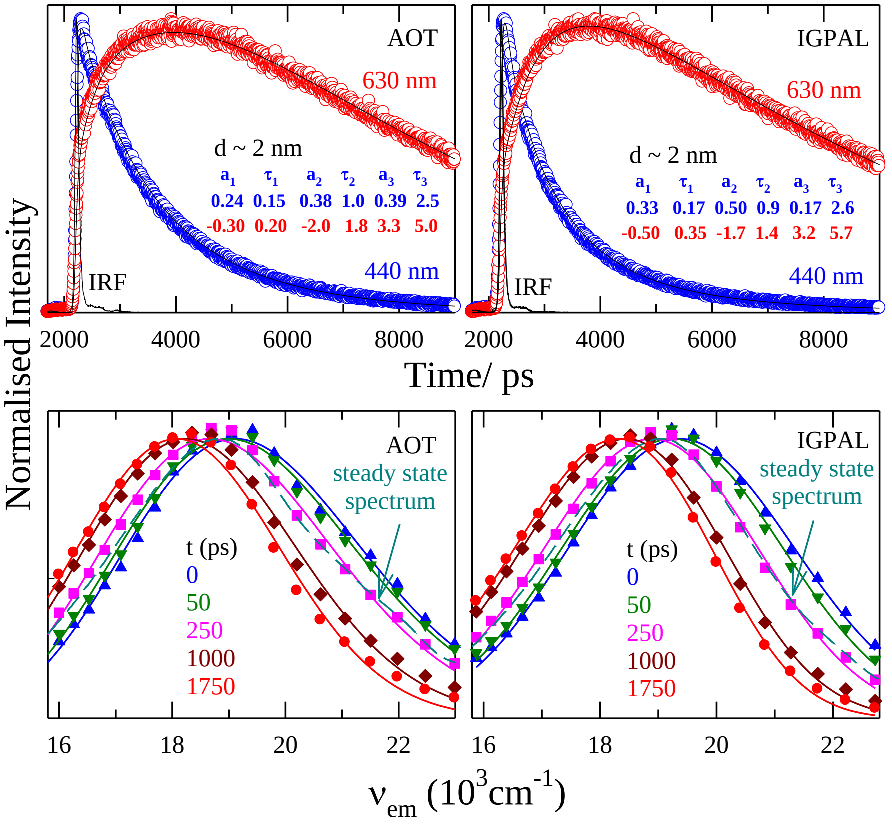

Fig. 6.5: Representative fluorescence intensity decays (upper panels) at blue (440 nm) and red (630 nm) wavelengths for C153 trapped inside AOT and IGPAL RMs with aqueous pool of ~2 nm diameter. Circles and solid lines represent the experimental data and fits through them, respectively. Instrument response functions (IRFs) are also shown (dashed lines). Insets in the upper panels show tri-exponential fit parameters for these intensity decays. Lower panels show the time resolved emission spectra (TRES) of C153 at different time slices constructed from the measured intensity decays for these RMs with the same pool size. Various time slices (in picosecond) are represented as follows: 0 (triangle), 50 (inverted triangle), 250 (square), 1000 (diamond) and 1750 (circle) immediately after laser excitation of the solute. Corresponding steady state emission spectra for the same solute are also shown by the dashed lines in the lower panels.

because the solute, which always prefers to reside nearer to the interface in both types of RMs (see Fig. 6.4), interacts with the interface and this solute-interface interaction can contribute to the observed total solvation energy relaxation. TRES shown in the lower panel indicate spectral movement continues to occur even after a nanosecond and beyond the corresponding steady state emission spectrum in these RMs. The difference between ν_{em} and ν_{∞} is quite large (~600-800 cm^{-1}) for both types of RMs at this pool diameter and originates from the steady state emission occurring from an excited solute with incompletely relaxed solvent environment.[90,91] This difference (ν_{em} - ν_{∞}) should decrease with increase in pool diameter as the aqueous environment becomes more mobile. This happens for AOT RMs but not for IGPAL RMs (see Table A12, Appendix). The trapped solute being closer to the neutral interface than to the charged one (see Fig. 6.4) is probably always having several extremely slowly relaxing moieties (either water molecules or hydroxyl and poly ethylene oxide groups of IGPAL) in its environment whose movements are not facilitated by the increase in pool size.

Dynamic Stokes shifts measured in AOT and IGPAL RMs at various pool sizes are summarized in Table 6.1 along with those measured for the charged and neutral RMs with no externally added water. The observed shift in both types of RMs increases with pool diameter and thus correlates well with earlier measurements for aqueous AOT RMs with an anionic dye, coumarin 343 (C343).[38,119] The observed shifts are quite large and increases from ~1000 cm^{-1} to ~2000 cm^{-1} for changing the pool size from ~2 nm to ~7 nm. The estimated shifts[83] are also quite similar (~2000-3000 cm^{-1}) for both types of RMs in this pool size range, suggesting a secondary role for the interfacial charge in dictating the magnitude of the dynamic Stokes shift in these RMs. Note that the inaccuracy in the estimated shifts tabulated here may be large as the interface effects on solute's spectrum (both absorption and emission) in a reference nonpolar solvent have not been included while determining the 'true' $\nu(t=0)$ by using the approximate relation described in Ref. 83. The interaction between the solute and an interface (charge or neutral) may affect the spectrum via either one or both of the following processes: (i) alteration of the underlying

Table 6.1: Estimated and observed dynamic Stokes shift for C153 dissolved in aqueous pools of different sizes inside charged (AOT) and neutral (IGPAL) reverse micelles at 298 K.

AOT				IGEPAL		
d (nm)	$\delta\nu^t_{est.}$ (cm^{-1})	$\delta\nu^t_{obs.}$ (cm^{-1})	% missed	$\delta\nu^t_{est.}$ (cm^{-1})	$\delta\nu^t_{obs.}$ (cm^{-1})	% missed
1.40	924	617	33	2373	1067	55
2.16	2764	1032	63	2372	1064	55
3.30	2943	960	67	2353	1343	42
4.06	2945	1268	57	2745	1428	48
5.20	3054	1670	45	2663	1702	36
5.96	2971	2341	21	2635	1712	35
6.91	3009	2080	31	2757	1939	30

vibrational characteristics as described earlier[81] and (ii) redshifting the spectra through the inhomogeneous solvent density profile near an interface.[120-125] The fact that interface effects on nonpolar reference spectra cannot be ignored is further reflected by the decrease of the missing component with pool size for both types of RMs, which should have been otherwise given that average relaxation rate of the confined environment becomes faster as pool size increases and the present experiments have employed rather a broad time-resolution.

Before we present the experimental solvation response functions ($S(t)$) at different pool sizes for these charged and neutral RMs, we would like to discuss how the width of the time-resolved emission spectrum ($\Gamma(t)$) changes with time in these systems. Fig. 6.6

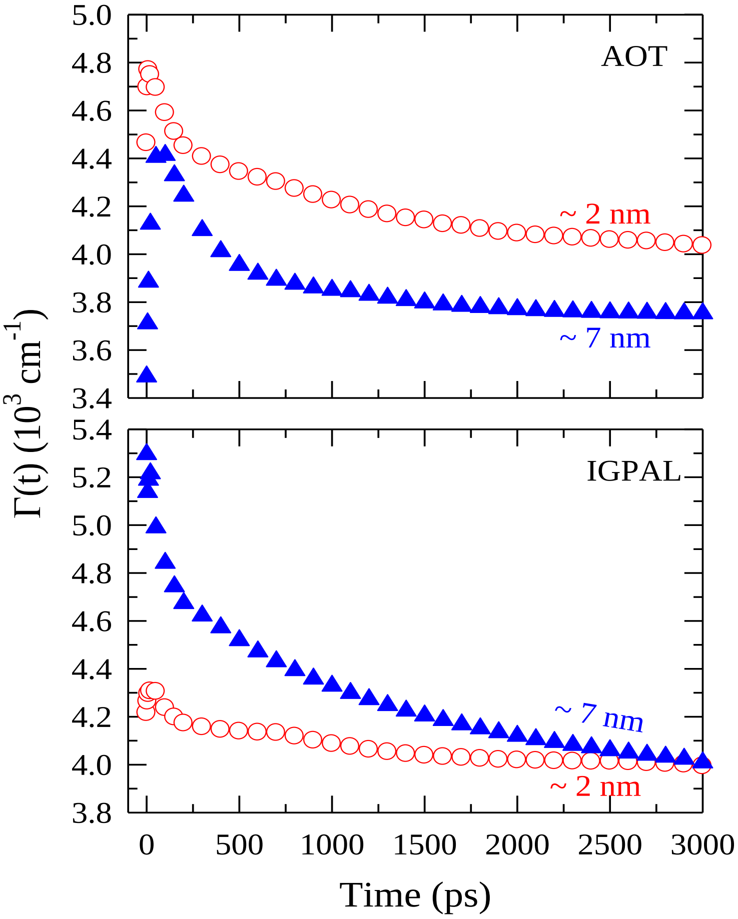

Fig. 6.6: Time dependence of the full-width-at-half-maximum (FWHM, Γ) of the time-resolved emission spectra of C153 in AOT (upper panel) and IGPAL (lower panel) RMs at two representative pool diameters, ~2 nm and ~7 nm.

shows this variation for both types of RMs at pool diameters ~2 nm and ~7 nm. At the smaller aqueous pool for both the RMs, $\Gamma(t)$ first increases and then decreases, showing an overall variation in width within ~10% of the corresponding steady state emission widths. The nature of the $\Gamma(t)$ observed here and the extent of its variation at this pool size are very similar to those observed with C153 in bulk non-aqueous polar solvents.[81] However, the extent of variation at the larger pool in both types of RMs is much bigger (~25-30%) and thus rather unusual with respect to the observations in bulk polar solvents. Interestingly, earlier measurements using different probes have also found similar or even larger variation in $\Gamma(t)$, and ascribed to solute migration during solvation energy relaxation.[32,35] We address this issue in Fig. 6.7 where the simulated trajectories for a

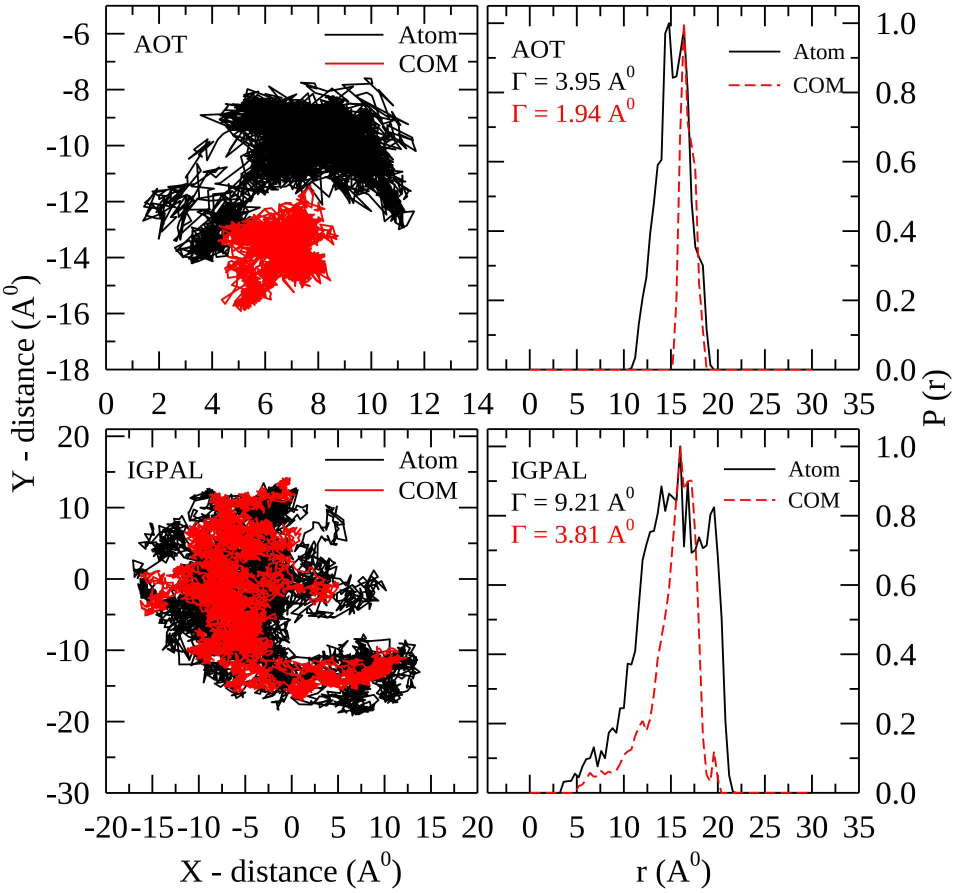

Fig. 6.7: Plots of centre-of-mass (com) and closest atom to the interface of the solute (atom) trajectories (left panels) explored during 5 ns simulations by C153 in aqueous AOT and IGPAL RMs with pool diameter of 5.2 nm. Corresponding normalised distance distributions are also shown (right panels). The widths (FWHM) of the distributions are also reported inside these panels.

duration of 5 ns associated with the centre-of-mass (com) motion of the excited solute (C153) and that of it's atom closest to the interface are shown. Note the excited state lifetime of C153 is ~5 ns in common polar solvents[81] and one is interested to know whether the solute is exploring, during its excited state lifetime, regions of different polarity in the confined environment and thus contributing to the observed substantial narrowing of the time-resolved emission spectrum in large pool sizes. The spread of both the trajectories ('com' and 'atom') shown Fig. 6.7 (left panels) indicates that the photo-excited solute is *not* stationary inside these RMs but the extent of movement is comparatively reduced in AOT RMs probably because of the charge-dipole interaction between the interface and the dipolar solute. In addition, the relatively larger spread of the atom trajectories indicates the solute is both rotating and translating. This broadens the distance distribution and is shown in the right panels of Fig. 6.7 where $P(r)$ from 'atom' trajectories are more than doubly broadened compared to those from 'com' trajectories. The large variation in width of the time-resolved spectra shown in Fig. 6.6 may then be attributed to this solute-motion induced broadening of $P(r)$ in these RMs. Note the importance of solute's motion on its own rate of solvation in various bulk media has already been recognised[126-129] and these simulation results place solvation energy relaxation in confined environments within the ambit of such a discussion as well.

Fig. 6.8 depicts both measured and simulated $S(t)$ decays at three different pool sizes in the charged and neutral RMs where fit parameters describing the decays are also shown for comparison. Regardless of the nature of the surfactants used to form these RMs., both measurements and simulations reveal faster solvation energy relaxation upon increase of pool size. This is in general agreement with earlier measurements that had employed different dipolar probes and time-resolutions.[9,10,38-40,42] However, the present experiments have completely missed the simulated bulk-like sub-hundred femtosecond solvation response due to broad time-resolution employed. Fits of the simulated decays generate a substantial (~30-50%) ultrafast component with time constant <100 fs and two other relatively slower components having time constants in ~10-20 ps range and in ~200-2000 ps range. Note such a substantial ultrafast component (~40-70%) with time constant ≤ 100 fs has already been observed in measurements using C343 (a negatively charged coumarin dye when dissociated) in cation-substituted AOT RMs[39] possessing moderately sized aqueous pools and similar RMs made of Brij-30 (a neutral surfactant having –OCH$_2$CH$_2$ units in its chain along with –OH head group).[42] Except for the largest AOT RMs, the agreement between the simulated and measured average solvation times ($<\tau_s>$) is only qualitative. This could be due to relaxation being incomplete in simulations, particularly for smaller pool sizes where severely restricted water motions demand much longer runs for capturing the complete decay. However, the simulations predict the right orders of the slower timescales (τ_2 in a few tens of picoseconds and τ_3 in a few to several hundreds of picoseconds) measured in experiments. The disagreement, therefore, does not indicate any serious incompatibility between these two (experiments and simulations) but reflecting merely the missing of both the ultrafast solvation in the present experiments and

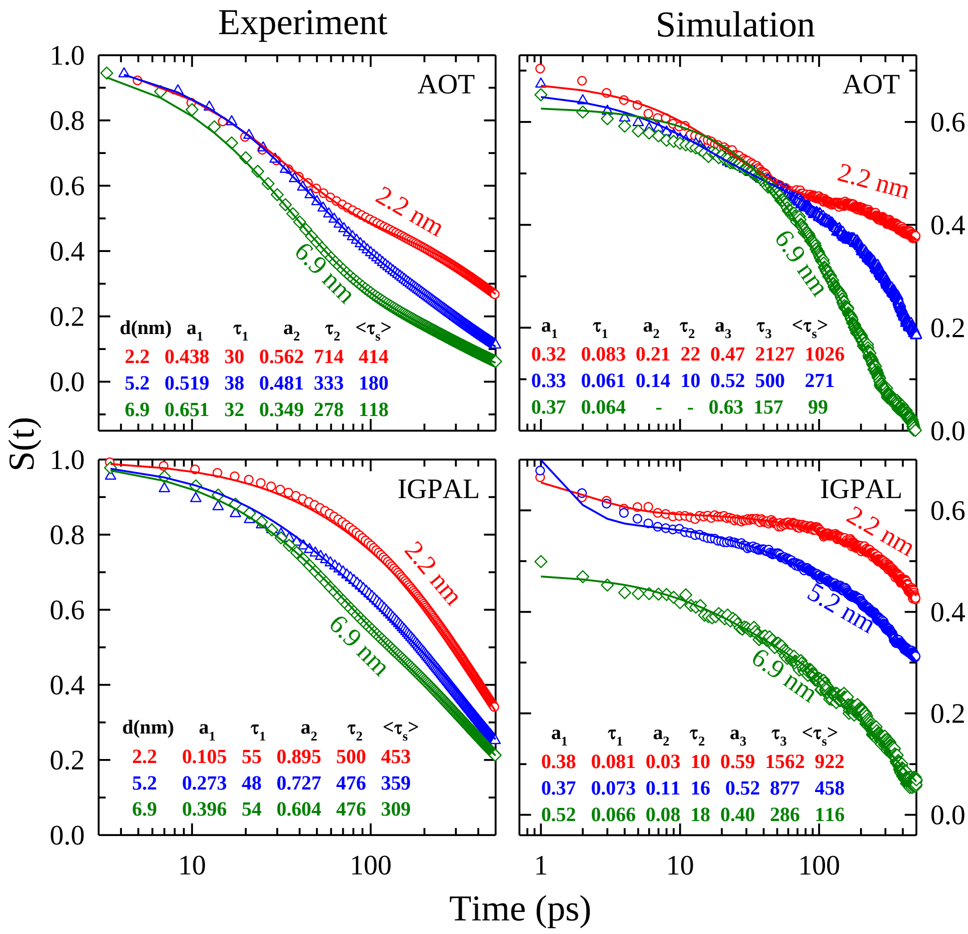

Fig. 6.8: Semi-log plots of representative measured (left panels) and simulated (right panels) solvation response function, $S(t)$, for C153 in aqueous AOT and IGPAL RMs. While the symbols represent experimental/simulated data points, the solid lines going through them denote the best fits. The multi-exponential fit parameters are also tabulated for comparison. Note the experimental decays are complete in all cases but shown only up to 500 ps to augment visual comparison with simulations.

sluggish long time dynamics in our simulations (for smaller pools). In addition, the semi-quantitative modelling of the surface structure of these RMs also play a role because interfacial roughness and fluctuations in shape and size in real RMs can have important effects on relaxation rates. The surface structure is particularly important for IGPAL RMs because the $–OCH_2CH_2$ units can intrude inside the cavity creating indentation which can significantly retard the solute's orientational and solvation energy relaxation rates. This will be discussed further when we present fluorescence anisotropy results.

Fig. 6.9 shows the pool size dependence of the average solvation times ($<\tau_s>$) in these RMs where both measured and simulated $<\tau_s>$ are presented for a comparison. Fit parameters describing the $S(t)$ decays measured for other pool sizes are provided in Tables A13 and A14 (Appendix). Two distinct features are to be noted in this figure. First, in large pool sizes the measured $<\tau_s>$ are faster for the charged RMs than those for the neutral ones. Second, this trend of $<\tau_s>$ is reversed in the smallest RMs. Because of the presence of interfacial charge, one expects slower solvation at all pool sizes in the charged

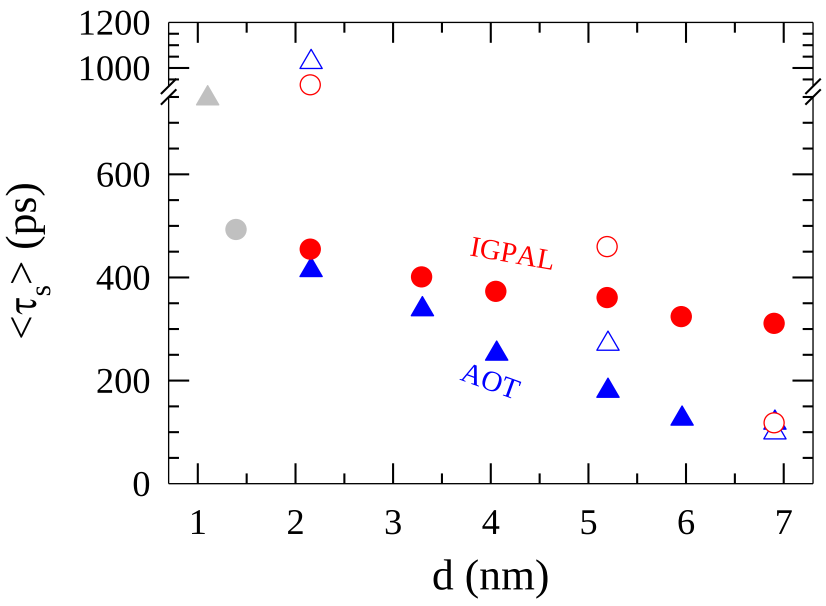

Fig. 6.9: Pool size dependence of the average solvation times ($<\tau_s>$) for C153 in aqueous AOT (circles) and IGPAL (triangles) RMs. While the experimental results are shown by filled symbols, open ones denote those from simulations. Filled grey symbols are for dry RMs.

RMs compared to that in neutral RMs. However, this is not what has been observed except for the smallest size where no external water has been added ('dry' RM). The following is a plausible explanation: owing to the presence of relatively less number of water molecules at small pool sizes, the electrostatic interaction in the charged RMs is insufficiently screened,[53] restricting severely the movement of water molecules. This is in addition to the curvature-induced jamming[64] of the captive aqueous environment. Moreover, the close proximity of the solute to the interface forces the solute to probe not only the dynamics of the rather slow interfacial water molecules but also to include the contribution from the fluctuating solute-interface interaction energy. As a result, the solvation in smaller pools proceeds at a rate much slower in the charged RMs than that in the neutral ones. But at larger pools where sufficient number of water molecules are available for solvating the charged head groups at the interface and the counter ions, the electrostatic restriction is reduced, allowing more facile movement of the aqueous environment. The movement of the solute away from the interface upon increasing the pool size (see Fig. 6.4) further assists the solvation rate. A plot of $<\tau_s>$ as a function of distance from the interface (Δd) shown in Fig. A25 (Appendix) also supports this notion. The distance of the solute (from the interface) being somewhat larger for the charged RMs than for the neutral ones also assists the solvation. This leads to larger average solvation rates inside charged RMs at large pool sizes than those inside the corresponding neutral ones.

We next investigate the possible contribution of the fluctuating solute-interface interaction energy to the sub-nanosecond (or nanosecond) solvation component observed in time-resolved fluorescence experiments. Fig. 6.10 depicts the decays of individual solvation response functions (along with fit parameters) obtained after separating the solute-water and solute-interface interaction contributions. Necessary theoretical works and approximations for dissecting the total simulated response ($S_{tot}(t)$) into solute-water ($S_{sw}(t)$) and solute-interface ($S_{si}(t)$) interaction contributions are provided in the Appendix. These simulated results are for AOT RMs with aqueous pool diameter of 5.2 nm and serve as a representative example. Comparison among the fit parameters associated with $S_{sw}(t)$, $S_{si}(t)$ and $S_{tot}(t)$ clearly suggests that while the bulk-like response arises solely from the $S_{sw}(t)$, the sub-nanosecond (or even slower) component of the total response derives contributions from both $S_{sw}(t)$ and $S_{si}(t)$. It has been shown earlier that the sub-hundred femtosecond response of bulk water arises mainly from the water librational modes,[130] and these modes survive even for confined interfacial water molecules but with a red-shift.[59,73] Consequently, the ultrafast timescale of bulk water remains largely unaffected upon confinement. The slow sub-nanosecond component has not been detected in the ultrafast IR measurements probably because of the huge difference in lifetimes between the fluorescence solute and the –OH stretch (~5ns and ~1.5 ps respectively). It should, however, be pointed out that subsequent two dimensional IR vibrational echo experiments did observe a long time offset in the measured frequency-frequency correlation function which appears to arise from dynamics that are too slow to be detected on the accessible experimental timescale.[132] It should be noted that although a contribution from the solute-interface interaction to the slow component of the interfacial water dynamics has been predicted in earlier simulation studies with model solutes,[66,106]

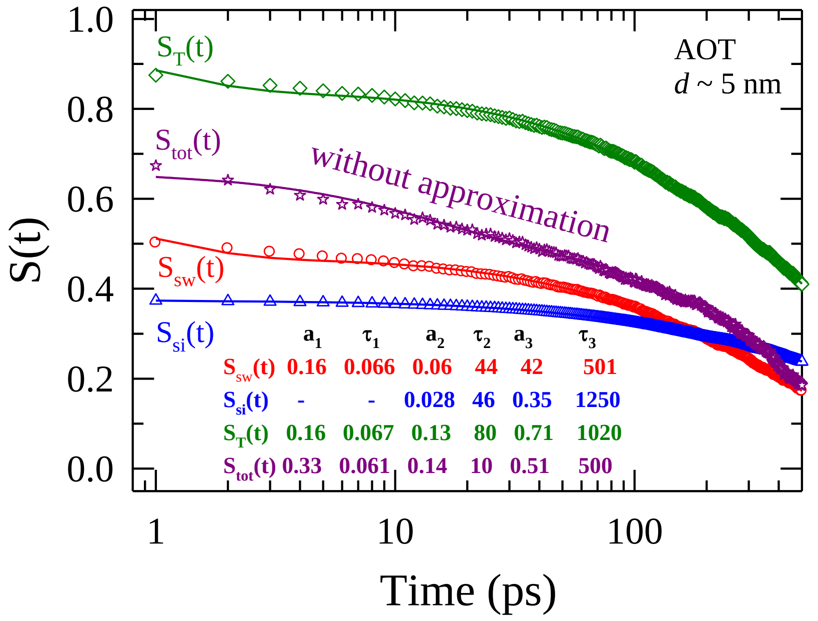

Fig. 6.10: Dissection of the simulated total solvation response functions into solute-water ($S_{sw}(t)$), solute-interface ($S_{si}(t)$) interaction contributions. Such a dissection requires approximations which are described in Appendix. The approximate total solvation response function is denoted by $S_T(t)$. The full simulated response function without any approximation, $S_{tot}(t)$, is also shown for comparison. The simulated system is C153 in AOT RM with aqueous pool diameter 5.2 nm. Fits (lines) through the simulated data along with fit parameters are also shown.

such a sub-nanosecond component with realistic solute has never been reported. All these results seem to suggest that both the dynamics of quasi-bound water molecules and the fluctuation in the solute-interface interaction energy due to solute movement are responsible for the observed sub-nanosecond component in the solvation energy relaxation measured by dynamic Stokes shift experiments. Another point is that the slowest time constant in the simulated full response ($S_T(t)$) is doubly faster than that found in the approximate total response, $S_{tot}(t)$. This arises probably because the assumed separation of timescales between the fluctuating solute-water and solute-interface interaction energies (see Appendix) does not hold for interfacial quasi-bound water molecules.

The above discussion then brings up the following point. If detection of the slow component is conditioned with the lifetime of the probes used in experiments, then the slow response arising from water alone, if exists, should be captured in simulation studies. In this context, it would be informative to investigate both translational and orientational motions of water molecules which are not only close to the solute and thus reside near the interface but also of those which are near to the centre of the pool. A layer-wise comparison of these mobilities then provide microscopic understanding of the reasons responsible for both the fast and the slow experimental timescales. Fig. 6.11 depicts the layer-wise centre-of-mass (translational) diffusion coefficients of confined water molecules in both types of RMs for three representative pool sizes. Note such a layer-wise translational mobility of water molecules inside AOT RMs has already been studied.[63] The ratio, D_T^{bulk}/D_T^{layer}, represents extent of slowing down of bulk water diffusion upon confinement and this ratio obtained from the present simulations is shown here as a function of layer number where the first layer (layer #1) is the layer immediate to the interface. We have used D_T^{bulk} ~3x10^{-5} cm^2/s for bulk SPC/E water[131]. Here each layer is of 4 A^0 width and D_T^{layer} has been calculated from the mean squared displacements (MSDs, $<[\Delta r(t)]^2>$) of only those water molecules which stayed within a specified layer during a certain simulation period.[63] Representative layer-wise MSDs are provided in Fig. A26 (Appendix) which shows, as observed previously,[63] that the diffusion coefficient of interfacial water molecules ($D_T^{layer\#1}$) is *not* independent of pool size. It is evident from this figure (Fig. 6.11) that D_T^{layer} for each layer in the charged RMs is different from that in the neutral RMs, and the difference in D_T^{layer} between layers rapidly diminishes as the centre of the pool is approached in both types of these RMs. For the aqueous pool with $d = 2.2\,\text{nm}$, D_T^{layer} of the first two layers (counted from the interface)

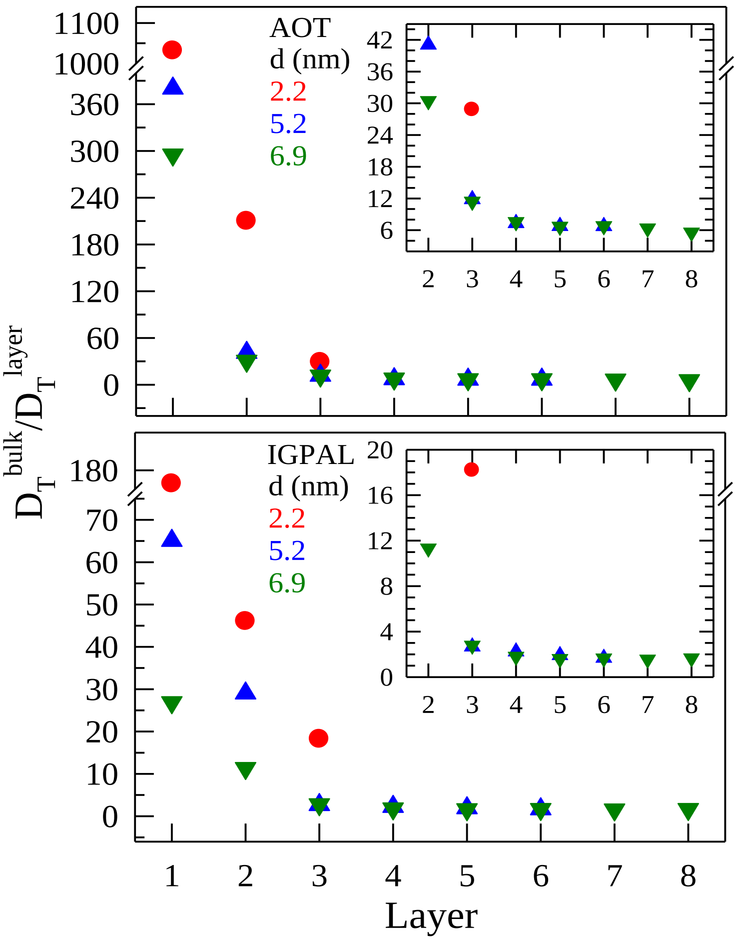

Fig. 6.11: Effects of confinement and surface charge on layer-wise mobility of water molecules inside AOT (upper panel) and IGPAL (lower panel) RMs. The ratio between diffusion coefficients of SPC/E water in bulk and in various layers (counted from the interface), D_T^{bulk}/D_T^{layer}, is shown as a function of layer number where the first layer is the one that lies closest to the interface. RMs with diameters 2.2 nm (circles), 5.2 nm (triangles) and 6.9 nm (inverted triangles) have been considered in simulations. Insets show the same data for distant layers with better resolution.

are ~6-4 times smaller in the charged RMs than those in the neutral ones. This reflects the difference in the chemical nature of the interface. This effect of charged interface extends to the distant layers even including the centre of the pool as D_T^{layer} of water molecules in these layers (beyond layer #3) is ~3-4 times greater in the neutral RMs than those in the charged RMs. This is clearly shown in the insets of Fig. 6.11. Interestingly, the diffusion coefficient for water molecules in the central layer (that includes the centre of the pool) is smaller than that of the bulk (for this layer, $D_T^{bulk} / D_T^{layer} \approx 2$) even at large pool sizes in neutral RMs, revealing the geometric confinement affects diffusion even for water molecules residing far away from the interface.

Fig. 6.12 is a representative of how $C_2(t)$, the second rank ($l = 2$) reorientational correlation function (RTCF), decays with time when simulated layer-wise for water molecules in these charged and neutral RMs with sizes, d (nm) $= 2.2$, 5.2 and 7. The lines going through the simulated data points represent tri-exponential fits and the fit parameters are summarized in Table A15 (Appendix). The second rank RTCF is defined as follows[93]

$$C_2(t) = \frac{\langle P_2[\vec{u}_i(t).\vec{u}_i(0)] \rangle}{\langle P_2[\vec{u}_i(0).\vec{u}_i(0)] \rangle}, \qquad (3)$$

where P_2 denotes the Legendre polynomial of rank 2 and $\vec{u}_i$ a unit vector parallel to the dipole axis of a water molecule, with the associated average reorientational correlation time: $\langle \tau_2^{or} \rangle = \int_0^\infty dt\, C_2(t)$. The second rank RTCF is chosen over the first rank ($C_1(t)$) because the latter ($C_2(t)$) relaxes faster owing to smaller angle spanned, and time-resolved fluorescence anisotropy measurements associates with $l = 2$. As expected, the decay of the layer-wise simulated $C_2(t)$ becomes faster as one moves away from the interface for both types of RMs at a given pool size. For the first two pool sizes, $C_2(t)$ at each aqueous layer decays faster for the neutral RMs than for the charged ones, and the extent of difference between them reduces with increase in RM size. The decay being slower for water molecules near the charged interface than those near the neutral interface is again a reflection of the difference in chemical nature of the surfactant molecules. Interestingly, such a clear difference between types of RMs does not exist at d (nm) $= 6.9$ where decay profiles either cross (for the nearest and the furthest layers from the interface)

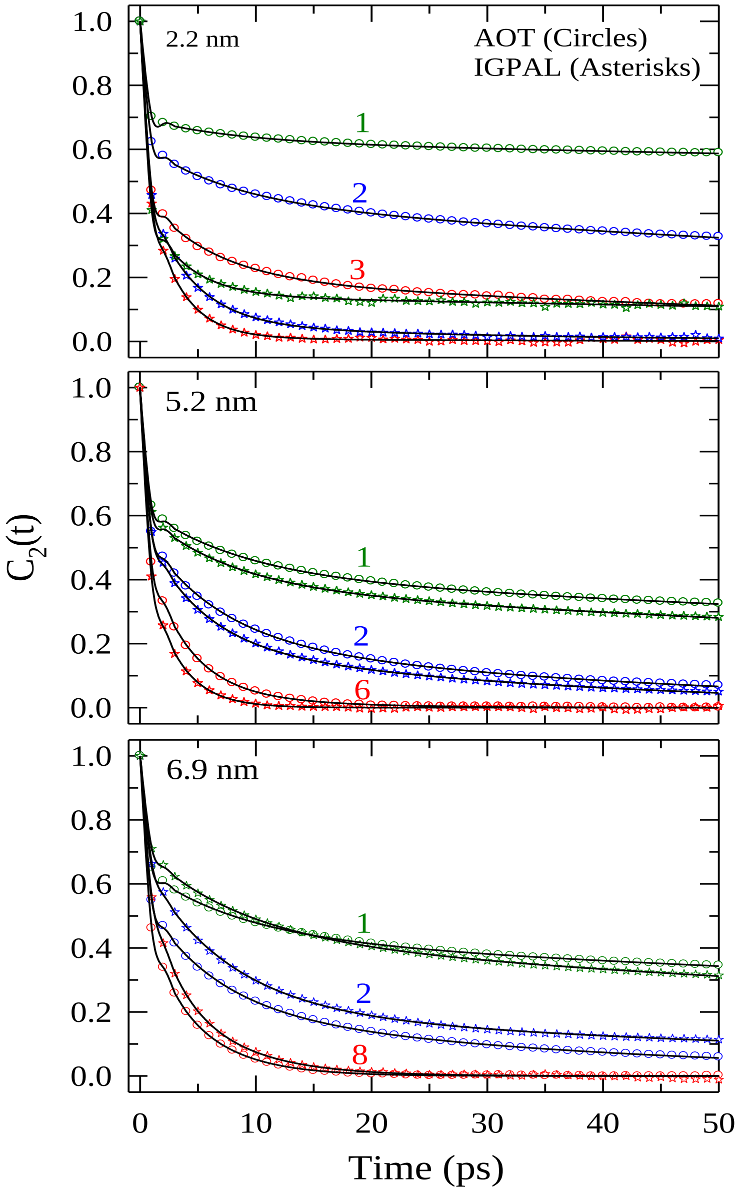

Fig. 6.12: Decays of the second rank ($l = 2$) reorientational correlation function, $C_2(t)$, simulated for water molecules residing at various layers and their comparisons between the types of RMs at pool sizes, 2.2 nm, 5.2 nm and 6.9 nm. Circles and asterisks represent simulated decay respectively in AOT and IGPAL RMs. Fits through these data points are represented by solid lines and fit parameters are sumamrized in Table A15 (Appendix).

or depict a trend reverse to that (for the second aqueous layer) observed for the other two sizes.

The above is more clearly shown by the fit parameters summarized in Table A15 (Appendix). It is evident that a nanosecond component with substantial amplitude exists for the interfacial layer in the charged RM at all these three sizes, whereas a sub-picosecond component (~30-50%) characterises the decay of the $C_2(t)$ simulated for all layers in this RM at these sizes. Expectedly, the nanosecond component vanishes as one moves toward the pool centre for larger RMs but leaves a signature on solute dynamics (solvation or rotation) as the excited solute resides within the interfacial (or first two) layers. The existence of sub-picosecond and nanosecond components along with the another time constant in ~2-50 ps range in $C_2(t)$ then strongly suggest observation of solvation timescales spanning these regimes in complete dynamic Stokes measurements of aqueous AOT RMs. Note such a multi-exponential decay for $C_2(t)$ in AOT RMs and faster relaxation rate with RM size have already been predicted in earlier simulations.[67] Interestingly, the nanosecond timescale of $C_2(t)$ found for AOT RMs is absent in the smallest IGPAL RM simulated but reappears when the larger RMs are considered although the sub-picosecond and picosecond timescales maintain their presence across the simulated IGPAL RM sizes. Intriguingly, layer-wise $C_2(t)$ decays in the largest IGPAL RM are, on an average, slower than those in the other two relatively smaller IGPAL RMs. This is probably due to indentation made by the intruding polyethylene oxide (-CH_2-CH_2-O-) units in the largest IGPAL RM under simulation. Note larger unfolding of polyethylene oxide units has been necessary for creating bigger IGPAL RMs in our simulations. On the other hand, if the simulated interface qualitatively mimics the real interface at this pool size, then the average decay rates ($\equiv \left\langle \tau_2^{or} \right\rangle^{-1}$) definitely provides some explanation for the solute rotation (presented later) being slower in larger IGPAL RMs than that in the corresponding AOT RMs.

Fig. 6.13 quantifies what Fig. 6.12 has reflected visually about the comparison of layer-wise $C_2(t)$ decay rates between types of RMs. Here the simulated average reorientation time of rank 2 ($\left\langle \tau_2^{or} \right\rangle$) is shown as a function of layer for both types of RMs. Note that the slowing down of water reorientation in layers close to the interface is the strongest for the charged RMs and in accordance with what has been found for the centre-of-mass diffusion. Moreover, different $\left\langle \tau_2^{or} \right\rangle$ values for the interfacial water molecules for different sized RMs further highlights the limitation of the two state model (bound and free) for confined water molecules in these RMs. The effects of charge dominate over the proposed ‘indentation effects’ in neutral RMs where the average relaxation rate of $C_2(t)$ for the charged interfacial layer is reduced by a factor ~4-6 than that in the corresponding layer of the neutral RM of the same size. For layers nearer to the pool, $\langle \tau_2^{or} \rangle$ does not differ much between the types of RMs (charged or neutral) which is in contrast to what has been found for centre-of-mass diffusion. The reason for such a contrasting result may lie in the natural difference between orientational and translational diffusion of a particle in a given environment.

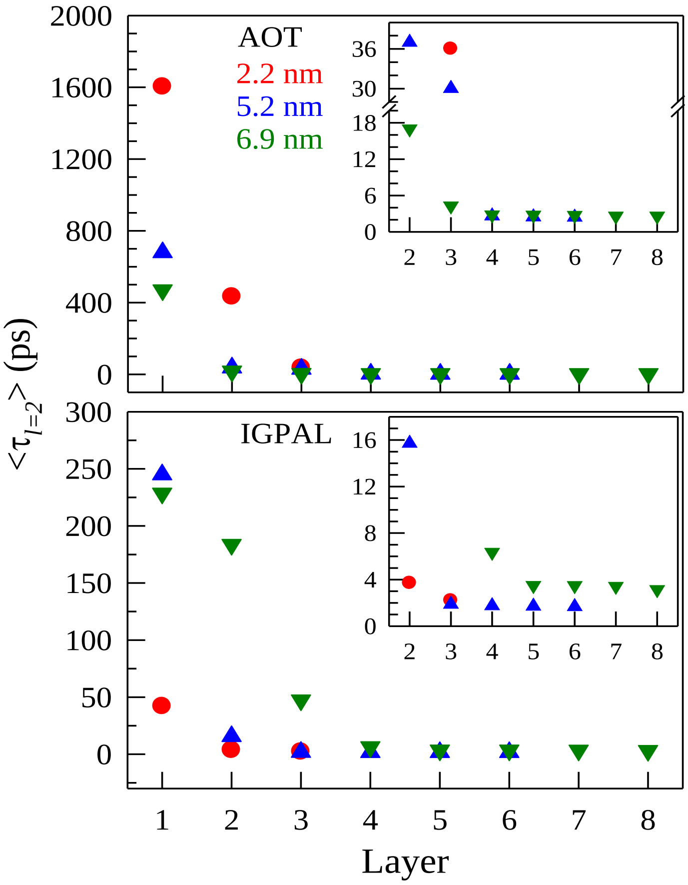

Fig. 6.13: Plots of layer-wise average reorientation time ($<\tau_{l=2}>$) of water molecules calculated from the simulated $C_2(t)$ decays shown in Fig. 12 for AOT (upper panel) and IGPAL (lower panel) RMs with pool diameters, 2.2 nm (circles), 5.2 nm (triangles) and 6.9 nm (inverted triangles). Insets show the average times for distant layers with better resolution.

Fig. 6.14 presents the experimental and simulated anisotropy decays in both types of aqueous RMs with d (nm) = 2.2, 5.2 and 6.9. Fits through the measured and simulated data are also shown along with fit parameters to facilitate comparison between types of

RMs and to demonstrate pool size dependence. Fit parameters for other pool sizes for which experiments have been carried out are also summarized in Table A16 (Appendix). Interestingly, both experimental and simulation results indicate that while the increase in pool size enhances the anisotropy relaxation rate for the AOT RMs, the reverse occurs for the IGPAL RMs. Note the simulated anisotropy decays remain incomplete within this 200 ps time-window and thus much longer and larger simulations are required to capture the full anisotropy relaxation dynamics. This is particularly true for the AOT RM with $d\ (\mathrm{nm}) = 2.2$ where the present simulations can capture only ~5% of the total decay within

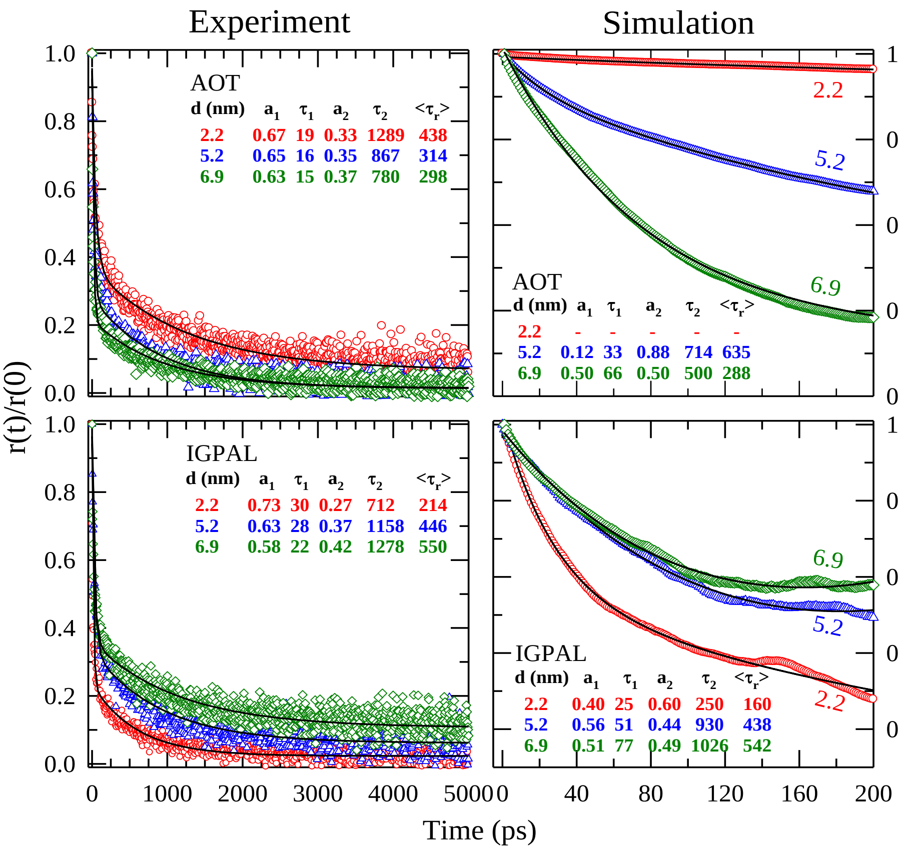

Experiment, AOT

d (nm)	a_1	τ_1	a_2	τ_2	$<\tau_r>$
2.2	0.67	19	0.33	1289	438
5.2	0.65	16	0.35	867	314
6.9	0.63	15	0.37	780	298

Simulation, AOT

d (nm)	a_1	τ_1	a_2	τ_2	$<\tau_r>$
2.2	-	-	-	-	-
5.2	0.12	33	0.88	714	635
6.9	0.50	66	0.50	500	288

Experiment, IGPAL

d (nm)	a_1	τ_1	a_2	τ_2	$<\tau_r>$
2.2	0.73	30	0.27	712	214
5.2	0.63	28	0.37	1158	446
6.9	0.58	22	0.42	1278	550

Simulation, IGPAL

d (nm)	a_1	τ_1	a_2	τ_2	$<\tau_r>$
2.2	0.40	25	0.60	250	160
5.2	0.56	51	0.44	930	438
6.9	0.51	77	0.49	1026	542

Fig. 6.14: Pool size dependent decays of time-resolved fluorescence anisotropy, $r(t)/r(0)$, of C153 in AOT (upper panels) and IGPAL (lower panels) RMs. Various pool sized shon in this figure are mentioned and color-coded. Symbols represent data points (measured/simulated), solid lines denote best fits through them. Fit parameters are also shown to facilitate comparison between types of RMs, and between experiments and simulations.

this 200 ps. This could be due to a combination of more ordered structure of confined aqueous environment inside the simulated RMs[64] (because of complete neglect of roughness along the simulated interface inside) or simulated location of the solute being closer than in real systems. Despite these lacunae, the simulated decays, as in experiments, fit to bi-exponentials producing fast and slow time constants which are in qualitative agreement with those from experiments. Even with a possibility of such an agreement between simulations and experiments being fortuitous, the observed similarity probably suggests that the basic features of solute rotational relaxation inside these aqueous RMs have been captured in simulations qualitatively correctly.

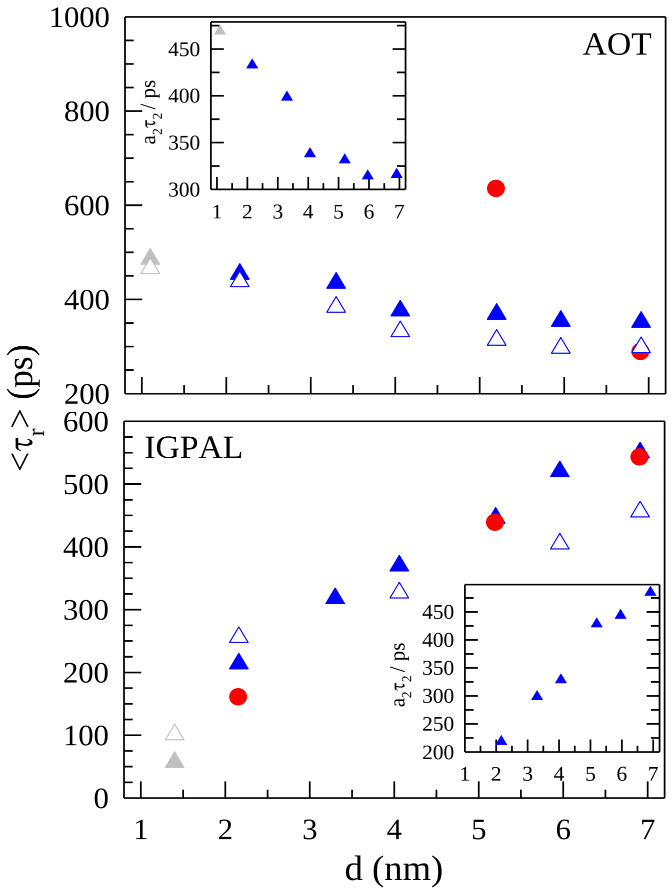

Fig. 6.15: Pool size dependence of the average rotation times ($<\tau_r>$) for C153 in AOT (upper panel) and IGPAL (lower panel) RMs, and a comparison between experiments (triangles) and simulations (circles). Filled and open triangles represent two sets of independent measurements. Gray symbols denote measured $<\tau_r>$ values for dry RMs. Insets depict the pool size dependence of the measured weighted long time constant ($a_2\tau_2$) and provides reason behind the observed different dependence.

Fig. 6.15 compares the pool size dependent experimental average rotation time ($\langle\tau_r\rangle$) with those from simulations for the AOT and IGPAL RMs. The qualitative difference in solute rotation inside these two types of RMs is quite clear in this figure. The weighted long time constant ($a_2\tau_2$) from the bi-exponential fits to experimental data are also shown as insets inside these panels. The decrease in $a_2\tau_2$ upon increase of pool size explains why $\langle\tau_r\rangle$ becomes faster with pool size for AOT RMs and parallels the pool size dependence of average solvation time, $\langle\tau_s\rangle$. However, the increase of $a_2\tau_2$ and the resultant $\langle\tau_r\rangle$ with size for the IGPAL RMs is opposite to the pool size dependence of $\langle\tau_s\rangle$ obtained for these RMs and thus anti-correlated to $\langle\tau_r\rangle$. As indicated before while discussing reorientational relaxation of interfacial water molecules, this unexpected pool size dependence of solute rotation for IGPAL RMs may have arisen from the interaction of the solute with the intruding polyethylene oxide units. The solute rotation and solvation being slower in large IGPAL RMs than in corresponding AOT RMs share an interesting commonality with another earlier experimental study[133] where the excited state reactive dynamics of a dye molecule has been found to be slower in aqueous IGPAL RM than that measured for AOT RM with equal-sized aqueous pool. In addition, solvation dynamics study of deuterated polyethylene glycols[134] have revealed slowing down of the long time dynamics by ~20% relative to that observed for undeuterated solvents, indicating interaction between the solute and the interfacial glycolic hydroxyl groups. Given the pool size dependence of the solvation response in these RMs and the relation between solvent effects (dynamic and static) on a chemical reaction,[22-24] the present simulated solute locations then put the observed slower reaction rates[133] in IGPAL RMs in proper perspective. Therefore, further simulation studies along with suitable experiments are required to quantify this aspect as difference in fluorescence dynamics between these two types of RMs originates not only from the difference in chemical nature of the surfactants involved but also from the difference in the interfacial structures and constructing units of a given surfactant molecule.

6.4 Conclusion

In summary, the present fluorescence spectroscopic measurements combined with all-atom simulations reveal the following features: (i) the average rates of solvation and rotation of a trapped dipolar solute are different for confined aqueous environments of same size inside AOT and IGPAL RMs, and this difference originates from the difference in chemical nature of the surfactants and the dissimilar interfacial structures,

(ii) the solute resides always closer to the interface in both types of RMs irrespective of the size of the confined aqueous environment, (iii) excited solute moves closer to the interface than the ground state solute in both types of RMs and are both rotationally and translationally mobile during its excited state lifetime which may contribute to the dynamic line-width and rate of its own solvation (iv) the slow sub-nanosecond solvation component derives contributions from both the dynamics of the slow 'quasi-bound' interfacial water molecules and solute-interface interaction, and (v) the enhanced solute-interface interaction due to intruding polyethylene oxide units inside IGPAL RMs not only makes average solvation rates slower than in AOT RMs of equal pool sizes but also leads to anti-correlation between the pool size dependent solvation and rotation rates for IGPAL RMs. The observation in the present simulations that the interaction between the solute and the quasi-bound water molecules, and that between the solute and the interface contributes to the slow sub-nanosecond (or nanosecond) component is important as it provides a possible resolution to a debate regarding the origin of the slow solvation timescale (sub-nanosecond) observed in dynamic fluorescence measurements with aqueous RMs but not detected in ultrafast IR measurements. All-atom simulations presented here also predicted substantial sub-picosecond solvation response for these different types of RMs which is in good agreement with upconversion measurements with AOT RMs. In addition, the present simulations has employed, for the first time, a realistic solute and attempted a uniform comparison with experiments where the same solute has been used as a probe.

Eventhough the present combined study has been able to provide some answers regarding the effects of surface charge on solvation energy and rotational relaxations of a confined solute inside RMs and characterize the aqueous dynamics at different layers, it is far from quantitative, particularly for solute rotation, as this is much slower (than solvation) and thus requires more extensive simulations not only to ensure complete relaxation but also to provide better averaging. While in fluorescence experiments a collection of RMs with confined solute is excited and contribute to the measured signal, present simulations involve only one such entity (single solute inside a given RM) at a time. Interfacial structure, as indicated by the present results, is an important factor than can affect the solute dynamics and vitiates a comparison on same footing of solute-based dynamics between equal-sized aqueous environments confined in RMs made of chemically different surfactant molecules. The contribution of the solute motions may further be quantified via simulations with a trapped but motionally frozen solute in such environments. The effects of solute locations can further be explored in simulations via using a similar sized dipolar probe but with a charge. For example, C343 may be a good choice for this purpose as corresponding experimental results are available. Further experimental and simulation studies with aqueous RMs made of other surfactant molecules as well as exploration of the effects of interfacial structure are therefore necessary to develop a thorough understanding of the aqueous interface which assumes importance not only in basic scientific arena but also for possible and better applications in cosmetic and pharmaceutical industries.

References:

1. Halle, B. *Phil. Trans. R. Soc. Lond. B* **2004**, *359*, 1207-1224.
2. Bagchi, B. *Chem. Phys. Lett.* **2012**, *529,* 1-9.
3. Bhattacharyya, K. *Chem. Commun*. **2008**, 2848-2857.
4. Bagchi, B. *Chem. Rev*. **2005**, *105,* 3197-3219
5. Bagchi, B.; Jana, B. *Chem. Soc. Rev*. **2010**, *39*, 1936-1954
6. Pal, S. K.; Zewail, A. H. *Chem. Rev*. **2004**, *104*, 2099-2124
7. Fayer, M. D.; Levinger, N. E. *Annu. Rev. Anal. Chem*. **2010**, *3*, 89-107.
8. Levinger, N. E.; Swaford, L. A. *Annu. Rev. Phys. Chem*. **2009**, *60*, 385-406.
9. Bhattacharyya, K. *Acc. Chem. Res.* **2003**, *36*, 95-101
10. Ghosh, S.; Mandal, U.; Adhikari, A.; Dey, S.; Bhattacharyya, K. *Int. Rev. Phys. Chem.* **2007**, *26*, 421-448
11. Bagchi, B. *Annu. Rep. Prog. Chem. Sect. C: Phys. Chem*. **2003**, *99*, 127-175
12. Liu, L.; Faraone, A.; Mou, C.-Y.; Yen, C.-W.; Chen, S.-H. *J. Phys.: Condens. Matter* **2004**, *16,* S5403-S5436.
13. Ramsay, J. D. F.; Poinsignon, C. *Langmuir* **1987**, *3*, 320-326.
14. Floquet, N.; Coulomb, J. P.; Dufau, N.; Andre, G.; Kahn, R. *Phys. B.* **2004**, *350*, 265-269.
15. Mitra, S.; Mukhopadhyay, R.; Tsukushi, I.; Ikeda, S. *J. Phys: Condens. Matter* **2001**, *13*, 8455-8465.
16. Bellisent-Funel, M.-C.; Chen, S.-H. Zanotti, J.-M. *Phys. Rev. E* **1995**, *51*, 4558-4569.
17. Biswas, R.; Rohman, N.; Pradhan, T.; Buchner, R. *J. Phys. Chem. B* **2008**, *112*, 9379-9388.
18. Biswas, R.; Das, A. R.; Pradhan, T.; Touraud, D.; Kunz, W.; Mahiuddin, S. *J. Phys. Chem. B* **2008**, *112*, 6620-6628.
19. Sarma, N.; Borah, J. M.; Mahiuddin, S.; Gazi, H. A. R.; Guchhait, B.; Biswas, R. *J. Phys. Chem. B* **2011**, *115*, 9040-9049.
20. Senapati, S.; Chandra, A. *J. Phys. Chem. B* **2001**, *105*, 5106-5109.
21. De, T.; Maitra, A.; *Adv. Colloid Interface Sci*. **1995**, *59*, 95-193.
22. Zwan, van der G.; Hynes, J. T. *Chem. Phys.* **1991**, *152*, 169-183.

23. Hynes, J. T. *Charge-Transfer Reactions and Solvation Dynamics In Ultrafast Dynamics of Chemical Systems;* Simon, J. D.' Ed.; Kluwer: Dodrecht, 1994; p 345-381.
24. Pradhan, T.; Biswas, R. *J. Phys. Chem. B* **2007**, *111*, 11524-11530.
25. Wong, M.; Thomas, J. K.; Graetzel, M. *J. Am. Chem. Soc.* **1976**, *98,* 2391-2397.
26. Karukstis, K. K.; Frazier, A. A.; Martula, D. S.; Whiles, J. A. *J. Phys. Chem.* **1996**, *100*, 11133-11138.
27. Amararene, A.; Gindre, M.; Le Hue´rou, J.-Y.; Nicot, C.; Urbach, W.; Waks, M. *J. Phys. Chem. B* **1997**, *101*, 10751-10756.
28. Zhang, J.; Bright, F. V. *J. Phys. Chem.* **1991**, *95,* 7900-7907.
29. Garcio-Rio, L.; Leis, J. R.; Iglesias, E. *J. Phys. Chem.* **1995**, *99*, 12318-12326.
30. Satoh, T.; Okuno, H.; Tominaga, K.; Bhattacharyya, K. *Chem. Lett.* **2004**, *33*, 1090-1091.
31. Bhattacharyya, K.; Hara, K.; Kometani, N.; Uozu, Y.; Kajimoto, O. *Chem. Phys. Lett.* **2002**, *361*, 136-142.
32. Datta, P.; Sen, P.; Mukherjee, S.; Halder, A.; Bhattacharyya, K. *J. Phys. Chem. B* **2003**, *107*, 10815-10822.
33. Sarkar, N.; Das, K.; Datta, A.; Das, S.; Bhattacharyya, K. *J. Phys. Chem.* **1996**, *100*, 10523-10527.
34. Datta, A.; Mandal, D.; Pal, S. K.; Bhattacharyya, K. *J. Phys. Chem. B* **1997**, *101*, 10221-10225.
35. Bhattachrayya, K.; Bagchi, B. *J. Chem. Sci.* **2007**, *119*, 113-121.
36. Bhattachrayya, K.; Bagchi, B. *J. Phys. Chem. A* **2000**, *104,* 10603-10613.
37. Dutt, G. B. *J. Phys. Chem. B* **2008**, *112*, 7220-7226.
38. Riter, R. E.; Willard, D. M.; Levinger, N. E. *J. Phys. Chem. B* **1998**, *102*, 2705-2714.
39. Pant, D.; Riter, R. E.; Levinger, N. E. *J. Chem. Phys.* **1998**, *109*, 9995-10002.
40. Riter, R. E.; Undiks, E. P.; Levinger, N. E. *J. Am. Chem. Soc.* **1998**, *120*, 6062-6067.
41. Willard, D. M.; Riter, R. E.; Levinger, N. E. *J. Am. Chem. Soc.* **1998**, *120*, 4151-4160.
42. Pant, D.; Levinger, N. E. *Langmuir,* **2000**, *16*, 10123-10130.
43. Willard, D. M.; Levinger, N. E. *J. Phys. Chem. B* **2000**, *104*, 11075-11080.

44. Corbeil, E. M.; Levinger, N. E. *Langmuir*, **2003**, *19*, 7264-7270.
45. Corbeil, E. M.; Riter, R. E.; Levinger, N. E. *J. Phys. Chem. B* **2004**, *108*, 10777-10784.
46. Correa, N. M.; Levinger, N. E. *J. Phys. Chem. B* **2006**, *110*, 13050-13061.
47. Tan, H. S.; Piletic, I. R.; Riter, R. E.; Levinger, N. E.; Fayer, M. D. *Phys. Rev. Lett.* 2005, 94, 057405(1)-057405(4).
48. Tan, H.-S.; Piletic, I. R.; Fayer, M. D. *J. Chem. Phys.* **2005**, *122*, 174501(1)-174501(9).
49. Piletic, I. R.; Moilanen, D. E.; Spry, D. B.; Levinger, N. E.; Fayer, M. D. *J. Phys. Chem. A* **2006**, *110*, 4985-4999.
50. Moilanen, D. E.; Levinger, N. E.; Spry, D. B.; Fayer, M. D. *J. Am. Chem. Soc.* **2007**, *129*, 14311-14318.
51. Moilanen, D. E.; Fenn, E. E.; Wong, D.; Fayer, M. D. *J. Am. Chem. Soc.* **2009**, *131*, 8318-8328.
52. Moilanen, D. E.; Fenn, E. E.; Wong, D.; Fayer, M. D. *J. Phys. Chem. B* **2009**, *113*, 8560-8568.
53. Moilanen, D. E.; Fenn, E. E.; Wong, D.; Fayer, M. D. *J. Chem. Phys.* **2009**, *131*, 014704(1)-014704(9).
54. Park, S.; Moilanen, D. E.; Fayer, M. D. *J. Phys. Chem. B* **2008**, *112*, 5279-5290.
55. Fenn, E. E.; Wong, D. B.; Fayer, M. D. *Proc. Natl. Acad. Sci. USA* **2009**, *106*, 15243-15248.
56. Cringus, D.; Lindner, J.; Milder, M. T. W.; Pshenichnikov, M. S.; Vohringer, P.; Wiersma, D. A. *Chem. Phys. Lett.* **2005**, *408*, 162-168.
57. Dokter, A.; Woutersen, S.; Bakker, H. J. *Proc. Natl. Acad. Sci. USA* **2006**, *103*, 15355-15358.
58. Onori, G.; Santucci, A. *J. Phys. Chem.* **1993**, *97*, 5430-5434.
59. Venables, D. S.; Huang, K.; Schmuttenmaer, C. A. *J. Phys. Chem. B* **2001**, *105*, 9132-9138.
60. Zhong, Q.; Baronavski, A. P.; Owrutsky, J. C. *J. Chem. Phys.* **2003**, *118*, 7074-7080.
61. Zhong, Q.; Baronavski, A. P.; Owrutsky, J. C. *J. Chem. Phys.* **2003**, *119*, 9171-9177.

62. Sando, G. M.; Dahl, K.; Owrutsky, J. C. *J. Phys. Chem. A* **2004**, *108*, 11209-11217.
63. Chowdhary, J.; Ladanyi, B. M. *J. Phys. Chem. A* **2011**, *115*, 6306-6316.
64. Pieniazek, P. A.; Lin, Y.-S.; Chowdhary, J.; Ladanyi, B. M.; Skinner, J. L. *J. Phys. Chem. B* **2009**, *113,* 15017-15028.
65. Chowdhary, J.; Ladanyi, B. M. *J. Phys. Chem. A* **2009**, *113*, 15029-15039.
66. Faeder, J.; Ladanyi, B. M. *J. Phys. Chem. B* **2005**, *109,* 6732-6740.
67. Harpham, M. R.; Ladanyi, B. M.; Levinger, N. E. *J. Phys. Chem. B* **2005**, *109*, 16891-16900.
68. Faeder, J.; Albert, M. V.; Ladanyi, B. M. *Langmuir* **2003**, *19,* 2514-2520.
69. Faeder, J.; Ladanyi, B. M. *J. Phys. Chem. B* **2001**, *105,* 11148-11158.
70. Faeder, J.; Ladanyi, B. M. *J. Phys. Chem. B* **2000**, *104,* 1033-1046.
71. Senapati, S.; Berkowitz, M. L. *J. Phys. Chem. A* **2004**, *108,* 9768-9776.
72. Abel, S.; Sterpone, F.; Bandyopadhyay, S.; Marchi, M. *J. Phys. Chem. B* **2004**, *108*, 19458-19466.
73. Rosenfeld, D. E.; Schmuttenmaer, C. A. *J. Phys. Chem. B* **2006**, *110*, 14304-14312.
74. Biswas, R.; Bagchi, B. *J. Chem. Phys.* **2010**, *133*, 084509(1)- 084509(7).
75. Biswas, R.; Chakraborti, T.; Bagchi, B.; Ayappa, K. G. *J. Chem. Phys.* **2012**, *137*, 014515(1)-014515(9).
76. Kinugasa, T.; Kondo, A.; Nishimura, S.; Miyauchi, Y.; Nishii, Y.; Watanabe, K.; Takeuchi, H. *Colloids Surf. A – Physicochem. Eng. Aspects* **2002**, *204*, 193-199.
77. Zulauf, M.; Eicke, H.-F. *J. Phys. Chem.* **1979**, *83*, 480-486.
78. Nandi, N.; Bagchi, B. *J. Phys. Chem. B* **1997**, *101*, 10954-10961.
79. Nandi, N.; Bhattacharyya, K.; Bagchi, B. *Chem. Rev.* **2000**, *100*, 2013-2046.
80. Lipgens, S.; Schubel, D.; Schlicht, L.; Spilgies, J.-H.; Ilgenfritz, G.; Eastoe, J.; Heenan, R. K. *Langmuir*, **1998**, *14*, 1041-1049.
81. Horng, M. L.; Gardecki, J. A.; Papazyan, A.; Maroncelli, M. *J. Phys. Chem.* **1995**, *99*, 17311-17337.
82. Abel, S.; Waks, M.; Marchi, M.; Urbach, W. *Langmuir* **2006**, *22*, 9112-9120.
83. Fee, R. S.; Maroncelli, M. *Chem. Phys.* **1994**, *183,* 235-247.
84. Horng, M. L.; Gardecki, J. A.; Maroncelli, M. *J. Phys. Chem. A* **1997**, *101*, 1030-1047.

85. Chapman, C. F.; Maroncelli, M. *J. Phys. Chem.* **1991**, *95*, 9095-9114.
86. Dahl, K.; Biswas, R.; Ito, N.; Maroncelli, M. *J. Phys. Chem. B* **2005**, *109*, 1563-1585.
87. Biswas, R.; Lewis, J. E.; Maroncelli, M. *Chem. Phys. Lett.* **1999**, *310*, 485-494.
88. Guchhait, B.; Gazi, H. A. R.; Kashyap, H. K.; Biswas, R. *J. Phys. Chem. B* **2010**, *114*, 5066-5081.
89. Guchhait, B.; Daschakraborty, S.; Biswas, R. *J. Chem. Phys.* **2012**, *136*, 174503(1) – 174503(16).
90. Chapman, C. F.; Fee, R. S.; Maroncelli, M. *J. Phys. Chem*. **1995**, *99*, 4811-4819.
91. Pradhan, T.; Biswas, R. *J. Phys. Chem. A* **2007**, *111*, 11514-11523.
92. Lakowicz, J. R. *Principles of Fluorescence Spectroscopy*, 2nd ed.; Kluwer Academic: New York, 1999.
93. Hansen, J. P.; McDonald, I. R. *Theory of Simple Liquids*, 2nd ed.; Academic, London, 1986.
94. Berendsen, H. J. C.; Grigera, J. R.; Straatsma, T. P. *J. Phys. Chem.* **1987**, *91*, 6269-6271.
95. Mayo, S. L.; Olafson, B. D.; Goddard, W. A. *J. Phys. Chem.* **1990**, *94*, 8897-8909.
96. Allen, M. P.; Tildesley, D. J. *Computer Simulation of Liquids*, Oxford, New York, 1987.
97. Wolf, D.; Keblinski, P.; Phillpot, S. R.; Eggebrecht, J. *J. Chem. Phys.* **1999**, *110*, 8254-8282.
98. (a) Matyushov, D. V. *J. Chem. Phys.* **2005**, *122*, 044502-1 – 044502-11; (b) Kometani, N.; Arzhantsev, S.; Maroncelli, M. *J. Phys. Chem. A* **2006**, *110*, 3405-3413.
99. Amararene, A.; Gindre, M.; Le Huerou, J. Y.; Urbach, W.; Valdez, D.; Waks, M. *Phys. Rev. E* **2000**, *61*, 682-689.
100. Nose, S. *J. Chem. Phys.* **1984**, *81*, 511-519.
101. Hoover, W. G. *Phys. Rev. A* **1985**, *31*, 1695-1697.
102. Forester, T. R.; Smith, W. *The DL_POLY Reference Manual*, CCLRC, Daresbury Laboratory, England, 1985.
103. Riddick, J. A.; Bunger, W. B.; Sakano, T. K. *Organic Solvents*; Wiley: New York, 1986.
104. Moran, P. D.; Bowmarker, G. A.; Cooney, R. P. *Langmuir*, **1995**, *11*, 738-743.

105. Pal, S.; Bagchi, B.; Balasubramanian, S. *J. Phys. Chem. B.*, **2005**, *109*, 12879-12890.

106. Pal, S.; Balasubramanian, S.; Bagchi, B. *J. Chem. Phys.* **2002**, *117*, 2852-2859.

107. Pal, S.; Bagchi, B.; Balasubramanian, S. *J. Phys. Chem. B.*, **2003**, *107*, 5194 - 5202.

108. Balasubramanian, S.; Pal, S.; Bagchi, B. *Phys. Rev. Lett.* **2002**, *89*, 115505-1 – 115505-4.

109. Balasubramanian, S.; Pal, S.; Bagchi, B. *Phys. Rev. E* **2003**, *67*, 061502-1 – 061502-10.

110. Dastidar, S. G.; Mukhopadhyay, C. *Phys. Rev. E* **2004**, *70*, 06901-1 – 06901-9.

111. Bruce, C. D.; Senapati, S.; Berkowitz, M. L.; Perera, L.; Forbes, M. D. E. *J. Phys. Chem. B* **2002**, *106*, 10902 – 10907.

112. Kuhn, H.; Rehage, H. *Progr. Colloid Polym. Sci.* **1998**, *111*, 158-161.

113. Shelley, J. C.; Sprik, M.; Klein, M. L. *Langmuir* **1993**, *9*, 916-926.

114. Bandyopadhyay, S.; Tarek, M.; Lynch, M. L.; Klein, M. L. *Langmuir* **2000**, *16*, 942-946.

115. Mackerell, Jr.; A. D. *J. Phys. Chem.* **1995**, *99*, 1846-1855.

116. Thompson, W. H. *J. Chem. Phys.* **2004**, *120*, 8125-8133.

117. Gomez, J. A.; Thompson, W. H. *J. Phys. Chem. B* **2004**, *108*, 20144-20154.

118. Kusalik, P. G.; Svishchev, I. M. *Science* **1994**, *265*, 1219-1221.

119. Sengupta, A.; Khade, R. V.; Hazra, P. *J. Phys. Chem. A.* **2011**, *115*, 10398-10407.

120. Zhu, Y.; Granick, S. *Phys. Rev. Lett.* **2001**, *87*, 096104-1–096104-4.

121. Raviv, U.; Perkin, S.; Laurat, P.; Klein, J. *Langmuir* **2004**, *20*, 5322-5332.

122. Das, A.; Chakrabarti, J. *Phys. Rev. E* **2012**, *85*, 050601-1 – 050601-5.

123. Li, T.-D.; Gao, J.; Szoszkiewicz, R.; Landman, U.; Riedo, E. *Phys. Rev. B.* **2007**, *75*, 115415-1– 115415-6.

124. Schoen, M.; Diestler, D. J.; Cushman, J. H. *J. Chem. Phys.* **1987**, *87*, 5464-5476.

125. Gotzelmann, B.; Dietrich, S. *Phys. Rev. E.* **1997**, *55*, 2993-3005.

126. Biswas, R.; Bagchi, B. *J. Phys. Chem.* **1996**, *100*, 1238-1245.

127. Kashyap, H. K.; Biswas, R. *Ind. J. Chem.* **2010**, 49A, 685-694.

128. Roy, D.; Maroncelli, M. *J. Phys. Chem. B* **2012**, *116*, 5951-5970.

129. Sajadi, M.; Weiberger, M.; Wagenknecht, H.-A.; Ernsting, N. P. *Phys. Chem. Chem. Phys.* **2011**, *13*, 17768-17774.

130. Nandi, N.; Roy, S.; Bagchi, B. *J. Chem. Phys.* **1995**, *102*, 1390-1397.

131. Mark, P.; Nilsson, L. *J. Phys. Chem. A* **2001**, *105*, 9954-9960.

132. Fenn, E. E.; Wong, D. B.; Giammanco, C. H.; Fayer, M. D. *J. Phys. Chem. B.* **2011**, *115*, 11658-11770.

133. Kondo, M.; Heisler, I. A.; Conyard, J.; Rivett, J. P. H.; Meech, S. R. *J. Phys. Chem. B.* **2009**, *113*, 1632-1639.

134. Shirota, H.; Segawa, H. *Chem. Phys.* **2004**, *306*, 43-50.

Chapter 7

Probing the Electrolyte Induced Heterogeneity in Polymer: A Case Study with PEG-Based Polymer Electrolyte

7.1 Introduction

Polymer electrolytes constitute a subject of intense study because of their potential applications in battery technology, dye sensitized solar cells, and chemical sensors.[1-4] These materials can be used for a wide temperature range, from ~220 K to moderate ~470 K. With increasing concern for future energy generation and storage, use of polymer electrolyte in battery technology has received special attention. Ion conduction is the key role in battery technology and the efficiency of battery depends upon the types of electrolytes.[5-6] For many years the research on polymer-electrolyte composites has been focussed on design of flexible polymers where shorter segmental relaxation induces higher ionic conductivity. Previously, ionic conductivity aspects of polymer electrolytes have been explored for amorphous and crystalline states. Cation shows greater transference in crystalline form whereas in amorphous form both ions show significant transference capability.[6-7] In these materials the ion transport is induced by local motion of polymer chain segment repeatedly creating new co-ordination sites into which the ion may then migrate.[6] These polymer-electrolyte composites usually possess low conductivity and, as a result, attempts have been made to improve conductivity by changing the electrolytes.[8-10] Various new types of polymers and catalysts have also been synthesized for improving conductivity, chemical, mechanical and dimensional stabilities.[11-12] As already mentioned, efficiency of this polymer electrolyte critically depends on segmental motion of host polymer and has been explored by several experimental methods.[6-7,13,14]

In order to take advantage of their potential application, it is important to understand the microscopic mechanism controlling ionic conductivity associated to segmental dynamics of polymers. Among the various polymer-electrolytes, the ones based on polyethylene oxide (PEO) are the best and mostly studied[6-9,13-21] because PEO possess large solubilising power for wide range of salts. It is commonly accepted that, in presence of appreciable amount of salt in polymer electrolyte, cation (usually Li^+) coordinates with polymer molecules with both inter- and intra-molecular fashion.[1,6,13] Quasi-elastic neutron scattering (QENS) studies have been performed in some higher molecular weight based polymer (polyethylene oxide, PEO) with Li^+ based electrolytes and two dynamic processes have been found, one is faster due to pure polymer and the other is slower because of polymer-Li^+ complex formation. These facts match well with molecular dynamics simulations of same type of system and the slow process has been explained in terms of heterogeneous dynamics.[14] QENS study has also revealed that the cations are co-ordinated with several ether oxygens of polymer which affects the segmental dynamics of polymer. When the ratio between the numbers of ether oxygens of polymer and metal ion (O:M) is ~ 10:1, the extent of segmental motion reaches a minimum due to formation of percolating network via cationic crosslink.[22] ^1H, ^7Li and ^{19}F NMR studies of PEO electrolyte systems have provided a picture of relaxation of ions and polymer segments. These experiments have shown that the cation motions are coupled with segmental motions but the anions move freely.[23] Different local environments of lithium cations due to preferential coordination in PEUU-based polymer electrolytes has also been investigated by ^7Li MAS NMR with high-power proton decoupling technique.[24] Furthermore, dielectric relaxation studies of polymer-electrolyte composites have indicated that the relative dielectric constant varies with frequency due to coupling of ion and polymer segmental motions.[18] Theoretical studies have explored the ion conduction mechanism in polymer electrolytes.[15-17,25,26] These theoretical studies have suggested that polymer chain dynamics plays a significant role in ion conduction mechanism and there exist ion-polymer interactions. A molecular dynamics[17] study of polymer-electrolyte with low molecular weight polymer has suggested that the polymer dissolves the salt by complexing the cation as a polydentate ligand through chelate effect! In addition, this study has shown that among different cations, Li^+ possesses the strongest affinity to be coordinated with ethereal oxygen atoms of the host polymer. Moreover, for a typical Na^+ ion, solvation in polymer electrolyte belongs to the nonlinear response regime; the nonlinear behaviour being associated with the specific binding of the cation to the negative oxygen sites the simulated solvation response bimodal.[27]

Eventhough several studies[14,18,22,23,28,29,30] have been performed to explore several aspects polymer-electrolyte composites, a complete understanding of the relaxation dynamics of these complex systems is yet to be achieved. Time dependent fluorescence Stokes shift and rotational relaxation studies of a laser exited dipolar solute can be used to explore both the interaction and dynamics of these composite materials. To the best of our knowledge, there is no such study of excited state relaxation (solvation and solute rotation) dynamics in polymer electrolytes except some reports on pure short chain polymers.[31,32] Thus, our proposed study is an attempt to understand the microscopic picture of relaxation phenomena in low molecular weight based polymer-electrolyte systems in liquid state. Note the relaxation dynamics of aqueous solution of polymer solution using a fluorescence solute[33,34] have revealed a biphasic solvation dynamics having short time constants of ~ 50 ps and long time constants of several hundreds of picoseconds. Aqueous solution of triblock copolymer, P123 gel, has also been studied via fluorescence method and a marked red edge excitation shift (REES) has been revealed.[35]

In this chapter, we have studied the fluorescence Stokes shift dynamics and rotational relaxation of a dipolar solute (C153) in polymer-electrolyte composites based on polyethylene glycol (PEG) and lithium/ potassium nitrate (Li/ KNO_3), and compared with the results obtained pure PEG. In order to explore the excited state dynamics in liquid state, a hydrophilic block copolymer, PEG (lower homolog of PEO) has been considered which also has many technological and biochemical applications.[36,37] We have used the following composition of polymer-electrolyte composite: $[0.85\text{PEG} + 0.15\{f\text{LiNO}_3 + (1-f)\text{KNO}_3\}]$. The fraction of cation (Li^+ and K^+) and temperature have been varied to investigate the effects cation on segmental motion and the subsequent heterogeneity.

7.2 Experimental Section

Laser grade C153 was obtained from Exciton and used as received. Polyethylene glycol (PEG) of molecular weight 300 was purchased from Merck and used without further purification. AR grade $LiNO_3$ and KNO_3 were obtained from Sigma-Aldrich and Fluka respectively and used as received. The experimental solutions were prepared by mixing of required amount of electrolyte/s with PEG at around 298 K. Proper care was taken to ensure complete dissolution of the added electrolyte. Steady state and time resolved measurement techniques and the corresponding data analysis procedures have been described in chapter 2 and also in refs.[38-43] For temperature dependent experiments we maintained the temperature with an attachment from Julabo (Model: F32).

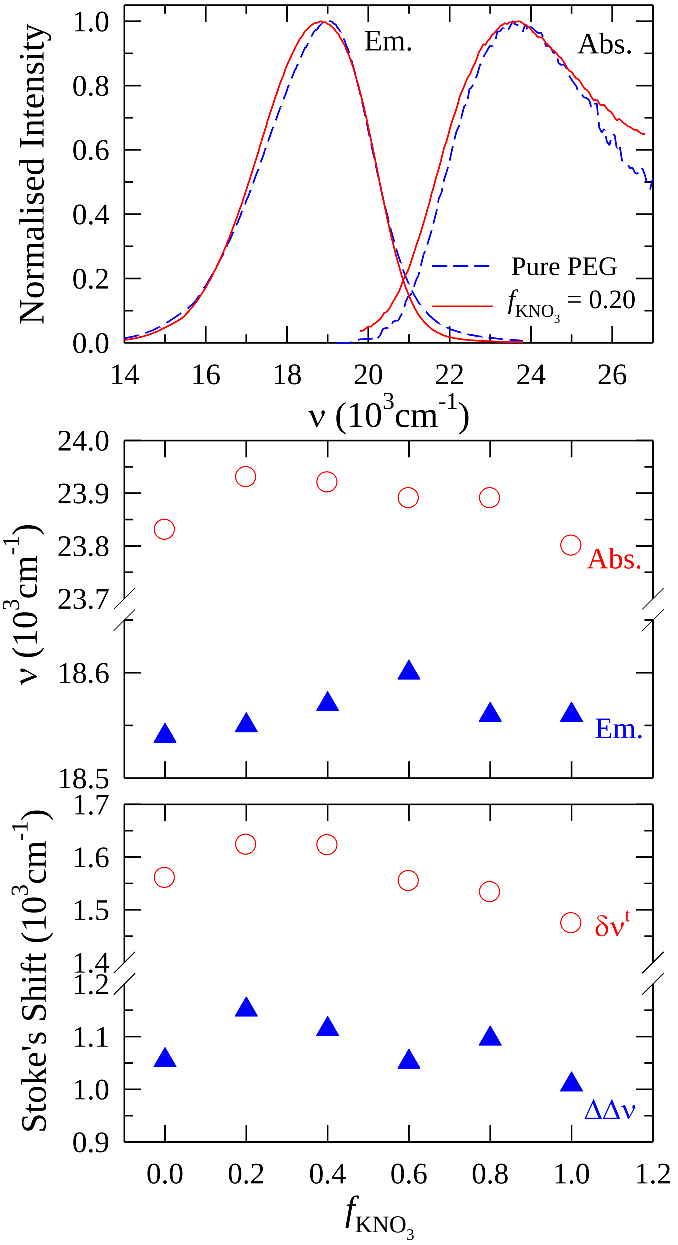

Fig. 7.1: Representative steady state absorption and emission spectra (color codded) of the dissolved solute, C153 in [0.85PEG + 0.15{f KNO$_3$ + (1-f) LiNO$_3$}] mixtures at f_{KNO_3} = 0.20 and those in pure PEG (upper panel). Data in the middle panel represent composition dependence of absorption and emission frequencies; lower panel shows the composition dependence of steady state and dynamic shifts: relative (ΔΔν) and estimated dynamic ($\delta\nu^t$) shifts. All the data are for 298 K.

7.3 Results and Discussion

7.3.1 Steady State Spectroscopic Studies

Steady state absorption and emission spectra of C153 in [85 PEG + 15 {*f*KNO_3 + (1-*f*) $LiNO_3$}] mixtures were collected at various fractions of the electrolyte/s. The representative absorption and emission spectra of C153 at f_{KNO_3} = 0.2 and those in pure PEG at 298 K are shown in upper panel of Fig. 7.1. The absorption and emission spectrum in this system is red shifted by ~ 250 and 350 cm^{-1} respectively in comparison to pure PEG. These results indicate that the probe (C153) experiences probably somewhat higher polarity in PEG-electrolyte systems compared to pure PEG. The spectral features are presented in middle and lower panel of Fig. 7.1. Absorption and emission frequency show a nonmonotonic KNO_3 concentration dependence (middle panel, Fig. 7.1) but within our instrumental resolution (~ 150 cm^{-1}). The nonmonotonicity is also reflected in KNO_3 concentration dependent relative ($\Delta\Delta\nu$) and estimated ($\Delta\nu_{est}(t)$) Stokes shift which is shown in the bottom panel of Fig. 7.1. Similar non-monotonic behaviour of solution conductivity has also been found earlier for deep eutectic solvents containing ions and explained in terms of polarization and mixed alkali effect (MAE).[45] When Li^+ is progressively replaced by K^+, the system becomes less structured and it results in a decrease in medium viscosity of polymer electrolytes. The emission FWHM (full width at half maxima) of C153 shows a red shift of about 300 cm^{-1} with increasing KNO_3 concentration (not shown). An important point here is that $\Delta\nu_{est}(t)$[46] in these PEG-electrolytes is larger by ~ 500 cm^{-1} than the $\Delta\Delta\nu$. This is because of sluggish environmental relaxation causing fluorescence emission arising from incompletely solvent relaxed excited solute.

7.3.2 Excitation Wavelength Dependence of the Steady State Fluorescence

We performed excitation wavelength dependence studies of the steady state emission in pure PEG and PEG-electrolyte composites at f_{KNO_3} = 0.2 and 0.8 using C153 (τ_{life} ~5 ns). In pure polyethylene glycol (PEG), the solute shows absorption and emission maxima at ~ 23700 cm^{-1} and ~ 19000 cm^{-1} respectively at 298 K. Emission maximum exhibits a little or insignificant dependence (less than 200 cm^{-1}) on excitation wavelength ($\lambda_{exc.}$) in pure

PEG. This indicates a homogeneous (with respect to the excited state lifetime of C153) nature of the PEG. In PEG-electrolyte system at f_{KNO_3} = 0.2, the absorption maximum of C153 is at ~ 23500 cm^{-1} and that of emission is at ~ 18700 cm^{-1} which indicates excitation wavelength dependence ($\lambda_{exc.}$). This is shown in the upper panel of Fig. 7.2. The emission frequency shows a red shift of ~ 600 and 500 cm^{-1} in going from $\lambda_{exc.}$ = 370 to

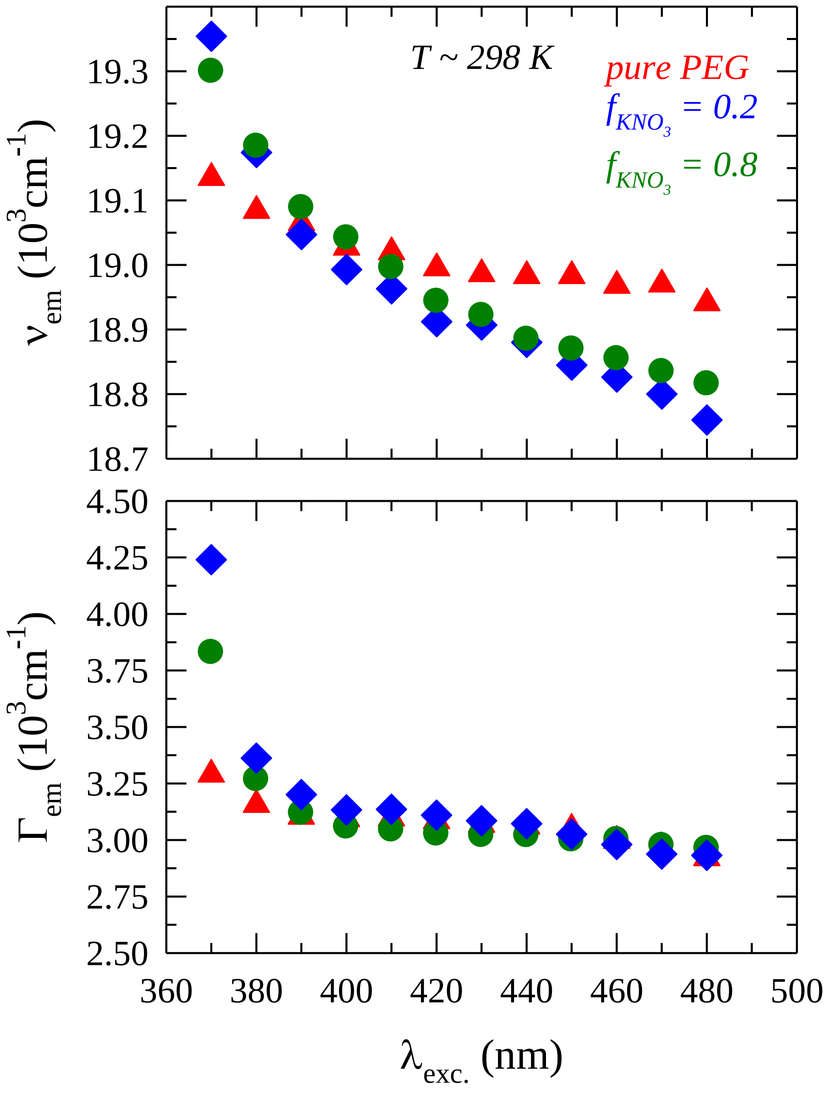

Fig. 7.2: Excitation wavelength dependence (λ_{exc}) of emission peak frequency (ν_{em}) for C153 (upper panel) and full width at half maxima, FWHM (lower panel) in pure PEG and [0.85PEG + 0.15{f KNO$_3$ + (1-f) LiNO$_3$}] solutions (color codded). The uncertainty in frequencies is better than $\pm 150\,\mathrm{cm}^{-1}$.

480 nm for f_{KNO_3} = 0.2 and 0.8 respectively. The width (FWHM) also shows a red shift (~ 1000 cm^{-1}) with increasing excitation wavelength in PEG-electrolyte systems which is a factor of 3 less than that (~ 300 cm^{-1}) in pure PEG. This $\lambda_{exc.}$ dependence of the emission characteristics suggest the presence of micro-heterogeneity and a distribution of fluorophores in different regions of varying polarity in PEG-electrolyte composites. Similar excitation wavelength dependence of dissolved dipolar solutes have also been found in ionic liquids[47(a)-47(d)] and reverse micelles[47(e)]. It is reported that presence of salt in polyethylene oxide (PEO) leads to transient bond formation between cation and ethereal oxygens (-O-). This may lead to formation of microscopic domains [1,6,13] which will fluctuate following a distribution of stability time. In the present case coordination of cations with O-atoms of PEG molecules induces the micro-heterogeneity leading to formation of ensembles of energetically different molecules which in turn causes the observed $\lambda_{exc.}$ dependence.

7.3.3 Solvent Relaxation Dynamics: Composition Dependence

For the measurements of solvent relaxation dynamics we collected 18-20 time resolved fluorescence intensity decays across the steady state emission spectral envelope for a fixed wavelength interval. The only decay in the blue end and rise accompanied by decay at red end clearly indicates the existence of time resolved Stokes shift in PEG-electrolyte systems. All the decays were fitted with tri-exponential function of time except around peak where decays were usually found to be bi-exponential. The time resolved emission spectra (TRES) were constructed from the measured decays following the reported method.[39] The representative time resolved emission spectra of C153 for f_{KNO_3} = 0.40 at 298 K are shown in Fig. A27 of the Appendix. The measured shift ($\Delta\nu_{obs}(t)$) in this case is ~ 1100 cm^{-1} which is less than the estimated shift, ($\Delta\nu_{est}(t)$ ~ 1600 cm^{-1}).[46] We have therefore missed a significant portion (~ 32 %) of the total dynamics due to broader time resolution of our setup (IRF ~ 70 ps). The observed and estimated Stokes shifts along with missing portions at different compositions of [0.85PEG + 0.15{fKNO$_3$ + (1-f)LiNO$_3$}] at ~ 298 K are presented in Table 7.1. In all the cases we observed the extrapolated $t = \infty$ emission spectrum is red-shifted by ~ 500 - 700 cm^{-1} with respect to the corresponding steady state emission spectrum. Similar observation has also been made earlier in fluorescence studies of ionic liquids,[48] molten mixtures[40,49,50] and confined environments[41,51] where slow solvent relaxation was made responsible for such a difference. The relaxation parameters of S(t) fitting for different composition (f_{KNO_3}) at ~ 298 K are presented in Table 7.2. From this table it is clearly seen that the decays of S(t) at each composition are described by two distinctly separate time constants. Note that biexponential dynamics has also been found earlier in short chain alcohols[32] and pure PEG[31] with short time constant very similar to those obtained here for polymer electrolytes.

Table 7.1: Dynamic Stokes' shift and percentage of missing portion of the dynamics for C153 in [0.85PEG + 0.15{fKNO$_3$ + (1-f)LiNO$_3$}] mixtures at 298 K.

$f_{\mathrm{KNO_3}}$	ν^{t}_{est} (10^3cm^{-1})	ν^{t}_{obs} (10^3cm^{-1})	% missed
0.00	1.560	1.013	35
0.20	1.642	1.095	33
0.40	1.603	1.091	32
0.60	1.550	1.097	29
0.80	1.550	1.017	34
1.00	1.474	1.026	30

Data in Table 7.2 indicates that at the highest LiNO$_3$ concentration (f_{KNO_3}= 0.0), $S(t)$ decay provides the following time constants: 100 ps and 1538 ps. With increasing KNO$_3$ concentration the long time constant decreases and decay becomes faster. At the highest KNO$_3$ concentration (f_{KNO_3}= 1.0), the decay consists of two distinct time components of 64 ps and 1052 ps and there occurs a decrease in average solvation time ($<\tau_s>$). The similar trend of $<\tau_s>$ has been reported earlier.[40,50] The long time constant for the present PEG-electrolyte system is relatively slower than that obtained for pure PEG.[31] The observed slowing down of the dynamics is attributed to the freezing of motion of individual polyethylene glycol molecules in presence of ions (cations) due to formation of transient co-ordination bonds between cation and ethereal -O atoms. The structure of the polyethylene oxide, PEO (higher homolog of PEG) with electrolyte in molten state has been studied previously with several other techniques, for example, conductivity,[8-10] NMR,[23,29] quasielastic neutron scattering,[14,22,30] X-ray diffraction[52,53] and computer simulations.[14,17,27] It was suggested that in polymer, the cations are bound with same or different polymer molecules by co-ordination with ethereal oxygens forming transient M-O bonds and the segmental motion of polymer molecules are coupled with cation motion whereas anions move independently.[17] It has also been reported that the simulated jump time of polymer segmental motion is 3-5 ns.[17] In PEG, structure formation takes place in presence of ions. Cations are coordinated with ethereal oxygens of the same or different PEG molecules. Again, each cation does not create exactly the same environment with PEG molecules and thus different microenvironments are produced in presence of electrolyte, which is absent in pure PEG. The consequence of the electrolyte-induced structural heterogeneity in PEG has already been observed via excitation wavelength dependence of steady state emission and will be seen later in temperature dependent time resolved studies.

Table 7.2: Decay characteristics of solvent response function, S(t) of C153 in [0.85PEG + 0.15{fKNO$_3$ + (1-f)LiNO$_3$}] mixtures at 298 K.

f_{KNO_3}	η (cP)	a_1	τ_1 (ps)	a_2	τ_2 (ps)	$\langle\tau_s\rangle$ (ps)
0.00	144.4	0.63	100	0.37	1538	632
0.20	140.7	0.64	67	0.36	1430	558
0.40	130.6	0.63	50	0.37	1250	494
0.60	128.6	0.61	53	0.39	1111	465
0.80	125.6	0.64	73	0.36	1110	446
1.00	117.4	0.66	64	0.34	1052	400

One point to note here is that the viscosity values of the PEG-electrolyte systems are very high[45] compared to pure PEG and it is primarily coming from co-ordination of the metal cation with O-atom of PEG. The $<\tau_s>$ decreases when $LiNO_3$ is progressively replaced by KNO_3. In presence of $LiNO_3$ the PEG molecules are coordinated with Li^+ ions via ethereal O-atoms, which makes the system more structured and the dynamics becomes slower. When $LiNO_3$ is replaced by KNO_3 the system becomes less structured due to decrease in extent of co-ordination of PEG molecules with larger sized K^+ ions and thus facilitates faster dynamics. The representative f_{KNO_3} dependent $S(t)$ decays are shown in upper panel of Fig. A28 (Appendix). It is to be noted here that, due to our limited time resolution (IRF ~ 70 ps) employed we missed significant portion. If one can detect the full dynamics, the small time constant (50-100 ps) observed in our measurement could be in sub-picosecond range because of presence of intermolecular libration.[54-59] Another important point is that with increasing KNO_3 concentration instead of $LiNO_3$ the viscosity of the medium decreases. The exact reason was not mentioned in the literature.[45] The change in viscosity from that of pure PEG upon addition of electrolytes arises from M-O transient bond formation. When Li^+ is replaced by K^+, the extent of co-ordination of metal cations with ethereal O-atoms decreases. Both viscosity and $<\tau_s>$ decreases with increasing KNO_3 due to decrease in effective coordination but the extent of decrease in $<\tau_s>$ is very large compared to viscosity. The relatively free ion (K^+) is directly participating in the solvation phenomenon in KNO_3 rich regions which gives faster dynamics.[60-62] Therefore slowing down of dynamics in PEG-electrolyte systems compared to pure PEG confirms that the freezing of motion of individual PEG molecules in presence of electrolyte. A previously reported QENS study[14] in PEO with Li^+ based electrolyte system supports the observed result. In that study a fast and a relatively slow dynamics had been captured due to pure polymer and polymer-Li^+ complex respectively. In this chapter, the dynamics becoming faster with increasing KNO_3 concentartion in PEG-electrolyte systems suggests that the extent of co-ordination decreases owing to size effect and that leads to more facile solvation.

7.3.4 Solvent Relaxation Dynamics: Temperature Dependence

We carried out temperature dependent solvent relaxation dynamics in [0.85PEG + 0.15{(1-*f*)LiNO$_3$ + *f*KNO$_3$}] systems for f_{KNO_3} = 0.2, 0.8 and in pure PEG. The temperature dependent shifts along with missing components have been enlisted in Table A17 (Appendix). With increasing temperature there occurs a decrease in observed Stokes shift. The lower panel of Fig. A28 (Appendix) shows the representative temperature dependent $S(t)$ decays for C153 in PEG-electrolyte system at f_{KNO_3} = 0.80. At all temperatures and compositions including pure PEG, the $S(t)$ decays were found to be bi-exponential. The small time constants are in the range of ~ 30-120 ps and did not show any systematic dependence but the long time components show strong temperature dependence. As expected, $<\tau_s>$ decreases as the temperature increases and $S(t)$ decay becomes faster.[63,64] Table A18 (Appendix) summarizes the fitting parameters of $S(t)$ of C153 in pure PEG and PEG-electrolytes (f_{KNO_3} = 0.2 and 0.8) at all temperatures considered. With increasing temperature the amount of observed Stokes shift decreases due to faster movement of polymer molecules. At about 298 K and at f_{KNO_3} = 0.2, the decay time constants of solvent correlation function are ~67 ps and 1500 ps whereas those at 323K are found to be 74 ps and 750 ps. The long time constant decreases as the temperature increases due to decrease in medium viscosity.[63,64]

Let us now focus on the dependence of average solvation time, $<\tau_s>$, of C153 on the medium viscosity (η) because the latter is crucially related to the relaxation phenomena occurring in liquid phase[65-69] and solutions.[31,32,70,71] Fig. 7.3 shows $<\tau_s>$as a function of temperature-scaled viscosity (η/T) for pure PEG and PEG-electrolytes (at f_{KNO_3} = 0.2 and 0.8). In the upper panel of Fig. 7.3 we have shown the results for pure PEG. Here we fitted the curve with a power-law, $<\tau_s>= A(\eta/T)^p$ and obtained a p value of about unity (*p* = 0.94). From the middle and lower panel of figure, it is clear that solvation in polymer-electrolyte composites follows a power-law dependence of $<\tau_s>$ on η/T, with a fractional power much less than unity (*p = 0.45* and *0.55* for f_{KNO_3} = 0.2 and 0.8

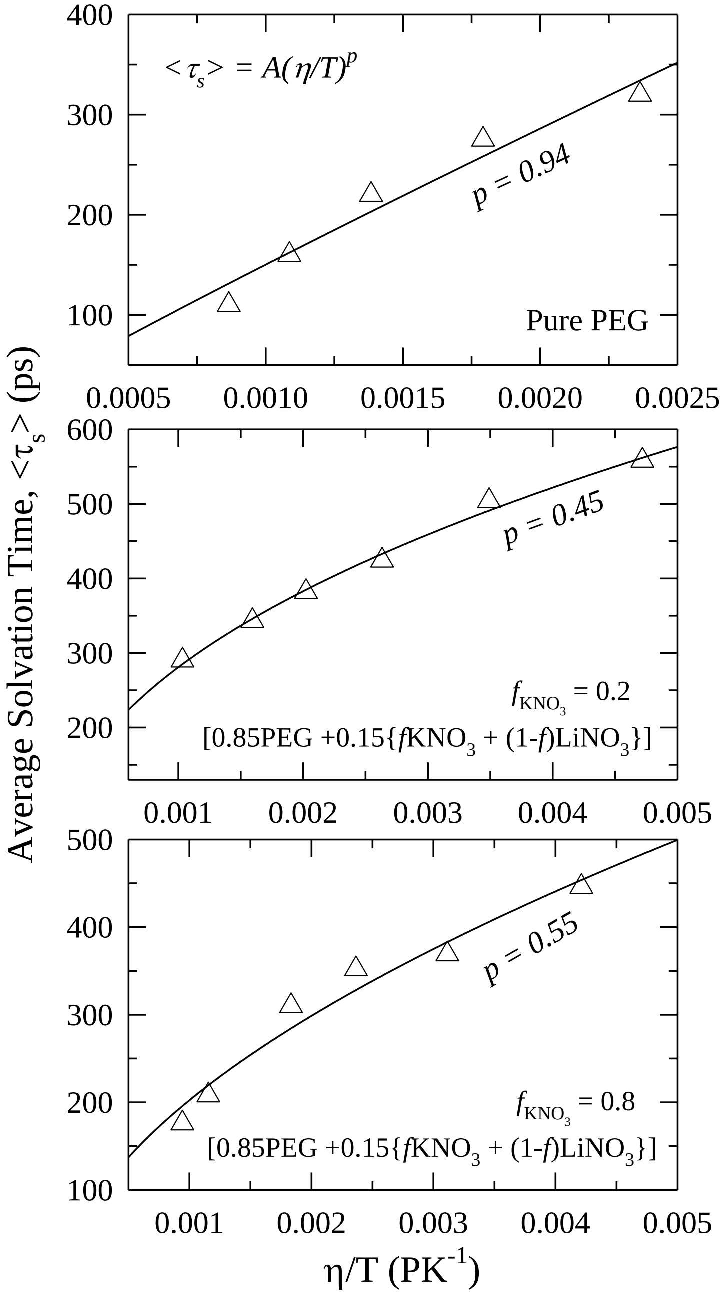

Fig. 7.3: Plot of average solvation time, $<\tau_s>$ versus temperature reduced viscosity, η/T. Triangle represent the experimental average solvation time, $<\tau_s>$ and solid lines are the fit through the data points to the relation $<\tau_s> = A(\eta/T)^p$. Upper panel represents experimental results in pure PEG, middle and lower panel represents the same in [0.85PEG + 0.15{f KNO_3 + (1-f) $LiNO_3$}] mixtures for f_{KNO_3} = 0.20 and 0.80 respectively. The associated p values obtained from the fitting are shown in respective figures.

respectively). This description suggests presence of pronounced heterogeneity in these polymer electrolytes. In other sense, the average solvation time is governed by translational diffusional motion of particles and is associated with the long time constant of $S(t)$ decay. $<\tau_s>$ of C153 were found to be proportional to η in pure polymer of different molecular weight reported earlier[31,72] but similar fractional viscosity dependence was also found in supercooled molten mixtures[40,50] where microscopic heterogeneity was the responsible factor. Validity of Stokes-Einstein (SE) relation in ionic liquid and ionic liquid mixtures have been checked by means of molecular dynamics simulation[73] and this study revealed that SE relation is not valid either in pure ionic liquid or ionic liquid cosolvent mixtures due to presence of dynamical heterogeneity. Break-down of SE relation in heterogeneous environments was found earlier where the homogeneous counterpart had satisfactorily been explained by normal SE relation.[74-83] In the present case non-hydrodynamic nature of diffusion of PEG-electrolyte leads to viscosity decoupling of average solvation time and this phenomenon signifies the presence of strong microscopic heterogeneity which is absent in pure PEG. As already discussed, the cation in PEG forms transient M-O bonds[1,6,13] resulting different domains[24] which leads to heterogeneity. Therefore presence of electrolyte in polyethylene glycol produces heterogeneity which is absent in the pure system. These results are well correlated with our steady state excitation wavelength dependence studies, where solute shows strong $\lambda_{exc.}$ dependence in polymer electrolyte but insignificant dependence in pure system.

7.3.5 Solute Rotational Dynamics: Composition Dependence

To further understand the solute-environment interaction we have followed solute rotational dynamics via dynamic fluorescence anisotropy measurements. The time-resolved fluorescence anisotropy decays have been measured here for variations in both temperature and electrolyte concentration. Temperature dependent rotational dynamics will be discussed in later section. Representative fluorescence anisotropy decay at f_{KNO_3} = 0.20 and at 298 K is shown in Fig. A29 (Appendix). All the anisotropy decays were fitted with bi-exponential functions of time. The bi-exponential anisotropy decay has been found previously for many organic solvents[42] and polymer systems.[31,72] Fitting parameters of measured composition and temperature dependent $r(t)$ decays along with average rotation times are enlisted in Table A19 and Table A20 (Appendix) for different composition. At f_{KNO_3} = 0.0 the average rotation time, $<\tau_r>$ is found to be 2551 ps, which shows significant decrease as $LiNO_3$ concentration decreases. At f_{KNO_3} = 1.0, the measured $<\tau_r>$

is 1880 ps and this is in accordance with decreases in medium viscosity.[45] Here it should be noted that, like $<\tau_s>$, the $<\tau_r>$ values obtained in PEG-electrolyte systems are also significantly larger than pure PEG. Slowing down of the solute reorientation dynamics occurs due to more structured environment of PEG in presence of electrolyte.

7.3.6 Solute Rotational Dynamics: Temperature Dependence

Now we will describe the temperature dependent rotational dynamics in pure PEG and PEG-electrolytes systems. For every case, average rotation time of solute decreases with increasing temperature. With increase in temperature the solute rotation becomes faster and is correlated with the concomitant decrease in medium viscosity.[45] The measured $<\tau_r>$ values for pure PEG are significantly smaller compared to those for PEG-electrolyte systems at all temperatures. It has already been mentioned that presence of electrolyte in PEG causes transient co-ordination bond that leads to solvent network and provides more rigid environment.[1,6,13] Solute rotation in such a constricted environment takes place slowly compared to that in pure system.

Let us now interpret solute rotational dynamics in light of viscosity of the medium. The temperature dependent $<\tau_r>$ are shown as a function of temperature-reduced viscosity, η / T. in Fig. 7.4. Like solvation dynamics, a power-law[40,50,84] of the form, $<\tau_r>= A(\eta / T)^p$, is needed to fit the data. While the pure PEG shows a p value of about unity (1.12), addition of electrolyte with PEG surprisingly gives p much less than unity (p ~ 0.66 and 0.71 for f_{KNO_3} = 0.2 and 0.8 respectively) shown in the middle and lower panel of Fig. 7.4. Note $<\tau_r>$ in pure PEG tracks η / T in accordance with the Stokes-Einstein-Debye (SED) prediction. When electrolyte is added to PEG, $<\tau_r>$ deviates substantially from the SED behaviour. A fractional SED[73,78,40,50,85,86] relation is required to interpret the data in PEG-electrolyte systems. Similar deviation from SED behavior in heterogeneous environments were found earlier.[84,87,88] Addition of electrolyte to PEG results structural heterogeneity and consequently normal hydrodynamics fails. Therefore, in the present case the observed result demonstrates that PEG-electrolytes possess appreciable amount of heterogeneity which is absent in pure PEG.

We have calculated the rotation times of solute from SED relation using stick and slip boundary condition as: $\tau_r^h = \frac{V\eta}{k_B T} fC$, where V and f is the volume and shape factor of solute (C153) respectively and C is the rotational coupling parameter of solute with surrounding environment.[48,89] The temperature dependent slip rotation times for pure PEG and PEG- electrolyte mixtures (f_{KNO_3} = 0.2, 0.8) are shown in the respective panel of Fig. 7.4 (stick rotation times are too large to fit in the same figure). From the Fig. 7.4 it is observed that the experimentally measured $<\tau_r>$ in pure PEG are very close to the slip boundary condition. It is well established that when size of the rotating solute is much larger than that of the solvent molecules, solute rotation is determined by the stick boundary condition (C = 1). Conversely, when the solute molecule is of comparable size or smaller, solute rotation is regulated by the slip boundary condition (0< C <1).[90-93] In the present case the solute size is much smaller compared to size of the solvent molecules (PEG) and this might be the reason for observed slip behaviour of $<\tau_r>$ in pure PEG. With addition of electrolyte in PEG, significant sub-slip signature at lower temperature appears. Similar sub-slip behaviour has also been reported earlier which originated mainly due to inhomogeneous microenvironment.[84,87,88] In PEG-electrolytes sub-slip behavior of $<\tau_r>$ arises from microscopic heterogeneity which is absent in pure PEG.[31,72]

We have also predicted hydrodynamic stick and slip limits by plotting f_{KNO_3} dependent $<\tau_r>$ of C153 as a function of η/T at a particular temperature. This has been shown in Fig. 7.5, where various panels represent data at various temperatures. From this figure it is clearly seen that at ~298 K the measured average reorientation times show a sub-slip behavior across the entire KNO_3 concentration range. As temperatures increases the measured $<\tau_r>$ increasingly goes towards slip limit. Interestingly, at a sufficient higher temperature (~343 K) the $<\tau_r>$ resides slightly above the slip limit. In the present case the solute size is much smaller compared to size of the solvent (PEG) molecule and thus slip behavior of $<\tau_r>$ is expected. Microscopic heterogeneity might be a reason for marked sub-slip behavior of $<\tau_r>$ of solute in this medium. Recent reports of similar sub-slip behavior for rotation of solute in alkylimidazolium ionic liquids[84,87,88] and molten

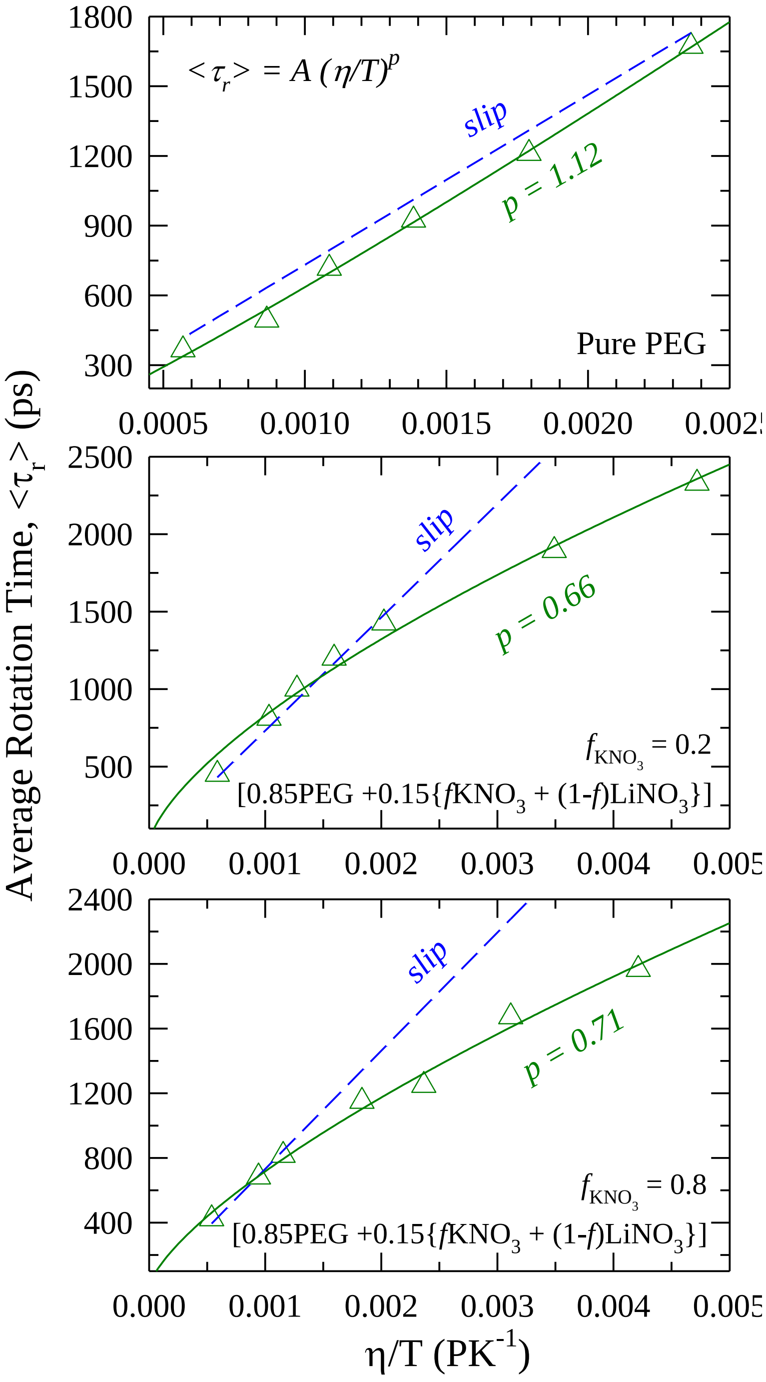

Fig. 7.4: Plot of average rotation time, $<\tau_r>$ versus temperature reduced viscosity, η/T. Triangles represent the experimental average rotation times, and solid lines are the fits through the data points to the relation $<\tau_r> = A(\eta/T)^p$. Upper panel represents experimental results in pure PEG, middle and lower panel represents the same in [0.85PEG + 0.15{f KNO$_3$ + (1-f) LiNO$_3$}] mixtures for f_{KNO_3} = 0.20 and 0.80 respectively. Associated p values obtained from the fitting are shown in respective figures. The dashed lines show the slip hydrodynamic limit.

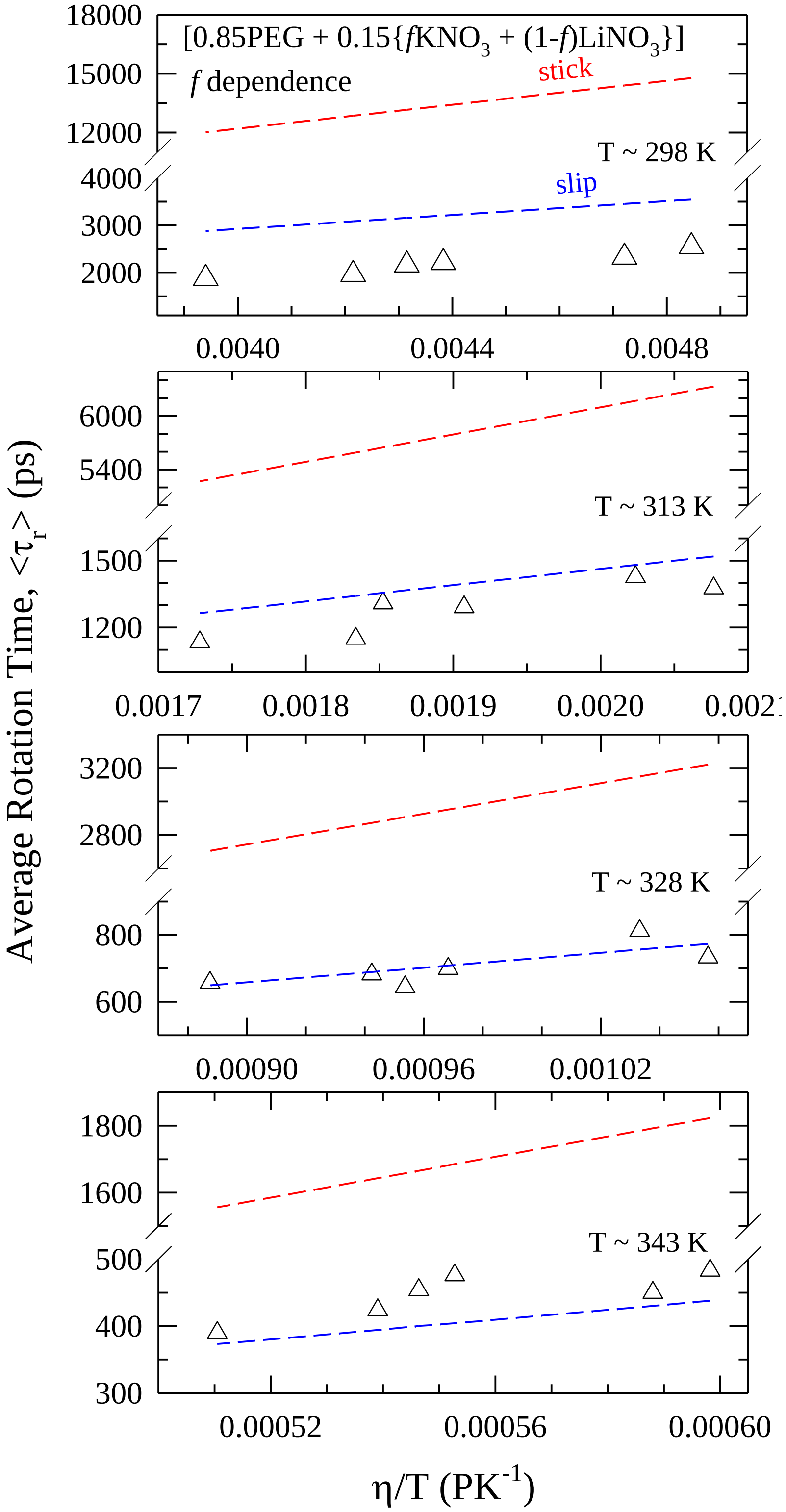

Fig. 7.5: Viscosity dependence of the average rotation times, $<\tau_r>$ of C153 for the [0.85PEG + 0.15{*f* KNO_3 + (1-*f*) $LiNO_3$}] mixtures studied. The measured $<\tau_r>$ for various mixtures compositions (f_{KNO_3}) at different temperatures are shown (triangles) as a function of η/T. The dashed lines show the hydrodynamic stick and slip limits (color coded).

mixtures[40,50] have suggested that the observed non-hydrodynamic behavior can be attributed to microscopic heterogeneity. Therefore heterogeneity is one of the reasons for observed non-hydrodyamic behavior of solute rotation in PEG-electrolytes. When the temperature of the system is increased, the extent of transient bond formation decreases due to thermal equilibrium distribution and consequently the systems tend towards homogeneity. This is reflected in observed $<\tau_r>$ at sufficiently higher temperatures.

7.4 Conclusion

In this chapter, we measured the Stokes shift and rotational dynamics of a non reactive solute (C153) in PEG-electrolytes as a function of electrolyte concentration and temperature. Addition of electrolytes in pure PEG slows down the dynamics significantly. A comparison with pure system using the hydrodynamic relations shows that PEG-electrolytes possess significant microscopic heterogeneity but the pure system doesn't. The normal SE and SED relations explain quantitatively the data of pure PEG but fractional relations are required to interpret the data in PEG-electrolytes. Addition of electrolyte in PEG leads to more structured and heterogeneous environment. The roles of different types of cations in PEG-electrolytes have also been investigated. The steady state excitation wavelength dependent study also supports the above facts. A translational and rotational decoupling probed via solvation and rotational dynamics has been demonstrated in PEG-electrolytes whereas the pure system exhibits no significant decoupling. These results have been explained in terms heterogeneity eventhough our study doesn't predict it quantitatively. The present study should motivate small angle neutron scattering (SANS) study and computer simulation in these systems so that the length-scales of heterogeneity could be determined. The validity of a fractional single-file diffusion model[94-97] could also be investigated to explain the observed breakdown of the SE and SED relations in PEG-electrolytes.

References:

1. *Application of Electroactive Polymers* Ed. Scrosati, B. Chapman & Hall, London, **1993**.
2. Tarascon, J.-M.; Armand, M. *Nature* **2001**, *414*, 359.
3. Barnesy, A.; Despotakisy, A.; Wongz, T. C. P.; Andersonz, A. P.; Chambersz, B.; Wrighty, P. V. *Smart Mater. Struct.* **1998**, *7*, 752.
4. Croce, F.; Appetecchi, G. B.; Persi, L.; Scrosati, B. *Nature* **1998**, *394*, 456
5. Watanabe, M.; Ogata, N. *British Polymer Journal* **1988**, *20*, 181.
6. Gadjourova, Z., Andreev, Y. G.; Tunstall, D. P.; Bruce, P. G. *Nature* **2001**, *412*, 520.
7. Gorecki, W.; Donoso, P.; Berthier, C.; Mali, M.; Roos, J.; Brinkmann, D.; Armand, M. B. *Solid State Ionics* **1988**, *28-30*, 1018.
8. Christie, A. M.; Lilley, S. J.; Staunton, E.; Andreev, Y. G.; Bruce, P. G. *Nature* **2005**, *433*, 50.
9. Zhou, D.; Mei, X.; Ouyang, J. *J. Phys. Chem. C* **2011**, *115*, 16688.
10. Smith, D. M.; Dong, B.; Marron, R. W.; Birnkrant, M. J.; Elabd, Y. A.; Natarajan, L. V.; Tondiglia, V. P.; Bunning, T. J.; Li, C. Y. *Nano Lett.* **2012**, *12*, 310.
11. Miyatake, K.; Chikashige, Y.; Highchi, E. Watanabe, M. *J. Am. Chem. Soc.* **2007**, *129*, 3879.
12. Huang, S.-Y.; Ganesan, P.; Park, S.; Popov, B. N. *J. Am. Chem. Soc.* **2009**, *131*, 13898.
13. MacGlashan, G. S.; Andree, Y. G.; Bruce, P. G. *Nature* **1999**, *398*, 792.
14. Triolo, A.; Arrighi, V.; Triolo, R.; Passerini, S.; Mastragostino, M.; Lechner, R. E.; Ferguson, R.; Borodin, O.; Smith, G. D. *Physica B: Condensed Matter* **2001**, *301*, 163.
15. Halley, J. W.; Duan, Y.; Curtiss, L. A.; Baboul, A. G. *J. Chem. Phys.* **1999**, *111*, 3302.
16. Johnson, J. A.; Saboungi, M.-L.; Price, D. L.; Ansell, S.; Russell, T. P.; Halley, J. W.; Nielsen, B. *J. Chem. Phys.* **1998**, *109*, 7005.
17. Muller-Plathe, F.; van Gunsteren, W. F. *J. Chem. Phys.* **1995**, *103*, 4745.
18. Agrawal, S.; Singh, M.; Tripathi, M.; Dwivedi, M.; Pandey, K. *J. Mat. Sci.* **2009**, *44*, 6060.

19. Chaurasia, S. K.; Singh, R. K.; Chandra, S. *J. Polym. Sci., Part B: Polym. Phys.* **2011**, *49*, 291.
20. Zalewska, A.; Stygar, J.; Ciszewska, E.; Wiktorko, M.; Wieczorek, W. *J. Phys. Chem. B* **2001**, *105*, 5847.
21. Stygar, J.; Biernat, A.; Kwiatkowska, A.; Lewandowski, P.; Rusiecka, A.; Zalewska, A.; Wieczorek, W. *J. Phys. Chem. B* **2004**, *108*, 4263.
22. Carlsson, P.; Mattsson, B.; Swenson, J.; Torell, L. M.; Käll, M.; Börjesson, L.; McGreevy, R. L.; Mortensen, K.; Gabrys, B. *Solid State Ionics* **1998**, *113-115*, 139.
23. Donoso, J. P.; Bonagamba, T. J.; Panepucci, H. C.; Oliveira, L. N.; Gorecki, W.; Berthier, C.; Armand, M. *J. Chem. Phys.* **1993**, *98*, 10026.
24. Wang, H.-L.; Kao, H.-M.; Wen, T.-C. *Macromolecules* **2000**, *33*, 6910.
25. Sutjianto, A.; Curtiss, L. A. *Chem. Phys. Lett.* **1997**, *264*, 127.
26. Arimura, T.; Ostrovskii, D.; Okada, T.; Xie, G. *Solid State Ionics* **1999**, *118*, 1.
27. Olender, R.; Nitzan, A. *J. Chem. Phys.* **1995**, *102*, 7180.
28. Greenbaum, S. G. *Solid State Ionics* **1985**, *15*, 259.
29. Pak, Y. S.; Adamic, K. J.; Greenbaum, S. G.; Wintersgill, M. C.; Fontanella, J. J.; Coughlin, C. S. *Solid State Ionics* **1991**, *45*, 277.
30. Mao, G.; Perea, R. F.; Howells, W. S.; Price, D. L.; Saboungi, M.-L. *Nature* **2000**, *405*, 163.
31. Shirota, H.; Segawa, H. *J. Phys. Chem. A* **2003**, *107*, 3719.
32. Argaman, R.; Huppert, D. *J. Phys. Chem. A* **1998**, *102*, 6215.
33. Sakamaki, T.; Fujino, T.; Hosoi, H.; Tahara, T.; Korenaga, T. *Chem. Phys. Lett.* **2009**, *468*, 171.
34. Sen, S.; Sukul, D.; Dutta, P.; Bhattacharyya, K. *J. Phys. Chem. B* **2002**, *106*, 3763.
35. Ghosh, S.; Adhikari, A.; Mandal, U.; Dey, S.; Bhattacharyya, K. *J. Phys. Chem. C* **2007**, *111*, 8775.
36. Saito, H.; Hoffman, A. S.; Ogawa, H. I. *J. Bioact. Compatible Polym.* **2007**, *22*, 589.
37. Bahmani, B.; Gupta, S.; Upadhyayula, S.; Vullev, V. I.; Anvari, B. *J. Biomed. Opt.* **2011**, *16*, 051303.
38. Horng. M. L.; Gardecki, J. A.; Papazyan, A.; Maroncelli, M. *J. Phys. Chem.* **1995**, *99*, 17311.
39. Maroncelli, M.; Fleming, G. R. *J. Chem. Phys.* **1987**, *86*, 6221.

40. Guchhait, B.; Gazi, H. A. R.; Kashyap, H.; Biswas, R. *J. Phys. Chem. B* **2010**, *114*, 5066.
41. Sarma, N.; Borah, J. M.; Mahiuddin, S.; Gazi, H. A. R.; Guchhait, B.; Biswas, R. *J. Phys. Chem. B* **2011**, *115*, 9040.
42. Horng, M. L.; Gardecki, J. A.; Maroncelli, M. *J. Phys. Chem. A* **1997**, *101*, 1030.
43. (a) Biswas, R.; Das, A. R.; Pradhan, T.; Touraud, D.; Kunz, W.; Mahiuddin, S. *J. Phys. Chem. B* **2008**, *112,* 6620; (b) Pradhan, T.; Ghoshal, P.; Biswas, R. *J. Chem. Sci.* **2008**, *120*, 275.
44. Cross, A. J.; Fleming, G. R. *Biophys. J.* **1984**, *46*, 45.
45. Kalita, G.; Sarma, K. G.; Mahiuddin, S. *J. Chem. Eng. Data* **2000**, *45*, 912.
46. Fee, R. S.; Maroncelli, M. *Chem. Phys.* **1994**, *183*, 235.
47. (a) Jin, H.; Li, X.; Maroncelli, M. *J. Phys. Chem. B* **2007**, *111*, 13473. (b) Samanta, A. *J. Phys. Chem. B* **2006**, *110*, 13704. (c) Mandal, P. K.; Sarkar, M.; Samanta, A. *J. Phys. Chem. A* **2004**, *108*, 9048. (d) Mandal, P. K.; Paul, A.; Samanta, A. *J. Photochem. Photobiol. A: Chem.* **2006**, *182*, 113. (e) Biswas, R.; Das, A. R.; Pradhan, T.; Touraud, D.; Kunz, W.; Mahiuddin, S. *J. Phys. Chem. B* **2008**, *112*, 6620.
48. Jin, H.; Baker, G. A.; Arzhantsev, S.; Dong, J.; Maroncelli, M. *J. Phys. Chem. B* **2007**, *111*, 7291.
49. Gazi, H. A. R.; Guchhait, B.; Daschakraborty, S.; Biswas, R. *Chem. Phys. Lett.* **2011**, *501*, 358.
50. Guchhait, B.; Daschakraborty, S.; Biswas, R. *J. Chem. Phys.* **2012**, *136*, 174503.
51. Pradhan, T.; Gazi, H.; Guchhait, B.; Biswas, R. *J. Chem. Sci.* **2012**, *124*, 355.
52. Pradhan, D. K.; Choudhary, R. N. P.; Samantaray, B. K. *Express Polymer Letters* **2008**, *2*, 630.
53. Hung, Y.; Tawfik, H.; Mahajan, D. *J. Power Sources* **2009**, *186*, 123.
54. Bagchi, B.; Biswas, R. *Adv. Chem. Phys.* **1999**, 109, 207.
55. Biswas, R.; Bagchi, B. *J. Phys. Chem.* **1996**, *100*, 1238.
56. Biswas, R.; Bagchi, B. *J. Phys. Chem.* **1999**, *103*, 2495.
57. Kashyap, H.; Pradhan, T.; Biswas, R. *J. Chem. Phys.* **2006**, *125*, 174506.
58. Kashyap, H.; Biswas, R. *J. Phys. Chem. B* **2008**, *112*, 12431.
59. Kashyap, H.; Biswas, R. *J. Phys. Chem. B* **2010**, *114*, 254.
60. Pradhan, T.; Biswas, R. *J. Phys. Chem. A* **2007**, *111*, 11514.
61. Pradhan, T.; Biswas, R. *J. Phys. Chem. A* **2007**, *111*, 11524.

62. Chapman, C. F.; Maroncelli, M. *J. Phys. Chem.* **1991**, *95*, 9095.
63. Pramanik, R.; Rao, V. G.; Sarkar, S.; Ghatak, C.; Setua, P.; Sarkar, N. *J. Phys. Chem. B* **2009**, *113*, 8626.
64. Seth, D.; Sarkar, S.; Sarkar, N. *J. Phys. Chem. B* **2008**, *112*, 2629.
65. Mark, M. *J. Mol. Liq.* **1993**, *57*, 1.
66. Fleming, G. R.; Cho, M. *Annu. Rev. Phys. Chem.* **1996**, *47*, 109.
67. Bagchi, B.; Biswas, R. *Adv. Chem. Phys.* **1999**, *109*, 207.
68. Paul, A.; Samanta, A. *J. Phys. Chem. B* **2007**, *112*, 947.
69. Ruff, I.; Baranyai, A.; Palinkas, G.; Heinzinger, K. *J. Chem. Phys.* **1986**, *85*, 2169.
70. Doi, M.; Edwards, S. F. *The Theory of Polymer Dynamics*; Oxford University Press: Oxford, **1986**.
71. Matsuoka, S. *Relaxation Phonomena in Polymer*; Carl Hanser Verlag: Munich, **1992**.
72. Shirota, H.; Segawa, H. *Chem. Phys.* **2004**, *306*, 43.
73. Koddermann, T.; Ludwig, R.; Paschek, D. *ChemPhysChem* **2008,** 9, 1851.
74. Harris, K. R. *J. Chem. Phys*. **2009**, *131*, 054503.
75. Kumar, P.; Buldyrev, S. V.; Becker, S. R.; Poole, P. H.; Starr, F. W.; Stanley, H. E. *Proc. Natl. Acad. Sci. USA* **2007**, *104*, 9575.
76. Mallamace, F.; Branca, C.; Corsaro, C.; Leone, N.; Spooren, J.; Stanley, H. E.; Chen, S.-H. *J. Phys. Chem. B* **2010**, *114*, 1870.
77. Xu, L.; Mallamace, F.; Yan, Z.; Starr, F. W.; Buldyrev, S. V.; Eugene Stanley, H. *Nat. Phys.* **2009**, *5*, 565.
78. Mazza, M. G.; Giovambattista, N.; Stanley, H. E.; Starr, F. W. *Phys. Rev. E* **2007**, *76*, 031203.
79. Canpolat, M.; Starr, F. W.; Scala, A.; Sadr-Lahijany, M. R.; Mishima, O.; Havlin, S.; Stanley, H. E. *Chem. Phys. Lett.* **1998**, *294*, 9.
80. Sumi, H. *Chem. Phys.* **1996,** 212, 9.
81. Evans, D. F.; Tominaga, T.; Chan, C. *J Sol. Chem.* **1979,** 8, 461.
82. Fernandez-Alonso, F.; Bermejo, F. J.; McLain, S. E.; Turner, J. F. C.; Molaison, J. J.; Herwig, K. W. *Phys. Rev. Lett.* **2007,** 98, 77801.
83. Chen, S. H.; Mallamace, F.; Mou, C. Y.; Broccio, M.; Corsaro, C.; Faraone, A.; Liu, L. *Proc. Natl. Acad. Sci. USA* **2006,** 103, 12974.
84. Miyake, Y.; Akai, N.; Kawai, A.; Shibuya, K. *J. Phys. Chem. A* **2011**, *115*, 6347.

85. Inamder, S. R.; Mannekutla, J. R.; Mulimani, B. G.; Savadatti, M. I. *Chem. Phys. Lett.* **2006**, *429*, 141.
86. Tan, X.; Gustafson, T. L. *J. Phys. Chem. A.* **2000**, *104*, 4469.
87. Fruchey, K.; Fayer, M. D. *J. Phys. Chem. B* **2010**, *114*, 2840.
88. Sturlaugson, A. L.; Fruchey, K. S.; Fayer, M. D. *J. Phys. Chem. B* **2012**. **DOI:** 10.1021/jp209942r.
89. Hu, C.-M.; Zwanzig, R. *J. Chem. Phys.* **1974**, *60*, 4354.
90. Goulay, A. M.; Vincentgeisse, *J. Chem. Phys.* **1985**, *100*, 281.
91. Goulay, A. M.; Vincentgeisse, J. *J. Chem. Phys.* **1980**, *73*, 4203.
92. Benamotz, D.; Drake, J. M. *J. Chem. Phys.* **1988**, *89*, 1019.
93. Ravi, R.; Benamotz, D. *Chem. Phys.* **1994**, *183*, 385.
94. R. Metzler and J. Klafter, *Phys. Rep.* **2000**, *339*, 1.
95. R. Metzler, E. Barkai, and J. Klafter *Phys. Rev. Lett.* **1999**, *82*, 3563.
96. T. Bandyopadhyay, *Europhys. Lett.* **2008** *81*, 16003.
97. T. Bandyopadhyay, *J. Chem. Phys.* **2008**, *128*, 114712.

Chapter 8

Clustering and Heterogeneity in solution of Water-Cycloether Binary Mixtures Probed by Reactive and Non-reactive Dynamics

8.1 Introduction

Binary solvent mixtures exhibit unusual physical and chemical properties which are not shown by individual components and thus in the center of longstanding experimental and theoretical investigations.[1-14] Mixtures of water with alcohol, ether, dimethyl sulfoxide, acetonitrile etc. possess strong intermolecular correlations due to hydrogen bonding and dipolar interaction. Several properties, such as dielectric, viscosity, density, isothermal and adiabatic compressibilities of aqueous binary mixtures do not hold a simple relation with pure solvents.[15,23] It has now been recognised that water forms aggregated structure in hydrophobic solvents inducing distinct thermodynamic properties and interactions in the aqueous mixtuers. The interactions of water with the hydrophobic mixture component also alter the dynamics of the pure bulk phase.

Cycloether, such as 1,4-dioxane (DX) and tetrahydrofuran (THF) and their aqueous solutions, are among the most widely used solvents in chemical technology as reaction media.[24-27] DX or THF can form hydrogen bond with water, but no hydrogen bond can be formed among them and this fact provides an opportunity to probe water structure indirectly. Various studies such as IR,[28,29] NMR,[30,31] dielectric relaxation,[5-6] Raman spectroscopy[32] and light scattering[31,33,34] have already been performed to investigate the properties of water-cycloether systems. Previous small angle neutron and X-ray scattering studies of aqueous solution of cycloether showed that guest molecules are trapped inside the hydrogen bonded network structure of water at lower cycloether region.[31] It was also seen that, at cycloether mole fraction ≥ 0.3, water structure is disrupted and monomeric water molecules formed. However, even at the cycloether rich region, a cooperative hydrogen bonded network relaxation was observed in a dielectric relaxation study covering a wide frequency range from 200 MHz to 3 THz.[5,6] A laser light scattering study has also suggested a complexation of cycloether with water through reporting two different diffusive relaxation modes.[34]

Extensive studies of some excess properties of solvent mixtures and their role in biochemical processes have inspired researchers to measure the microscopic solution structures and their dynamical evolution.[35-40] Coherent anti-stokes Raman scattering (CARS) technique has been used to explore heterogeneity in binary mixtures.[41,42] In this technique the broadening of the spatial distribution has been explained in terms of local structure formation. Moreover, microheterogeneity of binary mixtures has been characterised by mass spectrometric studies of molecular cluster generated by fragmentation of liquid droplets.[43] Of late, fluorescence spectroscopic investigation showed that water-alcohol binary mixtures are heterogeneous and provided evidences in favour of a structural transition from tetrahedral hydrogen bonding network of water to zigzag pattern of alcohol.[7-9] Very recently, molecular dynamics simulations have been performed in water with tertiary butanol or 2-butoxyethanol mixtures.[13,14] Aggregation and microheterogeneity have been observed at lower alcohol region in the above simulation studies. However, in spite of all these studies, heterogeneity aspect of binary mixtures have not been well explored yet and it is very important to investigate microscopic solution structural properties of binary aqueous solvent mixtures.

Various systems, such as simple solvent mixtures,[7-9,44,45] mixtures of ionic liquid with polar and non-polar solvents,[46,47] confined liquids[48] and biomolecular environments[49,50] are well characterised structurally by fluorescence techniques. Unlike NMR, fluorescence can detect heterogeneity of a system in a given population due to slow interconversion of structures in experimental time scales (picoseconds to nanoseconds).[4,8] Solution structural heterogeneity can be probed by rate of a photo-induced chemical reaction or dipolar rotation provided that the rates of these processes are faster than the life time of heterogeneity.[4,8,51] In this chapter we have conducted reaction dynamics of a charge transfer probe, 4-azetedinyl benzonitrile (P4C), and rotational dynamics (anisotropy) of a non-reactive probe, coumarin 153 (C153), to investigate the solution structure and dynamics in water-cycloether binary mixtures. The excited state intramolecular charge transfer (ICT) has been an important fundamental process in chemistry and biology. In recent times, excited state charge transfer processes have been carried out in different media including binary solvent mixtures,[7,9] ionic liquids[51] and confined environments.[52,53] Moreover, it is a key step in photochemical reaction and occurs in numerous biological processes including photosynthesis.[54] As already discussed in chapter 2, SCHEME 1 and 2 represent photo-excitation of a P4C and the subsequent formation of charge transferred (CT) state where k_f and k_r are the forward and backward rate constants, respectively. k_{LE} and k_{CT} indicate the net (radiative *plus* non-radiative) rate constants for LE and CT states, respectively. The charge transfer step is the interconversion between LE and CT states, which is much faster than the LE or CT population decays in polar solvents.[55] Time resolved fluorescence anisotropy of an excited solute is also sensitive to change in local environment in solution.[4,5,56]

In this chapter, we have explored the clustering and heterogeneity aspects of solution structure and the associated dynamical response in water-cycloether (DX/THF) binary mixtures. DX and THF can solubilise water in all proportion and thus provide a unique opportunity to study properties of those water molecules which are part of tetrahedral hydrogen bonded network and also those which are 'isolated' (at very dilute water concentration, water molecules are believed to form hydrogen bond only with DX or THF). Both DX and THF possess hydrophobic ($-CH_2-CH_2-$) and hydrophilic (-O-) sites and their complete solubility in water instigate various interactions, which can make the solution microheterogeneous. We have investigated the properties of the water-DX/THF binary mixtures using dynamic light scattering (DLS), steady state absorption, fluorescence and picoseconds resolved fluorescence spectroscopy techniques. Two main objectives of the present study are: first, exploration of change in water structure, which is related to formation, strengthening, and disruption of hydrogen bonded network structure over the entire concentration range; second, investigation of dynamical response associated to local structures formed in solution and how these local structures affect rate of an excited state process, be it intramolecular charge transfer reaction or solute rotation.

8.2 Experimental Sections

8.2.1 Materials

4-(1-Azetidinyl)benzonitrile (P4C) was synthesized by following the literature method[57] and recrystallized twice from cyclohexane (Merck, Germany). Subsequently, purity of the P4C was checked by thin layer chromatography (TLC) and monitoring the excitation wavelength dependence of the fluorescence. Coumarin-153 (C153) was obtained from Exciton and used as received. 1,4 dioxane (DX) and tetrahydrofuran (THF) were purchased from sigma-aldrich and used without further purification.

8.2.2 Dynamic Light Scattering (DLS) Measurements

The DLS measurements were performed with a 4 mW He-Ne laser equipped Malvern-

instrument (Nano S). The time dependent fluctuation of intensity of scatter light were collected at 173^0 angle. The hydrodynamic diameter, ($d_H = k_B T / 3\pi\eta D$, where $k_B T$ is the Boltzmann constant times absolute temperature, η is the solvent viscosity and D is the translational diffusion coefficient) is estimated form intensity-intensity autocorrelation function. The resolution of the instrument is 0.6 nm.

8.2.3 Spectroscopic Measurements

Steady state and time resolved measurement techniques for reactive (P4C) and non-reactive (C153) solute and the corresponding data analysis procedures have been described in chapter 2 of this Thesis. Here at all cycloether mole fractions in binary mixtures, each of the LE emission decays was found to fit to one short time constant and one long time constant, whereas each of the CT emission decays fit to one rise-time and one long time constant. In addition, the LE short time constant was found to be comparable with the CT rise time and hence this short time constant was assigned as the reaction time constant. Note time-resolved measurements of this molecule (P4C) in a non-polar solvent (for example, heptane or 2-methylbutane) produced only one long time constant and no short time constant.

8.3 Results and Discussion

8.3.1 DLS Studies

The clustering behaviour of water in presence of hydrophobic solvent was analyzed by means of DLS. Both DX and THF are aprotic as well as hydrophobic solvents and they are soluble in water in all proportion. In DLS measurements huge scattering intensity

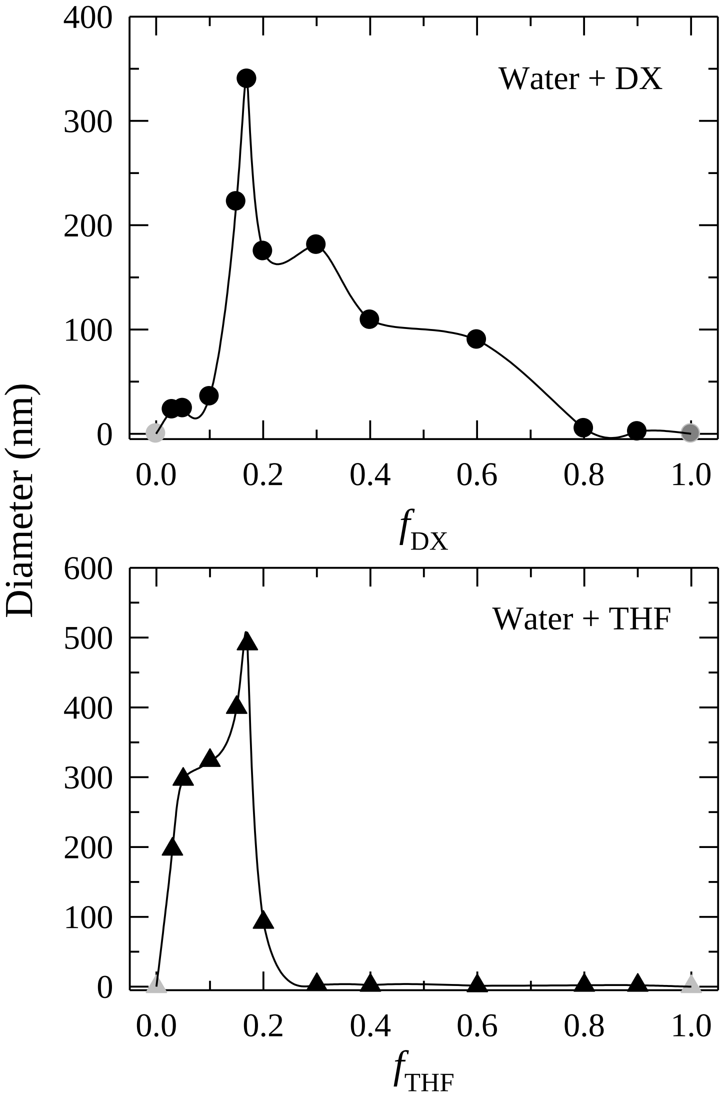

Fig. 8.1: Variation of the hydrodynamic diameters of water clusters in water-cycloether binary mixtures as a function of cycloether mole fraction. The data for water-DX and water-THF mixtures are presented in upper and lower panel respectively. Note that in pure components there has been no signature of clustering (gray symbols, diameter = 0 nm).

distribution has been found and can be assigned to cluster between water and cycloethers (DX/THF). The clustering features are strikingly dependent on mole fraction of cycloether, $f_{DX/THF}$. The onset of clustering has been observed even at very lower cycloether (DX/THF) concentration ($f_{DX/THF}$ ~ 0.03). The variation of hydrodynamic diameter of cluster with increasing $f_{DX/THF}$ has been shown in Fig. 8.1. The diameter of the water-cluster rapidly increases up to $f_{DX/THF}$ ~ 0.2 and then decreases with further addition of DX/THF into the mixtures. Tetrahedral-like network structure[59] of water strengthens due to hydrophobic interaction with clycloether and thus molecular clusters are produced in these binary mixtures. When $f_{DX/THF}$ reaches to ~ 0.2, onset of disruption of water cluster occurs due to replacement of water-water hydrogen bonds by water-ether hydrogen bonds which are weaker in nature than former and consequently the size of cluster decreases. From the present DLS measurements, the microheterogeneity of water-cycloether (DX/THF) mixtures has been evaluated on the basis of size distributions of clusters across the entire concentration region. It is clearly seen from Fig. 1 that the cluster size is not linearly dependent, rather it non-monotonically varies with $f_{DX/THF}$ and it indicates different microstructures in the water-cycloether mixtures. Another point to note here is that, after maximum, the hydrodynamic diameter decreases gently in water-DX mixtures, whereas it decreases sharply in water-THF with increasing $f_{DX/THF}$. Therefore, the microscopic structures of the solutions of water with two different cycloether (DX and THF) are not same; this is due to presence of one additional -O- unit in DX which makes it a better hydrogen bond acceptor. The present results of water-DX mixtures are consistent with those previously reported by some other methods.[34] Therefore, as experimentally evidenced, there has been a size variation of water-cluster due to association and modification of hydrogen bonded network structure throughout the composition range.

8.3.2 Steady State Absorption and Fluorescence Studies with a Reactive (P4C) and Non-reactive (C153) Solutes:

The absorption and fluorescence spectra of P4C have been measured in water-cycloether mixtures for the entire composition range. Representative absorption and fluorescence spectra of P4C in these two sets of binary mixtures are shown in Fig. 8.2. The upper and

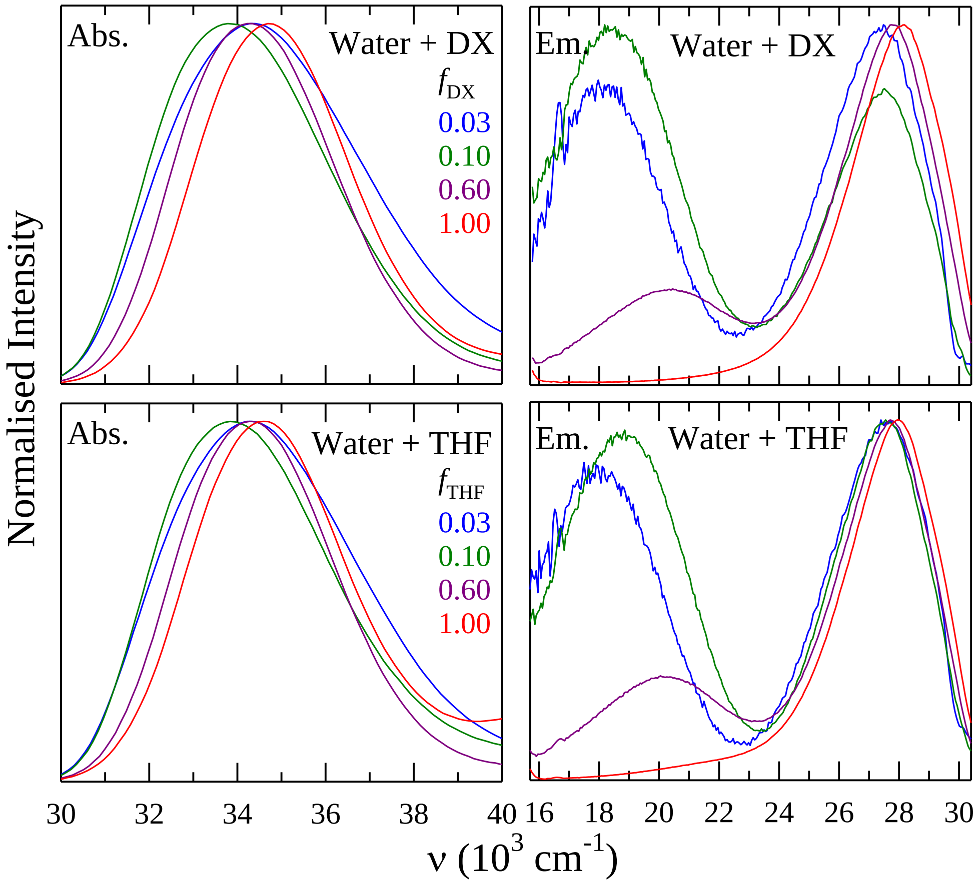

Fig. 8.2: Representative absorption and emission spectra of 4-(1-azetidinyl)benzonitrile (P4C) in different mole fractions of cycloethers of the mixture of water with DX/THF. The upper panels show the absorption and emission spectra in water-DX mixtures and lower panels show the same in water-THF mixtures. Data are color coded.

lower panels of the figure indicate separate results in water-DX and water-THF mixtures respectively. It has been observed that absorption spectra show a single peak in all the solutions studied but the emission spectra exhibit dual peak.[7,9,55,60] The second emission peak at lower energy has been assigned to the intramolecular charge transfer from donor to acceptor moiety in P4C molecule.[55] The molecular structure and scheme of the charge transfer process is shown in SCHEME 1 and 2 (chapter 2 of this Thesis). The area under the curve of the second emission band decreases with increasing $f_{DX/THF}$. This clearly indicates more polar CT state is being destabilised and the reaction is becoming unfavourable with gradual addition of non-polar solvent (DX or THF) into the mixtures. The absorption and fluorescence intensity increases (not shown) with increasing DX/THF

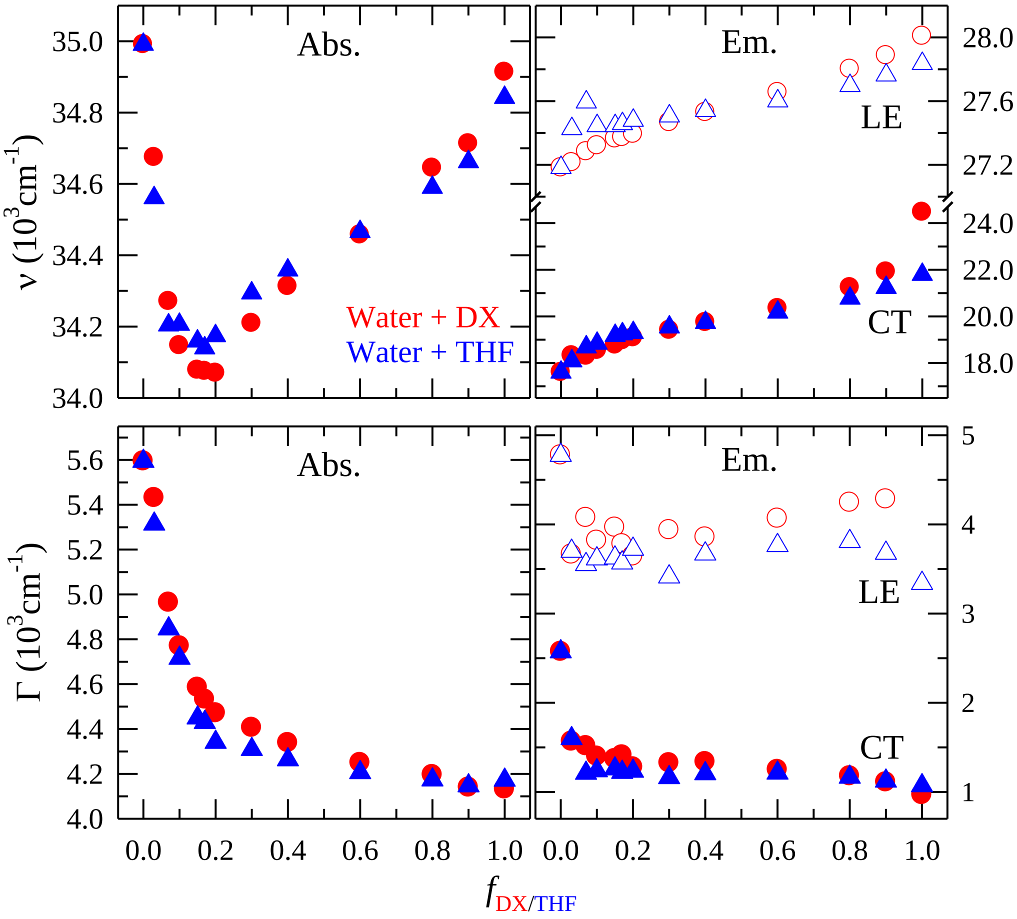

Fig. 8.3: $f_{DX/THF}$ dependence of spectral properties: frequencies of the absorption (ν_{abs}) and emission (ν_{LE} and ν_{CT}) spectra and their full width at half-maxima (Γ) of 4-(1-azetidinyl)benzonitrile (P4C). The left and right panels respectively represent absorption and emission features in water-cycloethers (DX/THF) binary mixtures. LE and CT deconvolution of the emission spectrum has been performed by broadening and shifting a reference spectrum with a Gaussian function (representing inhomogeneous solvent broadening). The estimated uncertainty in frequencies and widths is ± 200 cm^{-1}

content due to decrease of non-radiative rate in presence of non-polar aprotic solvent. Most interestingly, with increasing DX/THF content, absorption spectra show a red shift at lower $f_{DX/THF}$ (up to ~ 0.17) after that a blue shift occurs. On the other hand, emission spectrum exhibits an increasing blue shift with DX/THF concentration. The polarity of the medium decreases as DX/THF is added gradually into the mixtures, thus a blue shift in spectral feature is expected. The $f_{DX/THF}$ dependence of absorption, LE and CT fluorescence spectral frequencies and their width are presented in Fig. 8.3. The upper and lower panels respectively show frequencies and widths of P4C in two binary mixtures for the entire composition range. Various important aspects of binary mixture have been obtained from the figure. The absorption frequency exhibits a red shift up to $f_{DX/THF}$ ~ 0.17 and beyond this composition it shifts toward blue. The absorption feature contradicts with fluorescence, which shows a continuous blue shift with increasing DX/THF concentration and thus follows the average polarity of the binary mixture. In both of the mixtures the extent of initial red shift and the subsequent blue shift are similar in magnitude which is ~ 900 cm^{-1}. While the LE fluorescence band exhibits a blue shift of ~ 800 cm^{-1} in both the mixtures, CT band, owing to its more polar nature, shows almost eight and six times larger blue shift in water-DX and water-THF mixtures respectively for the whole concentration range.

The DX or THF induced structural enhancement and the associated microheterogeneity affect the ground and excited state behaviours of dissolved solute (P4C). From the present DLS measurements and several other previous studies, it has been seen that, water molecules exhibit clustering in presence of small amount of hydrophobic solvents (DX or THF). The structural enhancement occurs due to incorporation of DX/THF molecules into the cavity of tetrahedral hydrogen bonded network structure of water at low DX/THF concentration.[33] A similar enhancement of hydrogen bonded structure have been found in recent studies of water-tertiary butanol mixtures at low alcohol concentration.[7,8] In the present chapter, cycloether induced strengthening of water-cluster makes the medium less compressible and consequently, the solute (P4C)-environment interaction increases and this leads to red shift in absorption spectra. The strengthening of hydrogen bonding is related to shortening of OH...O bonds and lengthening of intramolecular O-H bonds. However, the tetrahedral-like hydrogen bonded network structure starts breaking when a critical concentration of DX/THF is reached. Several molar properties, such as heat of mixing, excess entropy and excess volume etc. of the binary water-cycloether mixtures are known to exhibit non-ideal dependence with composition showing a maximum or minimum.[15-17,18,39] However, the positions of inflections have not been observed at the same compositions. From the DLS figure (Fig. 8.1) it is also noted that at very less DX/THF concentration cluster formation starts and size of the cluster increases up to $f_{DX/THF}$ ~ 0.2 and then decreases with further addition of DX/THF. Interestingly, the absorption characteristics match well with the DLS size distribution of water-cluster in binary mixtures.

The contrasting variation of fluorescence frequencies with $f_{DX/THF}$ compared to absorption can be explained as follows. The clustering of water molecules in presence of small amount of hydrophobic solvent is a dynamic process. So, in the present systems there must be an exchange between cluster and free solvent molecules. This exchange time, which is essentially the life time of cluster, must be less than the life time (~ 1000 ps) of fluorophore. A very fast life time (20-30 ps) has been observed in previous molecular dynamics simulation study of a similar type of mixtures.[62] Therefore, fluorescence spectra give the environmental averaging information and thus exhibit contrasting features compared to absorption. The FWHM (shown in lower panel of Fig. 8.3) of the absorption spectra exhibit a red shift with increasing DX/ THF content, initially sharp (1200 cm^{-1}) up to $f_{DX/THF}$ ~ 0.17 followed by a gentle (~ 300 cm^{-1}) variation. The narrowing of absorption spectra is attributed to decrease of medium polarity. Therefore the blue shift in absorption with narrowing can be accountable; however, the initial red shift with narrowing is counterintuitive. This fact further supports the strengthening of hydrogen bonded network[7,8] structure at low concentration of cycloether. The widths of the LE and CT fluorescence bands also shift red due to decreasing medium polarity, except the LE band shows slight broadening at larger DX concentrations.

The ratios between areas under the CT and LE bands (α_{CT}/α_{LE}) and reaction free energy change ($-\Delta G$) as a function of DX/THF mole fraction are shown in upper panel of Fig. 8.4. One interesting feature of this figure is that α_{CT}/α_{LE} and $-\Delta G$ exhibit a nonmonotonic dependence on DX/THF fraction with a maxima at $f_{DX/THF}$ ~ 0.1. The CT state (L_a) exhibits more polar character compared to LE state (L_b)[55] and interaction of these sates with medium polarity of varying DX/THF must not be same, which is the reason for observed nonmonotonic dependence of area ratio.

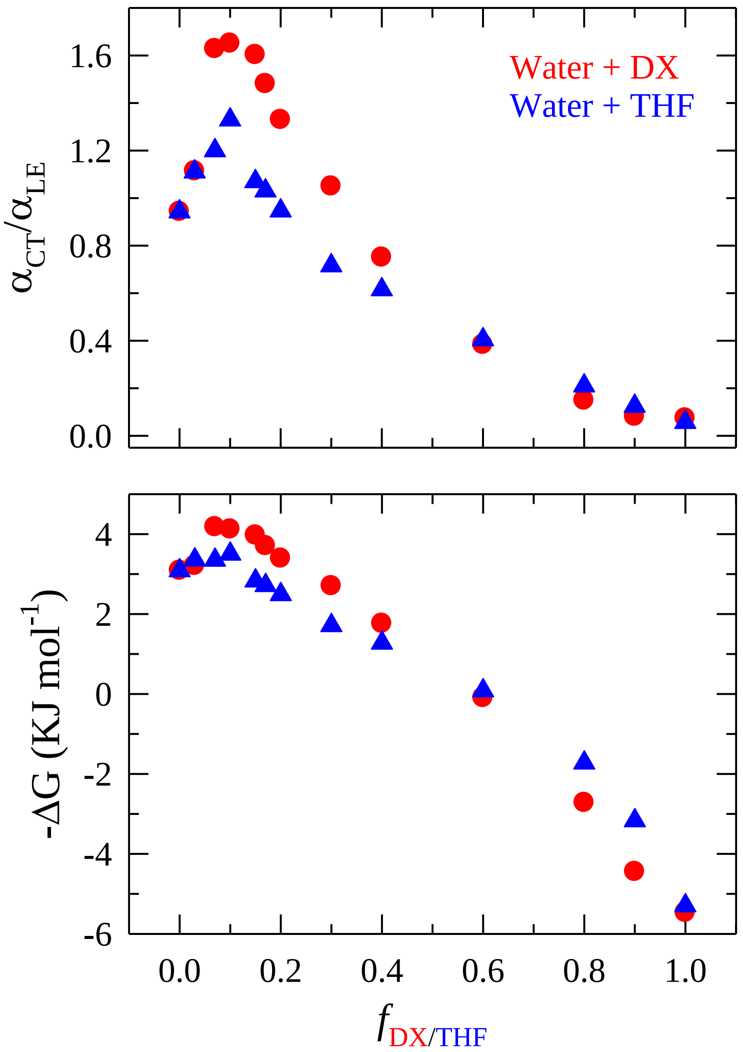

Fig. 8.4: Mole fraction ($f_{DX/THF}$) dependence of ratio (α_{CT}/α_{LE}) of area under the CT and LE bands and reaction free energy change ($-\Delta G$) of P4C in the mixture of water-cycloethers. Upper and lower panel represent α_{CT}/α_{LE} and $-\Delta G$ respectively at different $f_{DX/THF}$. Data are color coded.

We have also explored the absorption and fluorescence characteristics of a non-reactive solute (C153) in these binary mixtures. Fig. 8.5 shows the $f_{DX/THF}$ dependent frequencies of absorption and fluorescence spectra and their widths in these two sets of binary mixtures. From the figures it is seen that, like charge transfer solute (P4C), non-reactive solute also probes the strengthening of hydrogen bonded network structure as reflected in absorption frequency and width. However, inflection occurs at a cycloether mole fraction of ~ 0.1 but P4C shows such an inflection at ~ 0.17. Also like P4C, fluorescence properties of C153 display information regarding environmental averaging. The amount of

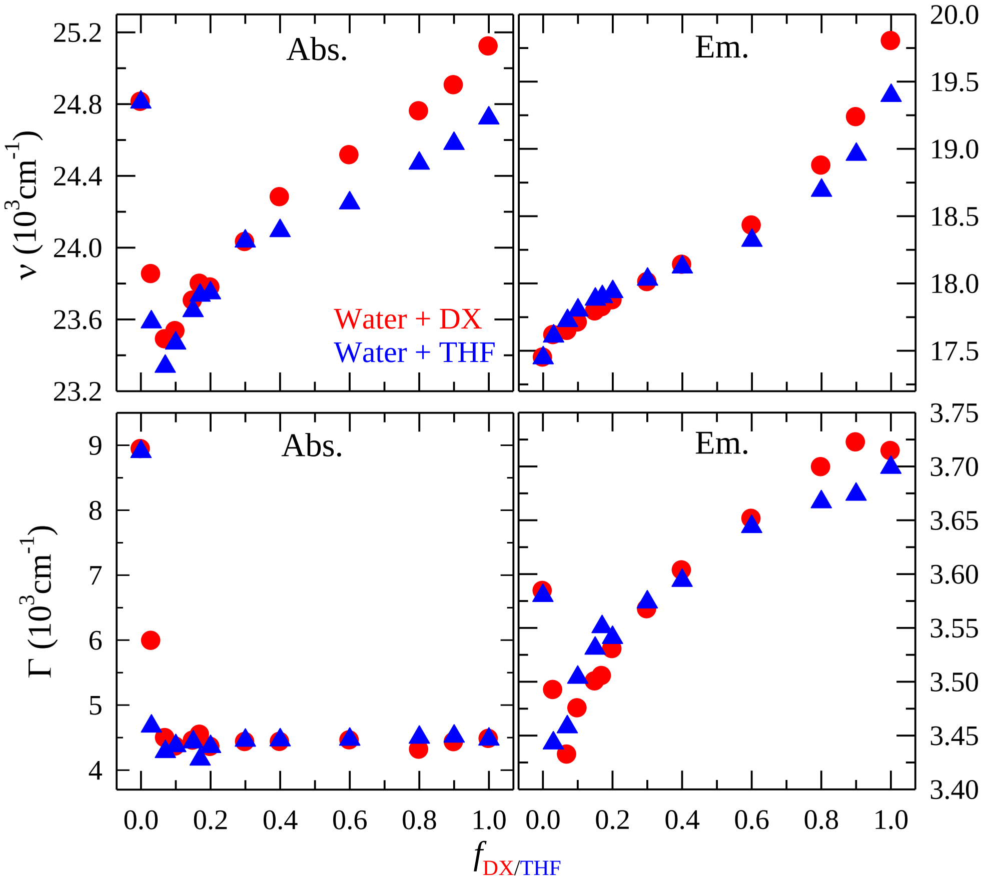

Fig. 8.5: $f_{DX/THF}$ dependence of absorption and emission frequencies (ν) and widths (Γ) of C153 in water-DX and water-THF binary mixtures. The left and right panels show absorption and emission features respectively in water-cycloethers (DX/THF) binary mixtures. Data are color coded. The estimated error in frequencies and widths is $\pm$ 200 cm^{-1}

red shift and subsequent blue shift in absorption spectra of C153 in both of these two sets of binary mixtures are 1.5 times or even larger compared to P4C. The absorption width shows initially much larger red shift ~4500 cm^{-1} followed by a plateau with increasing $f_{DX/THF}$. However, the amount of blue shift exhibited by fluorescence frequency of C153 is approximately equal to that observed in CT band of P4C for the entire composition range. The absence of any specific change in solute-solvent interaction during excitation and charge separation in excited state make C153 an appropriate polarity sensitive solvation probe.[63] C153 senses the polarity of the mixtures with greater extent which is attributed to larger shift in fluorescence spectra compared to P4C. These special properties of C153 might be a reason for shifting the inflection point in $f_{DX/THF}$ dependent absorption frequencies (Fig. 8.5). In the present measurements, the frequencies and widths of C153 in pure components (water, DX and THF) are in good agreement with those reported earlier.[63] We performed excitation wavelength ($\lambda_{exc.}$) dependence of fluorescence of non-reactive solute (C153) in water-THF binary mixture for few representative compositions (shown in Fig. A30, Appendix) and did not find any significant shift of fluorescence peak with $\lambda_{exc.}$. This again clearly indicates the clustering time or the heterogeneity time is much faster than the life time of the solute. Therefore, the above observations suggest that the water-cycloether binary mixture acts as a differently showing heterogeneity that is absent in either of the neat systems.

8.3.3 Time Resolved Studies: Reactive Dynamics

The fluorescence transients of P4C have been measured in water-cycloether binary mixtures at 360 nm and 500 nm for LE and CT excited states respectively. We were not able to collect CT fluorescence decay with a sufficient count in bulk water due to poor solubility of P4C. The representative fluorescence transient of P4C in LE and CT states dissolved in binary mixtures ($f_{DX/THF}$ = 0.2, 0.8) are shown in Fig. 8.6. The LE shows very quick decay and that of CT displays a rise followed by decay. The time resolved fluorescence data have been fitted with bi-exponential function of time with a good χ^2. The time constants associated to the rise component of CT states match well with those fast decay components at LE states in all compositions and assigned to the LE $\rightarrow$ CT interconversion rate constant.[55] The bi-exponential fitting parameters for LE fluorescence decays at all compositions in these two sets of mixtures are presented in Table A21. From the table, it can be noticed that in pure water, the reaction rate is faster (τ_{rxn} ~ 32 ps from LE decay only) compared to its binary mixtures with cycloethers. The $f_{DX/THF}$ dependent τ_{rxn} of P4C has been shown in upper panel of Fig. 8.7. The τ_{rxn} has been found to be ~ 93 and 182 ps in pure DX and THF, respectively. From the figure, it is clearly seen that τ_{rxn} increases from 32 ps to 370 ps/ 330 ps up to a certain concentration with gradual addition of DX/THF into the mixtures. However, it does not show any structural enhancement at lower $f_{DX/THF}$ region.

Upon addition of DX/THF into the mixture the average polarity of the medium decreases, consequently more polar CT state destabilises and thus reaction rate becomes slower. The

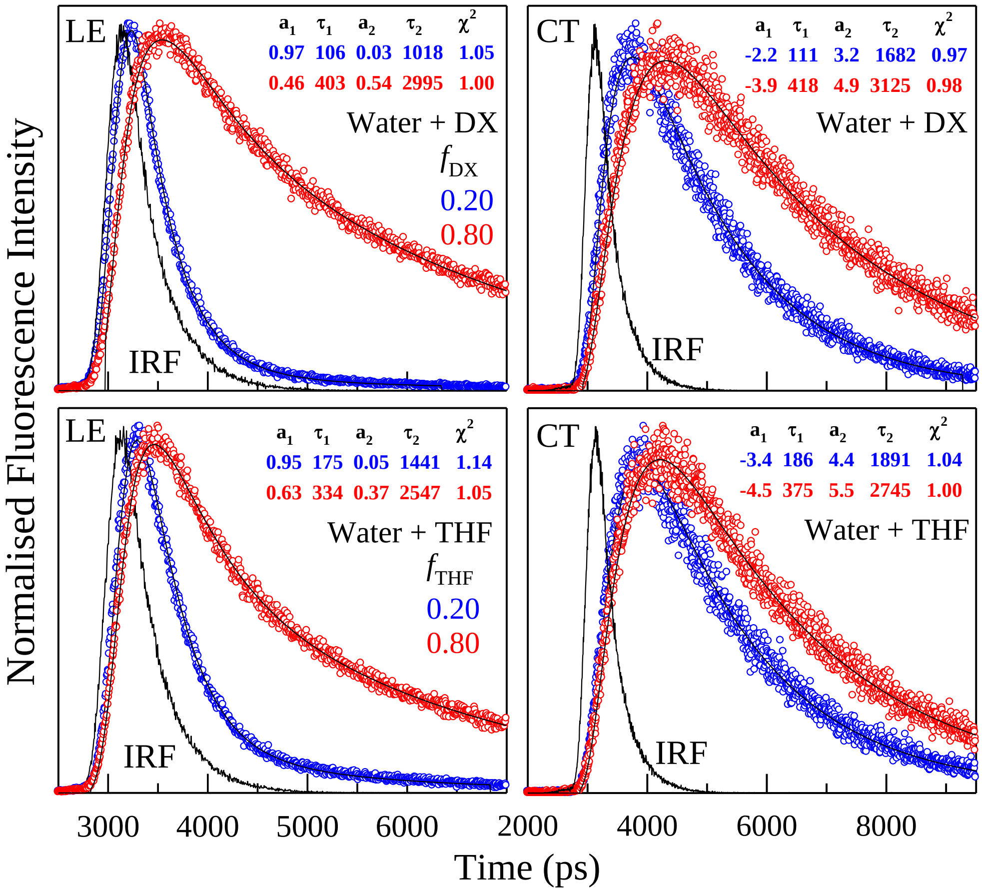

Fig. 8.6: Representative normalised LE and CT emission decays of P4C in the water-cycloether binary mixture at $f_{DX/THF}$ = 0.2 and 0.8. The data are represented by the circles, and the fit through the data is by the solid line. Upper and lower panel show the data in water-DX and water-THF mixtures respectively. The instrument response function is shown by the broken line. The biexponential fitting parameters are also provided in respective panels. The LE peak count was ~ 3000 and the CT peak count was ~1000.

disappearance of structural enhancement in τ_{rxn} at lower $f_{DX/THF}$ occurs due to broader instrumental resolution employed in this study. The instrumental resolution of setup was ~450 ps, so it can detect ~100 ps components with reasonable accuracy. As already mentioned, there has been an inter-conversion between free and aggregated solvent molecules in the binary mixtures with a faster time scales which are not detectable with the present time resolved setup. Interestingly, with further increase in DX/THF concentration, we observed a different maximum at ~ 0.8 in τ_{rxn}. Eventhough, medium

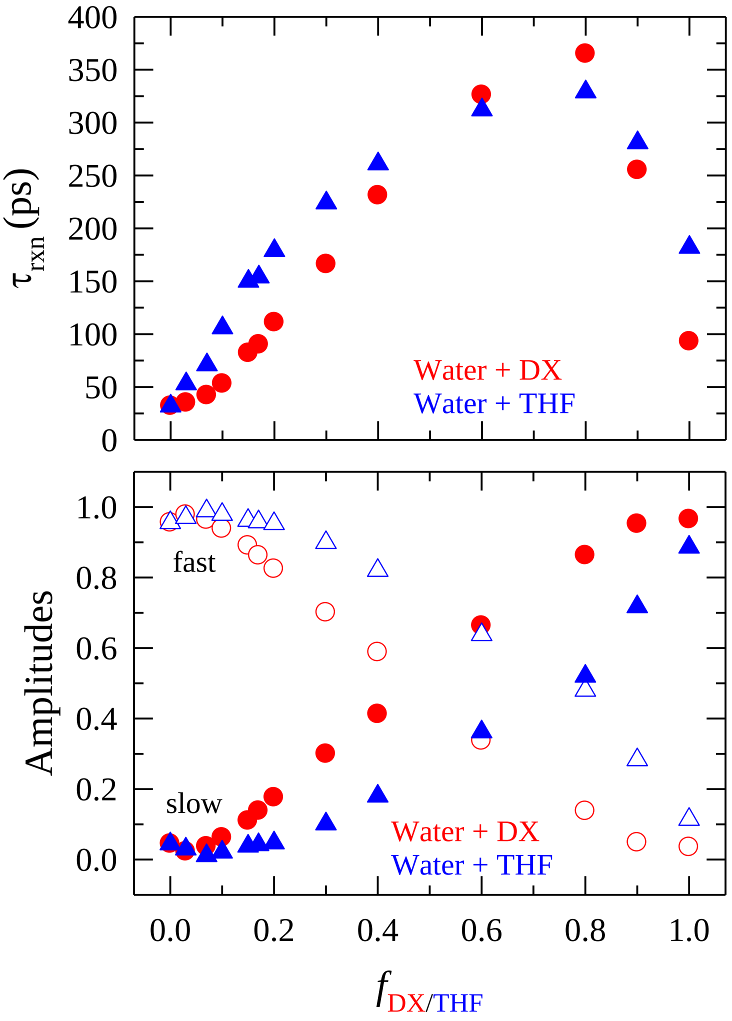

Fig. 8.7: $f_{DX/THF}$ dependence of the fast time constant (reaction time, τ_{rxn}) of LE fluorescence decay and that of amplitudes (*fast and slow*) associated with the LE → CT inter-conversion reaction of P4C in water-cycloethers (DX/THF) binary mixtures. The upper and lower panels show respectively the variation τ_{rxn} and amplitudes obtained from biexponential fits to the collected decays.

polarity decreases with increasing DX/THF content, after $f_{DX/THF}$ ~ 0.8 the reaction rate becomes strikingly faster. So, up to the maximum point, the rate of charge transfer reaction is consistent with steady state fluorescence observation, where a systematic blue shift and an increase in area under CT band have been found with increasing $f_{DX/THF}$. But after the maximum, the two measurements seem to provide contradictory results. A previous solvation dynamics experiment[64] with a non-reactive solute (C153) reported that large dynamic Stokes shifts and very fast solvent response in non-polar (DX, $\varepsilon_0 \sim 2.2$) or very weakly polar (THF, $\varepsilon_0 \sim 7.6$) solvent. The detected time resolved Stokes shifts and the average solvation times of C153 were found to be respectively 1320 cm^{-1} and 1260 cm^{-1}, and 0.94 ps and 1.67 ps in DX and THF. The ultrafast solvation response and large shifts have been explained in terms of nuclear quadrupole moment ($<Q>$) of the DX and THF. In the same study, *ab-initio* calculation showed that, though the solvent molecules possess zero or low dipole moment ($\mu_{DX} \sim 0\,\mathrm{D}$, $\mu_{THF} \sim 1.6\,\mathrm{D}$), the presence of polar bonds, -O-CH$_2$- in DX and THF can lead to higher moments (nuclear quadrupole moment, $<Q>$). The DX and THF exhibit $<Q>$ of about 11.68 and 5.39 respectively, which is responsible for ultrafast solvent response. In the present study, when the DX/THF content is very large (at $f_{DX/THF} > 0.7$), the quadrupole moment of DX/THF predominates over the average polarity of the medium.

Eventhough the average polarity of the medium decreases with successive addition of DX/THF into the mixtures, after $f_{DX/THF} = 0.8$, the nuclear quadrupole moment dictates the charge transfer process and thus reaction rate becomes faster. Here, a question may arises, why does $<Q>$ predominate at $f_{DX/THF} > 0.7$? From the present DLS study (Fig. 8.1) it is observed that after $f_{DX/THF} > 0.7$, the clustering diminishes or very less pronounced, which basically tells that the interaction between hydrophobic solvents (DX/THF) and water is minimised. The similar observation has already been found in a previous Rayleigh light scattering study[34] of water-DX binary mixtures. In such a situation $<Q>$ predominates over average medium polarity and interact with the charge separated state after $f_{DX/THF} > 0.7$ in water-cycloether binary mixtures. From the Fig. 8.1, we have seen that, the cluster size reached a negligible value (~ 2 nm) at $f_{THF} \sim 0.4$ and after that it shows a plateau but the reaction rate starts to be faster after $f_{THF} = 0.8$. This indicates that relatively weaker clustering ability of THF due to presence of less numbers of hydrogen bonding sites. However, the effects of $<Q>$ on reaction rate is more pronounced in water-DX mixtures compared to water-THF because of lower $<Q>$ value of THF.[64]

The long time constant in the table A21 (Appendix) has been assigned to the life time (τ_{life}) of solute (P4C) at LE state[7,55] which varies significantly with DX/THF contents. The relative amplitude associated with τ_{rxn} has been seen to decrease abruptly with variation of DX or THF concentration (shown in lower panel of Fig. 8.7). The decrease in average medium polarity with addition of non-polar solvent into water explains the above decrease of τ_{rxn}. Though the dependence of τ_{rxn} with $f_{DX/THF}$ is approximately the same in two types of mixtures, the reaction rates in water-DX mixtures are slightly different from those in water-THF mixtures. Despite the above facts the interactions between water and cycloether in these two sets of mixtures are very similar and their effects on reactive dynamics are comparable.

8.3.4 Time Resolved Anisotropy Studies: Non-reactive Dynamics

To further quantify the medium heterogeneity, rotational dynamics of a non-reactive dipolar solute (C153) has been studied in these binary mixtures. For this purpose we have used 409 nm laser light as an excitation source with an instrument response function ~ 70 ps. This time resolution can detect a response as with timescale ~ 15 ps with reasonable accuracy.[65] The magic angle and polarized fluorescence decays were fitted to bi-exponential functions of time in all mixtures compositions. The representative fluorescence anisotropy ($r(t)$) decays of C153 in water-cycloether binary mixtures have been displayed in Fig. 8.8. The $r(t)$ in binary mixtures have been found to be bi-exponential in all composition except pure component. Fig. 8.9 shows the variation of rotational correlation time ($<\tau_r>$) with mole fraction of cycloether ($f_{DX/THF}$) in both of the solvent mixtures. The measured $<\tau_r>$ of C153 shows a maximum; it increases as a function of $f_{DX/THF}$ up to ~0.17 and ~ 0.10 for water-DX and water-THF mixtures, respectively, and then decreases with further addition of DX/THF. As discussed earlier, addition of DX/THF into water leads to clustering and local structure formation, which has been reflected in $f_{DX/THF}$ dependent $<\tau_r>$. The initial increase of $<\tau_r>$ at lower DX/THF concentration is a further evidence of strengthening of tetrahedral hydrogen bonded network structure of water or the enhancement of interaction between water and DX/THF. As we have seen in previous section, the size of the cluster decreases after showing a maximum, consequently $<\tau_r>$ decreases after such a maximum ($f_{DX/THF}$ ~0.17 and 0.10). Eventhough the exact point of inflection in two different measurements (DLS and rotation dynamics) have not overlapped, the present time resolved anisotropy study clearly figures out the local structure formation as well as dynamic heterogeneity in

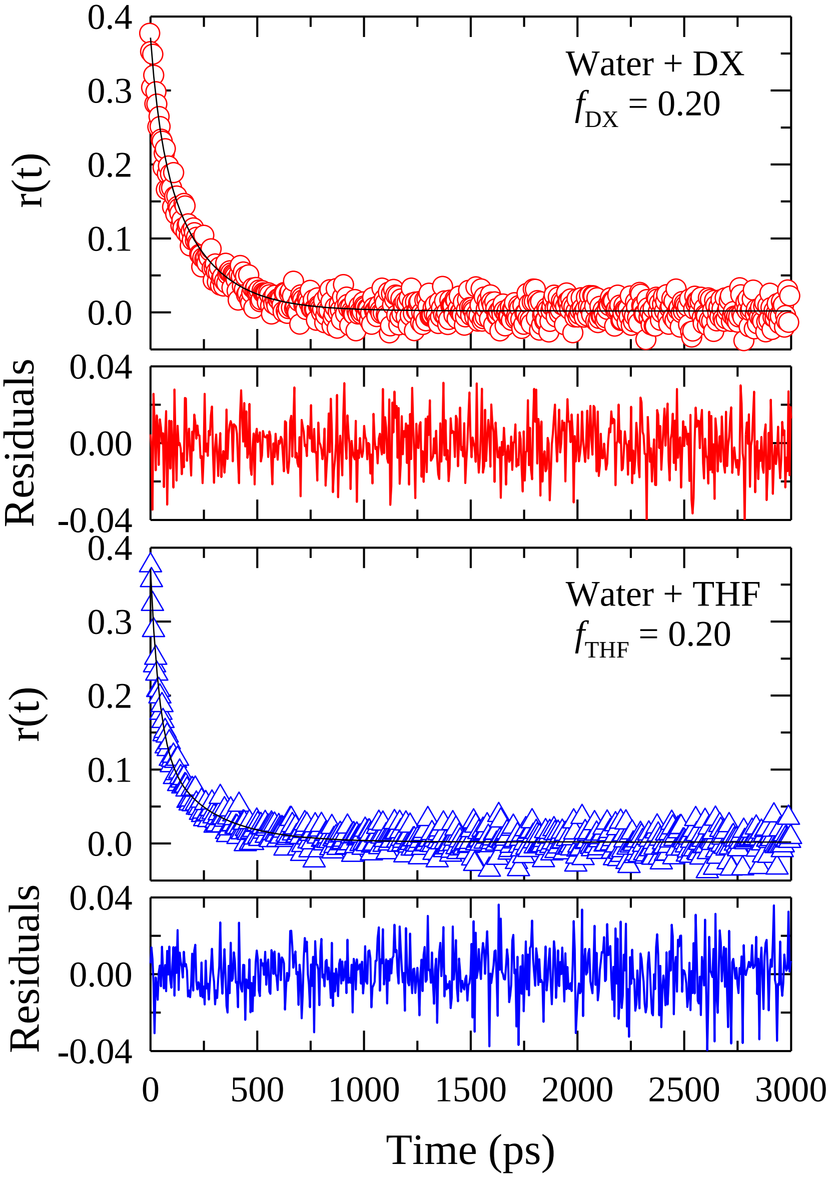

Fig. 8.8: Representative fluorescence anisotropy decays ($r(t)$) of C153 in water-cycloether binary mixtures at $f_{DX/THF}$ = 0.2. Open symbols represent the data and solid lines represent fits. The data in water-DX and water-THF mixtures are presented by red and blue color respectively. The corresponding residuals are also shown with same color.

these binary mixtures. The above observations, however, do not tell about the exact time scale of heterogeneity.

Experimental results indicate that after the inflection point, C153 rotates faster in water-THF mixtures compared to that in water-DX mixtures. This can also be clearly understood from the DLS results. As we have already seen in Fig. 8.1 that, the decrease of cluster size

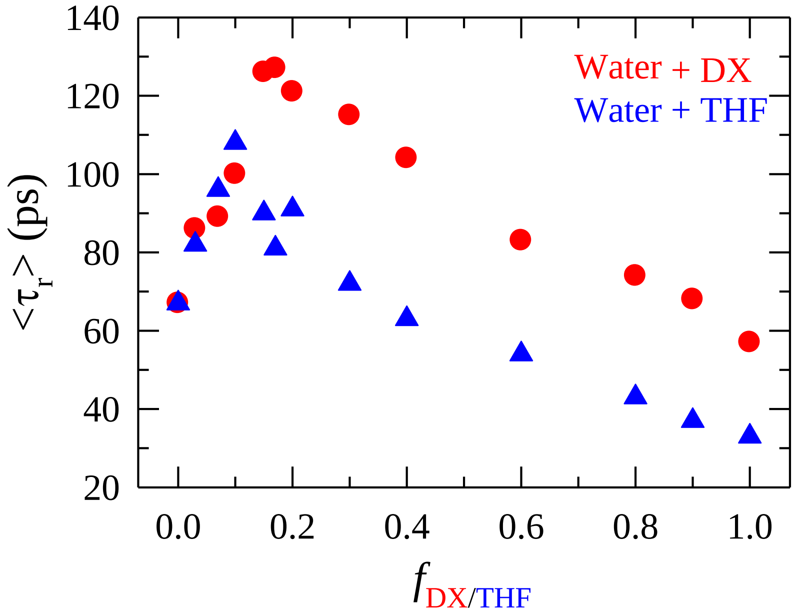

Fig. 8.9: Mole fraction ($f_{DX/THF}$) dependence of average rotation time ($<\tau_r>$) of C153 in water-cycloether binary mixtures. Circles represent data for water-DX mixtures and triangles represent data for water-THF mixtures.

with increasing $f_{DX/THF}$ after the maximum is different in two binary mixtures: a gentle decrease has been observed in water-DX mixtures, whereas water-THF mixtures showed a sharp decrease. The presence of smaller size cluster in water-THF mixtures after maximum leads to faster rotation of C153, while slower rotation can be attributed to the presence of relatively larger size cluster in water-DX mixtures. Moreover, in a previous measurement,[15] viscosity was found to increase with increasing DX/THF content up to $f_{DX/THF}$ ~ 0.2 and 0.1 for water-DX and water-THF mixtures respectively (shown in Fig. A31 of Appendix). Subsequently, it showed a decrease with further addition of DX/THF. However, after the maximum, water-THF mixtures showed a faster decrease in viscosity compared to water-DX. Therefore, from the present DLS and previous viscosity measurements, it can be argued that, the solute rotation is not controlled by dielectric friction;[66] rather it depends largely on mechanical friction originated from local structures. Previous studies[7,8] have reported a similar type of non-monotonic dependence of $<\tau_r>$ of solutes with mole fraction in water-ethanol and water-tertiary butyl alcohol mixtures and explained the observations in terms of local structure formation and specific interaction. From Fig.8.9, we also observed that $<\tau_r>$ of C153 in pure DX and THF are 58 ps and 32 ps respectively, which are faster compared to that (68 ps) in highly polar bulk water.

These $<\tau_r>$ in pure component are in good agreement with those reported earlier using the same solute.[66]

A comparison indicates that the two types of dynamics (reactive and non-reactive) have been controlled by different ways in binary mixtures. At lower DX/THF concentration the reactive dynamics does not show any inflection in τ_{rxn} due to limited time resolution of the experimental setup, whereas a maximum was observed at larger DX/THF concentration because of the domination of nuclear quadrupole moment ($<Q>$) over medium polarity. On the other hand, non-reactive dynamics shows a maximum in $<\tau_r>$ at lower DX/THF concentration because of sufficient instrumental resolution. However, steady state spectral features of both the reactive and non-reactive solute are comparable and also in accordance with time resolved characteristics at lower DX/THF content. In the reactive dynamics, charge transferred (CT) state is formed and it is controlled by medium polarity. We have seen in the earlier section, average medium polarity followed by nuclear quadrupole moment (at DX/THF rich region) governs the ICT reaction in water-cycloether binary mixtures. Solute rotation does not involve charge separation and it is mainly affected by the mechanical friction due to local structure formation.

8.4 Conclusions

In this chapter, the above reactive and non-reactive dynamics studies have revealed clustering and heterogeneous solution structure in water-cycloether (DX/THF) binary mixtures. The dynamic light scattering study shows water forms cluster in presence of very less amount of cycloether. The size of the cluster increases up to a certain cycloether concentration ($f_{DX/THF}$ ~ 0.2) and then decreases with further addition of cycloether. Absorption spectral features of both the reactive and non-reactive solutes successfully probe the strengthening and modification of hydrogen bonding network structure ofwater in these aqueous mixtures. The microscopic solution structure has not been reflected in steady state fluorescence features due to rapid fluctuation of the micro-domains. Eventhough the reactive dynamics does not reflect structural enhancement, it is effectively revealed by non-reactive dynamics. The sharp decrease in average reorientation time with cycloethers concentration at water rich region demonstrates structural modification due to hydrophobic effect of cycloethers. The anomalous increase of reaction rate at cycloether rich regions occurs due to predomination of nuclear quadrupole moment over average polarity of the medium.

References:

1. Basu, S.; Vutukuri, D. R.; Thayumanavan, S. *J. Am. Chem. Soc.* **2005**, *127*, 16794.
2. Juurinen, I.; Nakahara, K.; Ando, N.; Nishiumi, T.; Seta, H.; Yoshida, N.; Morinaga, T.; Itou, M.; Ninomiya, T.; Sakurai, Y.; Salonen, E.; Nordlund, K.; Hämäläinen, K.; Hakala, M. *Phys. Rev. Lett.* **2011**, *107*, 197401.
3. Dixit, S.; Crain, J.; Poon, W. C. K.; Finney, J. L.; Soper, A. K. *Nature*, **2002**, *416*, 829.
4. Inamdar, S. R.; Gayathri, B. R.; Mannekutla, J. R. *J. Fluoresc*. **2009**, *19*, 693-703.
5. Schrödle, S.; Fischer, B.; Helm, H.; Buchner, R. *J. Phys. Chem. A* **2007**, *111*, 2043.
6. Schrödle, S.; Hefter, G.; Buchner, R. *J. Phys. Chem. B* **2007**, *111*, 5946.
7. Pradhan, T.; Ghoshal, P.; Biswas, R. *J. Phys. Chem. A* **2008**, *112*, 915.
8. Pradhan, T.; Ghoshal, P.; Biswas, R. *J. Chem. Sci.* **2008**, *120*, 275.
9. Gazi, H. A. R.; Biswas, R. *J. Phys. Chem. A* **2011**, *115*, 2447.
10. Chandra, A.; Bagchi, B. *J. Chem. Phys.* **1991**, *94*, 8367.
11. Chandra, A. *Chem Phys Lett* **1995**, *235*, 133.
12. Daschakraborty, S.; Biswas, R. *J. Phys. Chem. B* **2011**, *115*, 4011.
13. Gupta, R.; Patey, G. N. *J. Chem. Phys.* **2012**, *137*, 034509.
14. Gupta, R.; Patey, G. N. *J. Phys. Chem. B* **2011**, *115*, 15323.
15. Nayak, J. N.; Aralaguppi, M. I.; Kumar Naidu, B. V.; Aminabhavi, T. M. *J. Chem. Eng. Data* **2004**, *49*, 468.
16. Nakayama, H.; Shinoda, K. *J. Chem. Thermodyn*. **1971**, *3*, 401.
17. Inglese, A.; Ferino, I.; Marongiu, B.; Solinas, V.; Torrazza, S. *Thermochim. Acta* **1983**, *65*, 169.
18. Morcom, K. W.; Smith, R. W. *Trans. Faraday Soc.* **1970**, *65*, 1073.
19. Qunfang, L.; Yu-Chun, H. *Fluid Phase Equilib***. 1999***154*, 153.
20. Pal, A.; Daas, G. *J. Mol. Liq.* **2000,** *84*, 327.
21. Syeda, A. B.; Bachu, R. K.; Koppula, A. J.; Boodida, S.; Nallani, S. *J. Chem. Eng. Data* **2009**, *55*, 1067.
22. Davila, M. a. J.; Aparicio, S.; Alcalde, R. *Ind. Eng. Chem. Res.* **2009**, *48*, 10065.
23. Harris, H. G.; Prausnitz, J. M. *AIChE J.* **1968**, *14*, 737.
24. Iwasaki, K.; Fujiyama, T. *J. Phys. Chem.* **1979**, *83*, 463; **1977**, *81*, 1908.

25. Marcus, Y.; Hefter, G. *Chem. Rev.* **2004**, *104*, 3405.
26. Seader, J. D.; Henley, E. J. *Separation Process Principles*; John Wiley & Sons: New York, **1998**.
27. (a) Li, S.; Tuan, V. A.; Noble, R. D.; Falconer, J. L. *Ind. Eng. Chem. Res.* **2001**, *40*, 4577. (b) T. Taura Inorg. *Chem. Commun.*, **1999,** *2*, 35 (c) L.I. Rubleva, R.V. Vizgert Russ. *J. Org. Chem*., **1998,** *34*, 1003.
28. Sirotkin, V. A.; Solomonov, B. N.; Faizullin, D. A.; Fedotov, V. D. *J. Struct. Chem*. **2000**, *41*, 997.
29. Mizuno, K.; Imafuji, S.; Fujiwara, T.; Ohta, T.; Tamiya, Y. *J. Phys. Chem. B* **2003**, *107*, 3972.
30. Takamuku, T.; Yamaguchi, A.; Tabata, M.; Nishi, N.; Yoshida, K.; Wakita, H.; Yamaguchi, T. J. *Mol. Liq.* **1999**, *83*, 163.
31. Takamuku, T.; Nakamizo, A.; Tabata, M.; Yoshida, K.; Yamaguchi, T.; Otomo, T. *J. Mol. Liq.* **2003**, *103*, 143.
32. Tominaga, Y.; Takeuchi, S. M. *J. Chem. Phys.* **1996**, *104*, 7377.
33. Yang, C.; Li, W.; Wu, C. *J. Phys. Chem. B* **2004**, *108*, 11866.
34. Ying Guang, W.; Masaaki, T.; Toshiyuki, T. *J. Mol. Liq.* **2001**, *94*, 273.
35. Chialvo, A. A. *Mol. Phys.* **1991**, *73*, 127.
36. Bohn, M.; Fischer, J.; Kohler, F. *Fluid Phase Equilib.* **1986**, *31*, 233.
37. Jain, P.; Singh, M. *J. Chem. Eng. Data* **2004**, *49*, 1214.
38. Ortega, J.; Espiau, F.; Postigo, M. *J. Chem. Eng. Data* **2004**, *49*, 1602.
39. Goates, J. R.; Sullivan, R. J. *J. Phys. Chem.* **1958**, *62*, 188.
40. Fernández, L. s.; Pérez, E. a.; Ortega, J.; Canosa, J.; Wisniak, J. *J. Chem. Eng. Data* **2010**, *55*, 5519.
41. Shigeto, S.; Kano, H.; Hamaguchi, H.-o. *J.Chem.Phys.* **2005**, *122*, 064504.
42. Shigeto, S.; Hamaguchi, H.-o. *Chem. Phys. Lett.* **2006**, *417*, 149.
43. Wakisaka, A.; Ohki, T. *Faraday Discuss.* **2005**, *129*, 231.
44. Molotsky, T.; Huppert, D. *J. Phys. Chem. A* **2003**, *107*, 8449.
45. Molotsky, T.; Huppert, D. *J. Phys. Chem. A* **2003**, *107*, 2769.
46. Chakrabarty, D.; Chakraborty, A.; Seth, D.; Sarkar, N. *J. Phys. Chem. A* **2005**, *109*, 1764.
47. Paul, A.; Samanta, A. *J. Phys. Chem. B* **2007**, *112*, 947.
48. Bhattacharyya, K. *Acc. Chem. Res.* **2002**, *36*, 95.

49. Haldar, S.; Kombrabail, M.; Krishnamoorthy, G.; Chattopadhyay, A. *J. Phys. Chem. Lett.* **2012**, *3*, 2676.
50. Sen, S.; Andreatta, D.; Ponomarev, S. Y.; Beveridge, D. L.; Berg, M. A. *J. Am. Chem. Soc.* **2009**, *131*, 1724.
51. Sahu, K.; Kern, S. J.; Berg, M. A. *J. Phys. Chem. A* **2011**, *115*, 7984.
52. Biswas, R.; Rohman, N.; Pradhan, T.; Buchner, R. *J. Phys. Chem. B* **2008**, *112*, 9379.
53. Pradhan, T.; Gazi, H.; Guchhait, B.; Biswas, R. *J. Chem. Sci.* **2012**, *124*, 355.
54. Stanley, R. J.; King, B.; Boxer, S. G. *J. Phys. Chem.* **1996**, *100*, 12052.
55. Dahl, K.; Biswas, R.; Ito, N.; Maroncelli, M. *J. Phys. Chem. B* **2005**, *109*, 1563.
56. Li, B.; Wang, Y.; Wang, X.; Vdovic, S.; Guo, Q.; Xia, A. *J. Phys. Chem. B* **2012**, *116*, 13272.
57. Rettig, W. *J. Luminesc*. **1980**, *26*, 21; *J. Phys. Chem*. **1982**, *86*, 1970.
58. A. J. Cross, and G. R. Fleming, *Biophys. J.* **1984**, *46*, 45.
59. Yoshida, K.; Yamaguchi, T.; Kovalenko, A.; Hirata, F. *J. Phys. Chem. B* **2002**, *106*, 5042.
60. Pradhan, T.; Biswas, R. *J. Phys. Chem. A* **2007**, *111*, 11514.
61. Goates, J. R.; Sullivan, R. J. *J. Phys. Chem.* **1958**, *62*, 188.
62. Kusalik, P. G.; Lyubartsev, A. P.; Bergman, D. L.; Laaksonen, A. *J. Phys. Chem. B* **2000**, *104*, 9533.
63. Horng, M. L.; Gardecki, J. A.; Papazyan, A.; Maroncelli, M. *J. Phys. Chem.*, **1995**, ***99***, 17311.
64. Reynolds, L.; Gardecki, J. A.; Frankland, S. J. V.; Horng, M. L.; Maroncelli, M. *J. Phys. Chem.* **1996**, *100*, 10337.
65. Guchhait, B. Gazi, H. R.; Kashyap, H.; Biswas, R. *J. Phys. Chem. B*, **2010**, *114*, 5066.
66. Horng, M. L.; Gardecki, J. A.; Maroncelli, M. *J. Phys. Chem. A* **1997**, *101*, 1030.
67. Nanjo, D.; Hosoi, H.; Fujino, T.; Tahara, T.; Korenaga, T. *J. Phys. Chem. B* **2007**, *111*, 2759.

Chapter 9

Concluding Remarks and Future Problems

In this Thesis we have studied several interrelated problems, the recurring theme being the medium heterogeneity and its emergence in various fluorescence spectroscopic measurements. Concluding remarks have been given at the end of each of these chapters and thus a separate chapter on Conclusion is probably not necessary. However, we enlist here some related and interesting problems that can be studied in future for generating a more comprehensive understanding of heterogeneity and structural effects on simple chemical events occurring in a variety of medium, ranging from normal solvents to confined ones bridging the binary or multi-component mixtures.

9.1 Quantification of Heterogeneity in Molten (Amide-Electrolyte) Mixtures

Time resolved fluorescence spectroscopic results presented in chapter 3, 4 and 5 show a pronounced medium heterogeneity present in molten amide-electrolyte systems. These mixtures exhibit non-hydrodynamic behaviour along with strong decoupling between average rates (of solute solvation and rotation) and medium viscosity.[1,2] However, the techniques used in the measurement do not quantify the heterogeneity. Therefore, these studies should motivate one to carry out small angle neutron scattering (SANS) and X-ray scattering (SAXS) measurements to quantify the amount of heterogeneity or the length scales over which the particles are correlated. Excitation wavelength dependent solvation and rotational dynamics study can also probe properly the dynamical response of various environments present in these heterogeneous melts. On the other hand, a model simulation has already been done for a molten mixture and a strong dynamic heterogeneity has been found. An atomistic molecular simulation is required to investigate the underlying mechanism of observed decoupling and the nature of heterogeneity.

9.2 Structure and Dynamics of Deep Eutectic Systems

The class of deep eutectic solvents (DES)[3-7] is an important field of study because of its possibility to be used as an alternative to room temperature ionic liquids. Also because of unusual properties, it was thought to be a good medium for electrochemical uses viz. mixture for thermal salt cells, electricity production and electrodeposition. Analysis of molten mixtures such as amides with inorganic salts constitutes a major portion of the present Thesis, but these are only initial attempts from our end. Thus, there exists a huge scope for further investigation of this class of solvent system. For example, DES containing a ketoamide[8] or haloamide may pose an interesting problem as far as heterogeneity and decoupling are concerned.

9.3 Structural Transition of PEG from Folded to Unfolded State in Presence of an Electrolyte

We have discussed the effect of addition of electrolyte in polyethylene glycol (PEG) in chapter 7. PEG assumes a helical conformation in presence of isobutyric acid and trace amount of water.[9-11] Moreover, PEG helices unfold or refold when the trace water is removed or added back to the system.[9] One would like to investigate this structural transition from folded to unfolded state following fluorescence dynamics. Furthermore, we have observed in chapter 7 that the dynamics of PEG in presence of electrolyte is markedly different from pure PEG. The segmental motion of PEG becomes slower due to co-ordination of metal cation with ethereal oxygens. This co-ordination or transient bond formation will have different effects on folded or unfolded states of PEG In this context, one would also like to investigate the above structural transition in presence of electrolyte.

9.4 Probing of Phase Transition Pathway in Water-Hydroxypropyl Cellulose Binary Mixtues

Structural enhancement and modification of hydrogen bonding network structure in water-cycloethers binary mixtures has already been discussed in chapter 8. This study can be extended to some water-biopolymer binary mixtures. The main driving force of these researches is that water in living cells is always linked to biopolymer. Water seems to play an important role in governing the structure, dynamics and function. Therefore, understanding hydrated system in general and how the dynamics of water affects or control the structure or function of the biopolymer in particular are most important questions. For example, water-hydroxypropyl cellulose binary mixtures[12-16] show phase transition from cholesteric phase to isotropic phase with increasing water content. It will therefore be of interest to use reaction rate and activation energy measurements of intramolecular charge transfer (ICT) reaction to explore the phase transition pathway of water-hydroxypropyl cellulose binary mixtures.

9.5 Effects of Electrolyte on Structural Modification of Hydrogen-Bonding Network in Water-Cycloether Binary Mixtures

In chapter 8, we have found clustering, strengthening and modification of hydrogen bonding network structure in water-cycloether binary mixtures. We have seen there the minimal interplay between hydrogen bonding and hydrophobic interactions across the mixture composition. Some specific anions have ability to disorder the aggregation of hydrophobic moiety as revealed by vibrational sum frequency spectroscopy (VSFS).[17,18,19] This effect of anion partially follows the well known Hofmeister series. Furthermore, anions have another effect on hydrogen-bonding structure of water.[20-21] In this context, the effect of electrolyte on hydrogen-bonding as well hydrophobic interaction could be studied with a suitable instrumental resolution.

9.6 Solute and Solvent Dynamics in Equal Sized aqueous Environments of Positively and Negatively charged Reverse Micelles

In Chapter 6, we measured dynamic Stokes shift and anisotropy of a dipolar solute in trapped water pools by surfactants of different charge character have suggested that solvation energy relaxation rates are slower in reverse micelles made of neutral surfactants (IGPAL) than those in reverse micelles of negatively charged (AOT) surfactant molecules.

Here, it will be interesting to see the effects of positively charged surfactant (CTAB)[22,23] on solute and solvent dynamics in equal sized reverse micelles. In addition, one should back up the experimental results with proper simulation studies so that the effects of solute location and charge (anionic or cationic) are also quantified.

These are only few representative problems related to the work described in this Thesis. Using the already existing knowledge of relaxation phenomena and medium effects on them, exploration of more complex and biologically relevant environment should be possible. In fact, understanding of these systems could be largely augmented by the applications of computer simulations using realistic potentials. The availability of speedy computing systems, extended resources coupled with sophisticated experimental techniques is expected to make an inroad to systems that were out of bound so far. We look forward to this exciting and more intellectually stimulating future of condensed phase dynamics dwelling at the interface of chemistry, biology and computational sciences.

References:

1. Guchhait, B.; Al Rasid Gazi, H.; Kashyap, H. K.; Biswas, R. *J. Phys. Chem. B* **2010**, *114*, 5066.
2. Guchhait, B.; Daschakraborty, S.; Biswas, R. *J. Chem. Phys.* **2012**, *136*, 174503.
3. Abbott, A. P.; Boothby, D.; Capper, G.; Davies, D. L.; Rasheed, R. K. *J. Am. Chem. Soc.* **2004**, *126*, 9142.
4. Abbott, A. P.; Capper, G.; Davies, D. L.; Rasheed, R. K.; Tambyrajah, V. *Chem. Commun.* **2003,** 70.
5. Abbott, A. P.; Capper, G.; Davies, D. L.; Munro, H. L.; Rasheed, R. K.; Tambyrajah, V. *Chem. Commun.* **2001,** 2010.
6. Abbott, A. P.; Capper, G.; Davies, D. L.; Rasheed, R. K. *Inorg. Chem.* **2004**, *43*, 3447.
7. Abbott, A. P.; Capper, G.; Davies, D. L.; Rasheed, R. K. *Chem. Eur. J.* **2004**, *10*, 3769.
8. Lobbia, G. G.; Berchiesi, G. *Thermochim. Acta* **1987**, *118*, 223.
9. Norman, A. I.; Fei, Y.; Ho, D. L.; Greer, S. C. *Macromolecules* **2007**, *40*, 2559.
10. Reddy, P. M.; Venkatesu, P.; Bohidar, H. B. *J. Phys. Chem. B* **2011**, *115*, 12065.
11. Castellanos, P.; Norman, A. I.; Greer, S. C. *J. Phys. Chem. B* **2006**, *110*, 22172.
12. Sudo, S. *J. Phys. Chem. B* **2010**, *115*, 2.
13. Cooper, J.; Hill, R. M. J. Colloid Interface Sci. 1996, 180, 27.
14. Wojciechoski, P.; Joachimiak, A.; Halamus, T. Polym. Adv. Technol. 2003, 14, 826.
15. Shinoda, H. G.; Moteleb, M. M. A. J. Appl. Polym. Sci. 2005, 98, 571.
16. Sugimoto, H.; Miki, T.; Kanayama, K.; Norimoto, M. J. Non-Cryst. Solids 2008, 354, 3220.
17. Gurau, M. C.; Lim, S.-M.; Castellana, E. T.; Albertorio, F.; Kataoka, S.; Cremer, P. S. *J. Am. Chem. Soc.* **2004**, *126*, 10522.
18. Zhang, Y.; Cremer, P. S. *Annu. Rev. Phys. Chem.* **2010**, *61*, 63.
19. Kim, H.; Lee, H.; Lee, G.; Kim, H.; Cho, M. *J. Chem. Phys.* **2012**, *136*, 124501.
20. Nucci, N. V.; Vanderkooi, J. M. *J. Mol. Liq.* **2008**, *143*, 160.
21. Chandra, A. *Phys. Rev. Lett.* **2000**, *85*, 768.

22. Moilanen, D. E.; Levinger, N. E.; Spry, D. B.; Fayer, M. D. *J. Am. Chem. Soc.* **2007**, *129*, 14311.
23. Mandal, D.; Sen, S.; Bhattacharyya, K.; Tahara, T. *Chem.Phys. Lett.* **2002**, *359*, 77.

Appendix

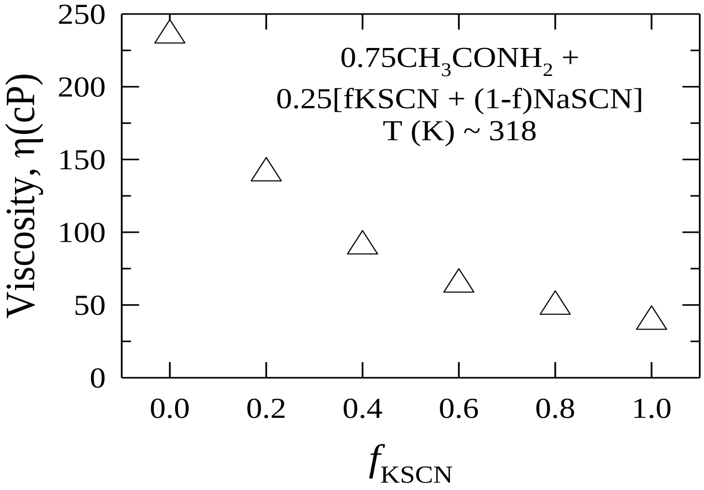

Fig. A1: Plot of viscosity (η) of molten mixtures of acetamide and sodium/ potassium thiocyanate at different fractions of KSCN at ~318 K. These have been taken from Ref. 44 of the chapter.

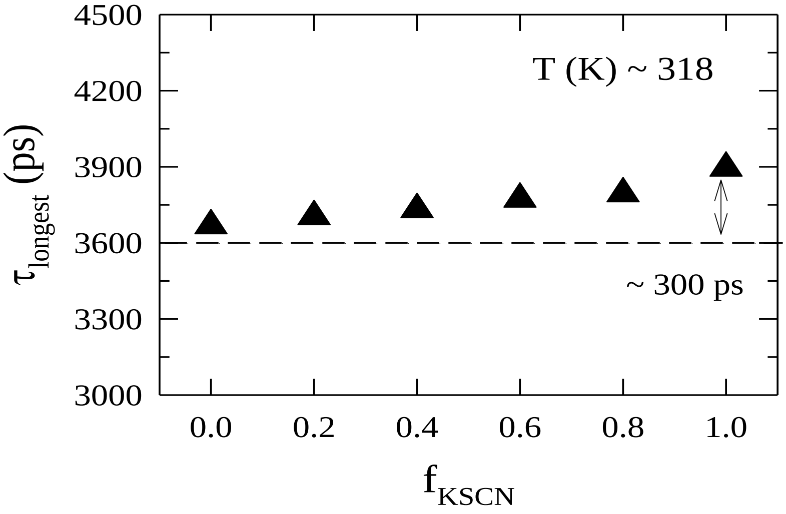

Fig. A2: Longest time constant ($\tau_{longest}$) versus KSCN fraction at ~318K for C153 in molten mixtures of acetamide with NaSCN and KSCN.

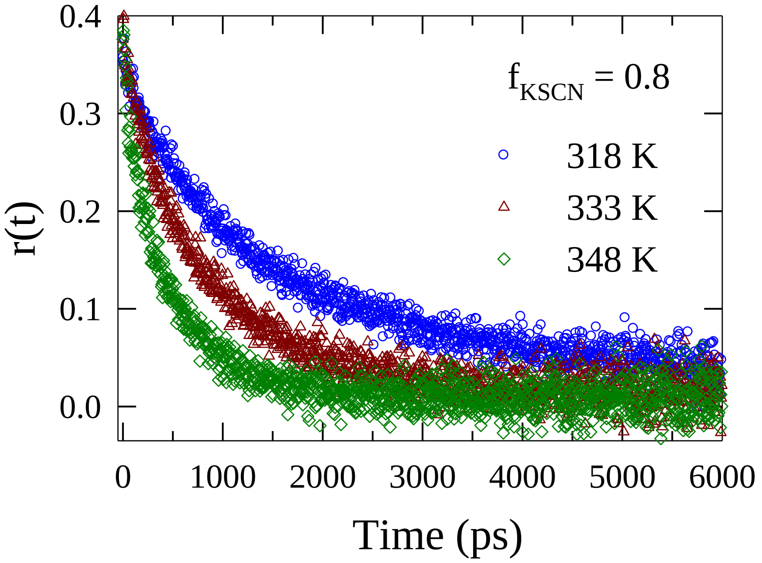

Fig. A3: Representative decays (color coded) of fluorescence anisotropy of C153 in molten mixture for f_{KSCN} = 0.80 at ~318, 333 and 348 K

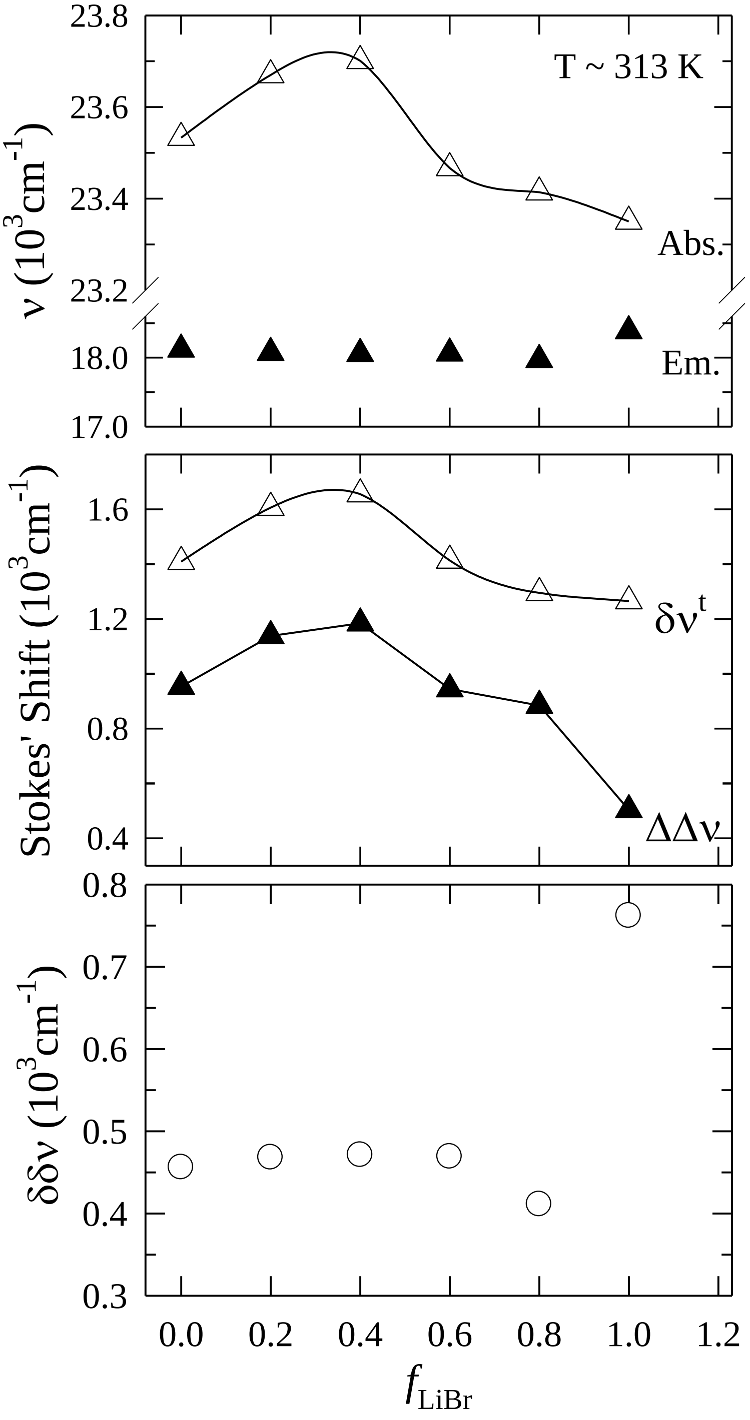

Fig. A4 : Composition dependence of spectral parameters for C153 in [$0.78CH_3CONH_2 + 0.22\{f$ LiBr + (1-*f*) $LiNO_3\}$] molten mixtures. See text for discussion.

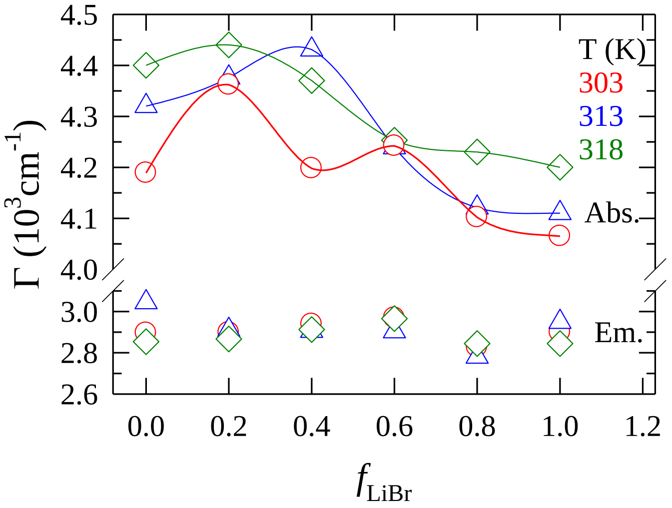

Fig. A5: Composition dependence of full width at half maxima (FWHM) of the absorption and emission spectra measured using C153 in molten mixtures of acetamide with lithium nitrate and lithium bromide at different temperatures (color coded).

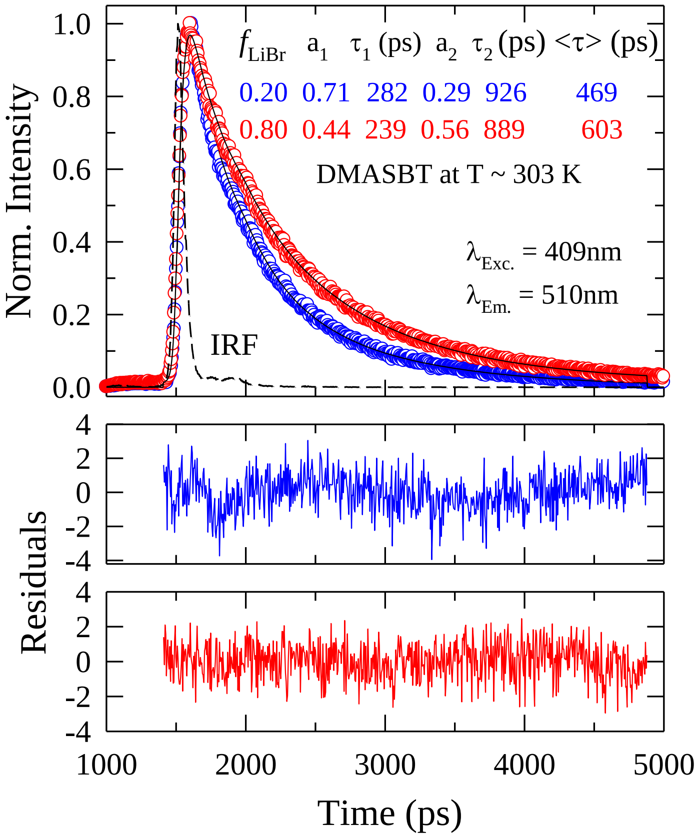

Fig. A6: Fluorescence intensity decay profile of DMASBT for f_{LiBr} = 0.2 and 0.8 (color coded) at 303 K. Experimental data are shown by circles and solid lines represent fits through experimental data. The instrumental response function (IRF) is also shown. The respective residuals (color coded) are presented in the bottom panels. Fit parameters are shown in the inset of the upper panel.

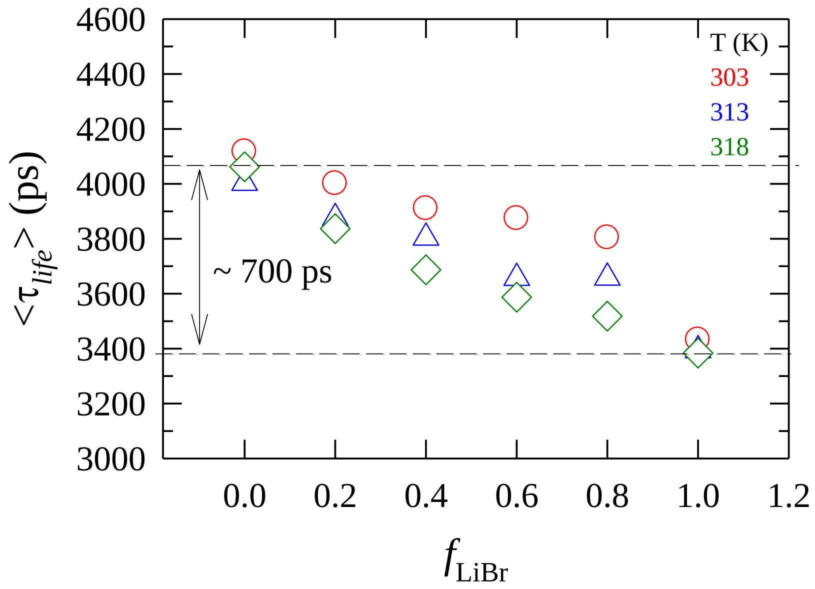

Fig. A7: Composition dependence of average lifetime, $< \tau_{life} >$ of C153 in [$0.78CH_3CONH_2$ + 0.22{*f* LiBr + (1-*f*) $LiNO_3$)] at different temperatures.

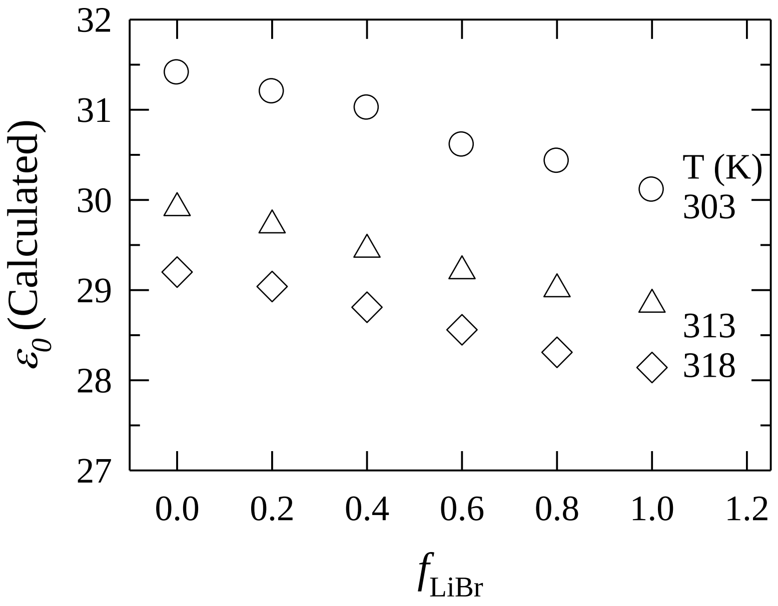

Fig. A8: Plot of calculated static dielectric constant versus f_{LiBr} for the molten mixtures of acetamide with lithium nitrate with lithium bromide at different temperatures. These ε_0 have been used in our calculations of solvation time correlation functions

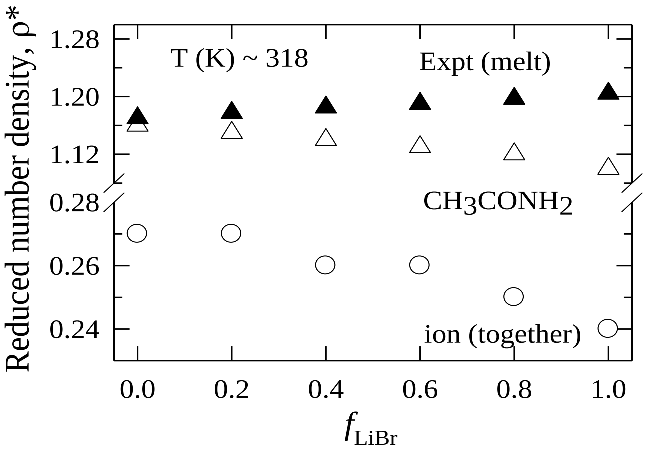

Fig. A9: Composition dependent total (filled triangles), dipolar (open triangles) and ion (circles) number densities (reduced by appropriate diameters) at 318 K. Values of experimental densities have been taken from Ref. 23.

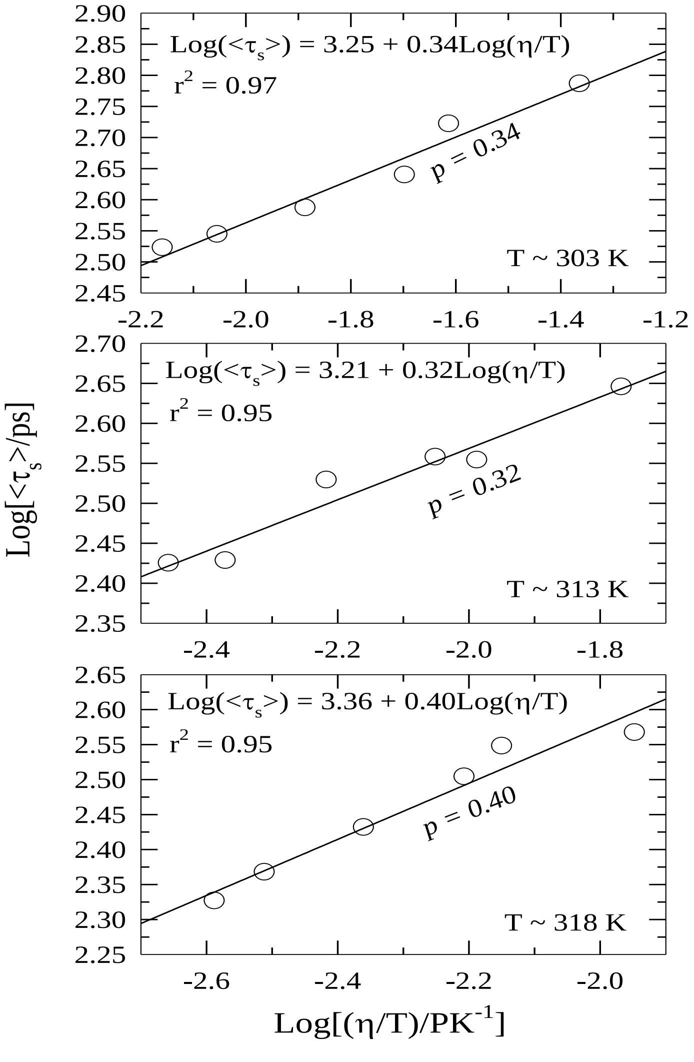

Fig. A10: Log-Log plot of average solvation time, $<\tau_s>$ versus temperature-reduced viscosity, η/T. Circles represent the experimental average solvation time and solid lines are the fits through the data points using the relation $\text{Log}[<\tau_s>] = B + p\text{Log}[(\eta/T)]$.

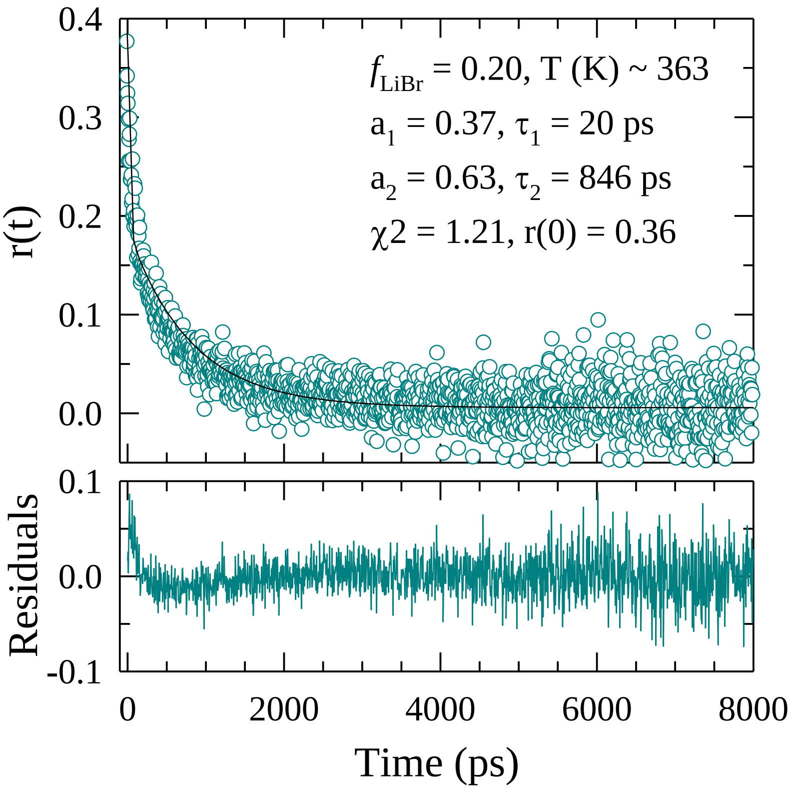

Fig. A11: Representative decay of the fluorescence anisotropy, *r*(*t*), of C153 in the molten mixtures of acetamide with lithium nitrate and lithium bromide for f_{LiBr} = 0.20 at 363 K. Circles represents data points and solid line fit through them. Residuals are also shown in the lower panel of the figure. Fitted parameters are shown in inset of the upper panel.

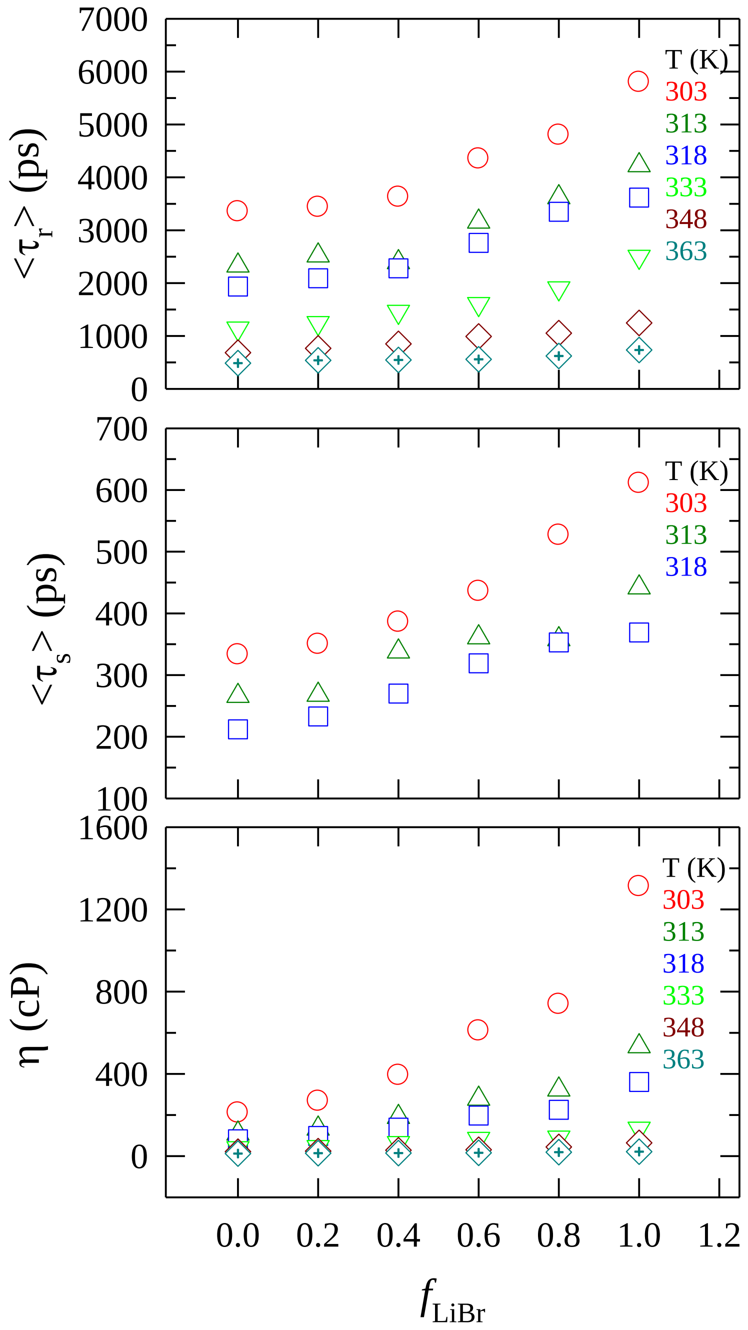

Fig. A12: Composition dependence of average rotational and solvation times ($<\tau_r>$ and $<\tau_s>$) measured using C153 in these melts and melt-viscosity at different temperatures (color coded).

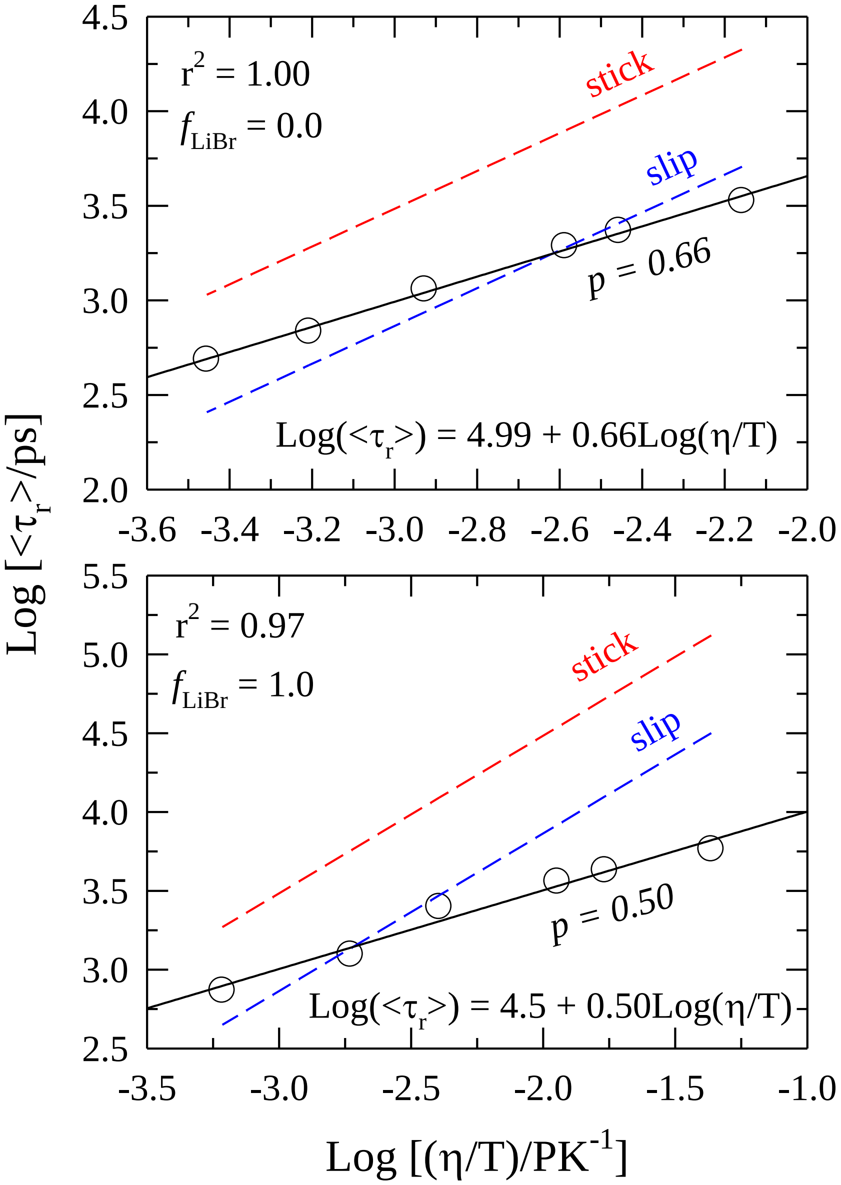

Fig. A13: Log-Log plot of average rotation time, <τ_r> of C153 versus η/T in molten mixtures of acetamide with lithium nitrate and lithium bromide for f_{LiBr} = 0.0 (upper panel) and 1.0 (lower panel). The solid line shows the best fit of the experimentally measured data with the relation Log[<τ_r>] = B + *p*Log[η/T], the associated B and *p* values are given in the repective plots. The dashed lines show the prediction of hydrodynamic stick and slip limits.

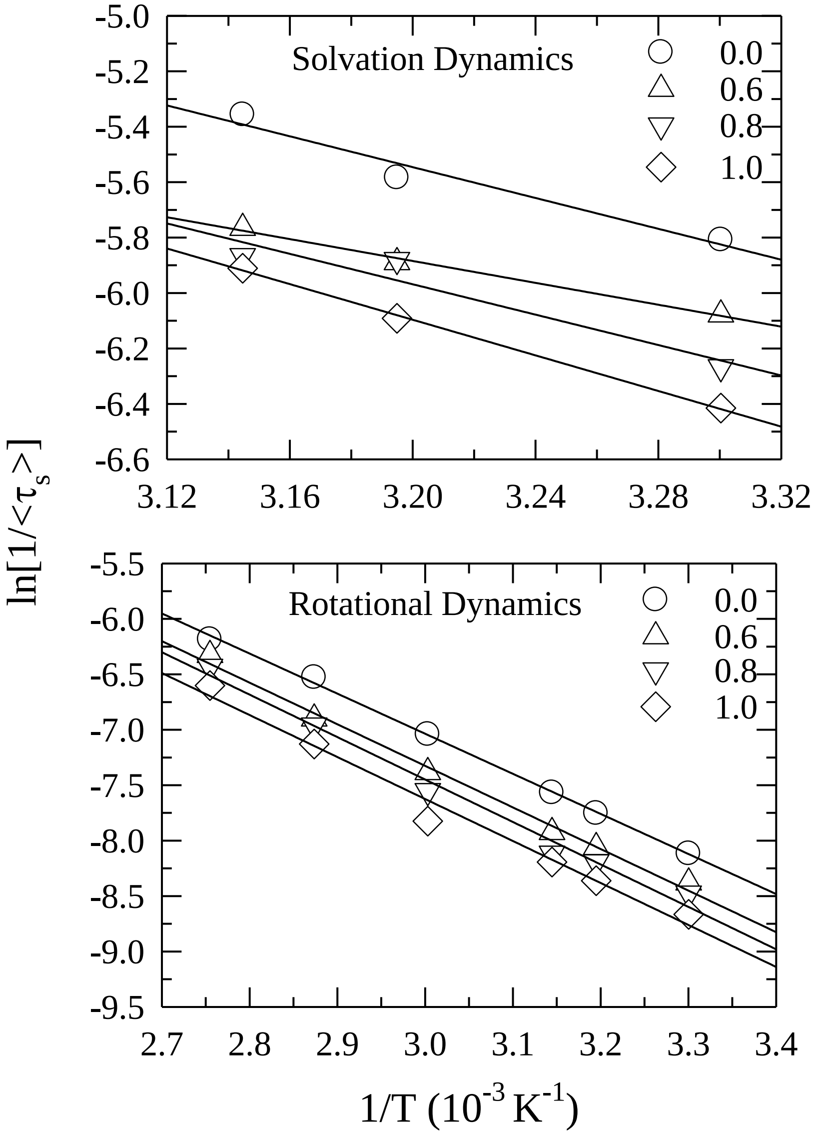

Fig. A14: Arrhenius plot of ln(1/<τ_x>), versus inverse of temperature (1/T) for solvation and rotational dynamics of C153 in molten mixtures of acetamide with lithium nitrate and lithium bromide. The solid lines are the linear fits through the data points. Circles represent natural logarithm of inversion of average solvation or rotation times at f_{LiBr} = 0.0, triangles at 0.60, inverted triangles at 0.80 and diamonds at 1.0.

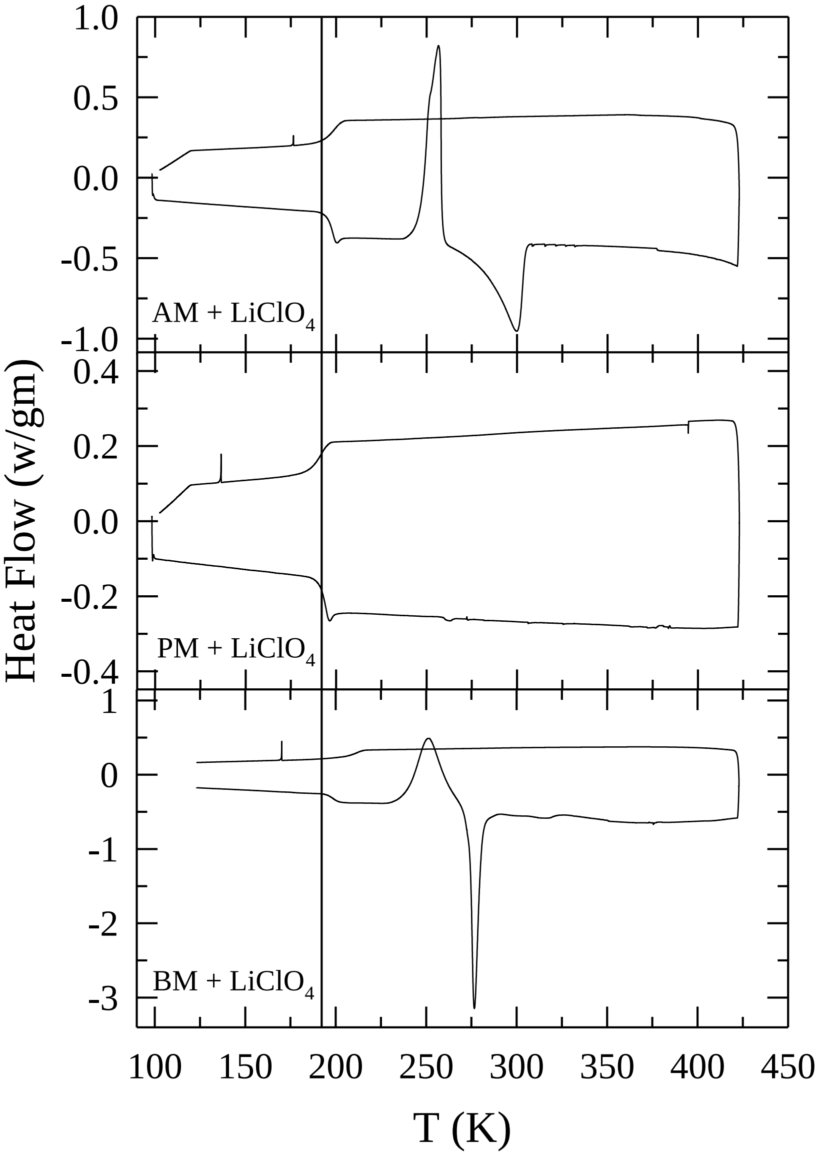

Fig. A15: Differential scanning calorimetric traces for three {alkylamide + $LiClO_4$} mixtures. The upper, middle and lower panels represent AM, PM and BM molten mixtures respectively. The glass transition temperatures (T_g) have been obtained from the figures.

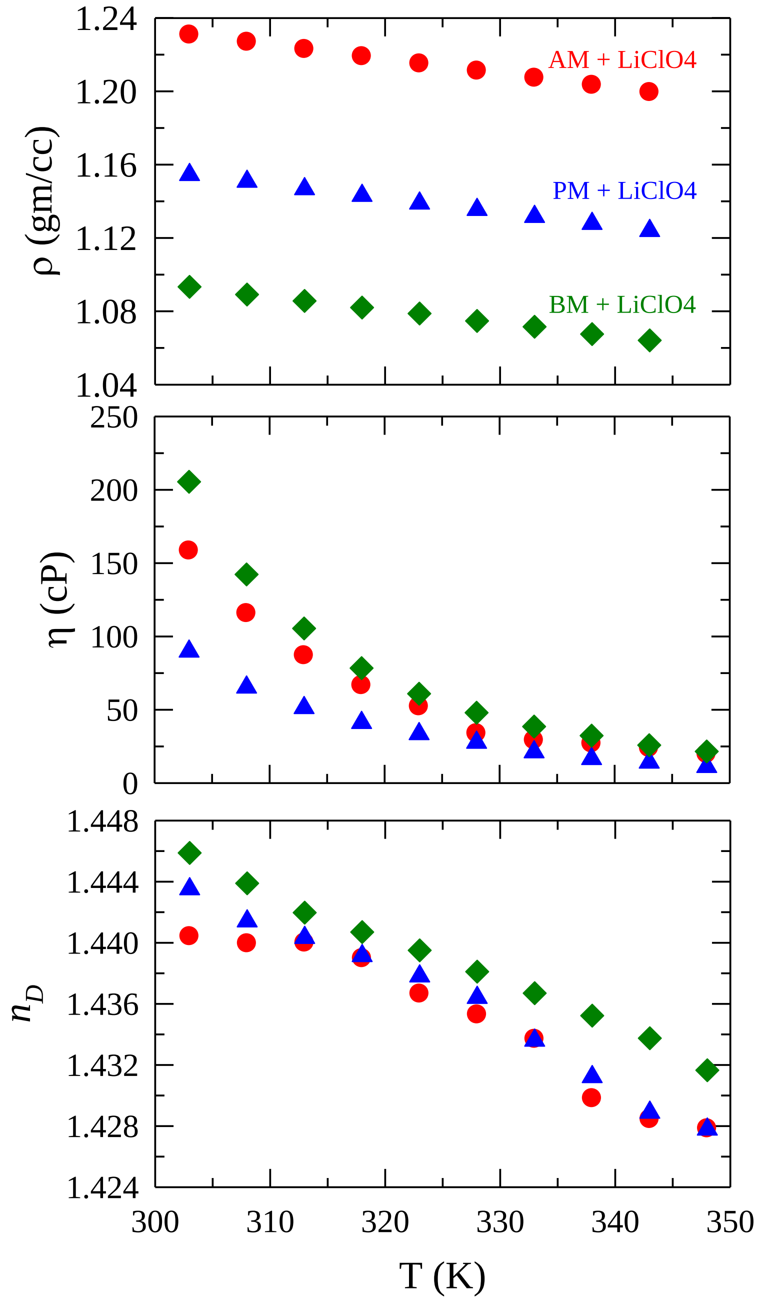

Fig. A16: Temperature dependence of densities (ρ), viscosities (η) and refractive indices (n_D) for deep eutectics made of acetamide (AM), propionamide (PM) and butyramide (BM) with Lithium perchlorate.

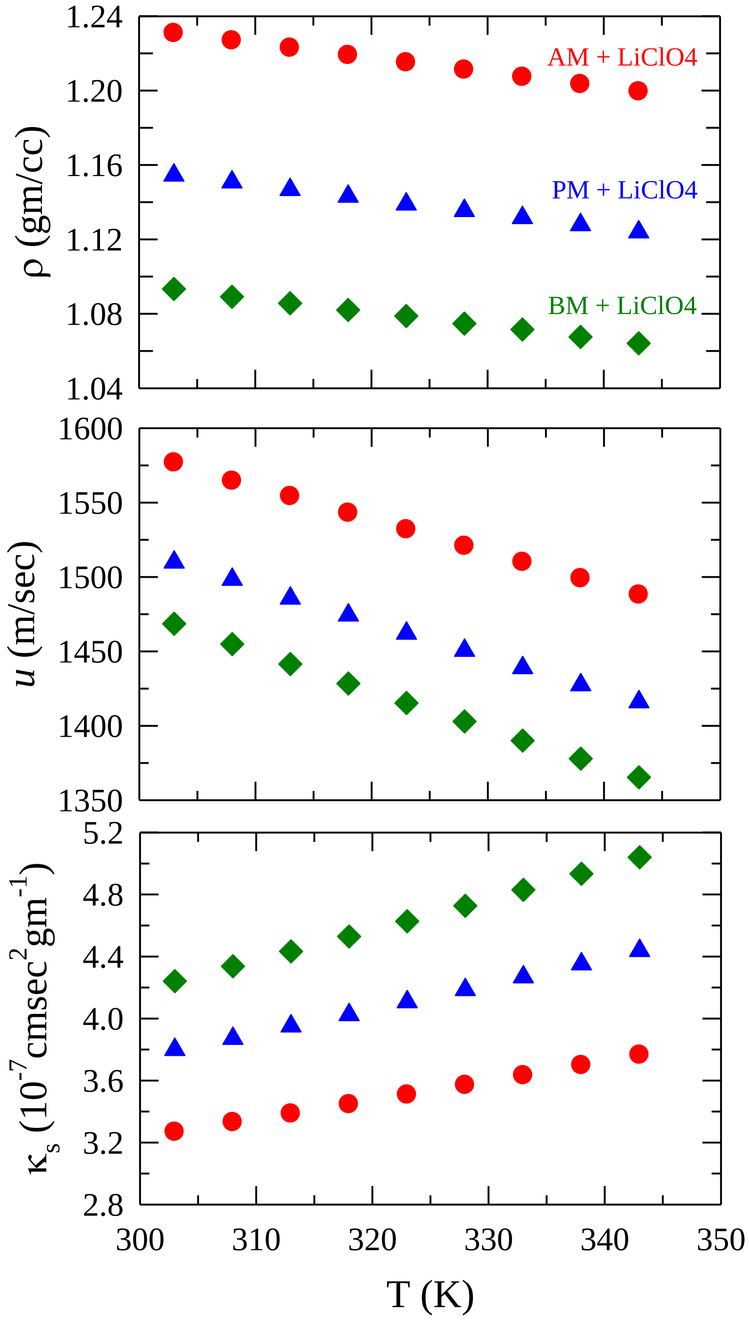

Fig. A17: Temperature dependence of densities (ρ), ultrasonic velocities (u) and isentropic compressibilities (k_s) for deep eutectics made of acetamide (AM), propionamide (PM) and butyramide (BM) with Lithium perchlorate.

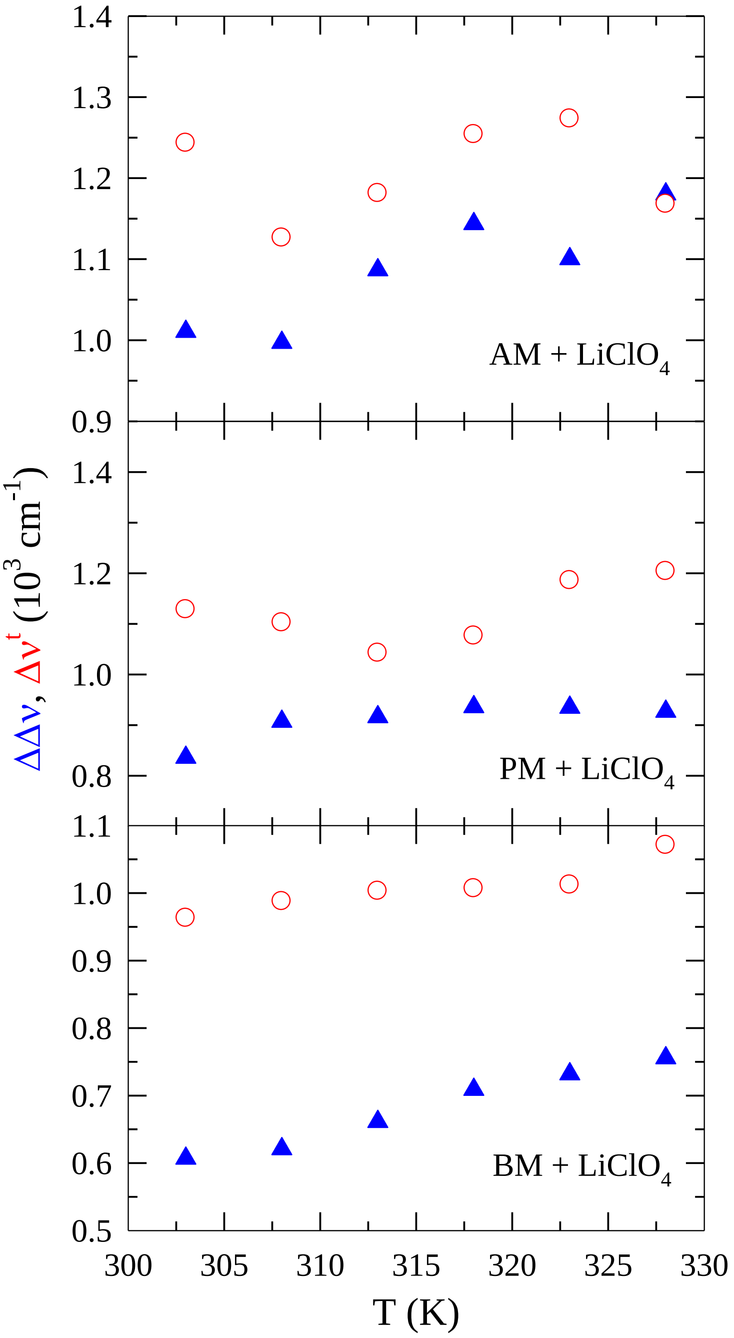

Fig. A18: Relative ($\Delta\Delta\nu$) and time resolved estimated ($\Delta\nu_{est}(t)$) Stokes shifts (color coded) for C153 versus temperature in three {alkylamide + LiClO$_4$} mixtures. Upper, middle and lower panels represent data in AM, PM and BM molten mixtures respectively. The two Stokes shifts are defined in several chapters of the Thesis.

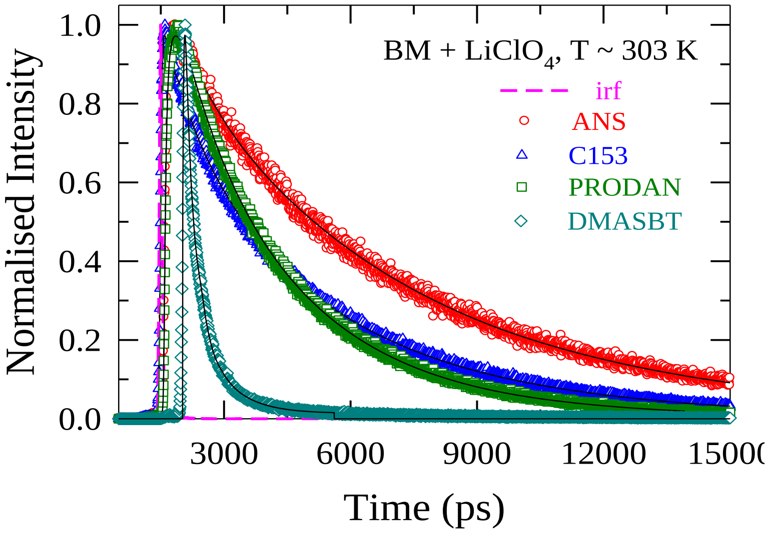

Fig. A19: Fluorescence intensity decay profiles for four dipolar solutes, ANS, C153, PRODAN and DMASBT (color coded) in molten {BM + LiClO4} mixtures at 303 K.

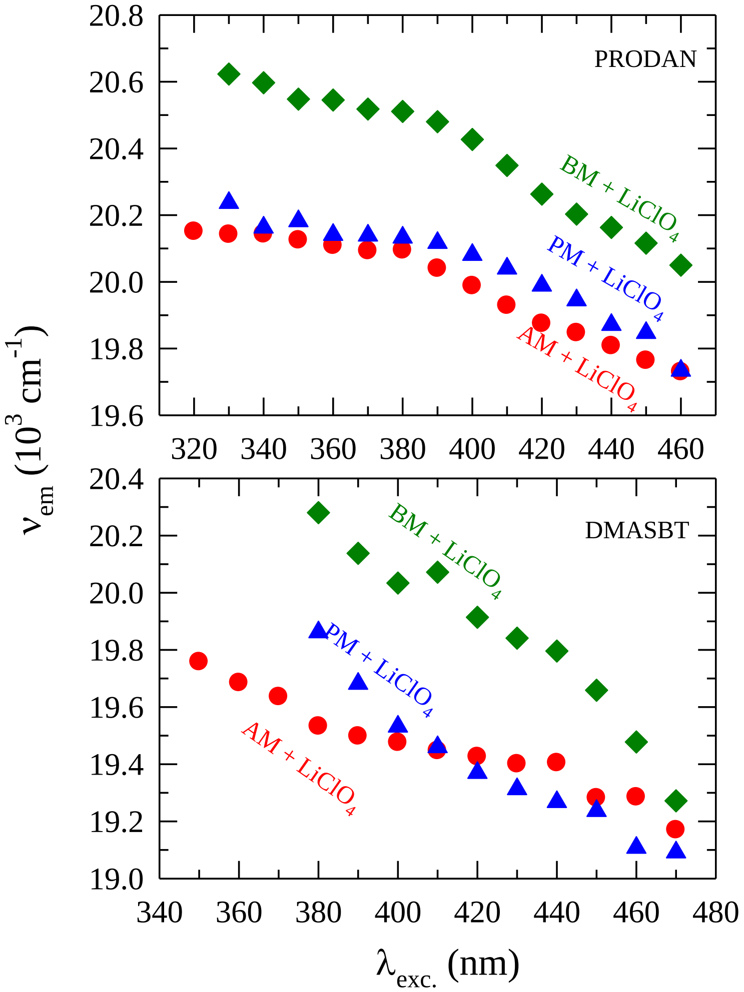

Fig. A20: Excitation wavelength dependence of fluorescence behaviors of PRODAN and DMASBT in three {alkylamide + LiClO$_4$} deep eutectic melts.

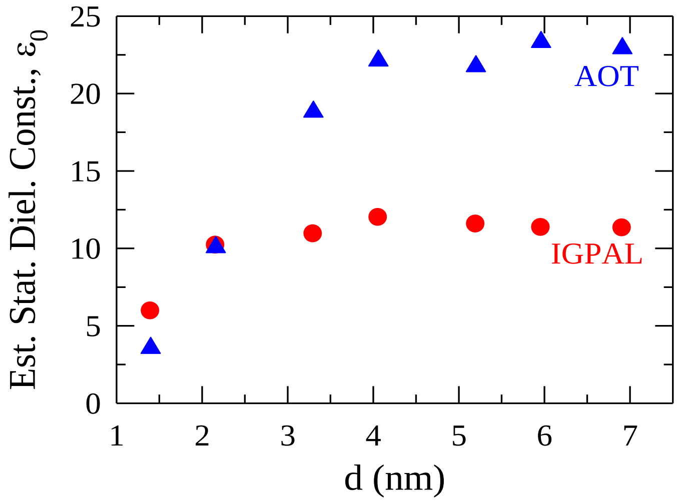

Fig. A21: Pool size dependence of the average polarity in terms of static dielectric constant (ε_0) estimated from the emission spectra of C153 in AOT and IGPAL RMs. The estimation is done via following the procedure described in Ref. 17 of the text and assuming refractive index of water did not change upon confinement.

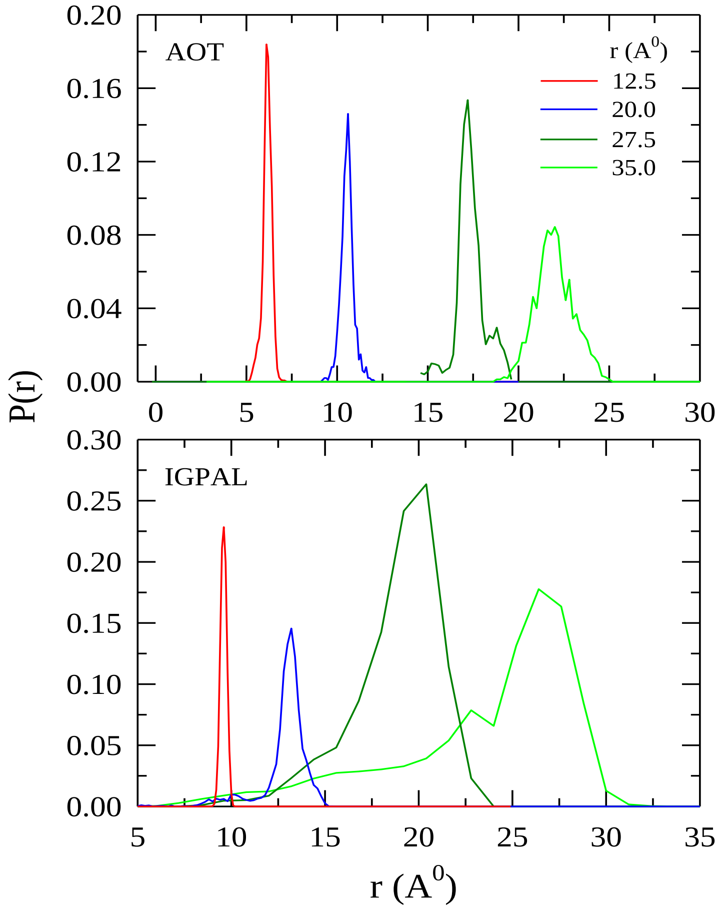

Fig. A22: Distance distribution of the ground state solute (C153) in aqueous AOT and IGPAL RMs at different pool sizes.

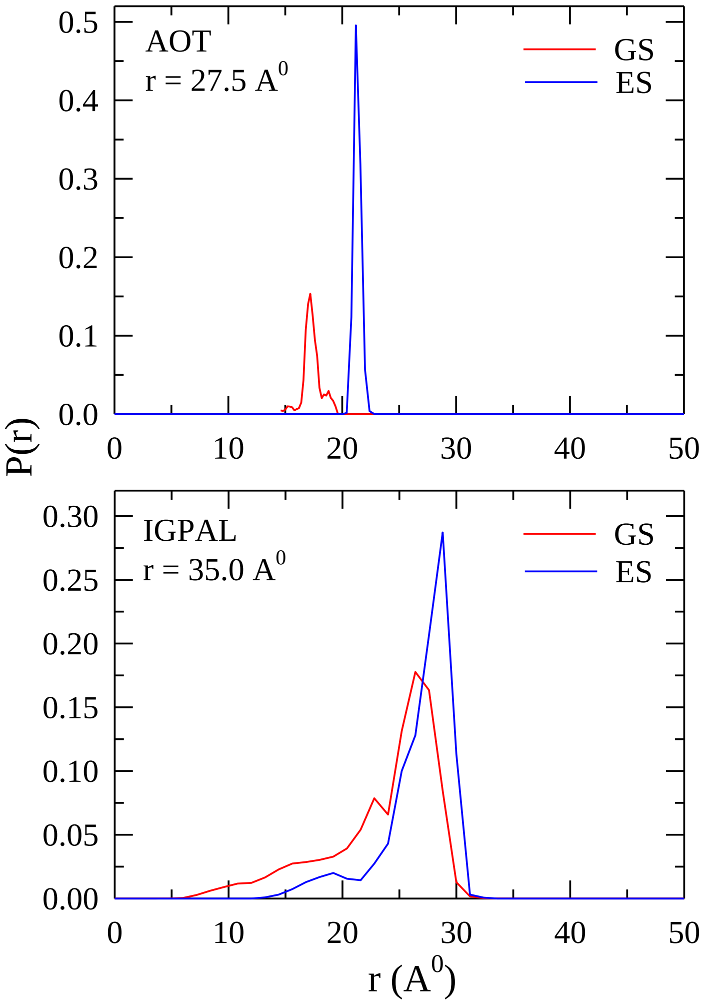

Fig. A23: Distance distribution of C153 in the ground (red) and excited states (blue) in AOT (d = 5.2 nm) and IGPAL (d= 6.9 nm) RMs.

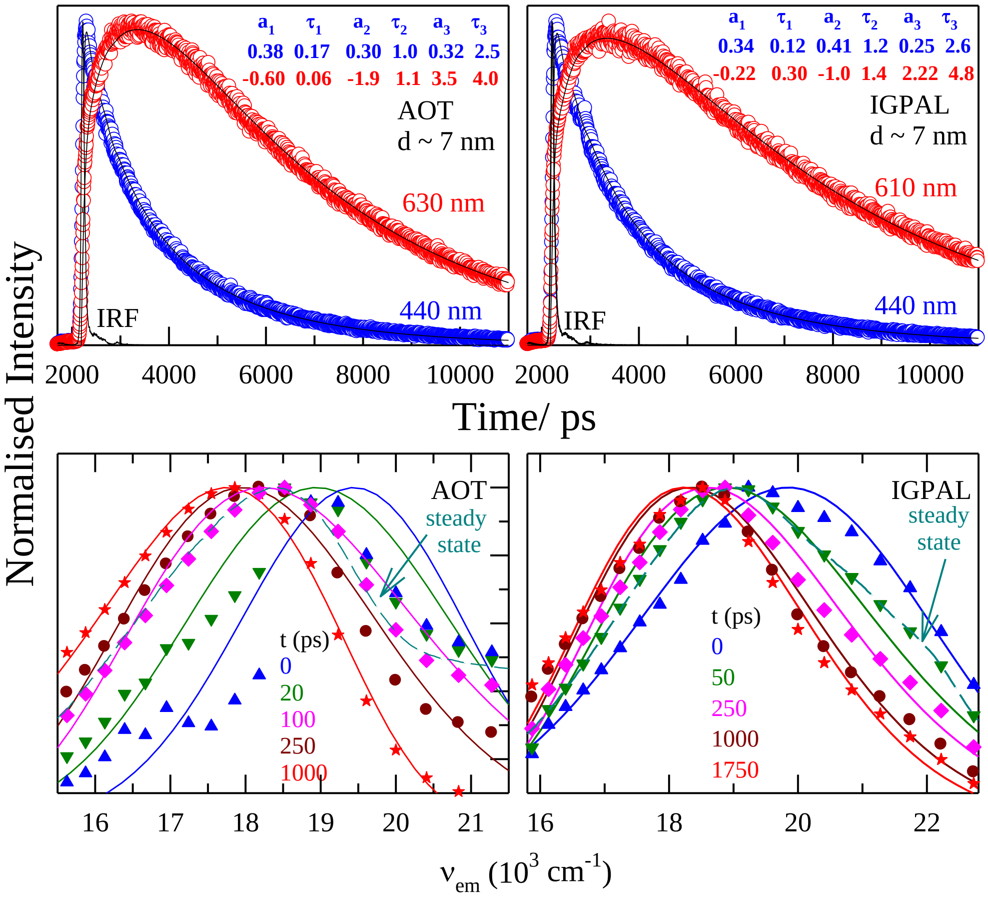

Fig. A24: Representative fluorescence intensity decays of C153 at blue and red wavelengths in AOT and IGPAL reverse micelles (upper panels) at $d \sim 7nm$. Circles and solid lines represent the experimental data and fits through them, respectively. Instrument response functions (IRFs) are also shown (dashed lines). Tri-exponential fit parameters of the decays are presented in the insets. Lower panes present the synthesized time resolved emission spectra (TRES) of C153 in these RMs.

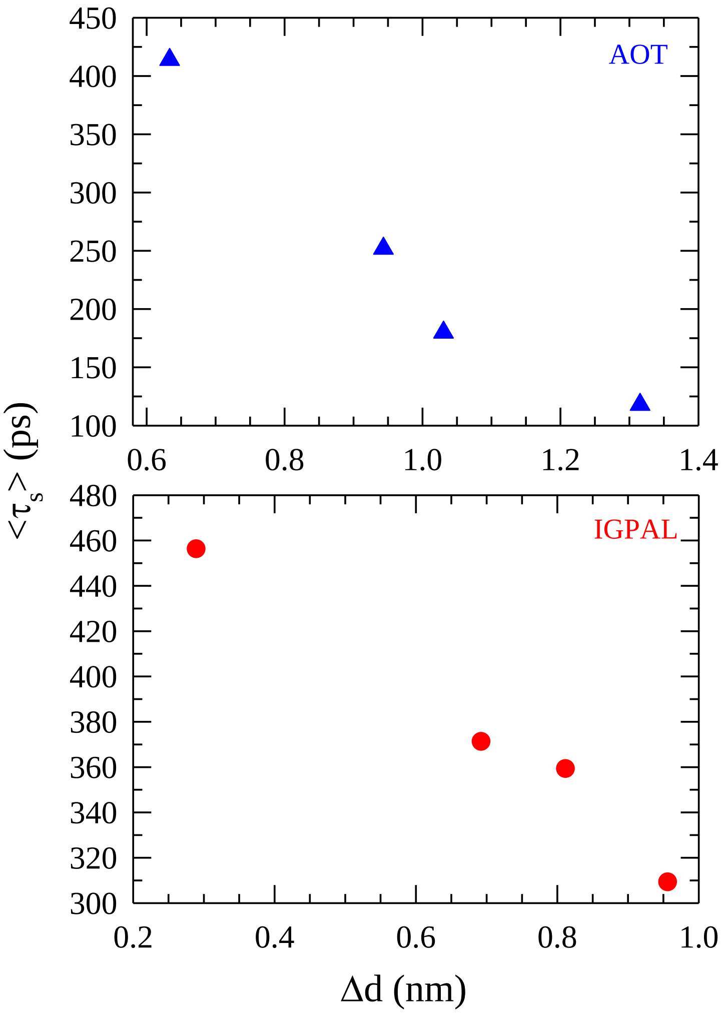

Fig. A25: Plots of experimentally measured average solvation time, ($<\tau_s>$) of C153 versus simulated distance of the solute from the interface, (Δd) in AOT (upper panel) and IGPAL (lower panel) reverse micelles at various pool sizes. Note Δd represent distances for ground state (S_0) solute while measured times associates with photo-excited (S_1) solute.

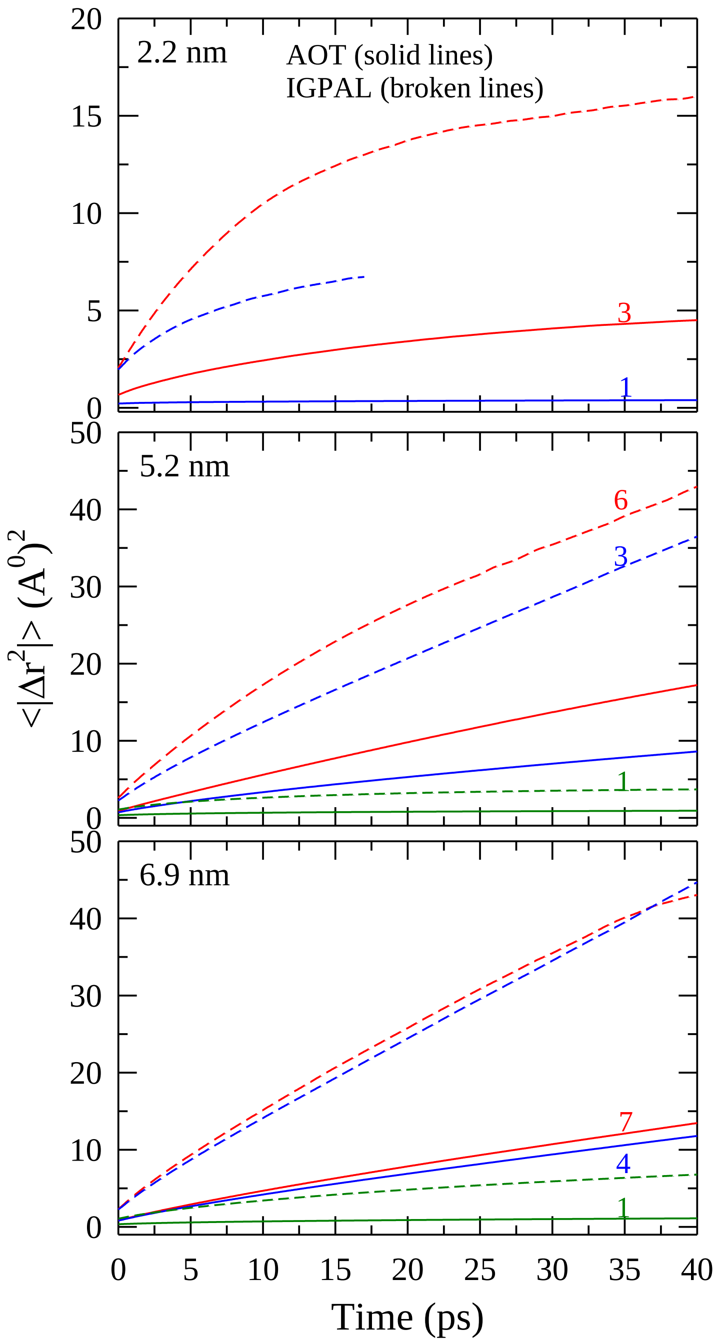

Fig. A26: Representative mean square displacements (MSDs, $\left\langle \left| \Delta r^2 \right| \right\rangle$) of water molecules in charged (AOT) and neutral (IGPAL) RMs for various layers. D_T^{layer}, shown in Fig. 11, have been calculated from these MSDs.

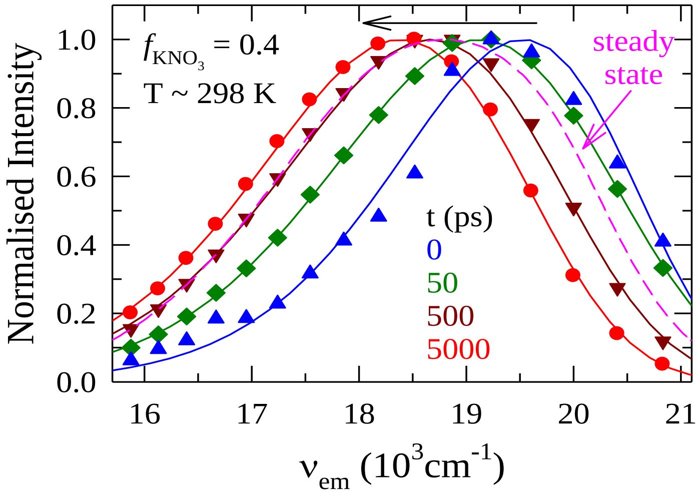

Fig. A27: Synthesized time resolved emission spectra (TRES) of C153 at different time slices from the experimentally obtained decays in PEG with Li^{+}/K^{+} Nitrate at f_{KNO_3} = 0.4 and 298 K.

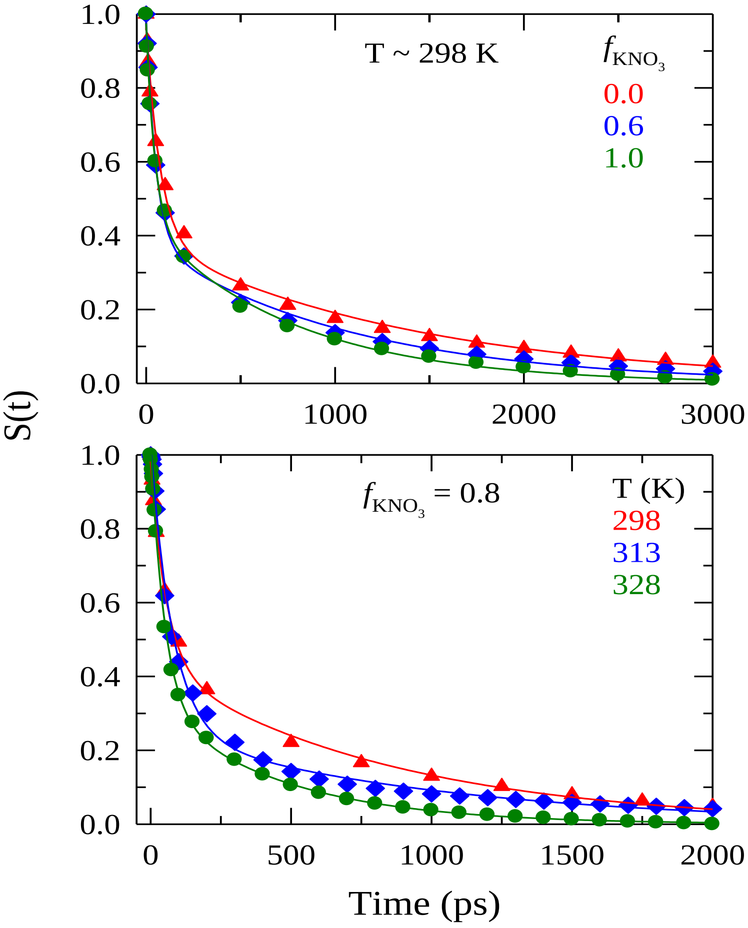

Fig. A28: Decays of solvent response function, $S(t)$, of C153 in [0.85 PEG + 0.15{*f* KNO_3 + (1-*f*) $LiNO_3$)] mixtures at different KNO_3 fraction (upper panel, color coded), and at different temperatures (lower panel, color coded).

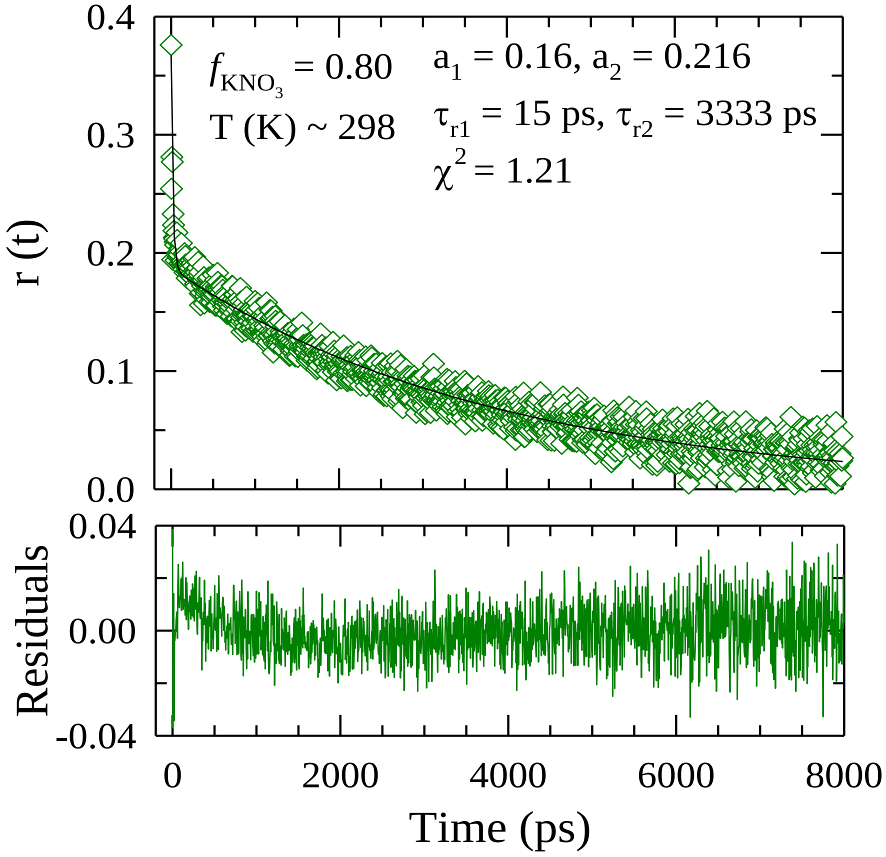

Fig. A29: Representative decay of the fluorescence anisotropy, *r*(*t*), of C153 in PEG with Li^+/K^+ Nitrate for f_{KNO3} = 0.80 at 298 K. Diamonds represents data points and solid line is fits through them, residuals are also shown in the lower panel of the figure. Fitted parameters are shown in inset of the upper panel.

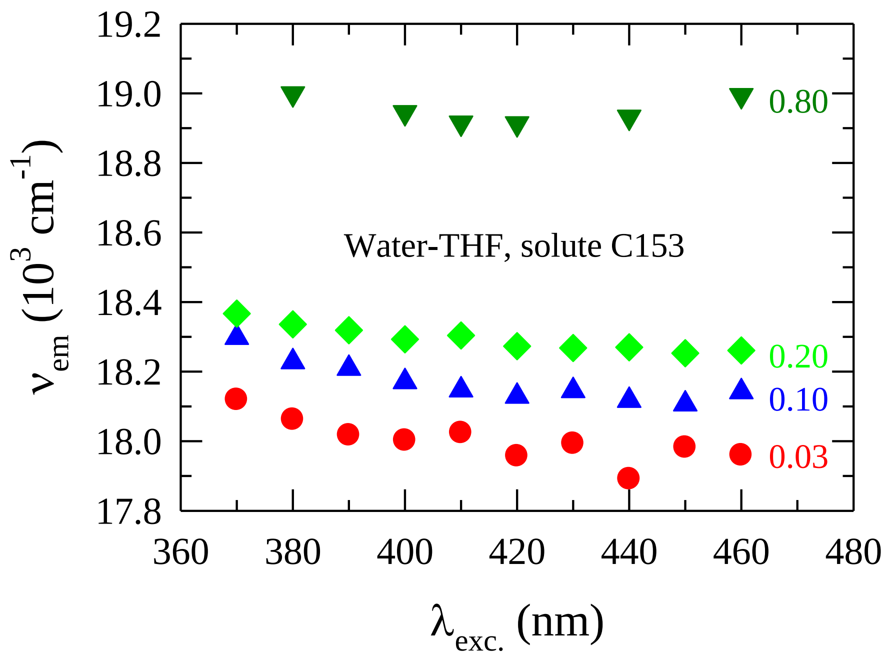

Fig. A30: Excitation wavelength ($\lambda_{exc.}$) dependence of fluorescence peak frequency of C153 in water-THF binary mixtures at f_{THF} = 0.03, 0.01, 0.02 and 0.08 (data are color coded). The error associated with this measurement is ± 200 cm^{-1}.

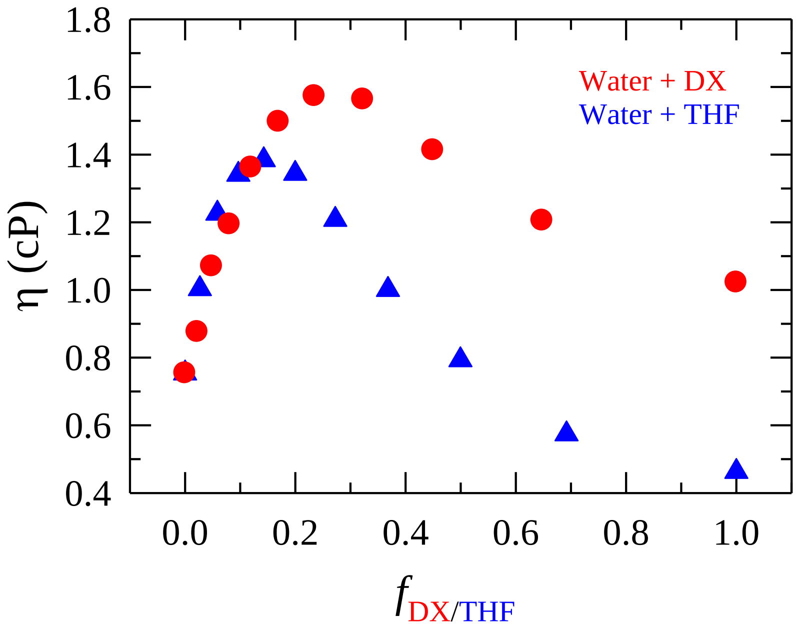

Fig. A31: The variation of viscosities (upper panel) and densities (lower panel) as function of cycloether mole fraction in water-cycloether binary mixtures. (Data are taken from *J. Chem. Eng. Data*. **2004**, *49*, 468.)

Table A1: The difference between the estimated Stokes' shift and relative Stokes' shift, $\delta\delta\nu = \delta\nu^t - \Delta\Delta\nu$, measured using C153 in molten mixtures of acetamide with lithium nitrate and lithium bromide at different concentrations of LiBr at 313 K.

f_{LiBr}	$\delta\delta\nu$ (10^3 cm^{-1})
0.0	0.456
0.2	0.468
0.4	0.471
0.6	0.469
0.8	0.411
1.0	0.762

Table A2: Summary of experimentally measured viscosity (η), temperature-reduced viscosity (η/T), average solvation and rotation times ($\langle\tau_s\rangle$ and $\langle\tau_r\rangle$, respectively), activation energies (E_a^x), for [$0.78CH_3CONH_2 + 0.22\{f\ LiBr + (1-f)\ LiNO_3\}$] molten mixtures at various compositions and temperatures.

f_{LiBr}	T (K)	η (cP)	η/T (10^{-3})	$\langle\tau_s\rangle$ (ps)	$E_a^{\langle\tau_s\rangle}$ (KJmol-1)	$\langle\tau_r\rangle$ (ps)	$E_a^{\langle\tau_r\rangle}$ (KJmol-1)
0.00	303	210.57	6.95	333	23.13	3351	30.06
	313	109.25	3.49	266		2331	
	318	82.24	2.586	212		1934	
	333	39.35	1.182	-		1143	
	348	21.59	0.62	-		684	
	363	12.73	0.351	-		486	
0.20	303	267.67	8.834	350	21.63	3436	28.99
	313	133.34	4.26	268		2521	
	318	98.05	3.083	233		2092	
	333	44.99	1.351	-		1246	
	348	24.27	0.698	-		767	
	363	14.66	0.404	-		539	
0.40	303	393.67	12.992	386	17.76	3626	28.43
	313	190.07	6.073	338		2393	
	318	138.88	4.367	270		2280	
	333	64.02	1.922	-		1460	
	348	28.51	0.819	-		850	
	363	15.11	0.416	-		547	
0.60	303	609.91	20.129	436	16.41	4350	31.18
	313	278.57	8.9	361		3162	
	318	197.67	6.216	319		2760	
	333	84.69	2.543	-		1607	
	348	30.99	0.891	-		992	
	363	16.51	0.455	-		559	
0.80	303	738.89	24.386	527	22.80	4800	31.83
	313	323.40	10.332	358		3622	
	318	225.51	7.092	353		3349	
	333	90.83	2.728	-		1904	
	348	44.62	1.282	-		1054	
	363	19.23	0.53	-		621	
1.00	303	1311.90	43.299	611	26.72	5800	31.48
	313	534.025	17.062	442		4227	
	318	360.49	11.336	369		3618	
	333	134.53	4.04	-		2499	
	348	64.88	1.865	-		1247	
	363	22.13	0.61	-		736	

.

Table A3: Bi-exponential fit parameters of the measured solvation response functions for the molten mixtures of acetamide with lithium bromide and lithium nitrate at different compositions and temperatures

f_{LiBr}	a_1	τ_1 (ps)	a_2	τ_2 (ps)	<τ_s> (ps)
T ~ 303 K					
0.0	0.51	53	0.49	625	333
0.2	0.50	32	0.50	667	350
0.4	0.45	53	0.55	667	386
0.6	0.42	49	0.58	714	436
0.8	0.34	57	0.66	769	527
1.0	0.24	112	0.76	769	611
T ~ 313 K					
0.0	0.57	48	0.43	556	266
0.2	0.55	33	0.45	556	268
0.4	0.49	38	0.51	625	338
0.6	0.48	76	0.52	625	361
0.8	0.45	32	0.55	625	358
1.0	0.41	50	0.59	714	442
T ~ 318 K					
0.0	0.60	36	0.40	476	212
0.2	0.58	40	0.42	500	233
0.4	0.55	36	0.45	556	270
0.6	0.55	68	0.45	625	319
0.8	0.47	46	0.53	625	353
1.0	0.51	37	0.49	714	369

Table A4: Bi-exponential fit parameters for the calculated solvation response functions at various mixture compositions and temperatures in the overdamped and underdamped limits

	Overdamped Limit					Underdamped Limit				
f_{LiBr}	a_1	τ_1 (ps)	a_2	τ_2 (ps)	<τ_s> (ns)	a_1	τ_1 (ps)	a_2	τ_2 (ps)	<τ_s> (ns)
T (K) = 303										
0.0	0.51	553	0.49	1983	1.25	0.38	2.62	0.62	1340	0.83
0.2	0.51	700	0.49	2512	1.59	0.38	1.85	0.62	1702	1.06
0.4	0.51	1032	0.49	3696	2.34	0.38	1.47	0.62	2497	1.55
0.6	0.50	1596	0.50	5709	3.65	0.38	1.30	0.62	3851	2.39
0.8	0.50	1938	0.50	6924	4.43	0.38	2.12	0.62	4653	2.89
1.0	0.50	3437	0.50	12274	7.86	0.38	2.13	0.62	8241	5.11
T (K) = 313										
0.0	0.50	274	0.50	982	0.63	0.39	1.28	0.61	670	0.41
0.2	0.49	334	0.51	1197	0.77	0.39	1.16	0.61	814	0.50
0.4	0.49	477	0.51	1706	1.10	0.39	1.08	0.61	1156	0.71
0.6	0.49	696	0.51	2495	1.61	0.39	1.00	0.61	1692	1.03
0.8	0.48	800	0.52	2876	1.88	0.39	0.98	0.61	1660	1.01
1.0	0.49	1336	0.51	4784	3.09	0.39	0.96	0.61	3224	1.97
T (K) = 318										
0.0	0.49	202	0.51	723	0.47	0.39	1.37	0.61	497	0.30
0.2	0.49	240	0.51	862	0.56	0.39	1.28	0.61	526	0.32
0.4	0.49	340	0.51	1220	0.79	0.39	1.16	0.61	594	0.36
0.6	0.48	484	0.52	1737	1.14	0.40	1.08	0.60	652	0.39
0.8	0.48	545	0.52	1954	1.28	0.40	1.06	0.60	1350	0.81
1.0	0.48	882	0.52	3164	2.07	0.40	1.05	0.60	2135	1.28

Table A5: Rotational relaxation parameters for C153 in [$0.78CH_3CONH_2$ + 0.22{f LiBr + (1-f) $LiNO_3$)] molten mixtures at different temperatures and compositions. These parameters have been obtained via bi-exponential fits to the measured $r(t)$ decays

T (K)	a_1	τ_1 (ps)	a_2	τ_2 (ps)	$\langle\tau_r\rangle$ (ps)
f_{LiBr} = 0.00					
303	39.33	15	60.67	5515	3351
313	33.94	17	66.06	3520	2331
318	31.64	8	68.36	2826	1934
333	31.85	12	68.15	1672	1143
348	33.94	21	66.09	1024	684
363	31.43	20	68.57	700	486
f_{LiBr} = 0.20					
303	40.92	18	59.08	5803	3436
313	37.35	14	62.65	4015	2521
318	34.04	19	65.96	3162	2092
333	31.42	24	68.58	1806	1246
348	33.68	20	66.32	1146	767
363	36.50	21	63.50	846	539
f_{LiBr} = 0.40					
303	48.80	17	51.20	7066	3626
313	42.69	22	57.31	4159	2393
318	38.60	25	61.40	3698	2280
333	32.62	15	67.38	2159	1460
348	33.14	27	66.86	1258	850
363	32.13	23	67.87	795	547
f_{LiBr} = 0.60					
303	48.55	14	51.45	8442	4350
313	45.15	16	54.85	5751	3162
318	39.87	21	60.13	4576	2760
333	34.53	9	65.47	2450	1607
348	33.25	28	66.75	1473	992
363	33.96	12	66.04	840	559
f_{LiBr} = 0.80					
303	51.95	9	48.05	9980	4800
313	48.43	23	51.57	7002	3622
318	41.89	15	58.11	5753	3349
333	34.53	19	65.47	2899	1904
348	32.71	21	67.29	1556	1054
363	32.29	25	67.71	906	621
f_{LiBr} = 1.00					
303	51.32	15	48.67	11900	5800
313	51.72	11	48.28	8744	4227
318	45.83	21	54.17	6662	3618
333	35.73	14	64.27	3880	2499
348	32.89	23	67.11	1846	1247
363	32.05	20	67.95	1074	736

Table A6: Fractional values of viscosity obtained from fitting of the measured $<\tau_s>$ and $<\tau_r>$ versus temperatures reduced viscosity, η/T with the relation $\mathrm{Log}[<\tau_x>] = B + p\mathrm{Log}[(\eta/T)]$, x being the solvation or rotation

f_{LiBr}	p^{solv}	p^{rot}
0.00	0.43	0.66
0.20	0.38	0.62
0.40	0.30	0.56
0.60	0.26	0.54
0.80	0.35	0.55
1.00	0.37	0.50

$$\left\langle p^{<\tau_r>}\right\rangle \Big/ \left\langle p^{<\tau_s>}\right\rangle = 0.57/0.35 \approx 1.6$$

Table A7: Some physical properties of the molten {alkylamide + $LiClO_4$} mixtures for different alkyl chain lengths and temperatures.

T (K)	η (cP)	ρ (gm/cc)	u (m/s)	n_D	V_m (cc/mol)	k_s (10^{-7} cms^2gm^{-1})
			AM + $LiClO_4$			
303	158.36	1.230799	1576.82	1.44041	55.53	3.2677
308	115.64	1.226882	1564.47	1.43994	55.71	3.3301
313	86.98	1.222944	1554.19	1.43999	55.89	3.3852
318	66.54	1.219008	1542.98	1.43897	56.07	3.4456
323	52.10	1.215082	1531.85	1.43665	56.25	3.5072
328	33.74	1.211157	1520.79	1.43529	56.43	3.5699
333	29.11	1.207282	1510.00	1.43369	56.61	3.6327
338	26.84	1.203378	1499.01	1.42980	56.79	3.6981
343	23.77	1.199485	1488.00	1.42844	56.98	3.7652
348	19.62			1.42783		
			PM + $LiClO_4$			
303	89.84	1.154491	1509.85	1.44352	68.96	3.7996
308	65.31	1.150825	1498.32	1.44141	69.18	3.8706
313	51.30	1.146778	1485.67	1.44033	69.43	3.9507
318	41.18	1.143151	1474.35	1.43914	69.65	4.0243
323	33.57	1.138939	1462.11	1.43781	69.90	4.1071
328	27.68	1.135479	1450.60	1.43641	70.12	4.1852
333	21.13	1.131648	1438.90	1.43360	70.36	4.2680
338	16.55	1.127814	1427.41	1.43122	70.59	4.3517
343	14.10	1.123979	1415.97	1.42889	70.84	4.4374
348	11.12			1.42778		
			BM + $LiClO_4$			
303	205.45	1.093375	1468.51	1.44588	83.13	4.2410
308	142.28	1.089202	1454.92	1.44389	83.45	4.3372
313	105.45	1.085697	1441.44	1.44197	83.72	4.4330
318	78.35	1.082059	1428.40	1.44070	84.00	4.5294
323	60.95	1.078821	1415.29	1.43950	84.26	4.6276
328	47.95	1.074740	1402.92	1.43811	84.58	4.7275
333	38.53	1.071574	1390.03	1.43670	84.83	4.8298
338	32.31	1.067597	1377.89	1.43523	85.14	4.9335
343	25.86	1.064148	1365.39	1.43375	85.42	5.0406
348	21.53			1.43165		

Table A8: Fluorescence life times (τ_{life}) of solutes (ANS, C153, PRODAN and DMASBT) obtained from fitting of magic angle decays in various deep eutectics.

Mixtures	τ_{life} /ps
ANS	
AM + $LiClO_4$	5150
PM + $LiClO_4$	5500
BM + $LiClO_4$	5800
C153	
AM + $LiClO_4$	3800
PM + $LiClO_4$	3870
BM + $LiClO_4$	3900
PRODAN	
AM + $LiClO_4$	2800
PM + $LiClO_4$	2700
BM + $LiClO_4$	2900
DMASBT	
AM + $LiClO_4$	520
PM + $LiClO_4$	500
BM + $LiClO_4$	650

Table A9: Calculated dynamic Stokes shifts of C153 in three deep eutectics made of acetamide, propionamide and butyramide with $LiClO_4$ at various temperatures.

T (K)	$\Delta\nu_{sd}$ (cm^{-1})	$\Delta\nu_{si}$ (cm^{-1})	$\Delta\nu_{total}$ (cm^{-1})
AM + $LiClO_4$			
303	1267	476	1743
308	1241	474	1715
313	1212	471	1683
318	1192	470	1662
323	1169	468	1637
328	1146	466	1612
PM + $LiClO_4$			
303	921	430	1351
308	904	428	1332
313	887	427	1314
318	871	425	1296
323	855	423	1278
328	840	421	1261
BM + $LiClO_4$			
303	741	396	1137
308	728	394	1122
313	715	392	1107
318	703	391	1094
323	691	389	1080
328	679	387	1066

Table A10: Fit parameters of solvent response function ($S(t)$) for C153 in molten {alkylamide + LiClO4} mixtures at various alkyl chain length and temperatures.

T (K)	a_1	τ_1 (ps)	a_2	τ_2 (ps)	$<\tau_s>$ (ps)
AM + $LiClO_4$					
303	0.5784	86	0.4216	909	433
308	0.6440	48	0.3560	909	354
313	0.7282	45	0.2718	833	259
318	0.7400	48	0.2600	769	235
323	0.7420	47	0.2580	625	196
328	0.7200	52	0.2800	500	177
PM + $LiClO_4$					
303	0.5749	69	0.4251	833	394
308	0.5561	44	0.4439	714	341
313	0.7000	62	0.3000	769	275
318	0.6839	30	0.3161	769	264
323	0.7100	50	0.2900	714	243
328	0.7300	55	0.2700	667	220
BM + $LiClO_4$					
303	0.4345	55	0.5655	909	538
308	0.5002	109	0.4998	909	509
313	0.5646	125	0.4354	833	433
318	0.5593	137	0.4407	769	416
323	0.5057	80	0.4943	714	394
328	0.6632	123	0.3368	769	341

Table A11: Anisotropy decay ($r(t)$) parameters of C153 in molten {alkylamide + $LiClO_4$} mixtures at various alkyl chain lengths and temperatures.

T (K)	a_1	τ_1 (ps)	a_2	τ_2 (ps)	$\langle\tau_s\rangle$ (ps)
AM + $LiClO_4$					
303	0.41	6	0.59	5937	3505
308	0.38	8	0.62	4851	3011
313	0.33	14	0.67	4056	2722
318	0.34	22	0.66	3072	2035
323	0.33	15	0.67	2574	1729
328	0.31	15	0.69	1953	1352
333	0.29	15	0.71	1613	1150
338	0.28	15	0.72	1364	986
348	0.29	15	0.71	823	589
PM + $LiClO_4$					
303	0.37	15	0.63	4023	2540
308	0.36	47	0.64	3362	2169
313	0.34	10	0.66	2785	1841
318	0.34	34	0.66	2294	1526
323	0.34	36	0.66	1943	1295
328	0.35	37	0.65	1621	1067
333	0.36	40	0.64	1427	928
338	0.36	36	0.64	1189	774
348	0.39	38	0.61	761	479
BM + $LiClO_4$					
303	0.49	11	0.51	5894	3011
308	0.47	10	0.53	4646	2467
313	0.44	20	0.56	4035	2268
318	0.41	19	0.59	3448	2042
323	0.39	26	0.61	3073	1885
328	0.37	33	0.63	2762	1752
333	0.37	30	0.63	2268	1440
338	0.39	41	0.61	1817	1124
348	0.41	40	0.59	1174	709

Table A12: Emission frequencies of C153 from steady state ($\nu(ss)$) and from time-resolved ($\nu(\infty)$) measurements in charged (AOT) and neutral (IGPAL) reverse micelles for two representative pool diameters.

	AOT			IGPAL		
$d(nm)$	$\nu(ss)/cm^{-1}$	$\nu(\infty)/cm^{-1}$	$\{\nu(ss)-\nu(\infty)\}/cm^{-1}$	$\nu(ss)/cm^{-1}$	$\nu(\infty)/cm^{-1}$	$\{\nu(ss)-\nu(\infty)\}/cm^{-1}$
2.16	18830	18000	830	19050	18300	750
6.91	18400	17750	665	19030	18250	780

Table A13: Bi-exponential fit parameters of the measured solvation response functions, $S(t)$, for C153 in AOT RMs at several pool diameters.

AOT					
d (nm)	a_1	τ_1 (ps)	a_2	τ_2 (ps)	$<\tau_s>$ (ps)
1.10	0.264	41.0	0.736	1000.0	747
2.16	0.438	30.0	0.562	714.0	414
3.30	0.218	55.0	0.782	417.0	338
4.06	0.424	51.0	0.576	400.0	252
5.20	0.519	38.0	0.481	333.0	180
5.96	0.643	27.0	0.357	303.0	126
6.91	0.651	32.0	0.349	278.0	118

Table A14: Bi-exponential fit parameters of the measured solvation response functions, $S(t)$, for C153 in IGPAL reverse micelles at different pool diameters.

IGPAL					
d (nm)	a_1	τ_1 (ps)	a_2	τ_2 (ps)	$<\tau_s>$ (ps)
1.40	0.127	48.0	0.873	556.0	491
2.16	0.105	55.0	0.895	500.0	453
3.30	0.233	68.0	0.767	500.0	399
4.06	0.276	32.0	0.724	500.0	371
5.20	0.273	48.0	0.727	476.0	359
5.96	0.352	39.0	0.648	476.0	322
6.91	0.396	54.0	0.604	476.0	309

Table A15: Tri-exponential fit parameters for layer-wise decays of the simulated reorientational correlation functions of water molecules in charged (AOT) and neutral (IGPAL) RMs. Layer #1 is the interfacial layer.

Layer#	Radius (A^0)	a_1	τ_1 (ps)	a_2	τ_2 (ps)	a_3	τ_3 (ps)	$<\tau>$ (ps)
AOT (d = 2.2 nm)								
1	12.5-8.5	0.32	0.46	0.10	20.0	0.58	2761.0	1604
2	8.5-4.5	0.47	0.83	0.25	37.0	0.27	1587.0	438
3	4.5-0	0.58	0.50	0.28	9.0	0.14	227.0	35
AOT (d = 5.2 nm)								
1	27.5-23.5	0.41	0.50	0.27	176.0	0.32	1976.0	680
2	23.5-19.5	0.55	0.80	0.39	16.0	0.047	763.0	43
3	19.5-15.5	0.44	0.35	0.39	3.25	0.17	8.46	2.86
4	15.5-11.5	0.42	0.34	0.37	2.97	0.20	6.9	2.62
5	11.5-7.5	0.44	0.36	0.48	3.40	0.07	9.0	2.42
6	7.5-0	0.44	0.36	0.48	3.45	0.07	8.9	2.43
AOT (d = 6.9 nm)								
1	35-31	0.38	0.50	0.27	15.0	0.347	1342.0	470
2	31-27	0.51	0.60	0.42	12.0	0.07	163.0	17
3	27-23	0.48	0.50	0.45	5.5	0.06	26.0	4.27
4	23-19	0.43	0.36	0.40	3.0	0.16	9.0	2.79
5	19-15	0.36	0.03	0.29	2.0	0.35	6.0	2.69
6	15-11	0.40	0.30	0.32	3.0	0.27	6.0	2.70
7	11-7	0.44	0.38	0.51	4.0	0.04	13.0	2.72
8	7-0	0.37	0.28	0.19	1.6	0.43	5.0	2.56
IGPAL (d = 2.2 nm)								
1	12.5-8.5	0.57	0.61	0.29	4.0	0.14	295	43
2	8.5-4.5	0.49	0.45	0.46	3.93	0.05	34.48	3.75
3	4.5-0	0.42	0.38	0.56	2.74	0.008	4.16	1.73
IGPAL (d = 5.2 nm)								
1	27.5-23.5	0.42	0.52	0.28	13.44	0.29	820.0	242
2	23.5-19.5	0.55	0.78	0.39	11.11	0.055	250.0	19
3	19.5-15.5	0.37	0.29	0.31	1.70	0.31	4.0	1.87
4	15.5-11.5	0.37	0.30	0.34	1.72	0.28	3.7	1.73
5	11.5-7.5	0.30	0.15	0.25	1.09	0.44	2.85	1.57
6	7.5-0	0.31	0.34	0.22	1.45	0.41	2.80	1.57
IGPAL (d = 6.9 nm)								
1	35-31	0.33	0.69	0.347	15.38	0.32	694.0	228
2	31-27	0.37	0.73	0.50	9.9	0.122	731.0	94
3	27-23	0.36	0.70	0.50	10.0	0.135	312.0	47
4	23-19	0.40	0.64	0.57	5.95	0.025	106.38	6.31
5	19-15	0.31	0.42	0.488	3.22	0.199	9.0	3.49
6	15-11	0.27	0.33	0.38	2.38	0.35	7.148	3.49
7	11-7	0.29	0.38	0.47	3.0	0.22	8.33	3.35
8	7-0	0.29	0.39	0.34	2.4	0.37	5.98	3.14

Table A16: Rotational relaxation parameters for C153 in charged (AOT) and neutral (IGPAL) RMs at different pool diameters. These parameters have been obtained via bi-exponential fits to the measured ($r(t)/r(0)$) decays. Numbers in parenthesis are from another set of independent measurements.

d (nm)	a_1	τ_{r1} (ps)	a_2	τ_{r2} (ps)	$<\tau_r>$ (ps)
AOT					
1.10	0.64(0.71)	22(13)	0.36(0.29)	1311(1575)	486(466)
2.16	0.63(0.67)	25(19)	0.37(0.33)	1184(1289)	454(438)
3.30	0.58(0.63)	21(16)	0.42(0.37)	1006(1011)	435(384)
4.06	0.63(0.65)	31(19)	0.37(0.35)	964(913)	376(332)
5.20	0.58(0.65)	18(16)	0.42(0.35)	854(867)	369(314)
5.96	0.55(0.62)	20(18)	0.45(0.38)	763(751)	354(297)
6.91	0.54(0.63)	19(15)	0.46(0.37)	742(780)	352(298)
IGPAL					
1.40	1.00(1.00)	57(101)	-	-	57(101)
2.16	0.73(0.65)	30(18)	0.27(0.35)	712(698)	214(256)
3.30	0.68	28	0.32	933	318
4.06	0.67(0.64)	35(30)	0.33(0.36)	1050(855)	370(327)
5.20	0.63	28	0.37	1158	446
5.96	0.58(0.68)	16(39)	0.42(0.32)	1215(1183)	520(405)
6.91	0.58(0.63)	22(32)	0.42(0.37)	1278(1177)	550(456)

Table A17: Dynamic Stokes' Shift of C153 in polyethylene glycol in absence and presence of Li^+/K^+ Nitrate at various temperatures. Uncertainty associated with the measured shift is $\pm 200\,cm^{-1}$.

T (K)	ν^t_{est} ($10^3 cm^{-1}$)	ν^t_{obs} ($10^3 cm^{-1}$)	% missed
Pure Polyethylene Glycol (PEG)			
298	1.724	1.135	34
303	1.713	1.001	42
308	1.617	0.876	46
313	1.548	0.849	45
318	1.547	0.874	44
0.85PEG + 0.15{f KNO3 + (1-f) LiNO3}, f_{KNO_3} = 0.20			
298	1.642	1.095	33
303	1.316	1.043	21
308	1.405	0.995	29
313	1.506	1.012	33
318	1.331	1.037	22
328	1.216	0.936	23
0.85PEG + 0.15{f KNO3 + (1-f) LiNO3}, f_{KNO_3} = 0.80			
298	1.550	1.017	34
303	1.429	1.044	27
308	1.279	0.879	31
313	1.206	0.815	32
323	1.286	0.880	32
328	1.272	0.773	39

Table A18: Bi-exponential fit parameters of the experimentally measured solvation response functions for the PEG with and without Li^+/K^+ Nitrate at different temperatures and compositions

T (K)	a_1	τ_1 (ps)	a_2	τ_2 (ps)	$<\tau_s>$ (ps)
Pure Polyethylene Glycol (PEG)					
298	0.67	62	0.33	845	320
303	0.71	70	0.29	778	275
308	0.78	100	0.22	650	220
313	0.63	47	0.37	355	160
318	0.60	33	0.40	226	110
0.85PEG + 0.15{*f* KNO3 + (1-*f*) LiNO3}, f_{KNO_3} = 0.20					
298	0.64	67	0.36	1430	558
303	0.58	72	0.42	1102	504
308	0.59	54	0.41	956	424
313	0.65	94	0.35	916	382
318	0.60	58	0.40	770	343
328	0.68	74	0.32	750	290
0.85PEG + 0.15{*f* KNO3 + (1-*f*) LiNO3}, f_{KNO_3} = 0.80					
298	0.64	73	0.36	1110	446
303	0.70	56	0.30	1098	369
308	0.73	121	0.27	946	352
313	0.75	79	0.25	995	310
323	0.69	41	0.31	579	208
328	0.69	50	0.31	456	176

Table A19: Rotational relaxation parameters of C153 in PEG with Li^+/K^+ Nitrate mixtures for different compositions at 298 K

f_{KNO3}	a_1	τ_{r1} (ps)	a_2	τ_{r2} (ps)	$<\tau_r>$ (ps)
0.00	0.38	19	0.62	4120	2551
0.20	0.39	15	0.61	3809	2329
0.40	0.39	13	0.61	3621	2214
0.60	0.40	12	0.60	3573	2164
0.80	0.41	11	0.59	3324	1966
1.00	0.40	9	0.60	3150	1880

Table A20: Rotational relaxation parameters of C153 in the medium PEG with and without Li^+/K^+ nitrate at different compositions and temperatures

T (K)	η (cP)	a_1	τ_{r1} (ps)	a_2	τ_{r2} (ps)	$\langle\tau_r\rangle$ (ps)
Pure Polyethylene Glycol (PEG)						
298	70.44	0.27	24	0.73	2282	1672
303	54.29	0.26	26	0.74	1628	1211
308	42.62	0.27	25	0.73	1257	924
313	34.00	0.29	27	0.71	999	717
318	27.52	0.30	25	0.70	695	494
328	22.55	0.37	7	0.63	576	366
0.85PEG + 0.15{*f* KNO3 + (1-*f*) LiNO3}, f_{KNO_3} = 0.20						
298	140.70	0.39	15	0.61	3809	2329
303	105.80	0.37	21	0.63	2996	1895
313	63.34	0.38	18	0.62	2290	1427
318	50.71	0.37	24	0.63	1891	1200
323	41.15	0.38	17	0.62	1602	1000
328	33.89	0.36	34	0.64	1250	812
343	20.17	0.41	24	0.59	746	450
0.85PEG + 0.15{*f* KNO3 + (1-*f*) LiNO3}, f_{KNO_3} = 0.80						
298	125.60	0.41	11	0.59	3324	1966
303	94.41	0.39	20	0.61	2730	1673
308	72.89	0.41	19	0.59	2104	1249
313	57.40	0.34	28	0.66	1728	1150
323	37.33	0.42	34	0.58	1382	816
328	30.91	0.38	44	0.62	1073	682
343	18.49	0.35	15	0.65	644	424

Table A21: The biexponential fit parameters of fluorescence decays of P4C associated to LE band in water-DX and water-THF binary mixtures at all mole fractions.

Water + DX (LE decays)						Water + THF (LE decays)				
$f_{DX/THF}$	a_1	τ_1 (ps)	a_2	τ_2 (ps)	χ^2	a_1	τ_1 (ps)	a_2	τ_2 (ps)	χ^2
0.00	0.96	32	0.04	3291	1.01	0.96	32	0.04	3291	1.01
0.03	0.98	35	0.02	1459	1.21	0.97	53	0.03	1670	1.14
0.05	0.96	42	0.04	1007	1.02	0.98	71	0.02	1187	0.97
0.10	0.94	53	0.06	1237	1.21	0.98	106	0.02	700	1.16
0.15	0.89	82	0.11	1406	1.07	0.96	150	0.04	981	1.08
0.17	0.86	90	0.14	1527	1.09	0.96	154	0.04	1025	1.08
0.20	0.82	111	0.18	1526	0.98	0.95	179	0.05	1314	1.15
0.30	0.70	166	0.30	1877	1.03	0.90	224	0.10	1773	1.14
0.40	0.59	231	0.41	2133	1.00	0.82	261	0.18	1979	1.03
0.60	0.34	326	0.66	2515	1.00	0.64	312	0.36	2291	1.03
0.80	0.14	365	0.86	3032	0.95	0.48	329	0.52	2580	1.03
0.90	0.05	255	0.95	3301	1.00	0.28	281	0.72	2717	1.06
1.00	0.04	93	0.96	3514	0.98	0.11	182	0.89	2756	1.05

Calculation of dissection of total solvation response into solute-water and solute-interface interaction contribution:

The normalized solvation response function from the total fluctuating solvation energy can be written as

$$S_{tot}(t) = \frac{<\delta\Delta E(t).\delta\Delta E(0)>}{<\delta\Delta E(0).\delta\Delta E(0)>} \quad , \qquad (1)$$

In this case, $\Delta E(t) = \Delta E_w(t) + \Delta E_s(t)$ where $\Delta E(t)$ is the total energy fluctuation, $\Delta E_w(t)$ and $\Delta E_s(t)$ are the contributions coming from the solute-water and solute-interface interactions, respectively. Using this approximate separation between these two contributions we can write

$$\begin{aligned}
&<\delta\Delta E(t).\delta\Delta E(0)> \\
&=<\{\delta\Delta E_s(t) + \delta\Delta E_s(t)\}.\{\delta\Delta E_w(0) + \delta\Delta E_s(t)\}> \\
&=<\delta\Delta E_w(t).\delta\Delta E_w(0) + \delta\Delta E_s(t).\delta\Delta E_w(0) + \delta\Delta E_w(t).\delta\Delta E_s(0) + \delta\Delta E_s(t).\delta\Delta E_s(0)>. \quad (2)
\end{aligned}$$

We now assume that the timescales associated with the fluctuations in solute-surface and solute-water interaction energies are decoupled. This is based on the assumption that water, no matter where it is located inside the RMs, moves much faster than the solute. Therefore, $<\delta\Delta E_s(t).\delta\Delta E_w(0)>$ and $<\delta\Delta E_w(t).\delta\Delta E_s(0)>$ goes identically to zero and we get,

$$<\delta\Delta E(t).\delta\Delta E(0)> =<\delta\Delta E_w(t).\delta\Delta E_w(0)> + <\delta\Delta E_s(t).\delta\Delta E_s(0)>, \ (3).$$

Hence ,

$$S_T(t) = \frac{<\delta\Delta E_w(t).\delta\Delta E_w(0)> + <\delta\Delta E_s(t).\delta\Delta E_s(0)>}{<\delta\Delta E_w(0).\delta\Delta E_w(0)> + <\delta\Delta E_s(0).\delta\Delta E_s(0)>}$$

$$= \frac{<\delta\Delta E_w(t).\delta\Delta E_w(0)>}{<\delta\Delta E_w(0).\delta\Delta E_w(0)> + <\delta\Delta E_s(0).\delta\Delta E_s(0)>} + \frac{<\delta\Delta E_s(t).\delta\Delta E_s(0)>}{<\delta\Delta E_w(0).\delta\Delta E_w(0)> + <\delta\Delta E_s(0).\delta\Delta E_s(0)>}$$

$$= \frac{<\delta\Delta E_w(t).\delta\Delta E_w(0)>}{<\delta\Delta E_w(0)^2> + <\delta\Delta E_s(0)^2>} + \frac{<\delta\Delta E_s(t).\delta\Delta E_s(0)>}{<\delta\Delta E_w(0)^2> + <\delta\Delta E_s(0)^2>}$$

$$= S_{sw}(t) + S_{si}(t), \ (4)$$

where $S_{sw}(t)$ represents the contribution from the solute-water interaction and $S_{si}(t)$ from the solute-interface interaction. Note the decays of $S_{tot}(t)$ and $S_T(t)$ may differ if the assumed decoupling between cross terms based on difference in fluctuating timescales does not hold. However, the analysis will still provide a qualitative understanding of the origin of the sub-nanosecond (or slower) timescale often reported by dynamic Stokes shift measurements with dipolar probes in aqueous reverse micelles. Eq. 4 forms the basis for analyzing the results shown in Fig. 10 of the text.

Chemical structures of the neutral (IGEPAL CO-520) and charged (AOT) surfactant molecules:

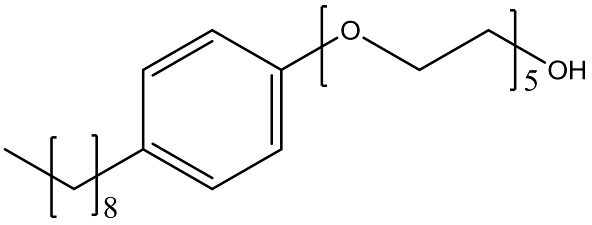

IGEPAL CO-520

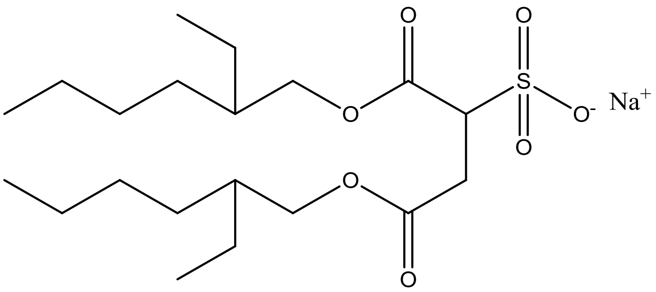

AOT